High-precision measurements of charge asymmetries at LHCb

Dufour, Laurent

High-precision measurements of charge asymmetries at LHCb

Cover: Charged tracks in the LHCb detector.

ISBN: 978-94-034-1896-4

This work is part of the research programme of the Foundation for Fundamental Research on Matter (FOM), which is part of the Netherlands Organisation for Scientific Research (NWO). The work is carried out at the National Institute for Subatomic Physics (Nikhef) in Amsterdam, The Netherlands.

rijksuniversiteit
groningen

High-precision measurements of charge asymmetries at LHCb

Proefschrift

ter verkrijging van de graad van doctor aan de
Rijksuniversiteit Groningen
op gezag van de
rector magnificus prof. dr. C. Wijmenga
en volgens besluit van het College voor Promoties.

De openbare verdediging zal plaatsvinden op

vrijdag 13 september 2019 om 16.15 uur

door

Laurent Johannes Iman Joseph Dufour

geboren op 14 juni 1988
te De Bilt

Promotores
Prof. dr. A. Pellegrino
Prof. dr. M.H.M. Merk

Copromotor
Dr. J.A.N. van Tilburg

Beoordelingscomissie
Prof. dr. D. Boer
Prof. dr. S. Bentvelsen
Prof. dr. T. Peitzmann

Contents

Chapter 1

Introduction

The universal description of physics from the smallest scales up to the phenomena in the observable universe has been a great success. Nonetheless, striking shortcomings exist in this success story, including a missing explanation for dark matter and for the large abundance of matter over antimatter. This seemingly distorted balance between matter and antimatter in our universe has caught the attention of physicists ever since the first observation of antimatter in the 1930s. Among others [1], a source of *CP* violation is required to explain the antimatter difference.

In 1964 the violation of *CP* symmetry was observed in neutral kaons. Nowadays, this phenomenon is attributed to the weak interaction, included in the Standard Model. The weak interaction is responsible for flavour-changing transitions, which for quarks are described by a unitary matrix, the so-called Cabibbo-Kobayashi-Maskawa (CKM) matrix [2]. Traditionally, the CKM matrix is expressed in the basis of mass eigenstates for the quarks, (d, s, b):

$$V_{\mathrm{CKM}} = \begin{pmatrix} V_{ud} & V_{us} & V_{ub} \\ V_{cd} & V_{cs} & V_{cb} \\ V_{td} & V_{ts} & V_{tb} \end{pmatrix} \quad . \tag{1.1}$$

The CKM matrix is fully described by only four independent, real parameters, one of which is responsible for the total amount of *CP* violation in the Standard Model. These parameters are only constrained by experimental measurements. Unfortunately, the measured *CP* violation is insufficient to explain the matter-antimatter difference in the universe. However, physics beyond the Standard Model can change the *CP* violation in the quark sector. By measuring *CP* violation in as many different decay channels as possible, one can overconstrain the parameters of the CKM matrix and eventually spot deviations due to physics beyond the Standard Model. Such tests of the consistency of the CKM model form the goal of flavour physics today.

CP violation was first observed for neutral kaons, mesons composed of a strange and a down quark, in the 1960s [3]. Approximately 40 years later, *CP* violation was

observed for mesons which contain a b quark, B mesons [4]. Several types of B mesons are exploited in tests of CP symmetry, including:

$$\begin{aligned} |B^0\rangle &= |\bar{b}d\rangle \quad , \quad |\overline{B}^0\rangle = |b\bar{d}\rangle \quad , \\ |B_s^0\rangle &= |\bar{b}s\rangle \quad , \quad |\overline{B}_s^0\rangle = |b\bar{s}\rangle \quad , \\ |B^+\rangle &= |\bar{b}u\rangle \quad , \quad |B^-\rangle = |b\bar{u}\rangle \quad . \end{aligned} \tag{1.2}$$

Decays of B mesons include transitions of the b quark to quarks of many different generations, which make them excellent probes of the CKM model. Moreover, due to the large mass difference between the heavy b quark and the u, d or s quark, effects related to the strong force can be approximated using heavy quark effective theory (HQET), with precise predictions available for some of the B meson properties. The study of B mesons is also convenient experimentally, as they have a relatively long lifetime, leading to a distinctive experimental signature that is helpful in their identification and detection.

Two dedicated experiments, Belle and BaBar, were designed specifically to test the CKM model using B^0 and B^+ mesons. These so-called B-factories exploit the production of $B^0 - \overline{B}^0$ and $B^+ - B^-$ mesons in $e^+ - e^-$ collisions. Also at the Large Hadron Collider (LHC), B mesons and baryons containing a b quark are produced abundantly. A dedicated B-physics experiment, LHCb, is designed to take advantage of the high production rate of b hadrons. As, in addition to b hadrons, also many other particles are created in proton-proton collisions, the rejection of backgrounds formed a crucial requirement in the design of the LHCb detector. LHCb has proven to be very successful [5–8].

The LHCb detector design and implementation are discussed in Part I. Here also original contributions to the detector operation are presented, including a study of the tracking performance degradation due to radiation damage and a determination of the impact of residual signals from the previous bunch-crossing, published in Ref. [9].

Novel physics results are presented in Part II. The improved understanding of the detector biases related to charge asymmetries obtained with the method described in chapter 5 was instrumental to reduce these to the per-mille level and rendered possible new high-precision measurements of CP asymmetries that led directly to two publications:

- LHCb collaboration, R. Aaij *et al.*, *Measurement of the CP asymmetry in B_s^0–$\overline{B}_s^0$ mixing*, Phys. Rev. Lett. **117** (2016) 061803, `arXiv:1605.09768`;
- LHCb collaboration, R. Aaij *et al.*, *Measurement of $D_s^\pm$ production asymmetry in pp collisions at $\sqrt{s} = 7$ and 8 TeV*, JHEP **08** (2018) 008, `arXiv:1805.09869`.

CP violation in $B_s^0 - \overline{B}_s^0$ mixing is a fundamental property of the $B_s^0 - \overline{B}_s^0$ meson system. The measurement in Ref. [10] is the most precise to date, to a level that is currently only accessible with the LHCb detector and the technical advances described in chapter 6.

The topic of Ref. [11], the measurement of the D_s^+ meson production asymmetry, is not discussed further in this thesis, as its physics content (different fragmentation models of open charm production) is a digression from the central topic of this dissertation.

Further developments in the detector calibration were required to ensure that future searches of physics beyond the Standard Model are not limited by shortcomings in the understanding of the detector performance. Part III presents these technical advances. After describing (Chapter 6) how experimental biases were reduced in the analysis presented in Part II, novel and improved methods for the detector calibration are discussed. An improved calibration of the detector bias for charged kaons has been developed [12] and is illustrated in detail in chapter 7; the uncertainty per fb^{-1} is reduced by more than a factor two in Run 2 in comparison to Run 1 of the LHC. In chapter 8, a novel method is proposed to probe directly the LHCb electron reconstruction efficiency, a crucial result for both measurements of *CP* asymmetries and the study of lepton universality. A publication describing this method is in preparation:

- LHCb collaboration, R. Aaij *et al.*, *Measurement of the electron reconstruction efficiency at LHCb*, to be submitted to JINST.

Finally, in chapter 9, an outlook is given on the potential precision for *CP* asymmetries in $B^0 - \overline{B}^0$ and $B_s^0 - \overline{B}_s^0$ mixing, based on the new methods presented in this dissertation.

Part I

The LHCb experiment

Chapter 2

The LHCb detector

The LHCb detector [13] is one of the four main experiments exploiting the hadron collisions at the Large Hadron Collider (LHC) at CERN. The detector is designed to study heavy-flavour physics by precision measurements of *CP* asymmetries and rare decays of b and c hadrons produced in proton-proton collisions. For most of its operational time, the LHC accelerates two beams of protons in opposite directions. The beams collided at a centre-of-mass energy of 7 TeV in 2011 and 8 TeV in 2012 (the so-called Run 1 of the LHC), and of 13 TeV from 2015 to 2018 (Run 2). Beauty and charm hadrons are produced copiously in such collisions and predominantly at small angles with respect to the beam axis. Therefore, the LHCb detector, shown schematically in Fig. 2.1, is designed as a forward spectrometer covering the region $2 \leq \eta \leq 5$, where the pseudorapidity is defined as

$$\eta = -\log\left[\tan\left(\frac{1}{2}\theta\right)\right],$$

θ denoting the angle with respect to the beam axis.

The charm and beauty hadrons are highly boosted in the laboratory frame. Having lifetimes of $\mathcal{O}(1\,\text{ps})$, they can fly several millimetres before decaying. Their relatively long lifetime is a distinctive feature in the high background environment of a hadron collider, that can be exploited by detectors with sufficient vertex resolution. The vertex resolution is also essential for measurements dependent on the proper time of the studied hadron, such as neutral-meson oscillations and time-dependent *CP* asymmetries. Moreover, the momentum resolution must be sufficient to provide a good invariant-mass resolution, such that true heavy-flavour decays can be discriminated from residual backgrounds. The LHCb detector is carefully designed to fulfil these requirements.

LHCb includes a high-precision tracking system surrounding the pp interaction region (the VELO), a large-area detector (the TT) located upstream of a dipole magnet with an average bending power of 4 Tm, and three tracking stations (T1–T3) placed downstream of the magnet. Two ring-imaging Cherenkov (RICH) detectors provide particle-identification (PID) information for charged particles that can be used to sep-

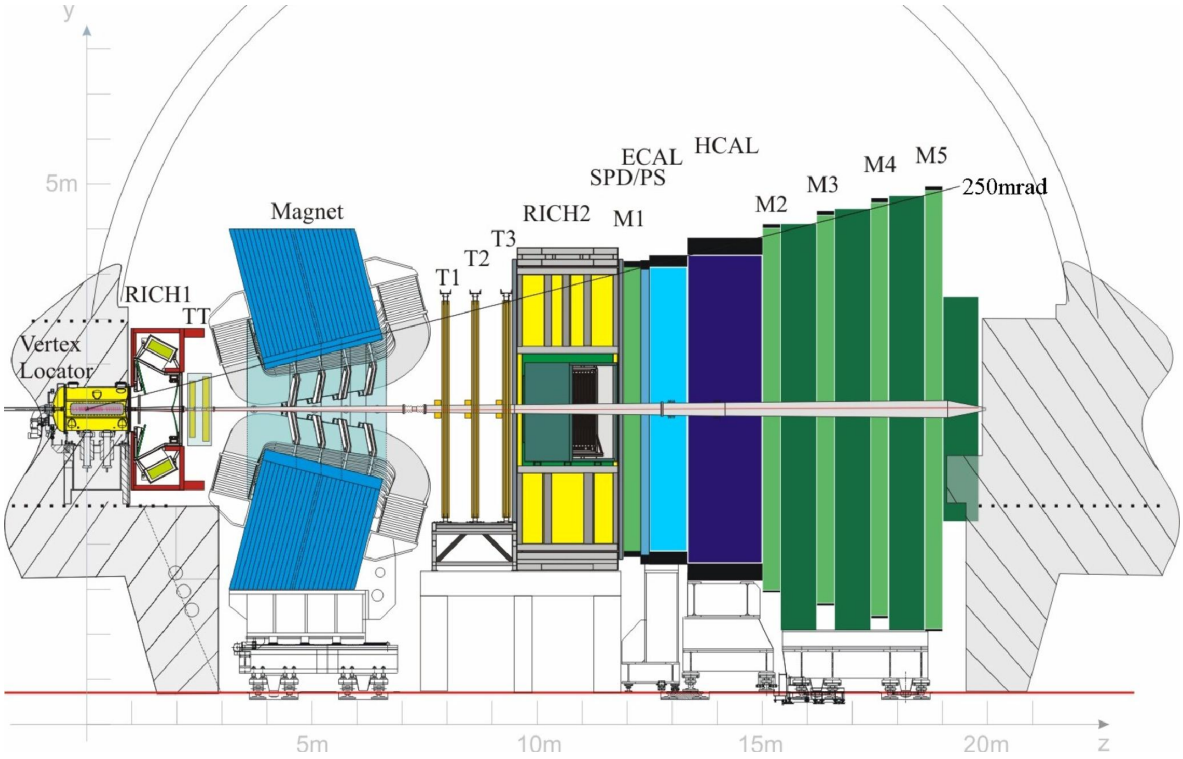

Figure 2.1: Schematic view of the LHCb detector, along with the used coordinate system. The x-axis is defined as $\hat{x} = \hat{y} \times \hat{z}$, pointing inwards for this schematic. Figure from Ref. [14].

arate decays such as $\Lambda_b^0 \to p\pi^-$ and $\Lambda_b^0 \to pK^-$. Two calorimeters (ECAL and HCAL) situated after the second RICH detector provide PID information for electrons, photons and neutral pions. Nearly all the particles that are of interest to LHCb deposit their energy in the two calorimeters, muons forming the only exception. A muon detector is therefore located downstream of the two calorimeters to identify these muons. Both the muon detector and the calorimeters are also used in the low-level trigger, discussed in Sect. 2.3.

The magnetic field, whose main component lies parallel to the y-axis, allows for an accurate measurement of the momentum of charged particles, and deflects oppositely charged particles towards opposite sides (in x) of the detector. Therefore, the difference in detection efficiency of oppositely charged particles crucially depends on the left-right symmetry of the detector downstream of the magnet. In order to reach the high precision desired for *CP* asymmetry measurements, any detection asymmetry must be controlled to a similarly high precision. To mitigate the effect of the detection asymmetry, the direction of the magnetic field is regularly flipped. This inverts the leading-order contributions due to the left-right asymmetry of the detector. Data sets of opposite magnet polarity are then combined, such that these leading-order contributions cancel. The

classification of the underlying sources of the detection asymmetry, along with contributions which could jeopardise the cancellation, is one of the main topics of this thesis (Chapter 6).

The proton beams collide in LHCb at an angle. The crossing angles, θ_x and θ_y, are defined as the half-angles between the two beams in the $x - z$ and $y - x$ plane, respectively. The crossing angle is decomposed in an external crossing angle, determined by the LHC, and an internal crossing angle, introduced by the LHCb magnet and the compensator magnets placed symmetrically opposite to the interaction point. The LHCb dipole magnet deflects the two beams in opposite directions in the $x - z$ plane and thus the reversal of the field polarity leads to a different crossing angle between the two beams. The magnitude of the internal crossing angle is inversely proportional to the beam energy, as the shift in p_x due to the Lorentz force is approximately constant for all beam energies. An overview of the crossing angles at LHCb for proton-proton collisions in different years is presented in Table 2.1. The total crossing angle can be negative. This is achieved by first exchanging the beams in additional crossing points, before and after the LHCb experiment, as shown in Fig. 2.2.

2.1 Main tracking detectors

Charged particles deposit a fraction of their energy as they traverse the detector material. The tracking detectors record this information in the form of hits, allowing for the reconstruction of the particle's trajectory, a track. Most of the tracks used in the analysis presented in this thesis are reconstructed using hits in the VELO and hits in the T-stations downstream of the magnet. These detectors are discussed in more detail in the next sections.

Table 2.1: Crossing angles over the years for magnet up conditions. For magnet down, the internal crossing angle is negative, but has the same magnitude. The change in the internal crossing angle is related to the change in beam energy over the years. The external crossing angle was left unchanged between the magnet polarities.

Year	$\theta_x^{internal}$ [µrad]	$\theta_x^{external}$ [µrad]	$\theta_y^{external}$ [µrad]
2011	270	−250	0
2012	236	0	100
2015	145	−250	0
2016	145	−250	0
2017	145	−250	0

2.1.1 VELO

The VELO, an acronym for VErtex LOcator, is a silicon-strip detector consisting of two halves that surround the interaction region, as shown schematically in Fig. 2.3. Each half consists of 21 modules positioned perpendicular to the z axis. The two detector halves overlap partially during operation to ensure the full angular coverage at high pseudorapidity. Each module contains one sensor that measures the radial coordinate, r, and one sensor that measures the azimuthal coordinate, ϕ. The sensors have an approximate half-circular shape.

The longer the extrapolation from the first measurement to the interaction region, the larger is the uncertainty in the reconstructed vertex position. The detector is therefore placed as close as possible to the collision point. The sensitive area of the sensors starts at 7 mm from the beam axis. The sensors retract during the LHC injection to ensure the detector's safety. There is no beampipe through this detector; instead, a thin aluminium foil separates the beam vacuum from the VELO vessel. Before any particle reaches the VELO modules, it has to traverse this so-called "RF foil". Elastic scattering of particles before the first measurement decreases the angular resolution dramatically. Therefore, the RF foil is as thin as possible.

Tracks originating from a displaced secondary vertex, for example from b-hadron decays, are identified by their impact parameter (IP). The IP is defined as the smallest distance from the particle trajectory to the primary vertex (PV). As more primary vertices can be present in a single bunch crossing, detached tracks are selected by requiring a minimum IP with respect to any PV. The strong discrimination power of the IP and the excellent proper-time resolution, both the result of the vertex resolution, make the VELO essential for the success of LHCb.

2.1.2 Downstream tracking stations

The particle flux produced by the proton-proton collisions is highest in the region close to the beampipe. Therefore, the T-stations consist of two detector technologies: the inner tracker, a silicon-strip detector covering the region close to the beampipe, and the outer tracker, a straw drift-tube detector covering the rest of the geometrical acceptance.

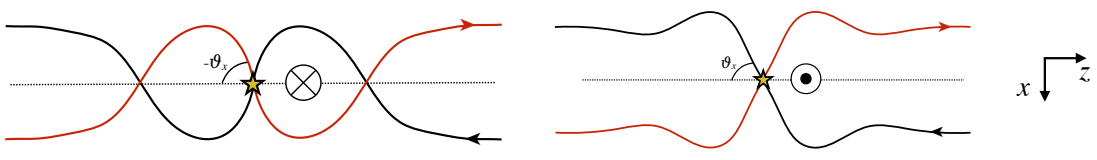

Figure 2.2: Schematic view of the beam-crossing angle in the (left) LHCb magnet up configuration and (right) LHCb magnet down configuration. A description of the different crossing configurations is presented in Ref. [15].

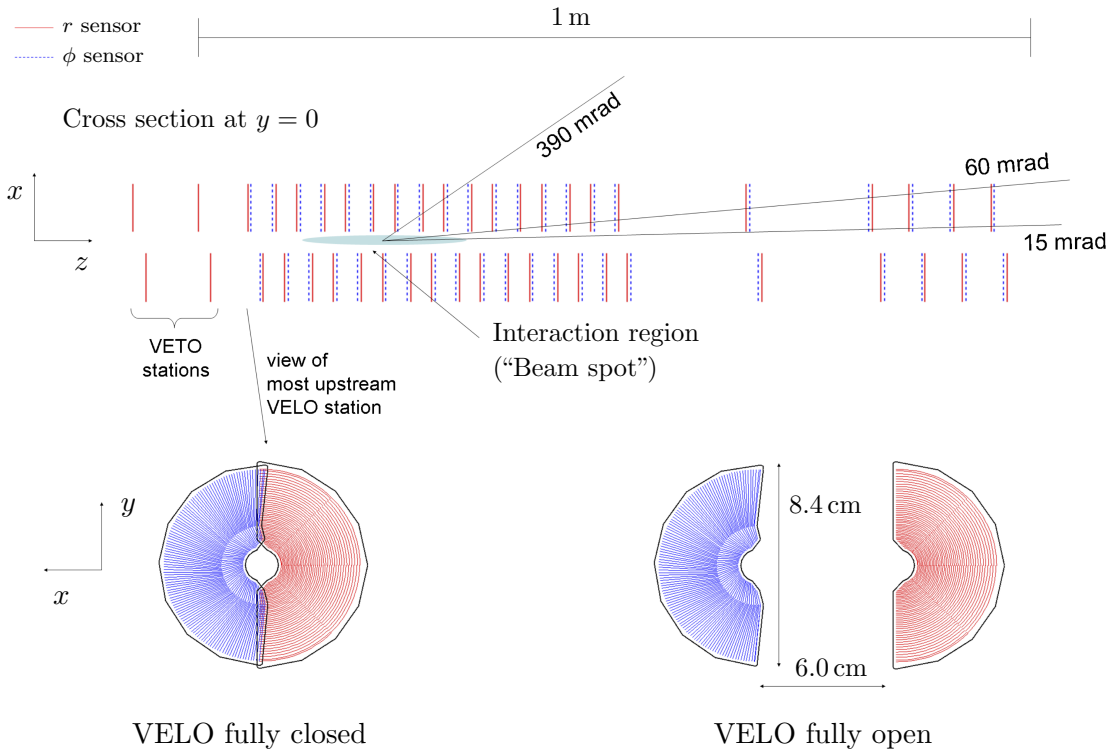

Figure 2.3: Schematic view of the VELO detector. Figure taken from Ref. [13].

Each of these detectors has four detection layers in an $x - u - v - x$ arrangement for each of the three stations. The two x layers are composed of vertical detector elements, and the u and v layers are composed of elements rotated by a stereo angle of $-5°$ and $+5°$, respectively. This configuration allows for a measurement of both the x and y coordinate of a traversing particle.

The inner tracker (IT) [16] covers the cross-shaped region closest to the beampipe, as shown in Fig. 2.4. Its support structure and cables are placed inside the geometric acceptance. Therefore, the material budget of the T-stations is non-uniform. The consequences of this design are discussed later, in sect. 6.2.2. The average hit resolution of the IT is 54.9 µm [17], allowing for an accurate measurement of the particle's momentum.

The outer tracker (OT) [18] is a gaseous straw detector, shown in Fig. 2.6. Each layer is divided in four quadrants, in turn consisting of nine half modules. Each module consists of two staggered layers of straws, called "monolayers". The straws have with an inner diameter of 4.9 mm, an anode wire in the centre and are filled with a gas mixture of argon, CO_2 and oxygen (with a ratio of 80%/28.5%/1.5%). This composition allows for a spatial resolution of approximately 170 µm [9].

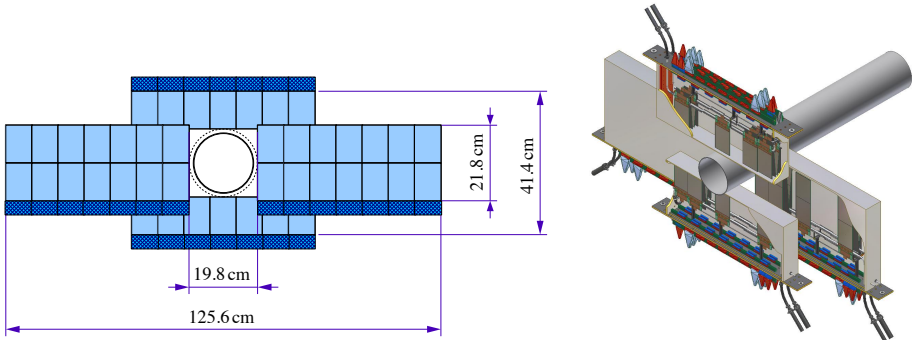

Figure 2.4: (left) Schematic view of an x-detection layer of the inner tracker, with the sensitive sensors in light blue and the readout electronics in dark blue. The small overlap between sensitive layers is visible. (right) A three-dimensional impression of the inner tracker boxes surrounding the beampipe. Illustrations from Ref. [13].

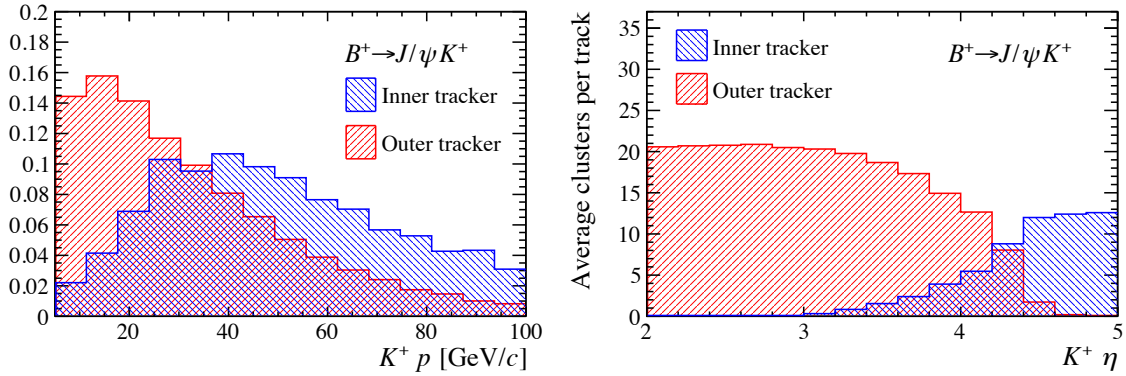

Figure 2.5: (left) The reconstructed momentum distribution for kaons in $B^+ \to J/\psi K^+$ decays. The distributions are made by requiring at least 10 clusters (out of 24) in the OT, or 5 (out of 12) clusters in the IT. (right) The number of clusters used to reconstruct the track as a function of pseudorapidity for kaons in $B^+ \to J/\psi K^+$ decays. For both illustrations only long tracks are considered, reconstructed in $\sqrt{s} = 13\,\text{TeV}$ proton-proton collision data recorded in 2017.

The OT hit resolution is worse than that of the IT. However, since the average momentum of particles traversing the OT is lower than that for the IT, as is shown in Fig. 2.5, this lower hit resolution is sufficient. For these momenta, the momentum resolution is dominated by multiple scattering [19], rather than by the hit resolution.

The different geometric coverage of the IT and the OT is clear when considering their relevance as a function of a particle's pseudorapidity. Figure 2.5 shows the distribution of hits in the IT and OT as a function of pseudorapidity for reconstructed charged kaons in $B^+ \to J/\psi K^+$ decays, selected in data recorded in 2017. At high pseudorapidity, $\eta > 4.3$, the IT is more relevant, while the OT is more relevant for $\eta < 4.0$.

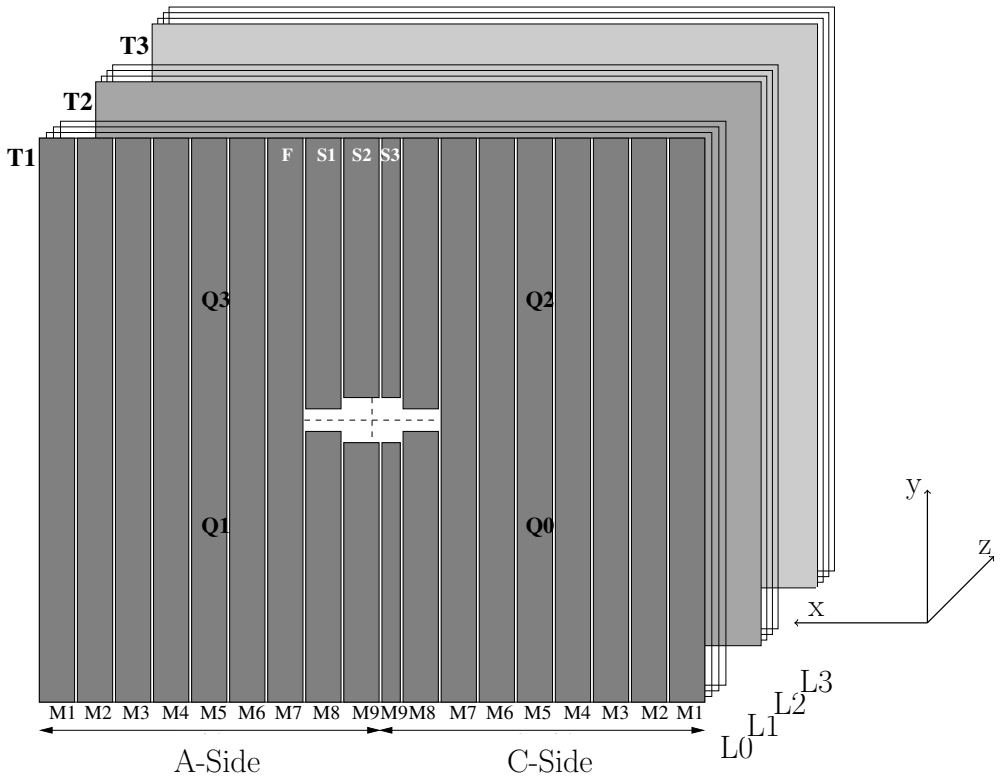

Figure 2.6: Schematic view of the OT, showing the arrangement of the OT modules and the naming scheme.

2.2 Track reconstruction

The track reconstruction consists of two separate phases. The pattern recognition, or track finding, combines the hit information of the subdetectors to form a track using initial values for the track parameters, which are the flight path of the particle and its momentum. The track fit subsequently finds the best values for the track parameters, and their corresponding errors. The track fit is described in detail in Ref. [19], and only the general scheme of the track finding, along with the different track types, is presented here.

2.2.1 Track types

The following track types are defined for LHCb (also shown in Fig. 2.7 for clarity):

- **VELO tracks** are made out of at least three hits in the r-sensors and at least three hits in the ϕ-sensors. If possible, these tracks are extended to the other subdetectors, then forming upstream or long tracks, defined below. The magnetic field in the VELO is negligible. Therefore, only the direction of the particle can

be inferred from the hits, and no information on its charge or momentum can be deduced. For most physics analyses, VELO tracks that are not extended are only used for the reconstruction of primary vertices.

- **T-tracks** are made out of at least one hit in both the x and stereo-layers for each of the T-stations. If possible, these tracks are extended to long tracks or downstream tracks.

- **Upstream tracks** are made out of VELO tracks with additional TT hit information. Because the deflection between the VELO and TT due to the magnetic field is limited, a momentum resolution of only $\delta p/p \approx 15\%$ is achieved. The reconstruction of these tracks is useful for low-momentum particles that are bent out of the acceptance in the dipole magnet.

- **Downstream tracks** are made out of T-tracks with additional TT hit information. This track type is mostly used for the reconstruction of K_{S}^0 and Λ decays, as these particles often decay outside the VELO acceptance. The momentum resolution is comparable to that of long tracks.

- **Long tracks** are made out of hits in both the VELO and the T-stations. Long tracks must meet the requirements for both a T-track and VELO track. When possible, hits from the TT are added, improving the momentum resolution. Long tracks have an accurate momentum measurement and form the main track type used in physics analyses. For particles with $p < 10\,\mathrm{GeV}/c$, a momentum resolution of $\delta p/p \approx 0.5\%$ is achieved, increasing to 1.0% at $200\,\mathrm{GeV}/c$.

2.2.2 Track finding

The pattern recognition starts with forming tracks using only hits in the VELO and tracks using only hits in the T-stations. These VELO and T-tracks are then used as seeds for the long, upstream or downstream tracking algorithms. A complete overview of the track finding strategies can be found in Ref. [19]. The general strategies for the track-finding algorithms relevant to this thesis are the following:

- **VELO tracking:** VELO tracks are formed with the use of the VELO hits in both r and ϕ sensors. The trajectories can be approximated by straight lines by the low magnetic field, simplifying the track finding.

- **Forward tracking:** VELO tracks are combined with hits in the T-stations to form long tracks.

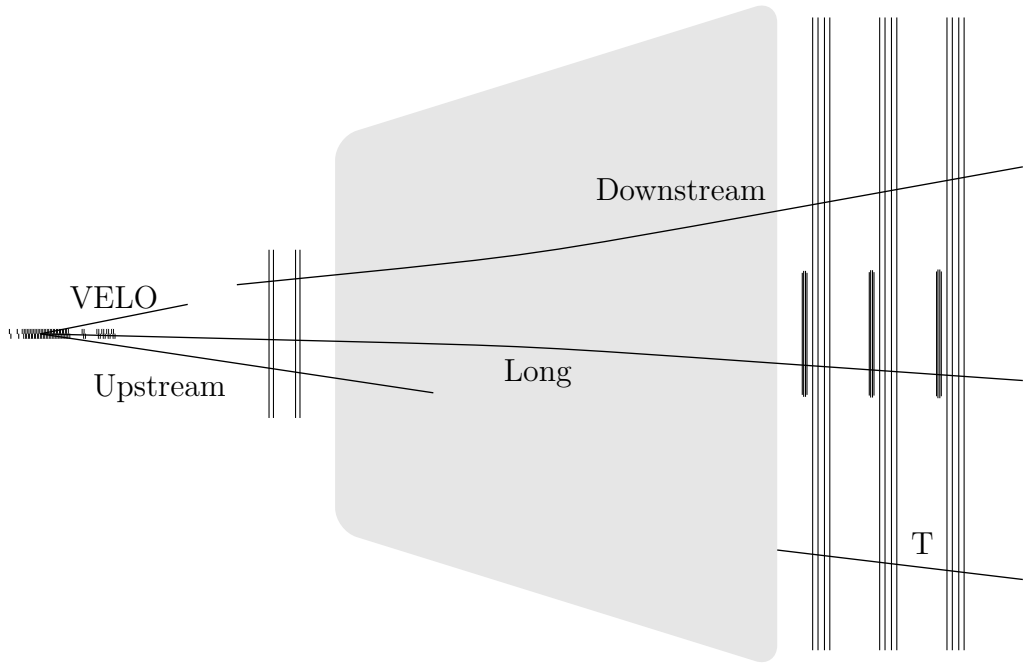

Figure 2.7: Schematic view of the different track types. Figure from Ref. [20].

- **T-seeding:** Tracks are formed with the use of all T-station hit information. Initially only the x layers are used, and the stereo layers are later added to reject random hit combinations.
- **Track matching:** The VELO tracks are combined with the result from the T-seeding to form long tracks.
- **Downstream tracking:** Tracks from the T-station are propagated back through the magnetic field, adding hits from the TT detector.

To protect against incorrectly reconstructed tracks, which are called "ghosts" and are composed of unrelated hits, all tracks must satisfy a number of quality requirements. When the track fit determines the track parameters along with their errors, a χ^2 based on the residuals of the hits with respect to the fitted track trajectory is calculated. All tracks are required to satisfy $\chi^2/\text{ndf} < 4$, where ndf stands for the number of degrees of freedom[1]. To reduce the ghost rate further, a neural network is used [21], the most important inputs of which are the χ^2 for each tracking detector, the kinematic properties and the number of hits on the track.

Both the forward tracking and the track matching provide long-track reconstruction. In case two long tracks are found that are similar, i.e. where for both the T-station

[1]For a long track, the number of degrees of freedom is nHits $-$ 5, where nHits denotes the number of hits on the track.

and the VELO more than 50% of the hits overlap, and both tracks satisfy all quality requirements, only the track with most hits is saved.

2.3 Online event selection

The online event selection of LHCb consists of a hardware and a software trigger [22]. The hardware trigger is based on information from the calorimeter and the muon detectors. The muon trigger selects events based on the p_{T} inferred in the muon detector, a typical requirement being $p_{\mathrm{T}} > 1.76\,\mathrm{GeV}/c$ (2012) [23]. The calorimeters are used to select events based on the transverse energy, with a typical requirement of $E_{\mathrm{T}} > 3.7\,\mathrm{GeV}$ for hadrons.

The software stage, the high-level trigger (HLT), is split in two levels. In the first level, HLT1, a partial event reconstruction is performed using a simplified track reconstruction. This track reconstruction has stringent requirements on the minimal p_{T} of the track and, since Run-2 of the LHC, is limited to tracks reconstructed with the use of the TT detector. These stringent requirements are motivated by the limited processing time available per event, as the minimal p_{T} requirement reduces the number of candidate tracks per event and speeds up the track finding process. The thresholds have changed over the years of data taking to reflect the available computing power and the improvements in the reconstruction algorithms [24].

The second level of the software trigger, HLT2, processes a sufficiently low number of events to perform an event reconstruction that is close to the one performed offline. In Run 1, the processing time available per event was still limited. Time was saved by only reconstructing tracks with $p_{\mathrm{T}} > 500\,\mathrm{MeV}/c$ and $p > 5\,\mathrm{GeV}/c$, a condition that was removed completely in Run 2. This does not mean that all the B decay products need to satisfy these requirements, as most B decays are selected by more inclusive trigger lines. This inclusive selection is predominantly performed by the so-called topological trigger [25], which selects n-body displaced decays ($n \geq 2$) based on their reconstructed invariant mass, impact parameter and momentum transverse to the flight direction. The typical selection efficiency of HLT2 for B decays is high, of the order of $60 - 70\%$ [26].

Since Run 2 of the LHC, all data processed by HLT1 is buffered on local disks. This allows for the detector calibration and alignment to run before the execution of HLT2. In addition, more processing time per event is permitted, which is used to perform the full, offline-quality event reconstruction, including particle-identification information. As the offline reconstruction for such events is no longer needed, reconstructed data can be immediately made available for analyses. By stripping these data of any information unrelated to the decay of interest, the event size is reduced significantly. This strategy is widely used for the charm physics programme. The reduced event size allows for the selection of enormous data samples containing charm hadrons, while avoiding having to reduce the b-hadron physics rate.

In addition to the data selected by the triggers described, a small portion of data is stored by a random event selection. These events are used to study the efficiency of the online event selection.

2.4 Simulation

A good simulation of the detector allows for performance studies during its design and for further optimisation during data taking. Ideally, all detection efficiencies are extracted from data. However, the unambiguous study of such efficiencies is not feasible because of the many, correlated dependencies in the event reconstruction. Simulated events are therefore essential for all analyses.

The LHCb simulation software, known as Gauss [27], consists of two phases: a generation phase and a simulation phase. In the generation phase, proton-proton collisions are simulated using Pythia [28], with a specific LHCb configuration [29]. The subsequent decay of the generated hadrons is described by EvtGen [30], in which final-state radiation is generated using Photos [31].

After generation, the particles are propagated through a model of the detector using the Geant4 toolkit [32], which simulates the interaction of the particles with the detector material. When a particle traverses detector material that is marked as sensitive, the entrance and exit points are recorded in so-called Monte Carlo Hits (MCHits). During this phase, unstable particles, such as, for instance, the K^0_S, are made to decay.

The MCHit information is used in a separate step, the digitisation, in which the response of the detector electronics is simulated. The resulting data format is similar to the response of the actual detector. The output is then processed by the same reconstruction software as real data.

The transport of the particles through the detector with Geant4 is costly. Each proton-proton collision contains many uninteresting particles, of which all detector interactions are simulated. To generate large samples of signal and background events, fast simulation techniques have been developed. For example, particle-gun simulations only simulate the decay of interest by generating the signal particle with a given momentum spectrum, independently of Pythia. The simulation of particle-gun events is, typically, 100 times faster than the conventional approach. However, as the track-reconstruction performance depends on the detector occupancy, the use of particle-gun events is limited to studies of the detector acceptance. Another technique, ReDecay [33], re-uses every simulated underlying event for a number of times, e.g. 100, in which only the decays of particles with an equal or higher mass than the signal particle are generated. Both fast simulation techniques are used in the detector studies presented in chapter 6.

Chapter 3

Outer tracker performance in Run 2

The OT is the largest main tracking detector downstream of the magnet. While the straws of the OT have a diameter of 4.9 mm, a much better spatial resolution is achieved by measuring the time that the ionisation electrons drift to the anode wire, which provides information on the distance to the wire with an average resolution of 171 μm. A study of the performance of the outer tracker therefore involves a study of the measured drift times.

The drift time for particles passing through an OT straw can be as high as 35 ns, while in Run 2 the LHC bunch spacing was lowered from 50 ns to 25 ns. Consequently, the OT suffers from "spillover": particles produced in the previous or next bunch crossing may also contribute to the hits recorded in the current event. In addition, the measured arrival times also include the time required for the signal to travel through the wire to the front-end electronics, which is up to 10 ns. Also accounting for the variation in flight times of the particles, a read-out window as large as three bunch crossings, 75 ns, is chosen. The impact of spillover hits is further increased, due to the fact that only the first hit in the read-out window is recorded, and thus hits from the previous bunch crossing can mask those in the current bunch crossing. This can degrade the performance in Run 2, in comparison with Run 1.

Spillover is not the only expected cause of performance changes. Radiation damage can decrease the hit efficiency. Ageing is a primary concern in the operation of the OT, as the central regions of the OT are exposed to a high ionising dose during the operation of the LHC. The ageing of the OT is therefore continuously monitored.

This chapter describes part of the work published in Ref. [9], and is divided in two parts. The first half of this chapter describes the effects of spillover on the tracking performance The second half of this chapter describes the monitoring of the performance degradation over time due to ageing, along with the latest results.

3.1 Spillover

It is not possible to unambiguously measure the impact of lowering the beam spacing by directly comparing Run-1 and Run-2 data, as improvements in the detector calibration were implemented simultaneously [9]. Thus, another approach is followed here. The LHCb hardware trigger decision unit not only saves information about the selected event, but also includes the sum of the transverse energy of all hadronic calorimeter clusters of the previous bunch crossing, $\sum E_{\mathrm{T}}^{\mathrm{prev}}$. In addition to the previous bunch crossing, the $\sum E_{\mathrm{T}}$ is stored for the previous-previous, next and next-next bunch crossings. The hadronic calorimeter suffers little from spillover, such that the influence of spillover can be studied by evaluating the tracking performance in bins of $\sum E_{\mathrm{T}}^{\mathrm{prev}}$.

The $\sum E_{\mathrm{T}}$ distributions for various spills are uncorrelated. However, the online event selection rejects events with little to no activity. Therefore, the $\sum E_{\mathrm{T}}$ distribution for an event passing the trigger requirements shows differences between the current and previous spills. Figure 3.1 shows the $\sum E_{\mathrm{T}}^{\mathrm{prev}}$ distribution, along with the $\sum E_{\mathrm{T}}$ distribution for the spill which passes the online event selection. The relative increase in the occupancy of the OT, IT and VELO due to spillover is shown as well. It is clear that in the events of interest to LHCb, the spillover in the OT is not negligible, while the VELO is nearly insensitive to the previous bunch crossing. On average, 17% of the OT hits originate from the previous bunch crossing.

3.1.1 Drift-time spectra

Estimating the impact of neighbouring bunch crossings requires studying the drift-time spectra. With the use of the $\sum E_{\mathrm{T}}$ information for each of the related bunch crossings,

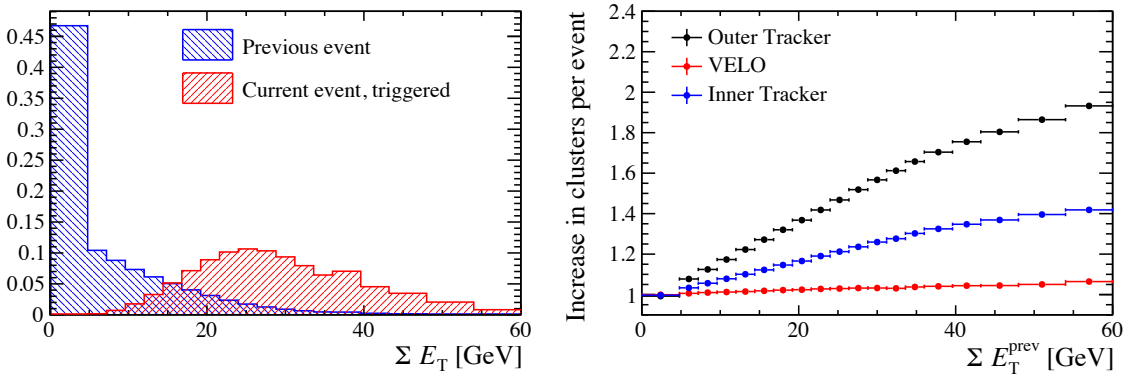

Figure 3.1: (left) Distribution of the recorded transverse energy of the previous bunch crossing, $\sum E_{\mathrm{T}}^{\mathrm{prev}}$ in blue, and of the current bunch crossing in red, for events that passed the online event selection. (right) Relative increase in the number of clusters per event is shown as a function of $\sum E_{\mathrm{T}}^{\mathrm{prev}}$, for the IT, OT and VELO.

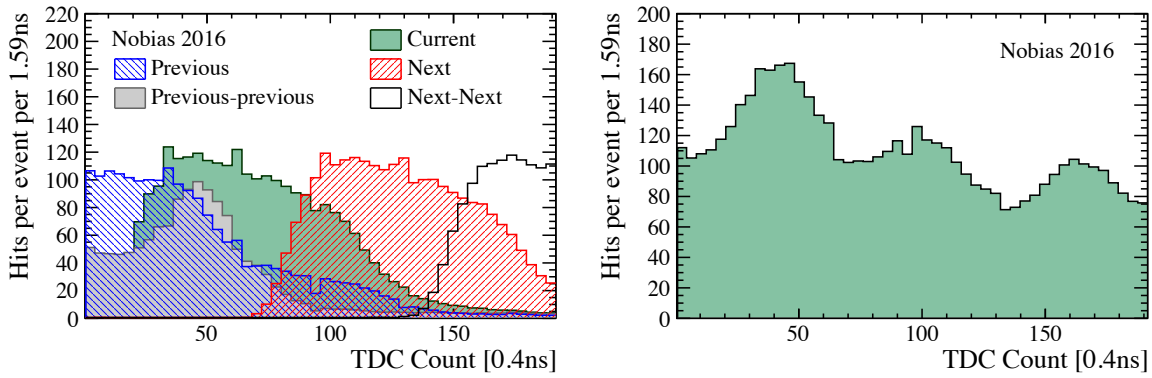

Figure 3.2: (left) The drift-time distributions for various spills in nobias proton-proton collision data (2016). A minimum deposited transverse energy of 7.2 GeV was required for the spill of interest, while requiring all of the recorded activity of other spills to be below 5.0 GeV, near the noise threshold of the calorimeters. (right) The total drift-time distribution, integrated over all modules, for nobias events recorded in 2016.

the digitised drift-time (TDC) spectrum can be decomposed , separating contributions from the next, next-next, current, previous and previous-previous bunch crossings. To study the TDC spectra of the various spills, proton-proton collision data are used which were selected independently of the LHCb triggers (so-called nobias events), such that all spills contribute equally. A minimum deposited transverse energy of 7.2 GeV in the hadronic calorimeter is required for the bunch crossing of interest, while requiring no activity in the neighbouring spills. The TDC distribution for unphysical hits, for example those introduced by noisy channels, can be also be deduced (e.g. by requiring no activity in any of the spills), and is used for a statistical background subtraction.

Figure 3.2 shows the resulting TDC spectra for data recorded in 2016. The previous and next spills are clearly visible. The spectra for these spills are compatible with the current spill, modulo a time translation of 25 ns. The contribution from the previous-previous spill is also clearly visible, with a peaking structure around 45 ns. This structure is, however, not observed at $45 + 25$ ns in the distribution for the previous spill. This unexpected behaviour is attributed to, among others, photon feedback, which cause a second pulse approximately 30 ns later than the original [34]. Because only one drift time per straw per read-out window is recorded, this second pulse is most prominent in hits due to the previous-previous event, while only slightly visible for the previous event. For the same reason, the previous spill is expected to leave the most impact on the hit resolution and tracking performance, which is studied in the following.

3.1.2 Hit resolution

When a particle traverses a straw for which a hit was recorded in the read-out window already, the drift time associated to it is incorrect. The incorrect drift time leads to a similarly incorrect estimate of the particle's position, which in turn leads to a decrease of the hit resolution. As a remedy to this problem, the drift time of an OT hit is not used in the track fit when it is found too incompatible with the expected trajectory through the straw[1]. For such hits the centre of the straw is rather used as the position, along with a large error of approximately 1.4 mm, such that the bias in the track fit is mitigated. Hits associated to tracks are therefore divided in two categories: hits associated to a track whose drift-time information was used, and hits associated to a track whose drift-time information was neglected. The resolution of the hits which fall into the first category is discussed here. Although the resolution determined in this category is biased, a decrease in the observed hit resolution still indicate a potential decrease in tracking performance.

Tracks reconstructed in proton-proton collision data, recorded in 2016, are used. The hit resolution is determined using data that passed the LHCb triggers, such that the detector occupancies are representative to those selected for physics analyses. The hit resolution is computed by predicting the hit position in a straw from the track parameters, and comparing it with the measured drift distance. To minimise the contribution due to multiple scattering, only tracks with a momentum larger than $10\,\text{GeV}/c$ are considered, which have at least 16 OT hits, and which are of good quality, i.e. $\chi^2/\text{ndf} < 2$ (where the χ^2 is computed independently of the hit under study). The results are corrected for the uncertainty in the track parameters.

The resulting distributions of position residuals for events with $\sum E_{\text{T}}^{\text{prev}} > 24\,\text{GeV}$ and $\sum E_{\text{T}}^{\text{prev}} < 24\,\text{GeV}$ are shown in Fig. 3.3. To describe the shapes of these distributions, a combination of two Gaussian functions is used with their mean fixed at 0 mm. One component, with a width σ_{narrow}, describes the narrow core of the distribution. The second component, with a width σ_{wide}, describes the contribution due to (somewhat) incorrect drift times. In the combined distribution function, f signifies the fraction of the narrow component in the total shape. The widths of the Gaussian functions are comparable between the two data sets, showing a core resolution of $(138.1 \pm 0.6)\,\mu\text{m}$ in an optimal, noise-free environment. In the events with more spillover, the wider component dominates the track resolution. The total hit resolution, defined as the RMS of the distribution of residuals, worsens from $(231.8 \pm 0.2)\,\mu\text{m}$ in events with little spillover, to $(286.5 \pm 0.6)\,\mu\text{m}$ in events with more spillover. Note that, traditionally, the hit residual is described with a single Gauss only, and the contribution from unrelated hits is mitigated. Therefore, the extracted total hit resolution is higher than the 171 µm reported in Ref. [9].

[1]Measured drift times are rejected when they differ more than 3 standard deviations from the expected.

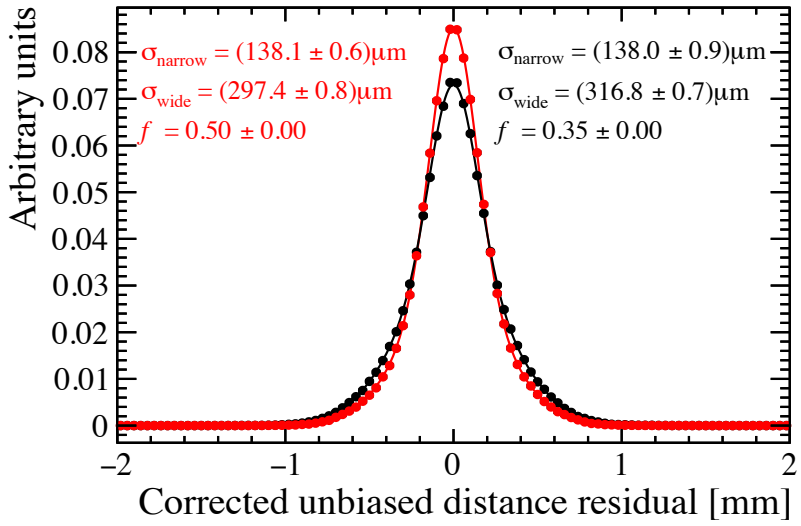

Figure 3.3: OT hit residuals, integrated over all modules, for events with (in black) $\sum E_{\mathrm{T}}^{\mathrm{prev}} > 24\,\mathrm{GeV}$ and (in red) $\sum E_{\mathrm{T}}^{\mathrm{prev}} < 24\,\mathrm{GeV}$, determined with data recorded in 2016 and events selected by the online event selection.

The scope of this study is limited, and only aims at establishing whether any loss in resolution is visible in events selected for physics analyses. Therefore, events which passed the online selection were used. Because this selection uses track quality requirements which could bias the observed resolution, the hit resolution is also determined with nobias events as a cross-check, for which a comparable effect no the hit resolution was found. In conclusion, the hit resolution could be seen to decrease when the activity in the previous event increases.

3.1.3 Hit-on-track performance

The number of drift times left unused because found too inconsistent with the track parameters is determined as a function of $\sum E_{\mathrm{T}}^{\mathrm{prev}}$, using tracks reconstructed in proton-proton collision data recorded in 2016. The left of Fig. 3.4 shows the average fraction of the OT hits on a track of which the drift time is used in the track fit for different track types. For long tracks, the average loss of used drift times is limited to about one hit per track, when increasing $\sum E_{\mathrm{T}}^{\mathrm{prev}}$ from 0 to 45 GeV.

The per-track average of the number of used OT hits is studied as well. The average number of OT hits associated to downstream and long tracks is shown in the right plot in Fig. 3.4. A slightly decreasing trend is visible, showing a loss of one OT hit per track for events with the largest $\sum E_{\mathrm{T}}^{\mathrm{prev}}$. The decrease of the average number of OT hits per track is closely related to the tracking performance, discussed in the next section.

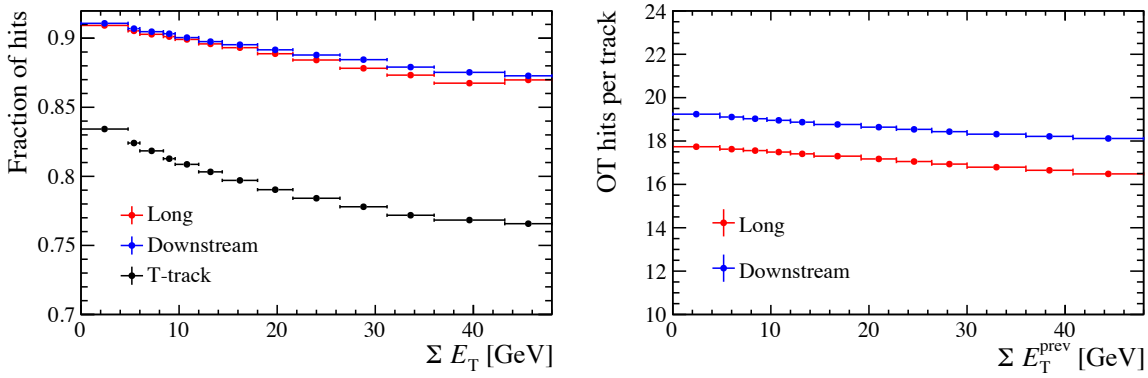

Figure 3.4: (left) The per-track average fraction of OT hits whose drift time was used in the track fit as a function of $\sum E_{\mathrm{T}}^{\mathrm{prev}}$. (right) The per-track average number of used OT hits as a function of $\sum E_{\mathrm{T}}^{\mathrm{prev}}$.

3.1.4 Impact on track reconstruction

With increasing occupancy in the OT and the corresponding loss of resolution, the difficulty of the track reconstruction increases. It was seen already in Sect. 3.1.2 that, on average, the drift times used in the track fit have a larger residual in high-spillover events. This leads to a decrease in the track quality, measured as an increase in the χ^2/ndf, illustrated in the left panel of Fig. 3.5. All reconstructed tracks in LHCb are required to satisfy $\chi^2/\mathrm{ndf} < 4$. As the average χ^2/ndf increases, this track quality requirement removes more tracks from the event, as observed in the number of reconstructed long and downstream tracks as a function of $\sum E_{\mathrm{T}}^{\mathrm{prev}}$ shown in Fig. 3.5. The track quality requirements thus disfavour tracks composed out of many OT hits. After the removal of the tracks failing the quality requirements, part of the tracks composed out of mostly OT hits are removed. Therefore, the per-track average of the average number of used OT hits decreases, as shown in Fig. 3.4.

The significant increase in the number of OT clusters slows down the track finding algorithms. By only considering events with limited activity in the previous bunch crossing, the number of hits in the OT, and the time taken by the track finding algorithms is reduced. The timing of these algorithms is particularly of importance in the trigger, where only limited time is available per event. For example, considering only events with $\sum E_{\mathrm{T}}^{\mathrm{prev}} < 24\,\mathrm{GeV}$ speeds up the forward and seeding tracking algorithms by 10% and 17%, respectively.

3.1.5 Countermeasure

LHCb is limited by the available bandwidth. While lower thresholds could be adopted for the single-muon and single-hadron hardware triggers without significantly affecting

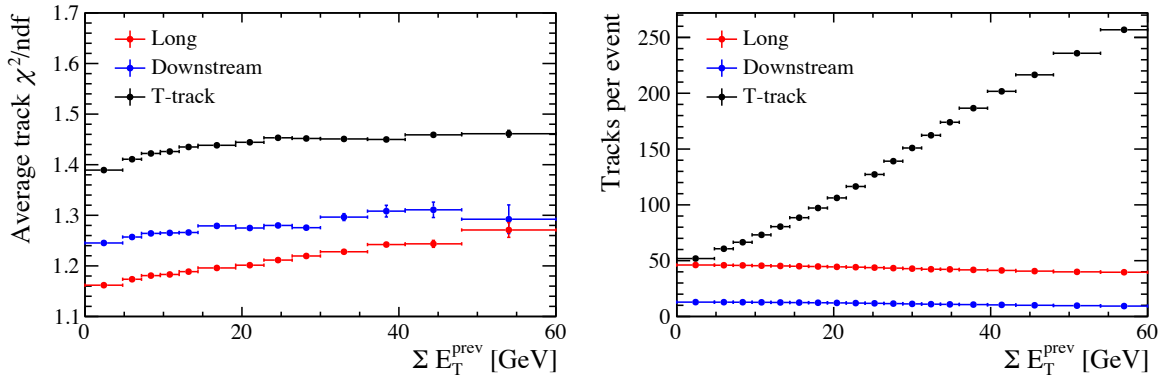

Figure 3.5: (left) The average number of reconstructed tracks per event as a function of $\sum E_{\mathrm{T}}^{\mathrm{prev}}$ for different track types, measured in events passing the online event selection. (right) The average track χ^2 as a function of $\sum E_{\mathrm{T}}^{\mathrm{prev}}$ for different track types, measured in events passing the online event selection.

signal significances for the main physics channels, they are set artificially high to match the available bandwidth. To make efficient use of the available bandwidth, the single-particle triggers only select events which satisfy $\sum E_{\mathrm{T}}^{\mathrm{prev}} < 24\,\mathrm{GeV}$ starting from 2017. This threshold is motivated by the physics output rate, since this study shows that events with many spillover hits show a decreased tracking performance, along with a slower event reconstruction. Most importantly, the size of the data for high-spillover events is larger due to the increase of OT clusters. The loss of physics events caused by this selection is compensated by introducing looser requirements on the deposited energy or transverse momentum. This effectively leads to a 1% increase of selected events.

3.2 Ageing

Gaseous detectors risk developing radiation damage over time. Amongst others, this can happen by the deposition of a thin insulating layer on the anode wire, that reduces the electric field and thus the amplification. In the last phases of the construction of the OT, gain losses were measured in the laboratory already after moderate irradiation doses. This gain loss was traced back to the outgassing of the plastifier component in the glue used to construct the modules [35]. The peculiar, crescent shape of the gain loss observed around a radioactive source, illustrated in Fig. 3.6, depends on the direction of the gas flow and indicates that ageing is prevented downstream of the source. This pattern is consistent with the hypothesis that radicals are produced close to the avalanche region. These are then transported out along with the gas and prevent the formation of the thin insulating layer on the anode wire. This hypothesis was confirmed by lab tests showing increased levels of ozone, a radical, after irradiation. Lab tests also showed that dark

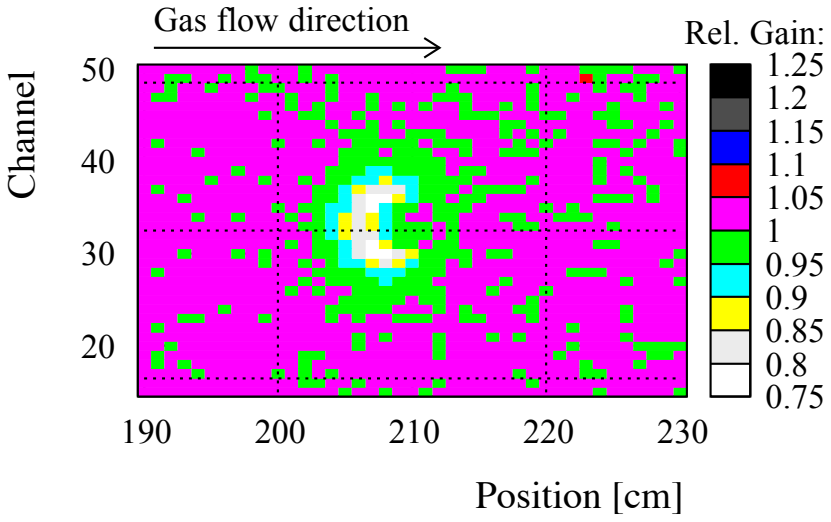

Figure 3.6: The ratio of two irradiation scans with a ^{90}Sr source, before and after irradiation, showing the relative gain loss after an irradiation of 20 hours. The source was centred on channel 32 on position 208 cm. Figure from Ref. [35].

currents induced by applying a high bias voltage of 1850 to 1920V reverses the ageing process. For further details on the causes and characteristics of the ageing of the OT, the reader is referred to Refs. [35, 36].

Several countermeasures were taken on the base of the lab results. By the continuous flushing of the gas, the vapours released by the outgassing of the glue are removed from the tubes. Oxygen was added to the gas mixture to further increase the presence of radicals, as O_2 is converted to ozone in the avalanche region. Last but not least, a method was developed to monitor the gain during the operation of the OT. This method is explained in this Section, describing the determination of gain loss in the OT during its operation in Run 2, along with updated results for Run 1.

3.2.1 Method

Ageing manifests itself as a relative difference between the gas gain, G, measured at different times. Monitoring the ageing therefore requires a reference measurement of the gas gain, G_{ref}, such that in the case of ageing

$$G_{\text{rel}} = G/G_{\text{ref}} < 1, \tag{3.1}$$

where G denotes the gas gain measured at a later time than G_{ref}. Gain losses of $5-25\%$ due to ageing were observed in the lab [36]. Measuring the effects of ageing, therefore, requires a precision on G_{ref} of a few percent. Unfortunately, it not possible to measure the gain directly during operation, as the OT readout electronics is designed to measure

drift times, but not the amplitude of the signal. Instead, the gas gain is measured via a so-called threshold scan.

In the readout electronics, signals first pass through an amplifier and a discriminator stage, both implemented in the ASDBLR chip, before their arrival time is registered in a TDC chip. Inside the ASDBLR, the amplified signal is discriminated against a remotely adjustable threshold value. Only signals exceeding this threshold are passed on to the TDC chip. Therefore, the signal amplitude can be determined by measuring the hit efficiency as a function of the amplifier threshold. The amplifier response, $R(v)$, as a function of the voltage v can be described naively by a delta function. More realistically, $R(v)$ can be described by a Gaussian function [37], which accounts for the effects of noise. All signals whose amplifier response $R(v)$ exceeds a set threshold t are recorded. Hence, for a given threshold t, the efficiency to record a hit is given by

$$\epsilon_{\text{hit}}(t) = \int_t^\infty \mathrm{d}v \; R(v) = P \int_t^\infty \mathrm{d}v \; \exp\left(-\frac{(v-\mu)^2}{\sigma}\right), \tag{3.2}$$

$$= P\left(1 - \text{Erf}\left(\frac{(t-\mu)}{\sqrt{2}\sigma}\right)\right), \tag{3.3}$$

in which Erf is the error function, P a normalisation constant, and μ and σ denote the mean and width of the amplifier response function $R(v)$, respectively. By measuring the hit efficiency for different amplifier thresholds, the average response, μ, of the amplifier is determined through a fit to the data. The determination of the gas gain via this method is also called a threshold scan. An example of a fit of Eq. 3.2 to threshold-scan data is shown in Fig. 3.7. The normalisation of the curve, P, represents the maximum hit efficiency. The value μ is also called the half-efficiency point, as operating with a threshold $t = \mu$ will result in an efficiency of $\epsilon_{\text{hit}}(\mu) = P/2 \approx 50\%$. A priori, additional degrees of freedom can be inserted in Eq. 3.2 to describe additional sources of non-Gaussian noise, e.g. noise after the amplifier. However, measurements show that the description by Eq. 3.2 is sufficient. To this assumption, and to the assumed shape of $R(v)$, systematic errors are assigned, further discussed in Sect. 3.2.3.

After the half-efficiency point has been determined, it is related to a change in the gas gain using the calibration measurements described in Ref. [37]. Comparing a measurement to a reference, the relation between the relative gain, G_{rel}, and the difference in half-efficiency points, ΔHEP, is described as

$$G_{\text{rel}} = \exp\left(\frac{\Delta\text{HEP[mV]}}{105 \pm 10\text{[mV]}}\right). \tag{3.4}$$

The uncertainty in the denominator is propagated in the systematic error, discussed later in Sect. 3.2.3.

To measure the single-hit efficiency for different values of the threshold, a source of particles is required. This measurement is therefore performed during operation of the

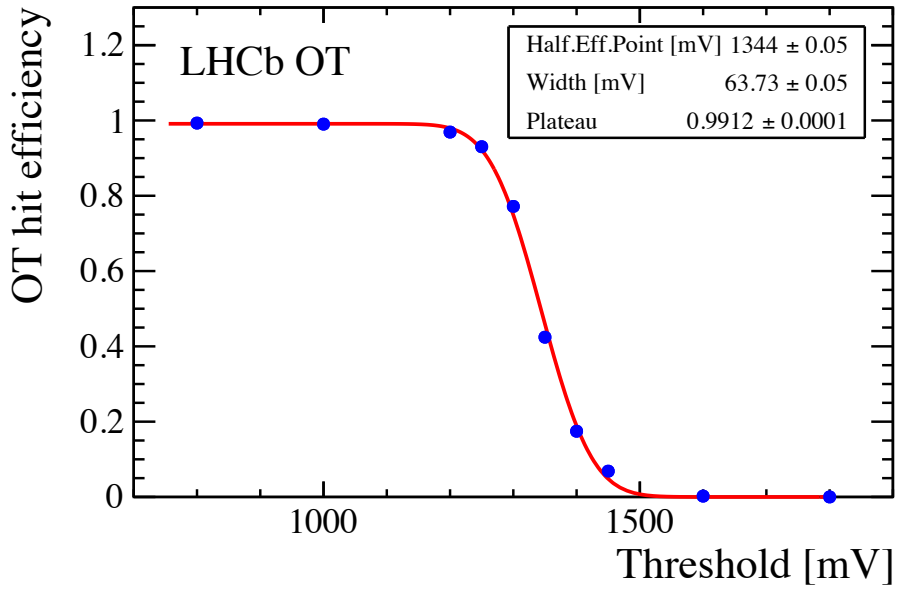

Figure 3.7: Example hit efficiency plot as a function of amplifier threshold for the first layer, for the scan performed in October 2015. The amplifier threshold is set to 800 mV during the normal operation of the OT.

LHC. For each layer separately, data is recorded with 10 different threshold settings, while all other layers operate at the nominal settings. Because of the rapidly varying efficiency of the OT layers as a function of threshold, these data are not useful for physics analyses. The number of events recorded in this measurement should therefore be minimal, yet still sufficient to determine the relative gas gain. Per threshold, 300,000 events are recorded. In Run 2 most of the gain loss measurements were performed when the LHC was sparsely filled. This configuration is well-suited for this measurement as such events suffer little from spillover.

For the reference measurement of the gas gain, G_{ref}, an early measurement of the gain, performed with the presented method in August 2010, is used.

3.2.2 Determination of the single-hit (pseudo-)efficiency

The single-hit efficiency is defined as the ratio of observed hits divided by the number of expected hits per detector region. The number of expected hits is estimated by predicting the hit position of reconstructed long tracks in the detector region under study. To ensure a reliable hit position, only tracks of good quality are used, with $\chi^2/\text{ndf} < 2$ and at least 21 hits in the OT detector (excluding any hit in the straw under study). To reduce the impact of an error in the track parameters, only hits expected to lie close to the straw are used. The efficiency is determined for different

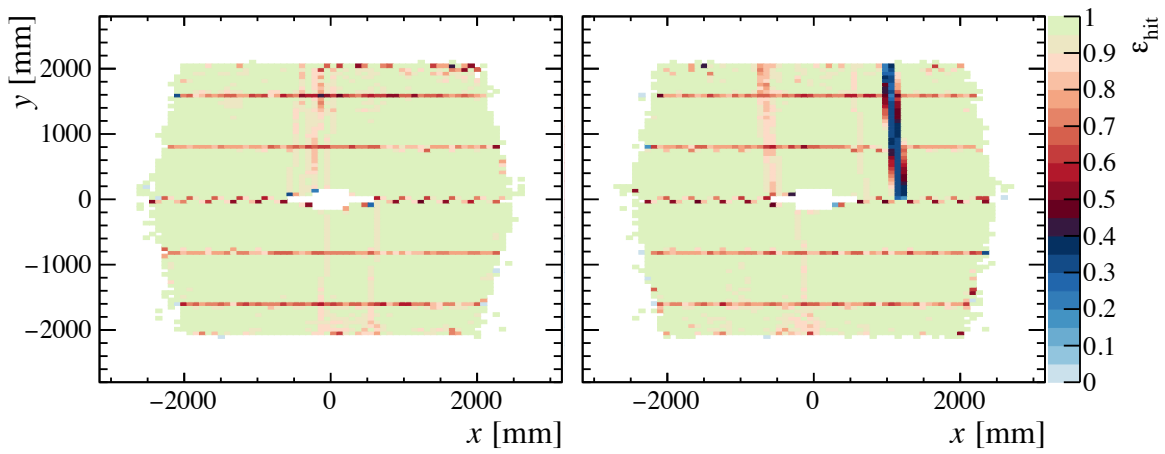

Figure 3.8: The hit efficiency as a function of the hit position, determined with data recorded during the threshold scan in April 2018, for (left) the second layer of the first station and (right) the third layer of the first station. The right plot is chosen to illustrate the effect of a partially disabled module. The shown efficiencies are determined with the amplifier threshold set to its standard operating value. The horizontal line at $y = 0$ originates from the geometrical split of the two detector halves, while the other horizontal lines correspond to the wire locators.

regions (in x, y) for each layer separately, and is repeated for 10 different amplifier thresholds. Figure 3.8 shows an example of the resulting efficiency for one of the layers, at the nominal operational threshold of 800 mV.

The determination of the hit efficiency is reliant on reconstructed, long tracks. The pattern recognition makes use of the hits found in the layer under study to form this track. The inferred efficiency is therefore not independent of the layer under study, and is therefore called a "pseudo-efficiency". This does not hinder this analysis, as only relative changes in the half-efficiency points are important. The residual bias due to this pseudo-efficiency are further discussed in Sect. 3.2.3.

3.2.3 Corrections and systematic effects

To minimise the influence of other, unrelated sources on the gain determination, most of the conditions are kept the same for each measurement, and only the relative change of the gas gain is considered. However, it is not possible to leave all conditions unchanged. Their effects, along with the corresponding countermeasures, are discussed here. An overview of all systematic errors is presented at the end of this Section.

Gas pressure

Ageing is not the only process which can change the gas gain, as changes in the gas density also lead to sizeable differences. To make a meaningful comparison between two measurements, G must be corrected for any changes in the gas density. As the gas density is strongly correlated with the atmospheric pressure, it is measured during each ageing scan. Calibration measurements [36] show a linear relation between the atmospheric pressure and the gas gain. Comparing the gain measured at atmospheric pressures p_0 and $p_1 = p_0 + \Delta p$ therefore requires a final correction factor

$$\frac{\Delta G}{G} = -5.18 \frac{\Delta p}{p_0}. \tag{3.5}$$

Each measurement of the gas gain is corrected to that of the reference scan, using Eq. 3.5. The effect on the gain of a change in the slope of Eq. 3.5 is small, and it is included in the systematic error.

Occupancy

In the case that more than one particle traverses the same straw, the single-hit efficiency is artificially increased. Therefore, the hit efficiency is prone to a positive bias in events with a high particle multiplicity. Changes in the average number of collisions per event, the type of collision (e.g. heavy ions) and the centre-of-mass energy all affect the event occupancy. This leads to different occupancies in the OT for measurements performed over the years. As an example, Fig. 3.9 shows the different OT hit occupancies for data recorded in 2016 and the reference measurement. A study of the influence of htis effect on the determination of the gas gain is therefore required.

To estimate the impact of the event occupancy on the inferred gas gain, the data recorded in October 2015 is used to create two data sets, based on the hit occupancy per event. One data set only contains events with at maximum 1500 OT hits, and the other only contains events with a minimum 5000 OT hits. The offline analysis is repeated separately for these two data sets to extract the half-efficiency points. The fits to the hit efficiencies as a function of the amplifier threshold are shown in Fig. 3.9. The relative gain differs by 10% when comparing the two data sets. As the two data sets originate from the same run, no correction for a difference in atmospheric pressure is required. Because the average event occupancy is higher in the events recorded from 2012 onwards, this could lead to an overestimation of the gas gain over time. To reduce to this bias, only events with a relatively low OT occupancy, indicated by the dashed line in Fig. 3.9, are considered. This requirement drastically reduces the sample of events used for gas gain measurements in Run 2. However, the reduction of this bias is considered more important than the decrease in statistical precision.

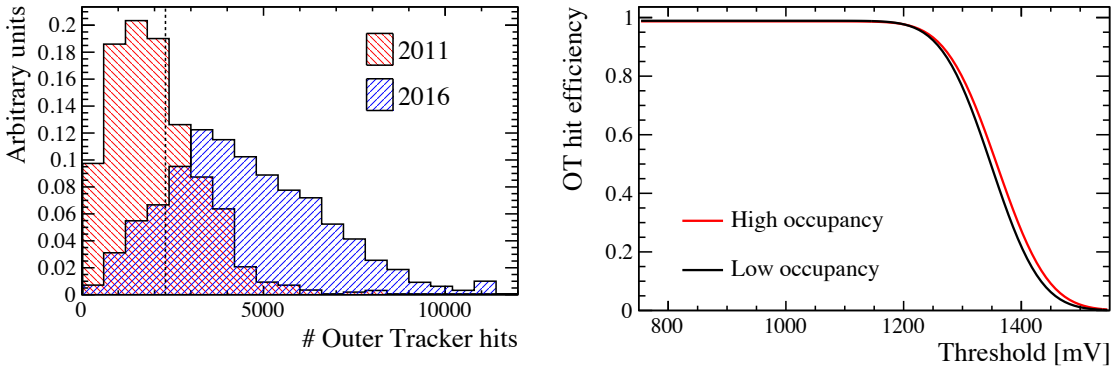

Figure 3.9: (left) The distribution of the outer tracker occupancy for the ageing measurements performed in 2011 and 2016. The maximum occupancy allowed in the presented study is indicated by the dashed line. (right) The hit efficiency as a function of threshold, measured with events recorded in October 2015 with high occupancy (i.e. #OT hits > 5000) and low occupancy (i.e. #OT hits < 1500) in red and black, respectively. Data points are omitted for clarity.

Hit-efficiency determination

Requiring the presence of sufficient hits on the track for the other OT layers,increases the chances that the track was also reconstructed without any hits in the layer under study. The fact that more long tracks are found per event when all layers are operating their nominal operating threshold, however, shows that the pattern recognition is not unbiased. To eliminate this bias would require to reconstruct tracks independently of the layer under study. However, this procedure is quite involved and thus not part of the nominal procedure. Its effect is therefore estimated by measuring the relative change in the gas gain (for the first station only) when using unbiased tracks, with the data recorded in April 2018 and August 2010. The hit efficiency as a function of the threshold is redetermined for both scans, as the associated bias affects both measurements. Figure 3.10 shows the effect on the hit efficiency of removing the layer under study from the pattern recognition. Differences of $\mathcal{O}(10\%)$ are visible in the hit efficiency across the entire layer. The extracted half-efficiency points are also shifted. For example, for the second layer of the first station, the half-efficiency point shifts from 1344 mV for the nominal analysis, to 1323 mV for the unbiased analysis. Fortunately, a similar effect occurs for the reference measurement, such that the impact on the inferred relative gain is only 0.9%, integrated over all layers considered. This effect is accounted for in the systematic error.

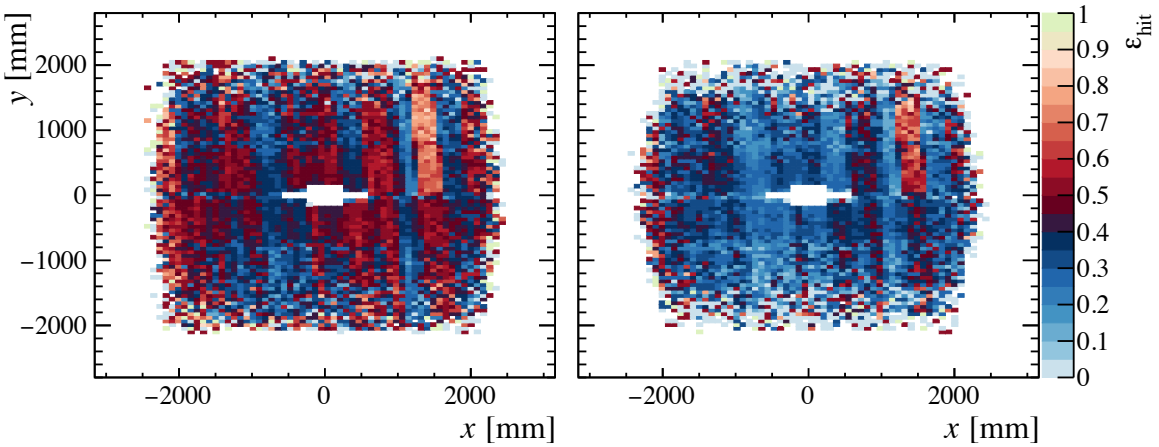

Figure 3.10: The hit efficiency as a function of the hit position with an amplifier threshold set close to the half-efficiency point (1350 mV), determined with data recorded during the threshold scan in April 2018, for the third layer of the first station when this is (left) included in the pattern recognition, and (right) excluded from the pattern recognition.

Overview of systematic errors

Table 3.1 shows all systematic errors associated to the relative gain measurement. The uncertainty associated to the fit model has the largest contribution. This uncertainty quantifies the sensitivity of this measurement to the parametrisation of the hit efficiency as a function of threshold, and has been studied in Refs. [36, 38]. The total systematic error assigned to the gain measurements is 2.4%. In the measurement of the relative gain for the entire OT, this systematic error dominates over the statistical error. This precision is sufficient to measure the expected gain loss.

Table 3.1: Overview of contributions (in percent) to the systematic error in the determination of G_{rel}.

Source	Systematic uncertainty
Fit model	2.0%
Gain calibration (Eq. 3.4)	0.8%
Pattern recognition	0.9%
Pressure correction	0.4%
Total	2.4%

3.2.4 Results

The results from all layers are combined and compared to the average gas gain as measured in August 2010. As a precaution, the x-layers which form the starting point for the track seeding (see Sect. 2.2) are excluded from this combination. The relative gain variation as a function of the delivered luminosity is illustrated in Fig. 3.11, and is compatible with the hypothesis that no ageing was observed. The uncertainty associated to each measurement is dominated by the systematic error discussed in Sect. 3.2.3. Since the gas flow is in the upwards vertical direction, and the ageing pattern observed in the laboratory depends on the gas flow (Fig. 3.6), the change in gas gain is determined separately for the bottom half of the detector as a cross-check. The results are consistent with those obtained in the nominal procedure. In comparison to earlier results, presented in Ref. [39], the trend in relative gain has changed due to the newly introduced requirement on the event occupancy. These results, which appeared to show an "anti-ageing" effect, are shown in Fig. 3.11 for comparison.

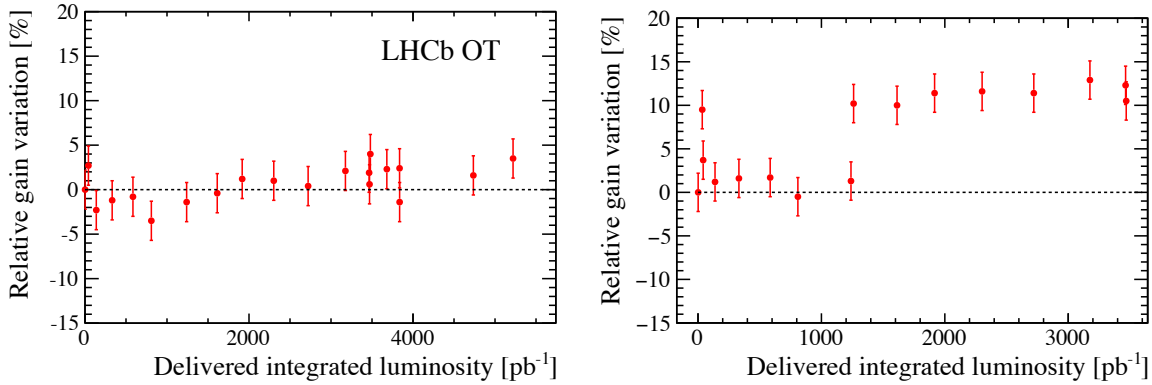

Figure 3.11: Pressure-corrected gain variation as a function of the delivered luminosity (left) with the occupancy corrections presented in this chapter and (right) without any corrections for the higher occupancy (some data points are missing as the data of two measurements were lost).

Part II

CP violation in the mixing of B mesons

Chapter 4

Neutral meson mixing

Neutral B^0 and B_s^0 mesons have proven to be excellent probes to study the weak interaction. The weak interaction allows neutral mesons, such as the B_s^0, to transform into their *CP* conjugate, $\overline{B}_s^0$. This meson-antimeson transition occurs continuously in the time evolution of the neutral meson, such that an initial B_s^0 transforms into a $\overline{B}_s^0$ and back. This makes the B_s^0 and $\overline{B}_s^0$ a coupled, two-state system. *CP* violation in this mixing process means that the probability of an initial B_s^0 meson to transform after a time t into a $\overline{B}_s^0$ meson differs from its charge-conjugate process.

The time evolution of a general wave function $|\psi(t)\rangle = a(t)|B_s^0\rangle + b(t)|\overline{B}_s^0\rangle$, composed of an arbitrary mixture of B_s^0 and $\overline{B}_s^0$, is governed by the Schrödinger equation. Using the $|B_s^0\rangle$ and $|\overline{B}_s^0\rangle$ as basis vectors, it can be written as[1]

$$i\frac{\mathrm{d}}{\mathrm{d}t}\begin{pmatrix} a(t) \\ b(t) \end{pmatrix} = \hat{H}\begin{pmatrix} a(t) \\ b(t) \end{pmatrix}, \tag{4.1}$$

with an effective, approximately time-independent Hamiltonian $\hat{H}$ [40]. To describe the finite lifetime of the B_s^0 and $\overline{B}_s^0$ mesons, the operator $\hat{H}$ can no longer be hermitian. It can, however, be decomposed as $\hat{H} = M - \frac{i}{2}\Gamma$, where M and Γ are two hermitian matrices describing the propagation of the coupled system and its decay, respectively. From *CPT* invariance it follows that $M_{11} = M_{22}$ and $\Gamma_{11} = \Gamma_{22}$, such that $\hat{H}$ can be written as

$$\hat{H} = \begin{pmatrix} M - i\Gamma/2 & M_{12} - i\Gamma_{12}/2 \\ M_{12}^* - i\Gamma_{12}^*/2 & M - i\Gamma/2 \end{pmatrix}. \tag{4.2}$$

The off-diagonal terms in this matrix describe the mixing of the B_s^0 and $\overline{B}_s^0$ states over time. The amplitude M_{12}, also called the dispersive part of the mixing amplitude, signifies transitions via virtual intermediate states. The absorptive part, Γ_{12}, describes the change in amplitude due to the decay to states accessible for both B_s^0 and $\overline{B}_s^0$. In the Standard Model it is mostly the dispersive behaviour which drives the $B_s^0 - \overline{B}_s^0$

[1] Natural units are used throughout this section.

mixing, resulting in oscillations between the B_s^0 and $\overline{B}_s^0$ states. This is a property of both $B_s^0 - \overline{B}_s^0$ and $B^0 - \overline{B}^0$ systems, and does not hold for, for example, the $K^0 - \overline{K}^0$ system. Figure 4.1 illustrates the most dominant processes responsible for the $B_s^0 - \overline{B}_s^0$ transition in the Standard Model. As the dominating amplitude M_{12} contains a loop, it is sensitive to contributions from virtual particles not described by the Standard Model.

The eigenstates of $\hat{H}$ are given by

$$|B_{\mathrm{H,L}}\rangle = p|B_s^0\rangle \mp q|\overline{B}_s^0\rangle, \tag{4.3}$$

where $|B_H\rangle$ is the heavy eigenstate, and $|B_L\rangle$ is the light eigenstate. The coefficients p and q are related by the eigenvalue equation as

$$\frac{q}{p} = -\sqrt{\frac{2M_{12}^* - i\Gamma_{12}^*}{2M_{12} - i\Gamma_{12}}}. \tag{4.4}$$

The solutions to the Schrödinger equation are given by

$$|B_{H,L}(t)\rangle = \exp\left(-(im_{H,L} + \Gamma_{H,L}/2)t/\hbar\right)|B_{H,L}(0)\rangle, \tag{4.5}$$

which defines the masses, $m_{H,L}$, and decay widths, $\Gamma_{H,L}$, of the two eigenstates. The production of B_s^0 and $\overline{B}_s^0$ mesons at the LHC is governed by the strong interaction, such that they are produced as flavour eigenstates. For the description of the time evolution of such states, it is convenient to also define the difference in mass, Δm_s, and the difference in decay width, $\Delta\Gamma_s$, between the heavy and light eigenstates. These are related to M_{12} and Γ_{12} as [41]

$$\begin{aligned}
\Delta m_s &= m_H - m_L \approx 2|M_{12}|\left(1 - \frac{|\Gamma_{12}|^2}{8|M_{12}|^2}\sin^2\phi_{12}\right) \\
\Delta\Gamma_s &= \Gamma_L - \Gamma_H \approx 2|\Gamma_{12}|\cos\phi_{12}\left(1 + \frac{|\Gamma_{12}|^2}{8|M_{12}|^2}\sin^2\phi_{12}\right),
\end{aligned} \tag{4.6}$$

with

$$\phi_{12} = \arg\left(-\frac{M_{12}}{\Gamma_{12}}\right).$$

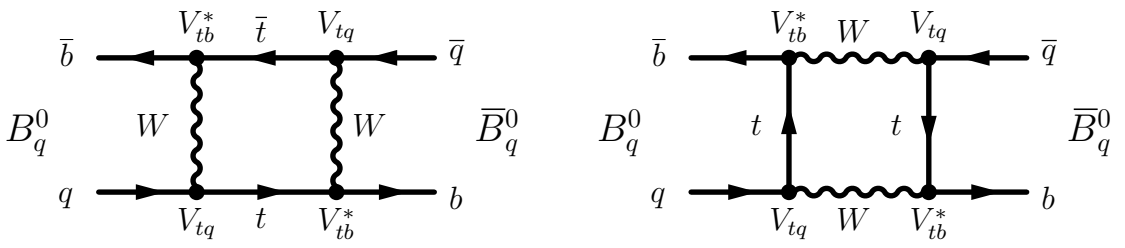

Figure 4.1: The dominant box diagrams that cause $B^0 - \overline{B}^0$ and $B_s^0 - \overline{B}_s^0$ mixing in the Standard Model ($q = s, d$).

The time evolution of a $|B_s^0\rangle$ or $|\overline{B}_s^0\rangle$ state can now be expressed with Eq. 4.3 as

$$\begin{aligned} |B_s^0(t)\rangle &= g_+(t)|B_s^0\rangle + \frac{q}{p} g_-(t)|\overline{B}_s^0\rangle, \\ |\overline{B}_s^0(t)\rangle &= g_+(t)|\overline{B}_s^0\rangle + \frac{p}{q} g_-(t)|B_s^0\rangle, \end{aligned} \tag{4.7}$$

where

$$g_\pm(t) = \frac{1}{2}\exp\left(-iMt - \Gamma t/2\right)\left(e^{i\Delta m_s t} e^{\Delta\Gamma_s t/4} \pm e^{-i\Delta m_s t} e^{-\Delta\Gamma_s t/4}\right).$$

The probabilities to observe a B_s^0 or $\overline{B}_s^0$ for an initially produced B_s^0 or $\overline{B}_s^0$ meson at time $t > 0$ are then given by

$$\begin{aligned} |\langle B_s^0|B_s^0(t)\rangle|^2 = \quad & |g_+(t)|^2 = \quad \frac{e^{-\Gamma t}}{2}\left(\cosh(\frac{1}{2}\Delta\Gamma_s t) + \cos(\Delta m_s t)\right), \\ |\langle \overline{B}_s^0|\overline{B}_s^0(t)\rangle|^2 = \quad & |g_+(t)|^2 = \quad \frac{e^{-\Gamma t}}{2}\left(\cosh(\frac{1}{2}\Delta\Gamma_s t) + \cos(\Delta m_s t)\right), \\ |\langle \overline{B}_s^0|B_s^0(t)\rangle|^2 = \left|\frac{q}{p}\right|^2 & |g_-(t)|^2 = \left|\frac{q}{p}\right|^2 \frac{e^{-\Gamma t}}{2}\left(\cosh(\frac{1}{2}\Delta\Gamma_s t) - \cos(\Delta m_s t)\right), \\ |\langle B_s^0|\overline{B}_s^0(t)\rangle|^2 = \left|\frac{p}{q}\right|^2 & |g_-(t)|^2 = \left|\frac{p}{q}\right|^2 \frac{e^{-\Gamma t}}{2}\left(\cosh(\frac{1}{2}\Delta\Gamma_s t) - \cos(\Delta m_s t)\right). \end{aligned} \tag{4.8}$$

The mass difference, Δm_s, provides the oscillation frequency for the $B_s^0 - \overline{B}_s^0$ mixing. The difference in decay widths splits the overall exponent in two components. Similar decay probabilities exist for the $B^0 - \overline{B}^0$ system, except that the numerical values of Δm_d and $\Delta\Gamma_d$ are different from Δm_s and $\Delta\Gamma_s$. This difference is shown in Fig. 4.2, which illustrates the probability of an initial B_s^0 (B^0) meson to decay as a $\overline{B}_s^0$ ($\overline{B}^0$) meson over time, where all parameters have been set to their latest measured values [42].

4.1 *CP* violation in mixing

Traditionally, different types of *CP* violation are distinguished. "Direct" *CP* violation occurs when the amplitude for a direct decay and its *CP* conjugate differ, while "indirect" *CP* violation also involves the mixing process. Indirect *CP* violation covers both *CP* violation in mixing, as well as *CP* violation in interference between the mixing and decay amplitudes. The measurement presented in this chapter involves *CP* violation in mixing, for which this section describes the formalism.

Using the $B_s^0 - \overline{B}_s^0$ system as a proxy for neutral meson systems, *CP* violation in mixing means that the probability of an initial B_s^0 meson to transform after a time t into a $\overline{B}_s^0$ meson differs from that of the charge conjugate process. In the mixing equations, Eq. 4.8, the mixing probability is described by the last two probabilities.

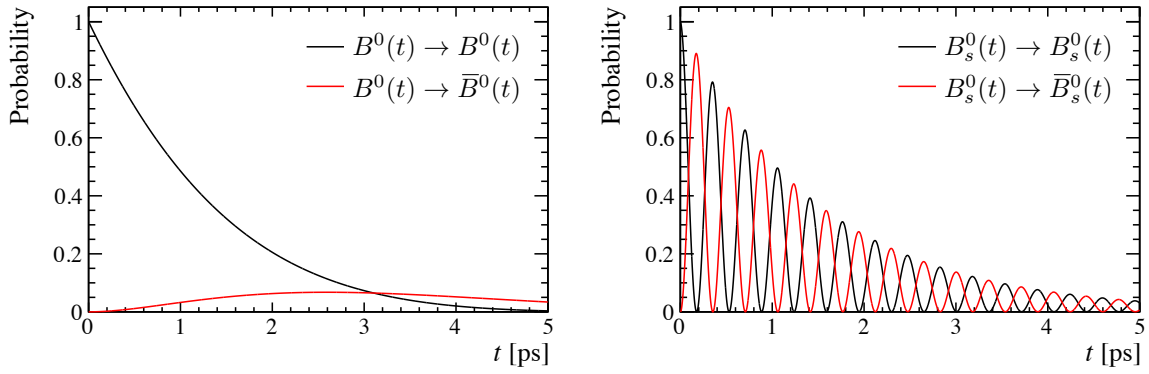

Figure 4.2: Probability for a B^0 (B_s^0) meson produced as B^0 (B_s^0) to decay as B^0 (B_s^0) or $\overline{B}^0$ ($\overline{B}_s^0$). To make these illustrations, the following values were used: $M_d = 5279.6\,\mathrm{MeV}/c^2$, $\Gamma_d = (1.52)^{-1}\,\mathrm{ps}^{-1}$, $\Delta m_d = 0.506\,\mathrm{ps}^{-1}$ and $\Delta\Gamma_d/\Gamma_d = -0.002$ for the $B^0 - \overline{B}^0$ system, and $M_s = 2366.89\,\mathrm{MeV}/c^2$, $\Gamma_s = 0.663\,\mathrm{ps}^{-1}$, $\Delta m_s = 17.8\,\mathrm{ps}^{-1}$ and $\Delta\Gamma_s/\Gamma_s = 0.132$ for the $B_s^0 - \overline{B}_s^0$.

The CP asymmetry in mixing can be expressed in terms of $\left|\frac{q}{p}\right|$ from these equations,

$$\begin{aligned} a^s_{CP,\mathrm{mix}}(t) &= \frac{P(\overline{B}_s^0 \to B_s^0)(t) - P(B_s^0 \to \overline{B}_s^0)(t)}{P(\overline{B}_s^0 \to B_s^0)(t) + P(B_s^0 \to \overline{B}_s^0)(t)} \\ &= \frac{|p/q|^2 - |q/p|^2}{|p/q|^2 + |q/p|^2} = \frac{1 - |q/p|^4}{1 + |p/q|^4} \\ &\approx 2\left(1 - \left|\frac{q}{p}\right|\right), \end{aligned} \tag{4.9}$$

which is independent of the decay time t. Any deviation of $\left|\frac{q}{p}\right|$ from unity is thus equivalent to a non-vanishing value of the CP asymmetry in mixing.

The mixing process of neutral mesons is described by the dispersion and absorption coefficients, M_{12} and Γ_{12}. CP violation in this process emerges due to a difference in phase between these two coefficients, which then implies that

$$\left|\frac{2M_{12}^* - i\Gamma_{12}^*}{2M_{12} - i\Gamma_{12}}\right| = \left|\frac{q}{p}\right|^2 \neq 1. \tag{4.10}$$

The only experimental evidence for this type of CP violation exists in the $K^0 - \overline{K}^0$ system. In comparison to the $K^0 - \overline{K}^0$ system, the Standard Model expectations for both $B^0 - \overline{B}^0$ and $B_s^0 - \overline{B}_s^0$ are tiny [41, 43]:

$$a^d_{CP,\mathrm{mix}} = (-4.7 \pm 0.6) \times 10^{-4}, \tag{4.11}$$

$$a^s_{CP,\mathrm{mix}} = (2.22 \pm 0.27) \times 10^{-5}. \tag{4.12}$$

Experimentally, *CP* violation in mixing is measured with the use of flavour-specific decays, i.e. decays in which the charges of the final-state particles determine the flavour of the B_s^0 (or $\overline{B}_s^0$) at the time of decay. This ensures that an initial B_s^0 meson will have to oscillate to a $\overline{B}_s^0$ in order to decay to $\overline{f}$. The relative difference in flavour-specific decay rates,

$$a_{\text{fs}}^s = \frac{\Gamma\left(\overline{B}_s^0 \to B_s^0 \to f\right) - \Gamma\left(B_s^0 \to \overline{B}_s^0 \to \overline{f}\right)}{\Gamma\left(\overline{B}_s^0 \to B_s^0 \to f\right) + \Gamma\left(B_s^0 \to \overline{B}_s^0 \to \overline{f}\right)}, \tag{4.13}$$

quantifies the amount of *CP* violation in B_s^0 mixing, $a_{CP,\text{mix}}^s$, with the omission of any potential direct *CP* violation in the decay $B_s^0 \to f$. A similar definition exists for the $B^0 - \overline{B}^0$ system, a_{fs}^d. Semileptonic decays of the type $B_s^0 \to D_s^- l^+ \nu_\ell X$, in which X denotes any number of additional particles, are examples of flavour-specific decays. These decays have large branching ratios and occur at tree level, suppressing direct *CP* violation in these decays even if they would be modified by physics beyond the Standard Model, such that $a_{CP,\text{mix}}^s = a_{\text{fs}}^s$ can safely be assumed. For these reasons one also refers to the semileptonic mixing asymmetry, denoted by a_{sl}^s and a_{sl}^d for the B_s^0 and B^0 system, respectively. The flavour of the B_s^0 at the time of decay can easily be inferred from the electric charge of the reconstructed lepton, but experimental challenges reside in the removal of nuisance asymmetries originating from backgrounds, and from instrumental and reconstruction effects.

Figure 4.3 shows all measurements to date of a_{sl}^d and a_{sl}^s, excluding the analysis presented in this thesis. The *CP* asymmetries in mixing for the $B_s^0 - \overline{B}_s^0$ and $B^0 - \overline{B}^0$ systems have gained interested due to an observed 3.6σ discrepancy from the Standard Model reported by the D0 collaboration [44], shown as the yellow ellipse in the illustration. As the *CP* asymmetry in mixing for the $B^0 - \overline{B}^0$ system was already constrained by measurements from B-factories at that time, this discrepancy hinted towards possible physics beyond the Standard Model in $B_s^0 - \overline{B}_s^0$ mixing. This motivated a precise measurement of *CP* violation in $B_s^0 - \overline{B}_s^0$ mixing, presented in the next chapter.

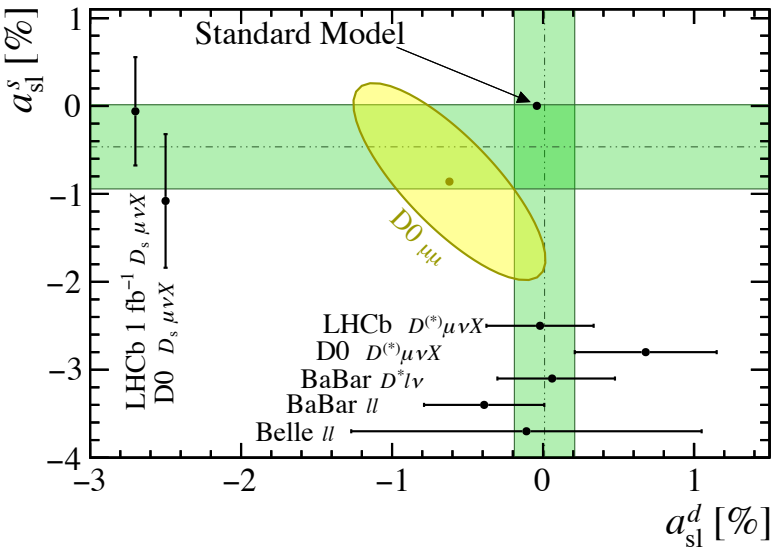

Figure 4.3: Overview of the published measurements of a^d_{sl} and a^s_{sl}, excluding the presented a^s_{sl} measurement. The horizontal and vertical bands indicate the naive averages of pure a^s_{sl} and a^d_{sl} measurements [45–51], which are individually represented by the black points. The yellow ellipse represents the D0 dimuon measurement with $\Delta\Gamma_d/\Gamma_d$ set to its Standard-Model expectation value [44]. The error bands and contours correspond to 68% confidence level.

Chapter 5

Measurement of CP violation in B_s^0 mixing

This chapter describes the measurement of $a^s_{\rm sl}$, published in Ref. [10], which is the most precise measurement of $a^s_{\rm sl}$ to date. The control and understanding of instrumental asymmetries required to perform this measurement are described in detail in Part III along with potential improvements.

5.1 Analysis strategy

In this analysis the semileptonic mixing asymmetry, $a^s_{\rm sl}$, is measured using the semileptonic decays, $B^0_s \to D^-_s \mu^+ \nu_\mu X$, with $D^-_s \to K^+K^-\pi^-$, and their charge-conjugates. Out of all of the B^0_s decay products, only the $D^-_s\mu^+$ pairs are reconstructed. From Eq. 4.13, one would expect that a measurement of $a^s_{\rm sl}$ requires information of the B^0_s flavour at its production, so-called "flavour tagging". This is challenging at a hadron collider due to overwhelming, partially reconstructed backgrounds. With an effective tagging efficiency of about 5% [52], requiring tagged B^0_s candidates would reduce the data set significantly. Fortunately, $a^s_{\rm sl}$ can be measured using untagged B^0_s decays as well. The time-dependent, measured asymmetry then becomes [50]

$$A_{\rm meas}(t) = \frac{N(D^-_s\mu^+, t) - N(D^+_s\mu^-, t)}{N(D^-_s\mu^+, t) + N(D^+_s\mu^-, t)} \tag{5.1}$$

$$= \frac{a^s_{\rm sl}}{2} - \left(A_P - \frac{a^s_{\rm sl}}{2}\right) \frac{\varepsilon(t) e^{-\bar{\Gamma}_s t}\cos(\Delta m_s t)}{\varepsilon(t) e^{-\bar{\Gamma}_s t}\cosh(\Delta\Gamma_s t/2)}, \tag{5.2}$$

in which A_P denotes the production asymmetry of $B^0_s - \overline{B}^0_s$ pairs, $N(f)$ denotes the number of observed $B^0_s \to f$ decays, t the B^0_s decay time, and $\varepsilon(t)$ denotes the decay-time dependent efficiency, generally called time acceptance, of the detector. At this stage no contamination by any backgrounds or instrumental asymmetries to $N(f)$ is

assumed. From Eq. 5.1, it would seem that a measurement of the time dependence of A^{meas} would be required to disentangle the mixing asymmetry, a^s_{sl}, from A_P. Unique to the $B_s^0 - \overline{B}_s^0$ system is the high oscillation frequency with respect to its average decay time, $\Delta m_s/\bar{\Gamma}_s = 26.81 \pm 0.10$ [42]. This nullifies the contribution of A_P in case a time-*integrated* measurement of a^s_{sl} is performed. In an independent measurement [53], A_P has been shown to be smaller than a few percent at LHCb. Combining these results, the time-integrated asymmetry observed in the LHCb detector relates to a^s_{sl} as

$$A_{\text{meas}} = \frac{N(D_s^-\mu^+) - N(D_s^+\mu^-)}{N(D_s^-\mu^+) + N(D_s^+\mu^-)} = \frac{a^s_{\text{sl}}}{2} + \mathcal{O}(10^{-5}), \tag{5.3}$$

where simulation is used to extract $\varepsilon(t)$. The estimated statistical precision on A_{meas} in the selected data is of order 10^{-3}. The last term, including the production asymmetry A_P, can therefore safely be ignored throughout this analysis.

Contributions from backgrounds and from instrumental asymmetries have been neglected thus far. The relative difference in detection efficiency between $D_s^-\mu^+$ and $D_s^+\mu^-$ pairs, A_{det}, gives rise to a direct shift in the measured value of A_{meas}, while backgrounds dilute A_{meas} with their charge asymmetry, A_{bkg}. Accounting for the total fraction of backgrounds events that are wrongly included in the selection, f_{bkg}, the measured asymmetry then relates to a^s_{sl} as

$$A_{\text{meas}} = (1 - f_{\text{bkg}})\frac{a^s_{\text{sl}}}{2} + f_{\text{bkg}}A_{\text{bkg}} + A_{\text{det}}. \tag{5.4}$$

From this relation it is clear that a high-precision measurement of a^s_{sl} requires a precise estimate of the present backgrounds, together with an excellent understanding of the instrumental asymmetry A_{det}.

5.2 Data selection

This analysis uses the data set recorded by LHCb in 2011 and 2012, corresponding to an integrated luminosity of $3.0\,\text{fb}^{-1}$. The protons were colliding at a centre-of-mass energy of 7 TeV in 2011, and 8 TeV in 2012. Averaging the result over the two LHCb magnet polarity configurations reduces the asymmetry introduced by left-right asymmetries in detector performance, but effects of order 10^{-3} are expected to remain from, for example, the beam crossing angle (see Sect. 6.2.7). It is therefore important to correct for these instrumental effects for each magnet configuration separately. In 2011 and 2012, data were recorded with both magnet polarities, corresponding to $1.4\,\text{fb}^{-1}$ with the up polarity, and $1.6\,\text{fb}^{-1}$ with the down polarity. The data sets for the two years were obtained using a similar, but not identical trigger configuration. The data sets for each year and magnet polarity are therefore analysed separately.

The B_s^0 candidates are formed by combining reconstructed $D_s^- \to K^-K^+\pi^-$ candidates with muons of opposite electric charge. Charge conjugate decays are implicitly

included from now onwards. Both D_s^- and μ^+ candidates considered are required to have a significant IP with respect to any PV, effectively reducing the contribution of promptly produced D_s^- candidates. The contribution is reduced even further by requiring a minimum IP of 0.05 mm for the D_s^- candidate. The muon tracks must be associated to a muon hardware trigger decision, and one of the final-state particles must be selected in the first stage of the software trigger, HLT1. Finally, the decay topology must be compatible with the description of b-hadron decays in the second stage of the software trigger, according to the topological trigger introduced in Sect. 2.3.

Different intermediate states are clearly visible in the Dalitz plot of the selected $D_s^- \to K^+K^-\pi^-$ candidates, shown in Fig. 5.1. Motivated by their variation in signal purity, three distinct regions of D_s^- phase-space are analysed separately and finally combined to maximise the statistical precision on A_{meas}. The region of phase space compatible with $D_s^- \to \phi\pi^-$ decays is defined by requiring the reconstructed K^+K^- mass to be within 20 MeV/c^2 of the ϕ mass, and is referred to as the $\phi\pi$ Dalitz plot region. The region referred to as K^*K and compatible with $D_s^- \to K^*(892)^0K^-$ decays corresponds to candidates for which the reconstructed $K^-\pi^+$ mass lies within 90 MeV/c^2 of the $K^*(892)^0$ mass. All remaining candidates are referred to as non-resonant (NR). Backgrounds originating from $\overline{\Lambda}_c^-$, D^- and D^{*-} decays, for which the decay products are mistakenly included in the $D_s^- \to K^+K^-\pi^-$ selection, are suppressed offline with additional particle-identification requirements, enhancing the signal purity. Such backgrounds are identified by their kinematic properties.

The results from the different data sets and Dalitz plot regions are combined as follows. First, for each magnet polarity and data-taking period, the weighted average of the asymmetries of the three Dalitz plot regions is taken. Then the arithmetic mean for the two magnet polarities is taken to minimise possible residual detection asymmetries, in accordance with Chapter 6. Finally, a weighted average is made over the two data-taking periods, such that the statistical precision of a_{sl}^s is maximised.

5.3 Determination of signal yields

The $K^+K^-\pi^-$ invariant-mass distribution is used to discriminate $D_s^-\mu^+$ from backgrounds, which are mostly formed by random track combinations. The distributions for the three Dalitz plot regions are shown in Fig. 5.2. The fit range is wide to constrain the shape of the combinatorial background, and also includes the Cabibbo-suppressed $D^- \to K^-K^+\pi^-$ decay mode. Both D_s^- and D^- shapes are modelled with a double-sided Hypatia function [54], and the random background is described using a second-order polynomial. A total of 1.59 million signal candidates is selected by this mass fit, 56.5% of which lie inside the $\phi\pi$ region, 25.9% in K^*K and 17.6% in NR.

The measured asymmetry, A_{meas}, is extracted directly from a binned, extended maximum-likelihood fit to the $K^+K^-\pi^-$ mass spectrum, performed simultaneously

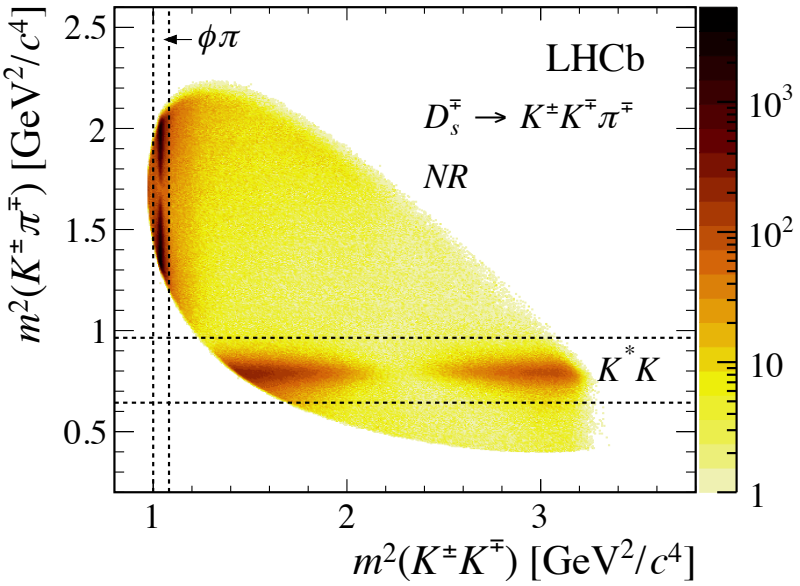

Figure 5.1: Dalitz plot of the $D_s^{\mp} \to K^{\pm}K^{\mp}\pi^{\mp}$ decay for all selected $D_s^{\mp}\mu^{\pm}$ candidates, with the three selection regions indicated. The red and dark areas indicate densely populated intermediate states. Data sets from both years and magnet polarities were combined for this illustration.

for both charges, and thus counting the number of $D_s^-\mu^+$ and $D_s^+\mu^-$ candidates. An overview on the fitted values of A_{meas} per year and Dalitz plot region is presented in Table 5.1. The effects on the measured asymmetry by changes in the fit model are small, and included in the systematic error.

Table 5.1: The measured $D_s^-\mu^+$ asymmetry, A_{meas}, with its statistical uncertainty for the considered data sets.

Sample	A_{meas} [%]		
	$\phi\pi$	K^*K	NR
2011 Magnet Up	1.54 ± 0.32	1.31 ± 0.49	1.24 ± 0.65
2011 Magnet Down	-1.97 ± 0.27	-1.13 ± 0.41	-1.56 ± 0.55
2012 Magnet Up	0.28 ± 0.19	0.41 ± 0.29	1.16 ± 0.38
2012 Magnet Down	0.01 ± 0.19	-0.12 ± 0.30	0.01 ± 0.40

5.4 Irreducible backgrounds

A study on simulation shows there is a large contribution of $D_s^- \mu^+$ candidates from other b-hadron decays, often with additional decay products. The most prominent background of this type originates from $B \to D D_s^+ X$ decays, in which the D meson decays semileptonically. Such backgrounds indeed form genuine $D_s^- \mu^+$ combinations. For other b-hadron species than the $B_s^0 - \overline{B}_s^0$ system, a production asymmetry still gives rise to a residual contribution in the measured asymmetry. With the use of simulation and the measured b-hadron production cross-sections [55–58], the $B \to D D_s^+ X$ contribution is estimated at approximately 10% of the selected signal sample before any offline selection. As on average more energy is left unreconstructed for this class of decays, their $D_s^- \mu^+$ invariant mass is typically lower than for genuine $B_s^0 \to D_s^- \mu^+ \nu_\mu X$ decays, as shown in Fig. 5.4. Most discrimination is, however, found in the corrected mass, m_{corr}. The corrected mass signifies the minimal mass of the B_s^0 candidate after the addition of a massless particle which compensates the reconstructed momentum transverse to the reconstructed B_s^0 flight direction, $p_\perp$

$$m_{\text{corr}} = \sqrt{m^2_{D_s^- \mu^+} + p_\perp^2} + p_\perp. \tag{5.5}$$

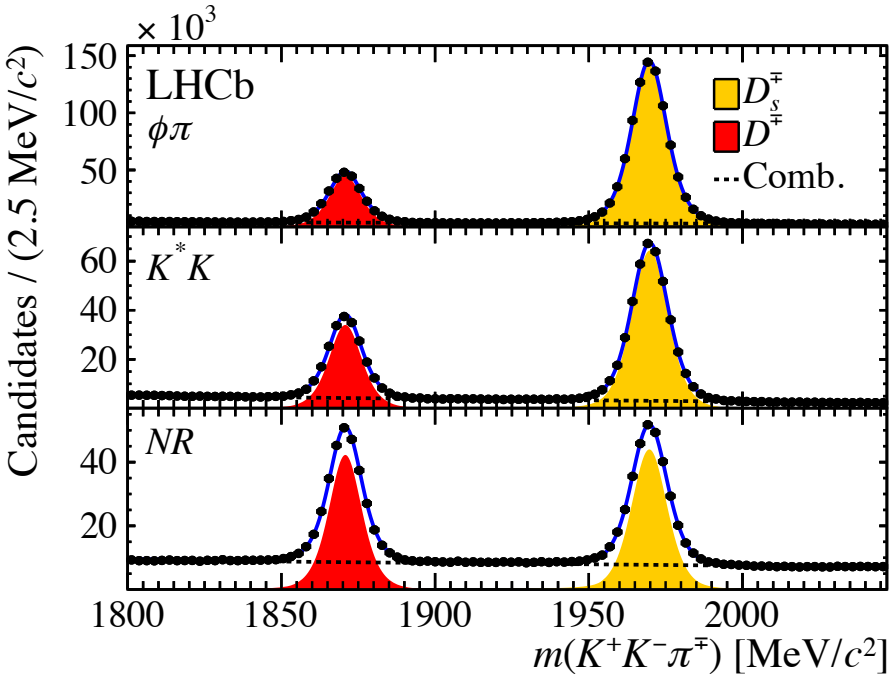

Figure 5.2: Distributions of the $K^- K^+ \pi^-$ invariant mass for candidates passing all selection criteria for the three Dalitz plot regions separately, along with the result of the fit. All data sets, including both years and both magnet polarities, are combined for this illustration.

An illustration of the corrected mass is given in Fig. 5.3. The m_{corr} distributions for prominent backgrounds, including the earlier-discussed $B \to DD_s^+X$ decays, along with the signal are shown in Fig. 5.4. As estimated from simulation, a requirement on the minimal corrected mass, $m_{\text{corr}} > 4.2\,\text{GeV}/c^2$, reduces the total background contribution with approximately a factor of 2 to $f_{\text{bkg}} = (18.4 \pm 6.0)\%$. Combining the individual background fractions with the measured production asymmetries and, where applicable, mixing asymmetries for Λ_b^0 [59], B^0 [49] and B^+ decays [60], the total contribution to A_{meas} is estimated as

$$f_{\text{bkg}} A_{\text{bkg}} = (-0.023 \pm 0.031)\%. \tag{5.6}$$

5.5 Instrumental asymmetries

The detection asymmetry, A_{det}, signifies the relative difference in detection efficiency, $\varepsilon(D_s^-\mu^+)$, between the two oppositely charged final states. In the case that multiple, independent efficiencies contribute to $\varepsilon(D_s^-\mu^+)$, e.g. $\varepsilon(D_s^-\mu^+) = \varepsilon_A\varepsilon_B$, the resulting detection asymmetry A_{det} can be decomposed as

$$\begin{aligned} A_{\text{det}} &= \frac{\varepsilon_A(f)\varepsilon_B(f) - \varepsilon_A(\overline{f})\varepsilon_B(\overline{f})}{\varepsilon_A(f)\varepsilon_B(f) + \varepsilon_A(\overline{f})\varepsilon_B(\overline{f})} \\ &= \frac{A_A + A_B}{1 + A_A A_B} \\ &\approx A_A + A_B + \mathcal{O}(A_A A_B^2 + A_A^2 A_B). \end{aligned} \tag{5.7}$$

This allows to decompose A_{det} linearly,

$$A_{\text{det}} \approx A_{\text{trigger}} + A_{\text{track}} + A_{\text{PID}} + \mathcal{O}(A_{\text{det}}^3), \tag{5.8}$$

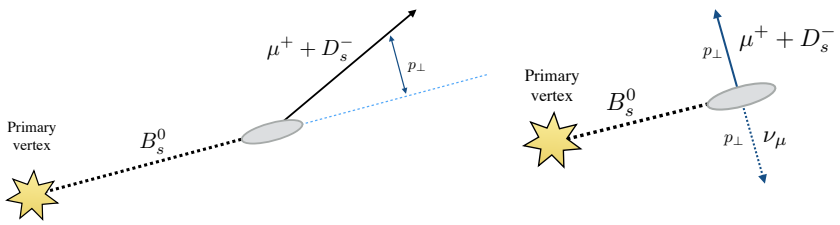

Figure 5.3: Definition of the perpendicular momentum in the calculation of the corrected mass, m_{corr}, (left) in the laboratory frame and (right) boosted along the reconstructed flight direction of the B_s^0 meson. The formula for the corrected mass, Eq. 5.5, is extracted from computing the invariant mass in the boosted frame, assuming a massless missing particle. Note that any longitudinal component of the missing momentum is neglected in the calculation.

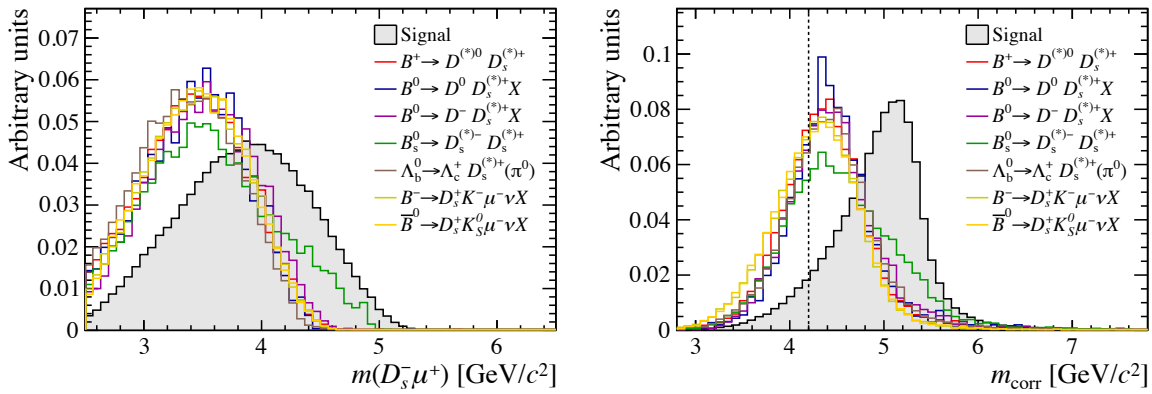

Figure 5.4: Normalised distributions of the (left) reconstructed $D_s^- \mu^+$ mass and (right) corrected mass for simulated decays. The selection applied in the analysis is indicated by a dotted line in the right figure.

to the components originating from acceptance and track reconstruction, A_{track}, from the requirements on the event trigger, A_{trigger}, and from the particle-identification requirements, A_{PID}. The largest correction is $\mathcal{O}(1\%)$, such that the approximation is valid for a measurement with a projected uncertainty above $A_{\text{det}}^3 \approx 10^{-5}$. The largest corrections to the measured asymmetry originate from the hardware trigger and the track reconstruction, which are therefore discussed in detail.

5.5.1 Event trigger

Both the software- and the hardware trigger can introduce a charge bias in the $D_s^+ \mu^-$ selection. The asymmetry induced by the trigger, A_{trigger}, is therefore split into contributions from the muon hardware trigger, A_{L0}, and from the software trigger, A_{HLT}. The charge asymmetry associated to the muon hardware trigger forms the largest correction to A_{meas}.

Hardware trigger

The charge bias in muon hardware trigger is calibrated with $J/\psi \to \mu^+\mu^-$ decays, where the J/ψ originates from a $B^+ \to J/\psi K^+ X$ decay. Candidates are selected using unbiased trigger requirements with respect to at least one of the muons, by requiring that a hardware trigger decision was caused by another particle in the same event. The detection efficiencies in bins of p_{T} and η are determined by interpreting the signal yield for candidates in which this muon passes the hardware trigger requirements, and those that do not,

$$\varepsilon_{\text{L0}} = \frac{N(\text{pass})}{N(\text{pass}) + N(\text{fail})}.$$

The signal yields, along with the efficiency, are extracted from simultaneous extended maximum-likelihood fits to the $\mu^+\mu^-$ invariant-mass distributions of the pass and fail candidates, which separates random track combinations from $J/\psi \to \mu^+\mu^-$ decays.

The asymmetries obtained from these efficiencies are shown in Fig. 5.5 as a function of the transverse momentum for the two data-taking years. This asymmetry is partly attributed to to left-right differences in the spatial distribution of the sensitive pads of the muon detector, unaccounted for in the hardware trigger. This leads to a relative bias in the calculated hardware-trigger p_{T} between the two detector sides. The effects from this asymmetry could be mitigated by only considering muons with p_{T} far above the trigger threshold. However, the limited p_{T} resolution of the muon detector of a few hundred MeV/c would then reduce the number of selected candidates greatly. Instead, all muons are accepted with $p_{\mathrm{T}} \geq 1.2\,\mathrm{GeV}/c$, and the asymmetry is calibrated with the use of the J/ψ decays. In the beginning of 2012, the hardware trigger itself was calibrated for the left-right differences at the time, such that its charge asymmetry was reduced. As is clear from Fig. 5.5, the correction after averaging over magnet polarities is small, as is expected from its geometrical origin.

Suitable corrections for the different signal samples are extracted by first assigning per-candidate weights to the calibration samples, such that the two-dimensional distributions of p_{T}, η of the calibration muon match those of the signal sample, and subsequently determining the asymmetry from the weighted calibration sample. The resulting correction, shown in Table 5.2, dominates the detector correction for each individual data set. The systematic error is estimated with variations of the weighting strategy, including the equalisation of the p, η distributions instead of p_{T}, η. The correction to the combined value of A_{meas} is

$$A_{\mathrm{L0}} = (-0.03 \pm 0.02 \pm 0.02)\%.$$

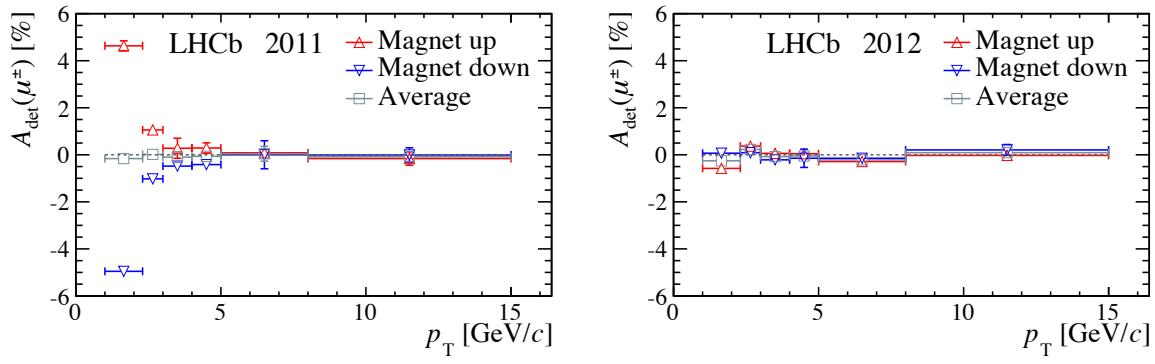

Figure 5.5: Combined muon particle identification and hardware trigger asymmetry as a function of muon transverse momentum, p_{T}, for (left) 2011 data and (right) 2012 data. The illustrated asymmetry is dominated by the hardware trigger asymmetry, A_{L0}.

Software triggers

The software trigger of LHCb is divided into two stages, HLT1 and HLT2, of which the first dominates the charge asymmetry [61]. Only a correction is therefore applied for the asymmetry introduced by the HLT1 requirements, while an upper limit to the HLT2 asymmetry is included in the systematic error of A_{HLT}. The same sample as used for the muon-hardware-trigger calibration can be used to calibrate the first-stage software trigger. Contrary to the hardware trigger requirements, candidates in which the HLT1 decision was based on one of the final-state hadrons are also included in the a^s_{sl} data set, which adds approximately 7.6% of signal candidates. For the hadronic HLT1 asymmetry a similar tag-and-probe procedure is followed, using promptly produced $D_s^+ \to K^-K^+\pi^+$ decays. The resulting correction to the combined measured asymmetry is

$$A_{\text{HLT}} = (0.00 \pm 0.01 \pm 0.02)\%.$$

5.5.2 Track reconstruction and acceptance

The asymmetry due to the track reconstruction and the detector acceptance, A_{track}, is split up into a contribution associated with the K^+K^- pair, $A^{K^+K^-}_{\text{track}}$, and a contribution associated with the $\mu^+\pi^-$ pair, $A^{\mu^+\pi^-}_{\text{track}}$. Both contributions are discussed separately below.

Kaon pair

The detection asymmetry for kaons is driven by the difference in K^+ and K^- cross sections with the detector material. This asymmetry depends on the momentum of the kaon, and is approximately 1%. However, the expected asymmetry for the kaon pair, $A^{K^+K^-}_{\text{track}}$, is small, as most asymmetry cancels by the similar momentum distributions for

Table 5.2: The corrections to A_{meas} for the muon hardware trigger requirements, A_{L0}, with their statistical uncertainty only, for all data sets.

Sample	A_{L0} [%]		
	$\phi\pi$	K^*K	NR
2011 Magnet Up	1.10 ± 0.06	1.02 ± 0.06	1.01 ± 0.06
2011 Magnet Down	-1.17 ± 0.07	-1.09 ± 0.05	-1.13 ± 0.05
2012 Magnet Up	0.06 ± 0.04	0.09 ± 0.04	0.03 ± 0.04
2012 Magnet Down	-0.12 ± 0.04	-0.13 ± 0.04	-0.18 ± 0.04

the two kaons, shown in Fig. 5.7. For $\phi \to K^-K^+$ decays, the kinematic distributions overlap perfectly due to the CP symmetry of the final state, but larger differences could be expected in the K^*K region. The observed difference in phase-space, as seen in the centre-left panel of Fig. 5.7, is actually small as a result of the offline selection. Despite the significant overlap, a calibration for the detection asymmetry of kaon pairs is required to make use of the full Dalitz plot.

The detection asymmetry for the kaon pair is calibrated with the use of $A_{\text{det}}^{K^-\pi^+}$, measured using $D^+ \to K^-\pi^+\pi^+$ and $D^+ \to \overline{K}^0\pi^+$ decays. This method will be described in detail in Chapter 7. The extraction of $A_{\text{track}}^{K^+K^-}$ from $A_{\text{det}}^{K^-\pi^+}$ proceeds in three steps. First, the detector bias is determined for a kaon-pion pair of which the kaon p_{T}, η distributions match those of the charged kaon with the same charge as the pion in the signal data set. Then, the same procedure is repeated, but now for the charged kaon with opposite charge. Lastly, the two results are subtracted, taking into account the correlation. The procedure is also illustrated in Fig. 5.6 for clarity. The observed deviation when using a parametrisation in bins of p, η is small, but added to the systematic error. The contribution from the pion asymmetry has been neglected in these steps, as their impact is expected to be small on the polarity-averaged value of $A_{\text{track}}^{K^+K^-}$. To check this assumption, the per-candidate weights in both steps are calculated such that the p_{T} distribution of the calibration pions match those found in the signal data set. The change in the polarity-averaged value of $A_{\text{track}}^{K^+K^-}$ as a result of this extra requirement is indeed small, around 0.03%, and also included in the systematic error. The total correction to A_{meas} as a result of the kaon detection asymmetry is

$$A_{\text{track}}^{K^+K^-} = (-0.01 \pm 0.00 \pm 0.03)\%.$$

Muon-pion pair

Due to the hardware trigger requirement on the selected muons, their transverse momentum spectrum is harder than that of the selected pions, as shown in Fig. 5.7. The effects from the track reconstruction algorithms and the geometric detector acceptance are therefore expected to be more prominent in the combined muon-pion asymmetry, $A_{\text{track}}^{\mu^+\pi^-}$, than in the case of the kaon pair. Nonetheless, part of the contributions due to detector acceptance and track reconstruction are expected to cancel. The detection asymmetry for both the pion and the muon is calibrated with two independent methods, which both assume the same detection asymmetries for the muon and the pion. The asymmetry for the muon-pion pair is calculated by the difference, $A_{\text{track}}^{\mu^+\pi^-} = A_{\text{track}}^{\mu^+} + A_{\text{track}}^{\pi^-} = A_{\text{track}}^{\mu^+} - A_{\text{track}}^{\pi^+}$, and the resulting statistical error accounts for the statistical correlation by the re-use of the same calibration sample.

The first method uses partially reconstructed $D^0 \to K^-\pi^+\pi^+\pi^-$ decays, where the D^0 originates from a $D^{*+} \to D^0\pi^+$ decay. The reconstructed mass difference,

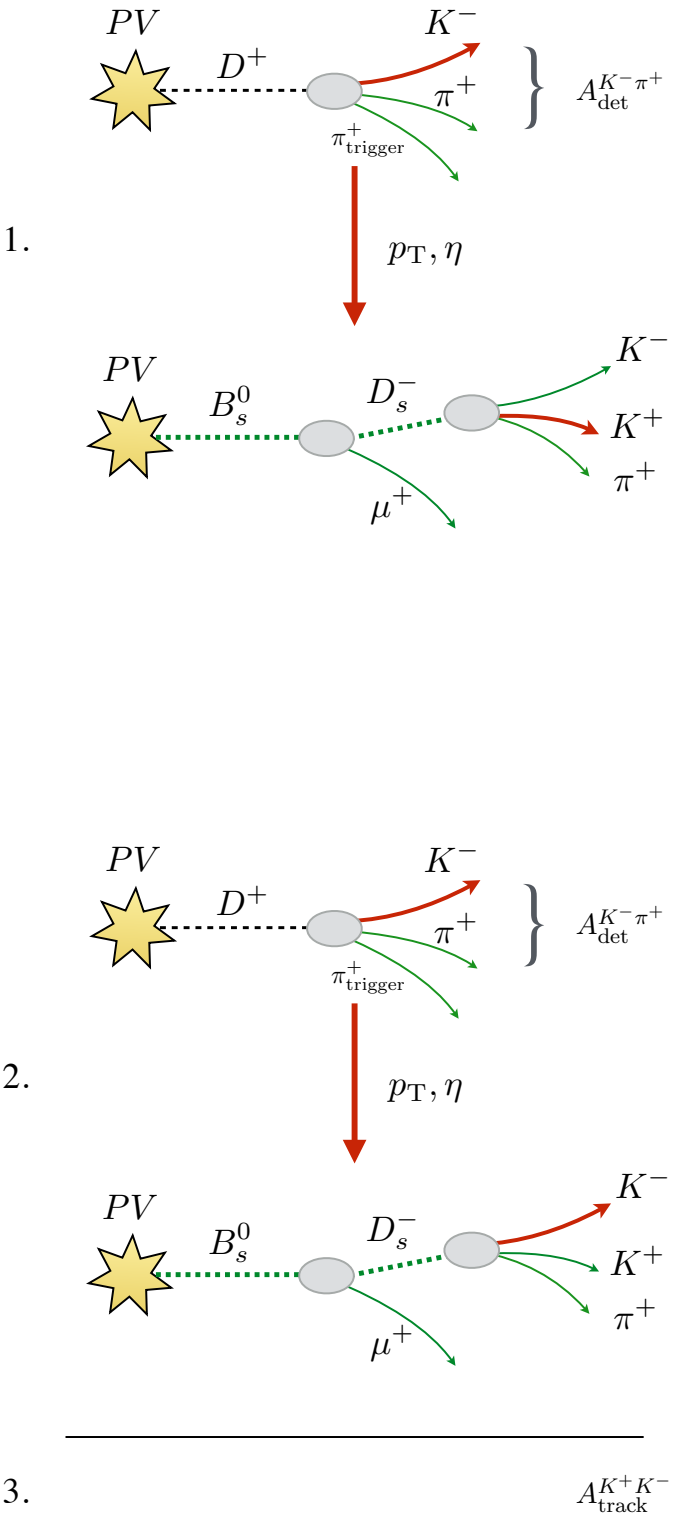

Figure 5.6: Schematic of the use of $A^{K^-\pi^+}_{\text{det}}$ to calculate $A^{K^+K^-}_{\text{track}}$. The kinematic variables in the two first steps are the ones from the track highlighted in red.

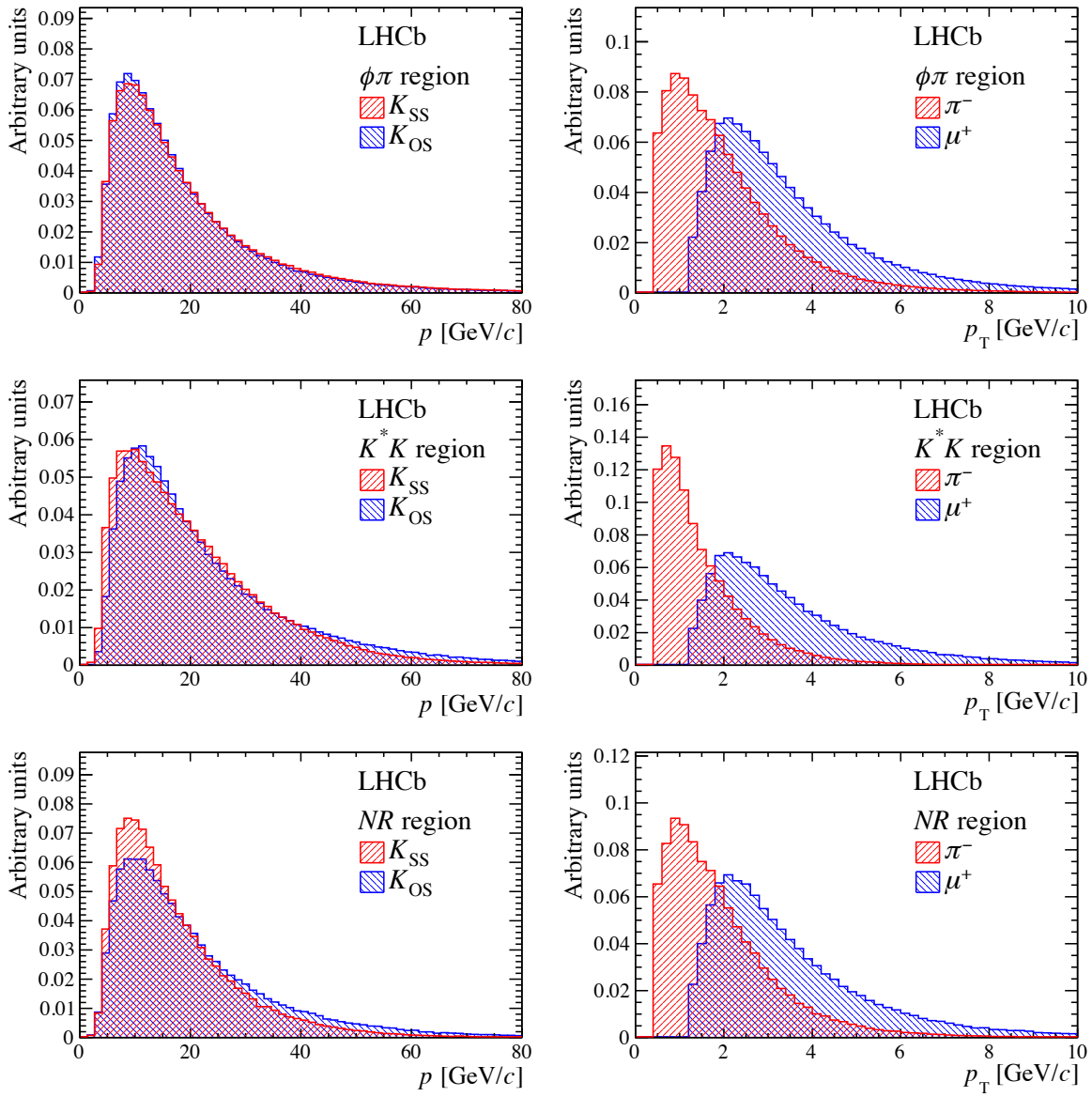

Figure 5.7: (left) Background-subtracted momentum distributions for the final-state kaons, where the kaon with the same (opposite) charge as the pion is denoted by $K_{\rm SS}$ ($K_{\rm OS}$), and (right) transverse momentum distributions of the final-state muon and pion. For these histograms all data including both years and both magnet polarities are combined.

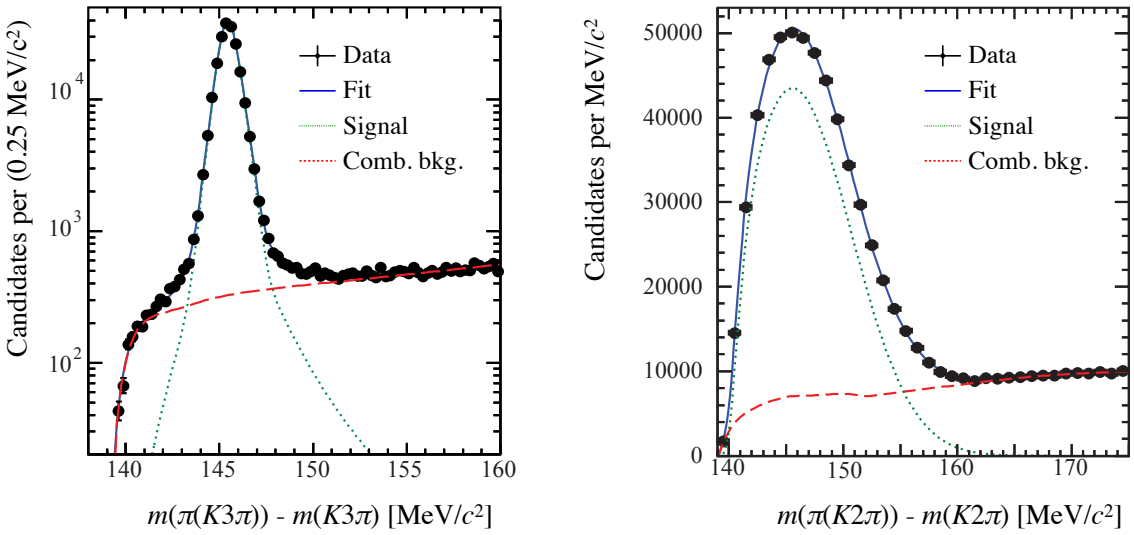

Figure 5.8: Example of the distribution of the mass difference Δm for (left) fully reconstructed and (right) partially reconstructed $D^{*+} \to D^0(\to K^-\pi^+\pi^-\pi^+)\pi^+$ decays, with the fit shown as well.

$\Delta m = m(D^*) - m(D^0)$, shows a peak even when missing one of the final-state pions. An example is shown in Fig. 5.8. A maximum-likelihood fit to Δm provides the yields for partially- and fully reconstructed D^0 decays, such that the pion reconstruction efficiency can be determined. Access to the missing pion momentum vector is obtained by constraining the reconstructed D^0 to originate from its associated PV, and applying the mass constraints. This allows to determine the momentum dependence of the pion detection asymmetry. Irreducible and prominent backgrounds, such as $D^0 \to K^-\pi^+\pi^+\pi^-\pi^0$ decays, combined with the limited D^0 vertex resolution introduce a bias in the fitted momentum and worsen its resolution. A delicate unfolding procedure is therefore required, using the fully reconstructed sample as training data. Despite these complications, the extracted detection asymmetry is the only data-driven calibration in Run-1 which includes all causes of asymmetries described in Chapter 6, including the beam-crossing angle and the charge-asymmetric collision rate with the detector material. With this method, the detection asymmetry of charged pions is determined in bins of pion momentum, which is then weighted with the corresponding distributions of the muon and pion found in the signal samples.

The second method uses $J/\psi \to \mu^+\mu^-$ decays, in which one track is reconstructed with alternative, independent reconstruction algorithms, as described in Ref. [62]. These algorithms are independent of at least one of the subdetectors required to form a long track, either the VELO or the main downstream tracking stations. To determine the momentum of the track, hits are only required in either the TT or the muon subdetector.

The reconstruction efficiency per subdetector is determined by checking for the existence of a fully reconstructed track corresponding to the probe track. The efficiencies of the VELO and downstream tracking stations are finally added to obtain the long tracking efficiency. As all particles considered are in the LHCb acceptance both upstream and downstream of the dipole magnet, any charge asymmetry in the acceptance is not probed. Because of this shortcoming, a correction of approximately 0.10% per magnet polarity is applied, which is obtained from simulation. The origin of this correction is further described in Chapter 6. The polarity-averaged effects from the acceptance are however small, and compatible with 0.00%. To find an adequate correction per magnet polarity for the $a^s_{\rm sl}$ signal candidates, the asymmetry is first determined in bins of $p_{\rm T}$ and η of the muon, and subsequently weighted with its distribution found in the signal samples.

Both methods described above assume identical detection asymmetries for muons and pions. This assumption is not completely valid due to the left-right asymmetric distribution of detector material. This asymmetry is mitigated by averaging the data sets over magnet polarities. As such, a small, common systematic error of 0.02% is assigned to both methods, derived from the asymmetry in cross sections of charged pions with the detector material. This effect is further discussed in Sect. 6.2.1.

Finally, both methods are combined using a weighted average, maximising the statistical precision per data set. The correction to $A_{\rm meas}$ averaged over all data sets is

$$A_{\rm track}^{\mu^+\pi^-} = (-0.01 \pm 0.05 \pm 0.04)\%.$$

5.5.3 Particle identification

The efficiency of the particle-identification requirements for hadrons and their associated asymmetry has been evaluated with prompt $D^{*+} \to D^0(\to K^-\pi^+)\pi^+$ decays, using the standardised method explained in detail in Ref. [63]. This method relies on the selection of such candidates from data without relying on PID information for one of the D^0 decay products, which allows to calibrate the PID performance. For the muons, the same sample of $J/\psi \to \mu^+\mu^-$ candidates is used as in Sect. 5.5.1. The correction to the combined value of $A_{\rm meas}$ is

$$A_{\rm PID} = (0.01 \pm 0.02 \pm 0.03)\%.$$

5.6 Result

The measured values of all detection asymmetries and $A_{\rm meas}$ with their statistical and systematic uncertainties, combined over all data sets are shown in Table 5.3. The twelve resulting values for $a^s_{\rm sl}$ for each data set are illustrated in Fig. 5.9, and found

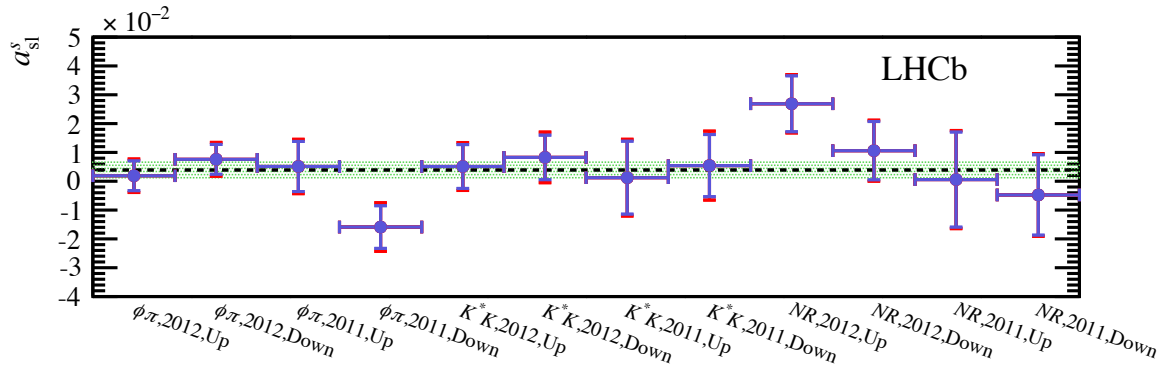

Figure 5.9: Measured values of $a^s_{\rm sl}$ for the twelve individual data sets, after applying all corrections. The blue error bars represent the statistical uncertainties, and the red error bars show the total errors. The uncertainties are partially correlated between the three Dalitz plot regions, mainly by the statistical correlation of the re-used calibration samples. The dashed line and the green horizontal band represent the combined value of $a^s_{\rm sl}$ and its total uncertainty.

to be consistent with each other. Combining all data sets and taking into account all correlations, the measured value of $a^s_{\rm sl}$ is

$$a^s_{\rm sl} = (0.39 \pm 0.26 \pm 0.20)\%. \tag{5.9}$$

The quoted statistical error includes the statistical error from the used calibration samples. This result, which is the most precise direct measurement of $a^s_{\rm sl}$ to date, is consistent with the prediction from the Standard Model. An overview of all direct measurements of $a^s_{\rm sl}$ and $a^d_{\rm sl}$, including this result, is shown in Fig. 5.10. The compatibility of these direct measurements with the combined $a^d_{\rm sl} - a^s_{\rm sl}$ measurement from the D0 collaboration is reduced from a p-value of 10.7% to a p-value of 0.5%.

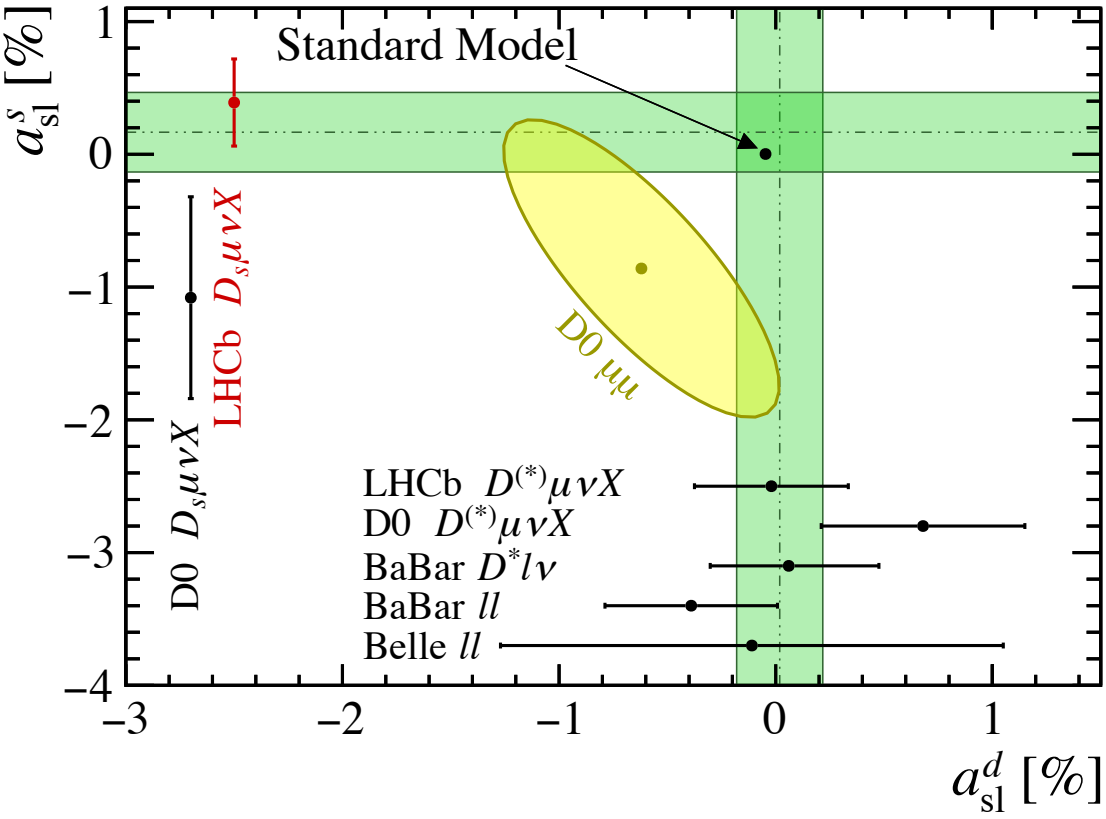

Figure 5.10: Overview of the published measurements of $a_{\rm sl}^d$ and $a_{\rm sl}^s$, including the presented $a_{\rm sl}^s$ measurement in red. The horizontal and vertical bands indicate the naive averages of pure $a_{\rm sl}^s$ and $a_{\rm sl}^d$ measurements [45–51], which are individually represented by the black points. The yellow ellipse represents the D0 dimuon measurement with $\Delta\Gamma_d/\Gamma_d$ set to its Standard-Model expectation value [44]. The error bands and contours correspond to 68% confidence level.

Table 5.3: Overview of contributions (in percent) in the determination of $a^s_{\rm sl}$, averaged over Dalitz plot regions, magnet polarities and data taking periods, with their statistical and systematic uncertainties. The central value of $a^s_{\rm sl}$ is calculated according to Eq. 5.4. The uncertainties are added in quadrature and multiplied by $2/(1-f_{\rm bkg})$, to obtain the uncertainties on $a^s_{\rm sl}$.

Source	Value	Stat. uncert.	Syst. uncert.	
$A_{\rm meas}$	0.11	0.09	0.02	
$-A^{K^+K^-}_{\rm track}$	0.01	0.00	0.03	
$-A^{\mu^+\pi^-}_{\rm track}$	0.01	0.05	0.04	
$-A_{\rm PID}$	−0.01	0.02	0.03	
$-A_{\rm L0}$	0.03	0.02	0.02	
$-A_{\rm HLT}$	0.00	0.01	0.02	
$-f_{\rm bkg}\ A_{\rm bkg}$	0.02	−	0.03	+
$(1-f_{\rm bkg})a^s_{\rm sl}/2$	0.16	0.11	0.08	
$2/(1-f_{\rm bkg})$	2.45	−	0.18	×
$a^s_{\rm sl}$	0.39	0.26	0.20	

Part III

CP-asymmetry measurements beyond Run 1

Chapter 6

Classification of detection asymmetries at LHCb

The control of charge-related detection biases is essential for the measurements of *CP* asymmetries at LHCb. Therefore, calibration measurements are carried out to determine any relative difference in detection efficiency between positively and negatively charged particles. The detection efficiency depends, amongst others, on the cross-sections of the interaction of the corresponding particle with detector material. Therefore, such calibrations are performed for different particle species separately. In this chapter, the possible causes of a charge bias for particle species h are presented. This bias is quantified by the detection asymmetry, $A_{\text{det}}^{h^+}$, which is defined as the relative difference in efficiencies,

$$A_{\text{det}}^{h^+} = \frac{\varepsilon_{\text{det}}(h^+) - \varepsilon_{\text{det}}(h^-)}{\varepsilon_{\text{det}}(h^+) + \varepsilon_{\text{det}}(h^-)}, \tag{6.1}$$

where $\varepsilon_{\text{det}}(h^\pm)$ denotes the absolute detection efficiency of a single particle species. For physics analyses, this detection efficiency typically includes contributions from the detector acceptance, track reconstruction, PID and the trigger. In this chapter, the details related to the asymmetry in the acceptance and the track reconstruction will be discussed. The definition of these contributions, along with examples, are given below.

1. **Acceptance**: Particles are required to traverse enough layers in the tracking detectors to meet the requirements of the track reconstruction, in accordance to Sect. 2.2.1. Since analyses in LHCb mostly use long tracks, only the asymmetry for finding and reconstructing long tracks is considered. Such tracks require the presence of at least three hits for each of the VELO sensor types (r and ϕ), as well as at least one hit in the x-layers and at least one hit in the stereo layers for each of the three T-stations. As the dipole magnet deflects particles of opposite charge in the horizontal plane, left-right differences in the detector performance downstream of the dipole magnet are one of the main causes of acceptance asymmetries. A further subdivision of inefficiencies is made in the following categories:

(a) **Material**: Inelastic interactions with the detector material cause the particle of interest to be absorbed before traversing sufficient tracking stations. This can lead to a charge asymmetry due to a left-right asymmetric material budget, or due to asymmetric cross-sections themselves. For example, kaons and protons are known to have a sizeable charge asymmetry in their nuclear-interaction cross-sections.

(b) **Geometric**: Even when not undergoing any collision, some particles are bent out of the LHCb acceptance, e.g. into the beam-pipe region. In addition, any left-right asymmetric design of detector elements can lead to a different acceptance between the two detector sides.

(c) **Detector**: Parts of the tracking detector material are not sensitive, such as inefficient channels. In case these inefficient regions are located left-right asymmetric, this causes a charge asymmetry.

2. **Tracking**: Left-right choices in track reconstruction algorithms can introduce a bias for a bending direction, leading to a magnet-dependent charge asymmetry. Moreover, as most secondary particles are negatively charged (electrons), the negatively charged particles are reconstructed with a higher local occupancy than positively charged particles. Since the track-reconstruction efficiency depends on the occupancy, the higher occupancy for negatively charged particles leads to a different track-reconstruction performance per charge for each magnet polarity.

Similarly to other analyses which used the Run-1 data set of LHCb, the measurement of $a^s_{\rm sl}$ presented in Chapter 5 made use of partially reconstructed D^0 decays to calibrate the detection asymmetry of charged pions, parametrised by the pion's momentum. The measured asymmetry, shown in Fig. 6.1, shows a clear dependence on both magnet polarity and the pion momentum. As seen in the right panel of the same figure, the behaviour is partially reproduced in simulation. This allows to study the causes of these asymmetries. While the simulated detection asymmetry describes the momentum dependence qualitatively, the cause of this observed asymmetry was not understood prior to this study. Understanding its origins allows to determine a suitable parametrisation of these detection asymmetries, assign a well-motivated systematic error to the calibration methods, and improve the simulated detector description. This chapter presents a quantitative study on the sources of the detection asymmetries in LHCb, and as such, is particularly important for future measurements of *CP* asymmetries, which are expected to be limited by systematic uncertainties related to the calibration of the detection asymmetry.

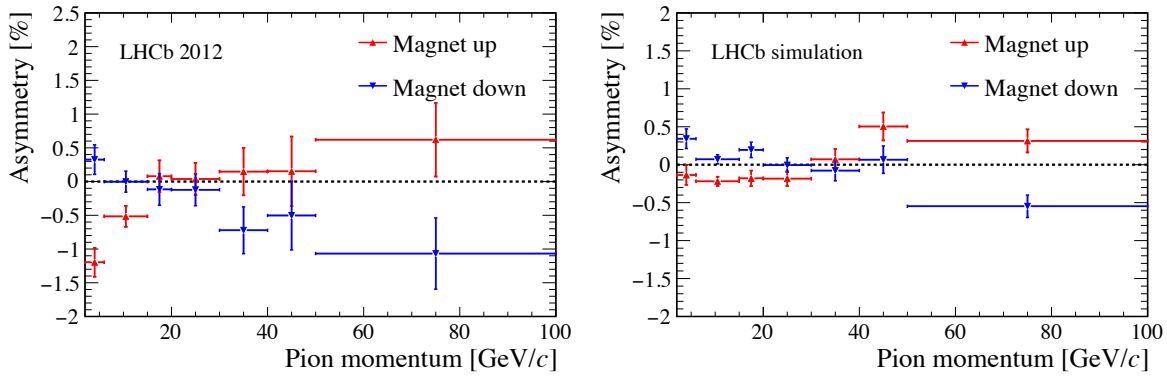

Figure 6.1: (left) Pion detection asymmetry determined using partially reconstructed $D^0 \to K^-\pi^+\pi^-\pi^+$ decays, originating from $D^{*+} \to D^0\pi^+$ decays, in 2012 data. (right) Pion detection asymmetry for simulated $D^0 \to K^-\pi^+$ decays, originating from $D^{*+} \to D^0\pi^+$ decays.

6.1 Method

Large data sets are needed for the multidimensional parametrisation of phase-space, required to investigate the detection efficiency and detection asymmetry. The acceptance effects will be addressed by the use of fast simulation in combination with a toy model of the spectrometer, as both of these methods are suited to generate large samples of events. These methods, and a comparison between them, are presented here.

6.1.1 Particle-gun production

The first method uses the particle-gun mode of the LHCb simulation software, introduced briefly in Sect. 2.4 already. The decay modes $D^+ \to K^-\pi^+\pi^+$ and $D^+ \to K^-\mu^+\mu^+$ (and their charge conjugates) are generated without simulating the rest of the event. Various decay modes could have been used, and the first decay is chosen as a large fast simulation sample was already available. The latter, non-physical, decay mode is chosen to remove effects from hadronic interactions, which affect the pions but not the muons. Large sample sizes of 10^8 events per magnet polarity have been prepared in this way. The performances of the reconstruction algorithms differ from a simulation including the full proton-proton collision, as the tracking performance also depends on the (local) event occupancy. Therefore, these samples are only suited for the study of the detector acceptance asymmetry. Both samples of simulated D^+ decays are generated with a phase-space model for their decay, i.e. no intermediate resonances are simulated. Thanks to the small difference in π-μ mass, this results in a nearly equal phase space for the final-state particles in the two decay modes. The momentum spectrum for the generated D^+ is adopted from the simulation of 13 TeV proton-proton collisions in

Pythia. The azimuthal angle at the production of the D^+, $\phi = \tan^{-1}(p_y/p_x)$, is generated according to a uniform distribution, implying that no beam-crossing-angle effects are simulated. Similarly, any angle- or momentum-dependent production asymmetry is not simulated. Later in this chapter the consequences of the beam-crossing angle are investigated separately. The average spatial distribution of primary vertices, the so-called beam spot, is set to the average position for 2016 data taking, which is slightly displaced from the centre of the x-axis in the LHCb coordinate system (and therefore left-right asymmetric).

The results from the particle-gun simulation for $D^+ \to K^-\pi^+\pi^+$ and $D^+ \to K^-\mu^+\mu^+$ are shown in Fig. 6.2. The requirements on the reconstructed tracks are identical for both samples. The sample is split in three bins of pseudorapidity, $[1.9, 3.0]$, $[3.0, 4.0]$ and $[4.0, 5.1]$, motivated by the dependence on the material budget of the detector and the transition from the outer to the inner tracker for high η. The detection asymmetry shows a stronger magnet dependence for pions compared to muons. For both muons and pions the magnet-averaged detection asymmetry is compatible with zero.

From these results it can be concluded that the strong magnet-dependent asymmetry as seen for low-momenta pions in Fig. 6.2 is due to hadronic interactions[1]. The asymmetry arising for high momenta and high η is shared among the two modes and is likely the result of an effect of geometric acceptance. By the nature of the simulation sample, this magnet-dependent asymmetry at high momenta cannot originate from any beam-crossing angle, occupancy or misalignment, but can only be explained by the nominal positions of the detector elements and the beam spot in combination with the magnetic field map.

6.1.2 Deterministic model

A deterministic toy model, which does not use Geant4, is used to further simplify the detector simulation. In this method, generated particles are propagated through the detector by numerically solving its equations of motion from its origin vertex up to the last T-station. The same detector geometry, material and magnetic field descriptions are used as in the standard simulation software, Gauss. Any sensitive detector element is modelled as efficient, such that each particle passing through a sensor accounts for a hit. A generated particle can then be tested to be in the geometric acceptance by requiring the number of hits in the tracking stations to meet the minimum requirements to reconstruct a long track. Unlike the standard simulation, this model does not account for stochastic processes such as multiple scattering, which makes this model deterministic. This is considered an advantage for this study, as the efficiency can be modelled with a smaller data sample.

[1]The significant asymmetry is affected by effects in the track reconstruction as well, discussed later in this chapter

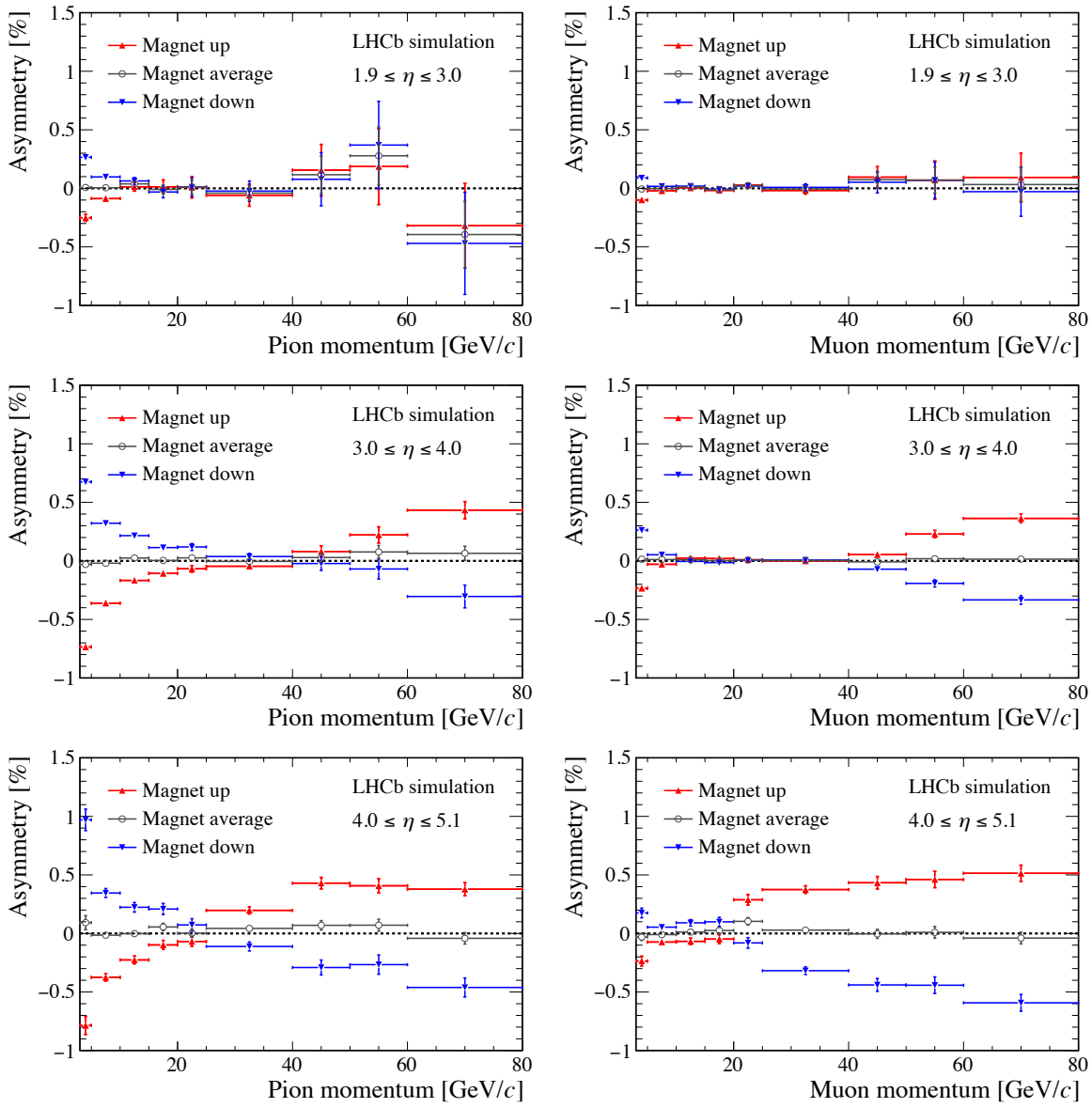

Figure 6.2: Single-track detection asymmetries for (left) π^+ and (right) μ^+ projected in bins of momenta for the generated $D^+ \to K^-\pi^+\pi^+$ and $D^+ \to K^-\mu^+\mu^+$ samples for (top) $\eta \in [1.9, 3.0]$, (middle) $\eta \in [3.0, 4.0]$, and (bottom) $\eta \in [4.0, 5.1]$. The sample used for this plot was generated using the particle-gun method, and no crossing angle or production asymmetry is included. The position of the beam spot, however, is included in this simulation.

The efficiency for the toy model is defined as the ratio of particles which are in acceptance divided by the total number of generated particles,

$$\varepsilon^{\pm}_{\text{toy}}(\vec{p},\vec{x}) = \frac{N(\text{in geometrical acceptance})}{N(\text{generated})}, \tag{6.2}$$

and is evaluated as a function of charge and phase-space parameters. Using this definition of the detection efficiency, the definition for the detection asymmetry follows from Eq. 6.1. Note that the asymmetry in the geometrical acceptance ("geo-acceptance") has no contribution from inelastic material interactions.

Validation

The asymmetry extracted from the deterministic toy is validated by a comparison with the standard proton-proton collision simulation in Gauss, which also includes the beam-crossing angle. A simulation sample of $B^0_s \to D^-_s \mu^+ \nu_\mu X$ decays containing 5 million events is used. The asymmetry for the muon in the B^0_s decay is calculated with the deterministic toy using the kinematic distributions as generated by Gauss, such that the kinematic distributions in the comparison are equal. The resulting asymmetries for the muon detection asymmetry in bins of momentum, η, and ϕ of the muon are shown in Fig. 6.3. The overall behaviour agrees well. The dependence on both ϕ and η is strong in both simulations. The variation in bins of ϕ is an order of magnitude larger than in other variables. The deterministic toy model is considered to describe the asymmetry sufficiently accurate to study its phase-space and magnet-polarity dependence.

Dependence on azimuthal angle

Although there is a strong dependence of the geo-acceptance asymmetry as function of ϕ, this variable is not used in the remainder of this study. The behaviour in ϕ is a consequence of the varying acceptance of charged particles due to their curvature in the $x-z$ plane. Particles with $2|\phi| > \pi$ have an initial direction towards negative x ($p_x < 0$), and the other way around for $2|\phi| < \pi$. The magnet polarity brings a preference for a direction in x per charge: the magnet adds (subtracts) momentum in the x direction for positively (negatively) charged particles for the downwards polarity. For the most inner region of the tracking stations, a small change in x can make the difference of being inside or outside the geometric acceptance of the detector. Positively charged particles are bent into the beam-pipe hole and outside of the geometrical acceptance on one side of the detector, while those particles are bent inside the acceptance on the other side. The same happens but with opposite orientation for the opposite charge. Similarly, this also occurs on the outer edges of the geometrical acceptance: the left and right ends of the outer tracker.

The particle distribution is concentrated around the beampipe, such that the bending effect around the beampipe has a much larger impact than the effect at the outer edges of

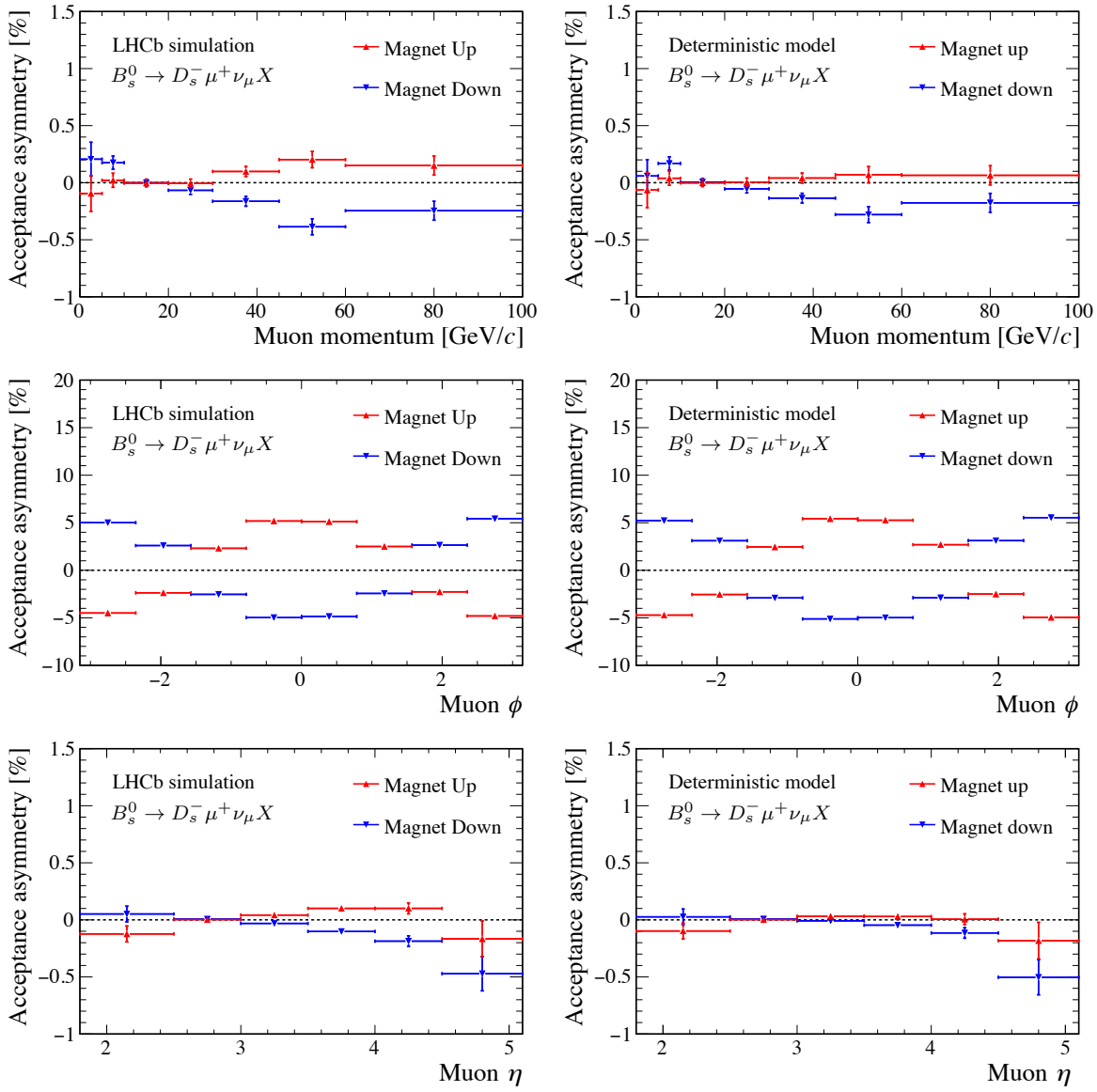

Figure 6.3: Simulated detection asymmetry for muons, with (left) the GAUSS simulation and (right) the deterministic model, using $B_s^0 \to D_s^- \mu^+ \nu_\mu X$ decays. This simulation includes the effects from the beam-crossing angle as used throughout 2012 data taking.

the tracking stations. Therefore, the strong dependence on the initial angle is understood as a natural consequence of the magnet. The generated ϕ distribution is flat in case of no beam-crossing angle, such that this strong magnet dependence is cancelled by the equal distribution of left- and right-travelling particles.

Material description

A difference in detection asymmetry between muons and pions is visible in Fig. 6.2. Therefore, a simulation of hadronic interactions is required to describe the detection asymmetry of hadrons. The standard simulation is used to motivate the description of inelastic and elastic hadronic interactions in the deterministic model. Approximately 84% of the hadronic interactions, for the energies relevant to LHCb, are inelastic. Any inelastic interaction before the last T-station (T3) effectively reduces the track reconstruction efficiency drastically, as shown in Fig. 6.4. The material thickness of the LHCb detector is therefore considered up to and including the second tracking station, $z = 8900\,\text{mm}$. Elastic scatters, which can cause a kink in the particle's trajectory, also lower the efficiency of the track reconstruction. In Appendix A it is shown that approximately 54% of the elastically scattered hadrons are not (correctly) reconstructed. However, for simplicity and because the contribution from elastic scatters is small, the *total* cross-sections are used to describe the hadronic interactions with the detector material.

The contribution of material interactions to the detection efficiency is quantified by recording, along the path of any particle, the thickness of encountered detector material in the simulated detector. The material thickness, $d^{\pm}$, is expressed in units of nuclear collision length. The nuclear collision length is defined as the typical length that a hadron travels before it undergoes an (in)elastic scatter with a nucleus in the material. This collision length, λ_{T}, is inversely proportional to the total hadronic cross-section, $\sigma_T^{\pm}$, and is dependent on the momentum and charge. In addition, λ_T depends on the atomic mass number of the encountered material.

When the asymmetric cross-sections for any target material are assumed to scale with momentum as those for deuterium, the dependence on the atomic mass number, A, and momentum can be factorised,

$$\lambda_{\text{T}}^{\pm}(A,p) = \lambda_{\text{T}}^{\text{avg}}(A, 20\,\text{GeV}/c)\frac{\sigma_{\text{T}}^{\text{avg}}(\text{deuterium}, 20\,\text{GeV}/c)}{\sigma_{\text{T}}^{\pm}(\text{deuterium}, p)} \tag{6.3}$$

$$\equiv \lambda_{\text{T}}^{\text{ref}}\frac{\sigma_{\text{T}}^{\text{ref}}}{\sigma_{\text{T}}^{\pm}(p)}, \tag{6.4}$$

in which the reference collision length, $\lambda_{\text{T}}^{\text{ref}}$, and reference cross-section, $\sigma_{\text{T}}^{\text{ref}}$, are defined. This definition is advantageous, as the charge-dependence of the cross-section on deuterium targets is measured with better precision than that for heavier elements. The material distribution of LHCb is approximately isoscalar, i.e., a nearly equal mix of

neutrons and protons. Therefore, the asymmetry in the cross-sections as measured on deuterium targets forms a good approximation for that of the LHCb detector material. For the traversed thickness in units of the collision length, one has for a single piece of material somewhere in the detector

$$\frac{d^{\pm}(\vec{p},\vec{x})}{\lambda_{\mathrm{T}}^{\pm}(p)} = \frac{d^{\pm}(\vec{p},\vec{x})}{\lambda_{\mathrm{T}}^{\mathrm{ref}}}\frac{\sigma_{\mathrm{T}}^{\pm}(p)}{\sigma_{\mathrm{T}}^{\mathrm{ref}}}, \tag{6.5}$$

where the dependences of the path through the LHCb detector on momentum, $\vec{p}$, origin vertex $\vec{x}$ and charge are shown explicitly. The total thickness of the detector is obtained by summing the contributions of the traversed detector pieces. In the remainder of this study, the dependences of the path will be implicit. The detection efficiency of hadrons depends exponentially on the total thickness,

$$\varepsilon_{\mathrm{det}} \propto \exp(-d/\lambda_{\mathrm{T}}). \tag{6.6}$$

This definition of the efficiency due to nuclear collisions naturally leads to the definition of the charge asymmetry,

$$A_{\mathrm{material}} = \frac{\exp(-d^{+}/\lambda_{\mathrm{T}}^{+}) - \exp(-d^{-}/\lambda_{\mathrm{T}}^{-})}{\exp(-d^{+}/\lambda_{\mathrm{T}}^{+}) + \exp(-d^{-}/\lambda_{\mathrm{T}}^{-})} \tag{6.7}$$

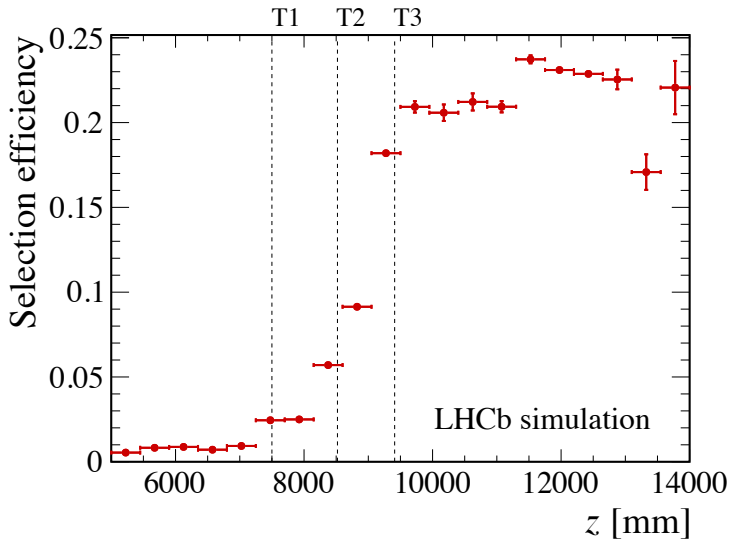

Figure 6.4: Selection efficiency for $B^{+} \to D^{0}(\to K^{-}\pi^{+})\mu^{+}\nu_{\mu}X$-decays, simulated by GAUSS, as a function of the z position of the first hadronic, inelastic scatter of the charged pion. The vertical lines show the central positions of the three T-stations. The efficiency includes the reconstruction of all particles in the final state, along with a typical event selection for a physics analysis (including PID requirements), and therefore does not go up to 100%. Figure adapted from Ref. [64].

It is illustrative to split up the charge dependence of the material asymmetry in a component originating from the cross-sections, $\lambda_{\mathrm{T}}^{\pm}$, and a component originating from the path length, $d^{\pm}$, as

$$\frac{d^{\pm}}{\lambda_{\mathrm{T}}^{\mathrm{avg}}} \equiv d^{\pm}\frac{2}{\lambda_{\mathrm{T}}^{+}+\lambda_{\mathrm{T}}^{-}}, \tag{6.8}$$

and

$$\frac{d^{\mathrm{avg}}}{\lambda_{\mathrm{T}}^{\pm}} \equiv \frac{1}{\lambda_{\mathrm{T}}^{\pm}}\frac{d^{+}+d^{-}}{2}. \tag{6.9}$$

The former measures the cross-section-symmetrised collision rates, due to different paths through the detector. Applied to LHCb, this quantifies the effect of any left-right asymmetric material budget. Meanwhile, the latter measures the effect of the charge asymmetry in the interaction cross-sections only, averaging over the different paths through the detector.

To illustrate the main contributors to the material thickness of LHCb, the simulated material thickness, expressed in units of $\lambda_{\mathrm{T}}^{\mathrm{ref}}$, is determined as a function of momentum and pseudorapidity for pions from $D^{+} \to K^{-}\pi^{+}\pi^{+}$ decays. Only particles which are in the geometrical acceptance are considered. The result is shown in Fig. 6.5. The thickness is much higher for $\eta > 4.0$, with a considerable contribution from the beampipe in the magnet and RICH1. In comparison, the variation of the material thickness within the three bins of pseudorapidity is smaller as a function of momentum.

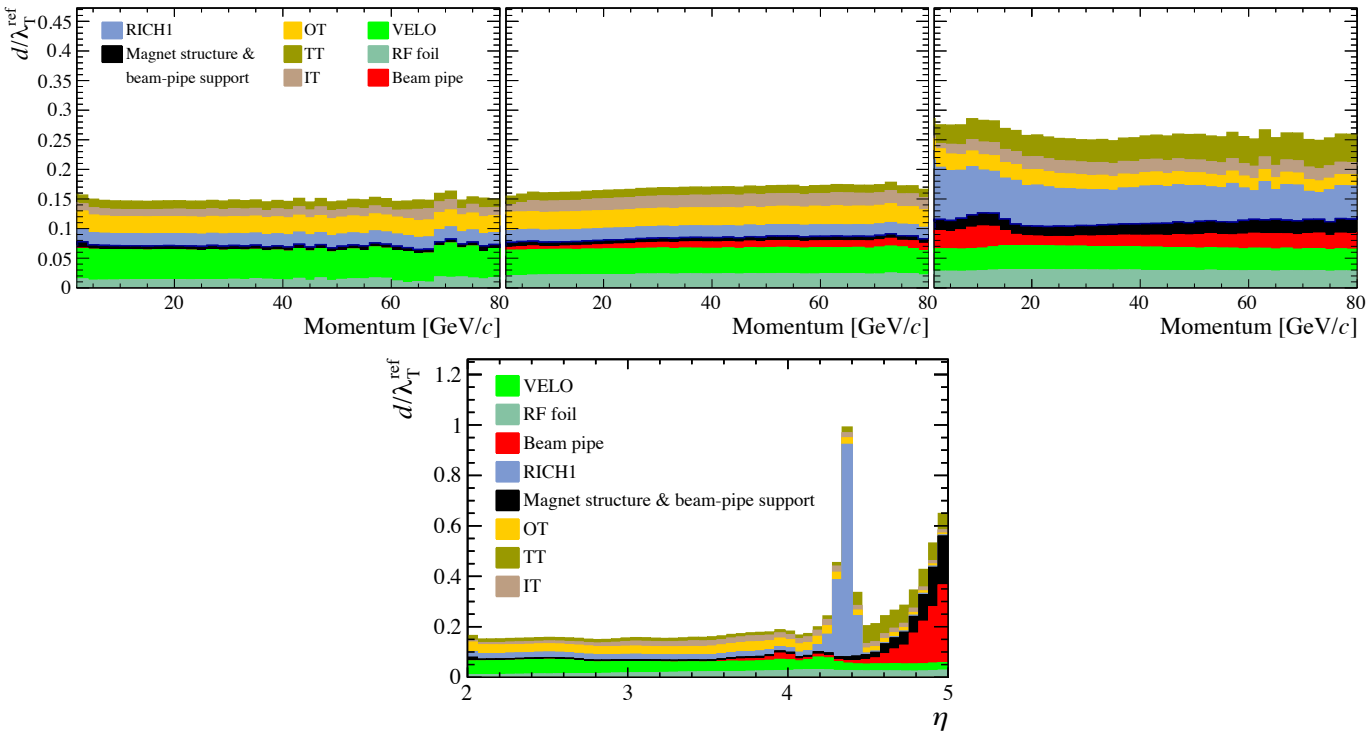

Figure 6.5: (top) Distribution of the reference material thickness for tracks of different momentum and for (left) $\eta \in [1.9, 3.0]$, (middle) $\eta \in [3.0, 4.0]$ and (right) $\eta \in [4.0, 5.1]$, and (bottom) distribution of the reference material thickness as a function of η, integrated over all momenta. Only particles that are inside the geometrical acceptance of the detector are considered. Note that part of the inner beampipe, responsible for peak around $\eta = 4.3$, is included in the RICH1 material contribution.

6.2 Detector acceptance

The asymmetries arising from the design of the detector, along with beam parameters are discussed in this section. As elaborated in Sect. 6.1, both fast simulation techniques and a deterministic model of LHCb are used to estimate the impact of all effects. The impact of each source is determined by considering the difference with respect to the detection asymmetry presented Fig. 6.2, i.e. the detection asymmetry in a situation with no beam-crossing angle, but with the left-right asymmetric beam spot (as measured in 2016).

6.2.1 Charge-asymmetric hadronic cross-sections

The cross-sections on deuterium, as reported in Ref. [42], are illustrated in Fig. 6.6 for charged kaons, pions and protons. The charge asymmetry in the total cross-section of pions on deuterium is negligible for momenta $\geq 5\,\text{GeV}/c$, the momentum range relevant for LHCb physics analyses. For kaons and protons, however, the difference in cross sections is sizeable.

The charge-dependent cross-sections are combined with the simulated material thickness to determine the collision probability, using Eq. 6.5. The resulting expectation for the magnet-averaged detection asymmetry is shown as a black line in the left panel of Fig. 6.7 for kaons. By averaging over magnet polarities, asymmetries in the path lengths are cancelled, such that effectively the path-length-averaged asymmetry remains. A comparison with the expected asymmetry from the deterministic model shows a good agreement in general with an overestimation for low momenta. This is understood to be caused by the underestimation of reconstruction efficiency for elastically scattered par-

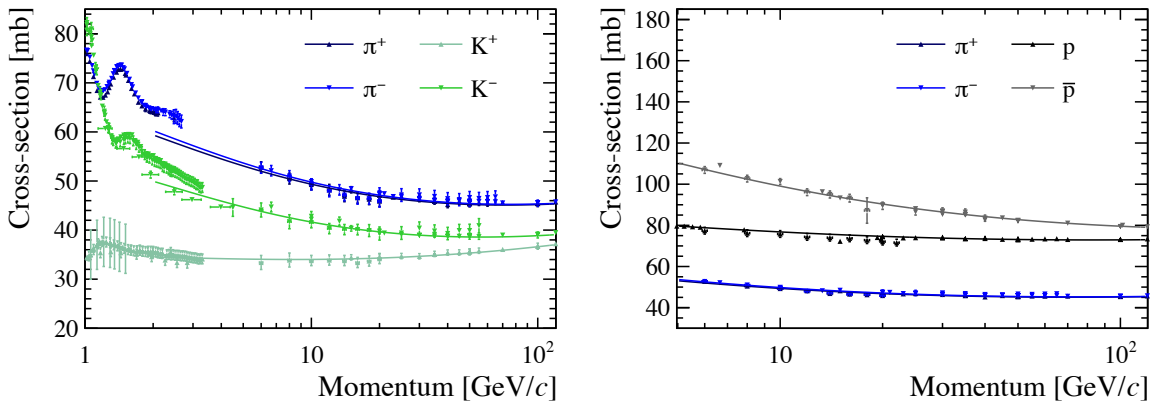

Figure 6.6: Total cross-sections for (left) pions and kaons, and (right) pions and protons on a deuterium target for relevant momenta. Data points are obtained from Ref. [42], together with the overlaid fit function.

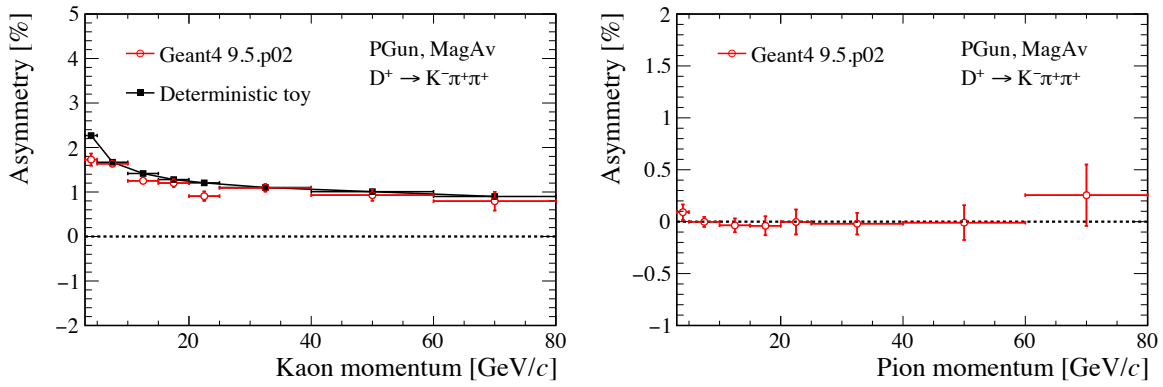

Figure 6.7: (left) Magnet-averaged kaon detection asymmetry, simulated with GEANT4. In black, an estimation using the asymmetry in the kaon–deuterium cross-sections. The overestimation in the first bin is likely due to the inclusion of elastic scatterings. (right) Magnet-averaged pion detection asymmetry, which is compatible with zero as expected from the almost symmetric cross-sections.

ticles. For low momenta, the contribution of elastic scatters to the total cross-section is larger. The asymmetry in the cross-sections for kaons is responsible for a $\mathcal{O}(1\%)$ momentum-dependent detection asymmetry, which is independent of magnet polarity. A calibration of the kaon detection asymmetry is thus a necessity for all *CP*-asymmetry analyses with a percent-level accuracy, or better. This calibration will be discussed in detail in Chapter 7. For pions, on the contrary, the asymmetry due to asymmetric cross-sections is compatible with zero, as can be seen in the right panel of Fig. 6.7.

6.2.2 Left-right asymmetric material distribution: inner tracker support

Left-right asymmetries in the material distribution in LHCb downstream of the magnet give rise to a polarity-dependent charge asymmetry in the particle interaction rate. In Fig. 6.2 it is seen that hadrons suffer from an additional magnet-dependent asymmetry at lower momenta. As the inelastic cross-section for pions is significantly higher than that for muons, this effect is likely to originate from interactions with detector material.

Any left-right asymmetry in the detector arises as a magnet-dependent asymmetry in the distribution of $d^{\pm}/\lambda_{\mathrm{T}}^{\mathrm{ref}}$. The asymmetry in the material thickness in units of the reference collision length is considered as a function of the z position to identify responsible detector components. This asymmetry is shown in Fig. 6.8 for both magnet polarities. The largest left-right asymmetry in material is witnessed for particles with $3.0 \leq \eta \leq 4.0$ traversing the main tracking stations. This strong feature is caused by the asymmetric material distribution in the tracking stations behind the magnet. A map of the material thickness of the tracking stations, for particles travelling parallel to the z

axis, is shown in Fig. 6.9. This map clearly shows the asymmetric material distribution of the inner tracker support structure, cables and cooling system (subsequently referred to as "support").

Similar samples of simulated $D^+ \to K^-\pi^+\pi^+$ and $D^+ \to K^-\mu^+\mu^+$ decays are generated using the particle-gun method, however, now with a modified detector description. In this modified detector, the inner tracker support is removed. By comparing the resulting simulated detection asymmetries to those in the standard detector configuration, the effect of the inner tracker support is singled out. The results are shown in Fig. 6.10. The IT support is a clear source of charge asymmetry for pions below 25 GeV/c and $\eta < 4.0$. Pions with a higher pseudorapidity and sufficient momentum (> 5 GeV/c) are likely to traverse the inner tracker (in accordance to Fig. 2.5), and are therefore not hindered by the extra support material. The size of this asymmetry for pions around 20 GeV/c is approximately 0.15% per magnet polarity. For muons the difference is compatible with no change. A relatively small magnet-dependent charge asymmetry upstream of the magnet, visible in Fig. 6.8 for $1200 \leq z \leq 2200$ mm and $4.0 \leq \eta \leq 5.1$, is discussed in the context of the beam spot influence in Sect. 6.2.3.

6.2.3 Beam spot

The VELO is centred around the beam spot at the beginning of each fill, however, the beam spot itself is not centred around $x = 0$. The centre of the beam spot is measured in data and updated in the simulation for each year and magnet polarity separately. To simulate the 2016 running conditions, $x = 0.86$ mm is used for both magnet polarities. This offset in x has negligible impact after the 4 Tm magnetic field. Only upstream of

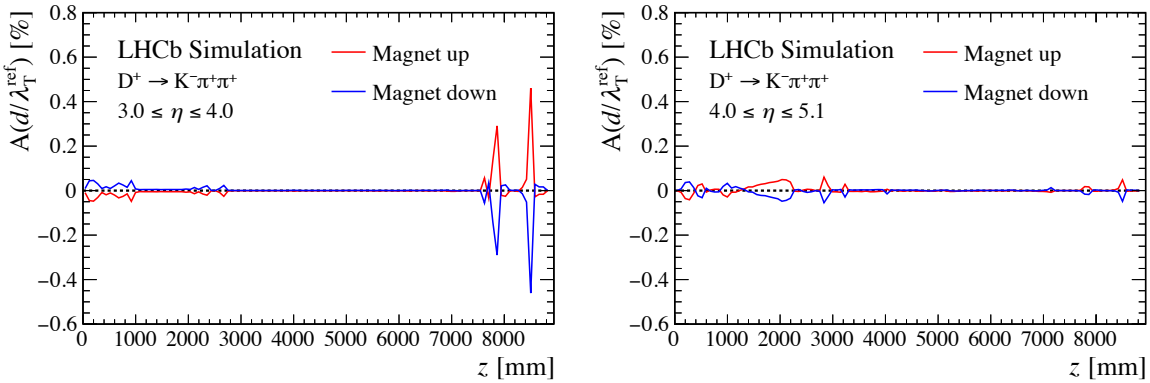

Figure 6.8: Simulated charge asymmetry in the material thickness for pions originating from $D^+ \to K^-\pi^+\pi^+$ decays (left) for medium pseudorapidity, and (right) for high pseudorapidity. The beam spot is set to the average position in 2016 for the creation of this figure, and only particles inside the geometric acceptance are considered. No significant structures were observed for pions with $1.9 \leq \eta \leq 3.0$.

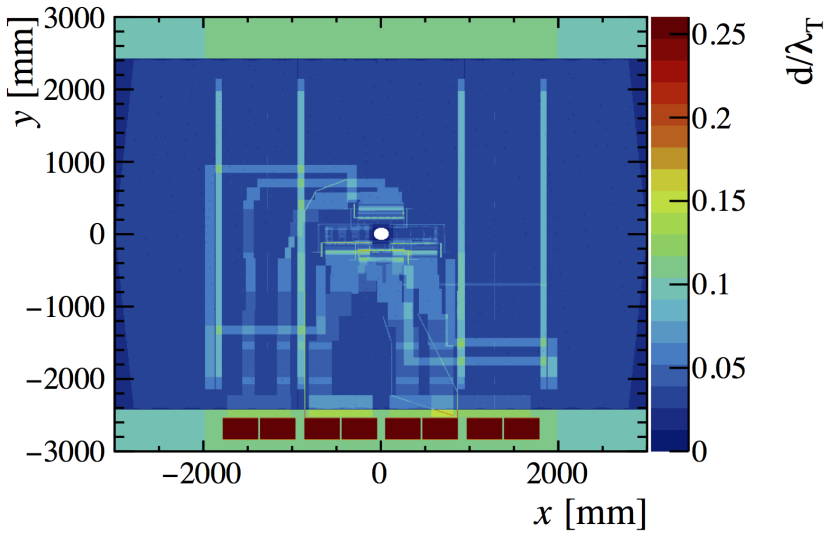

Figure 6.9: The simulated material distribution is shown for the T-stations, with on the z axis the material thickness in units of hadronic collision length, computed using the cross-section of a 20 GeV/c charged pion. The asymmetric support for the inner tracker can be clearly observed.

the magnet, where the deflection by the magnetic field is still small, some effect of this offset is observed. The beam spot does not lie entirely parallel to the z axis, but has a small slope in the x–z plane. However, the measured slope in the 2016 proton-proton collision data causes a variation of the order of 0.05 mm only, and can be neglected in our study. Thus, in this subsection only the impact of the average offset in x is discussed.

Figure 6.8 shows an asymmetry in the collision rate for $1100 \leq z \leq 2200$ mm, for particles with a moderate or high pseudorapidity. The offset of the beam spot which is used to generated this figure, corresponds to the average beam spot position for 2016 data. It is found that, in this interval, the loss in efficiency for the selected hadrons with respect to muons originates from the interactions with the beampipe in RICH1. Removing all events from the simulated sample in which the particle of interest undergoes an inelastic scattering in the RICH1 fiducial volume reduces the detection asymmetry for lower momenta and makes it nearly compatible with the muonic detection asymmetry. By comparing the position of the particle after extrapolation through the magnetic field with a straight-line approximation, the integrated bending power can be evaluated. For the studied muons and pions with low p and high η, the average bending power of the fringe magnetic field is about 1 mm at the end of RICH1, although the distribution extends up to 10 mm. Unlike the inner tracker support, the beampipe inside RICH1 is positioned symmetrically around the z-axis. The origin of the charge asymmetry in interaction rate is found in the offset of the beam with respect to the LHCb frame. The offset is small, but of similar order of magnitude as the bending power of the

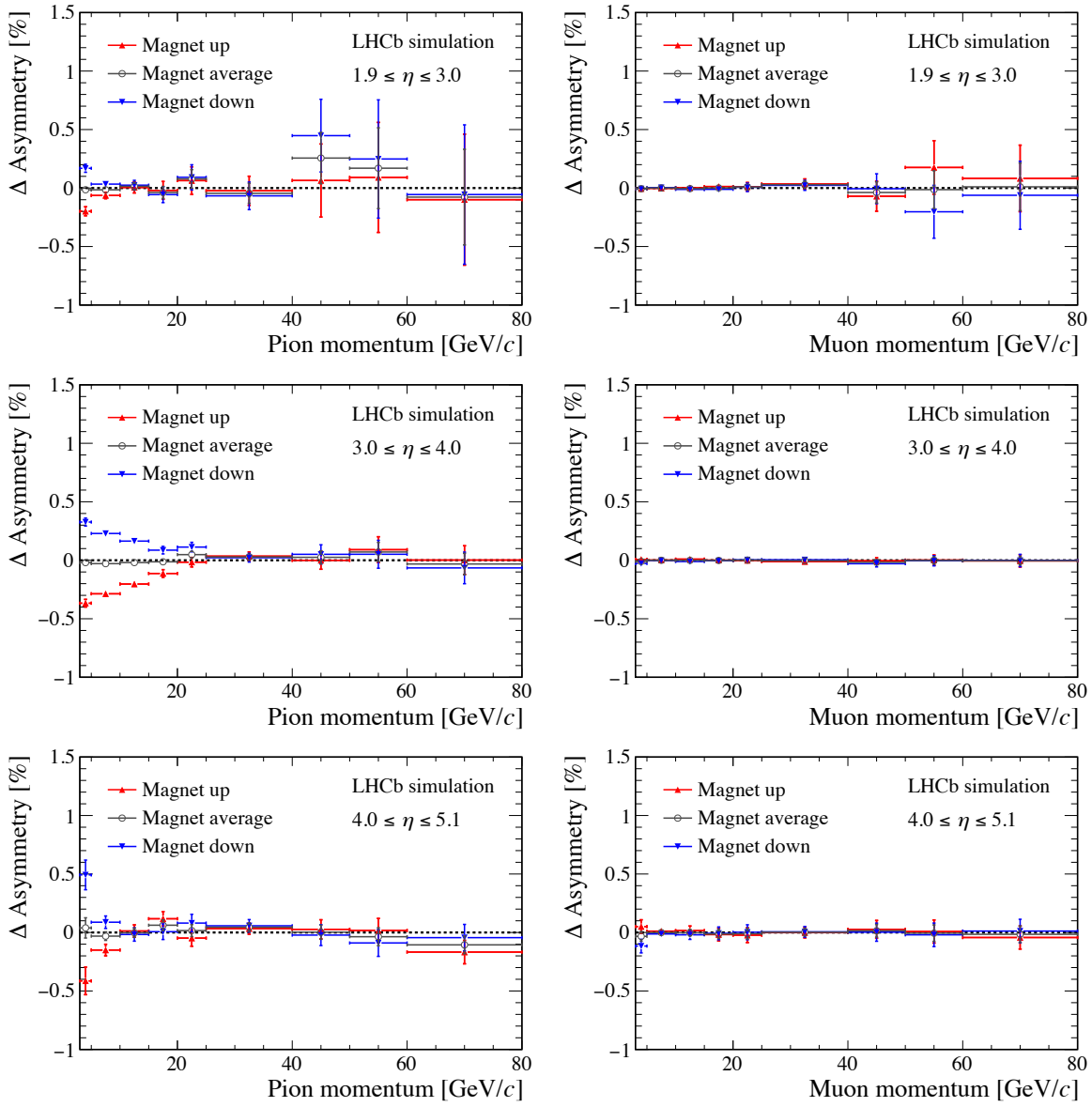

Figure 6.10: Difference in the single-track detection asymmetry when removing the IT support for (left) π^+, and (right) μ^+ as function of the generated momenta for (top) $\eta \in [1.9, 3.0]$, (middle) $\eta \in [3.0, 4.0]$, and (bottom) $\eta \in [4.0, 5.1]$. No crossing angle is simulated in this sample. The difference is calculated as the asymmetry *with* the IT support, minus the asymmetry *without* it.

fringe field. By comparing the detection asymmetry with the one obtained from a sample with the beam spot fixed at $(x, y, z) = (0, 0, 0)$ (and aligning the VELO to match this beam-spot position), a magnet-dependent asymmetry for pions with high pseudorapidity and low momentum is isolated. This difference is shown in Fig. 6.11. This contribution is responsible for a large fraction of the detection asymmetry, as observed in Fig. 6.2, for low-momentum, high-pseudorapidity pions. Unlike the inner tracker support, this asymmetry is expected not only for long tracks, but also for upstream tracks.

The small difference in asymmetry for low-momenta, high-pseudorapidity muons is understood as the effect of elastic scatterings and possible muon capture by the RICH1 beampipe, which is charge-asymmetric due to the beam position offset and the (weak) magnetic field upstream.

6.2.4 VELO module arrangement

All long tracks are required to include sufficient hits in the VELO detector. To determine the effect of the VELO station geometry, it is compared to a perfect detector: a 100% efficient detector for particles with $1.9 \leq \eta \leq 5.1$. The result is shown in Fig. 6.13, where the difference in the detection asymmetry is shown between the real VELO acceptance and a perfect VELO acceptance. It is clear that the requirement for particles to be reconstructed in the VELO has a significant impact on the detection asymmetry. For pseudorapidities above 4.7, the number of VELO ϕ and r hits is reduced to the threshold value (3 for each sensor type). Therefore, at such high pseudorapidity, the inner acceptance is completely determined by the first sensor encountered by such a particle.

To allow for the overlap of the two halves of the VELO, the sensors are positioned at different z positions in the left and right half of the detector, with a distance of around $\Delta z = 17\,\text{mm}$ between the sensors. The left- and right sensors move inwards far enough to create a projective overlap of the sensitive detector areas. This increases the angular acceptance but also complicates its parametrisation. The ϕ sensors have a smaller inner acceptance due to their non-trivial shape, shown in Fig. 6.12, such that the left-right-averaged acceptance already starts to decrease beyond $\eta = 4.7$, while for r sensors the acceptance is fully covered up to $\eta = 4.8$. The shape of the ϕ sensor therefore dominates the VELO acceptance. Because of the overlap between the two detector halves, the first ϕ sensor encountered is not always in the third station in the VELO detector, counting from the back. Therefore, the inner acceptance of both the second-to-last and one-to-last VELO ϕ sensors are discussed.

To further understand the source of the acceptance asymmetry introduced by the VELO acceptance, the deterministic model is used. The VELO acceptance for charged particles is described as a function of η and the sign of p_x, while fixing the absolute momentum to $70\,\text{GeV}/c$. By the module arrangement, a difference of the projective

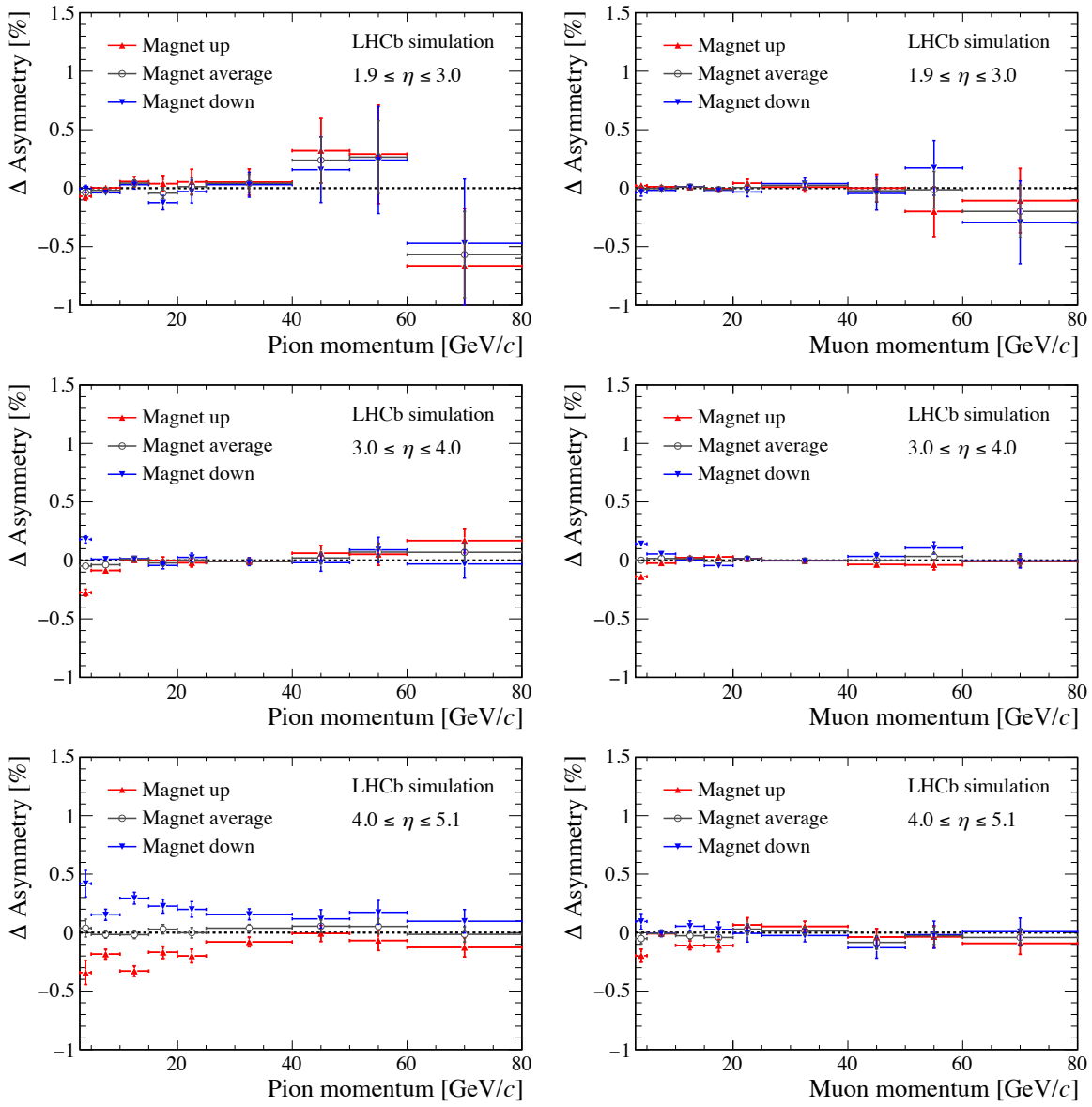

Figure 6.11: Difference in the single-track detection asymmetry when centring the beam spot and moving the VELO accordingly for (left) π^+ and (right) μ^+ as function of the generated momenta for (top) $\eta \in [1.9, 3.0]$, (middle) $\eta \in [3.0, 4.0]$, and (bottom) $\eta \in [4.0, 5.1]$. No crossing angle is simulated in this sample. The difference is defined as the asymmetry *with* a beam spot offset (as is measured in 2016 data), minus the asymmetry *without* the 2016 beam spot configuration.

acceptance is observed between the left and right VELO sensors far downstream. The difference in acceptance for a left φ sensor at $z = 684\,\text{mm}$ and right φ sensor at $z = 701\,\text{mm}$ is illustrated as function of η, only considering particles with $p = 70\,\text{GeV}/c$, in Fig. 6.14. For pseudorapidity above 4.7 a difference between the two sides is clearly visible, and the dip around $\eta = 4.3$ is due to the insensitive region in the φ sensors on the interface of the inner and outer strips. The difference is particularly large around $\eta = 5.1$, the edge of the LHCb geometric acceptance.

The left-right asymmetry does not have any charge-asymmetric consequences in the VELO itself, but it has significant consequences in combination with the magnetic field. By the dipole magnet particles are bent into the beampipe or out of the beampipe depending on their charge. The left-right difference itself does not change with the magnet polarities, provided the position of the beam spot remains unchanged. Therefore, the effect is expected to cancel out when combining data sets with opposite magnet polarities, as observed in Fig. 6.13.

To conclude, the VELO acceptance impacts the detection asymmetry as a result of the left-right asymmetric projective acceptance of the sensors far downstream. A reliable simulation of this asymmetry requires an accurate description of the VELO module arrangement and the sensor type. The asymmetry can be largely avoided by considering only tracks with $\eta < 4.7$.

6.2.5 Outer tracker module arrangement

The OT, schematically shown in Fig. 2.6, consists of separate modules, positioned adjacently to form a layer. Between the modules is an insensitive region of approximately 5 mm in x, which spans the full y-range of the detector. A station consists of two x layers. The distance in z between two x modules is approximately 175 mm, which

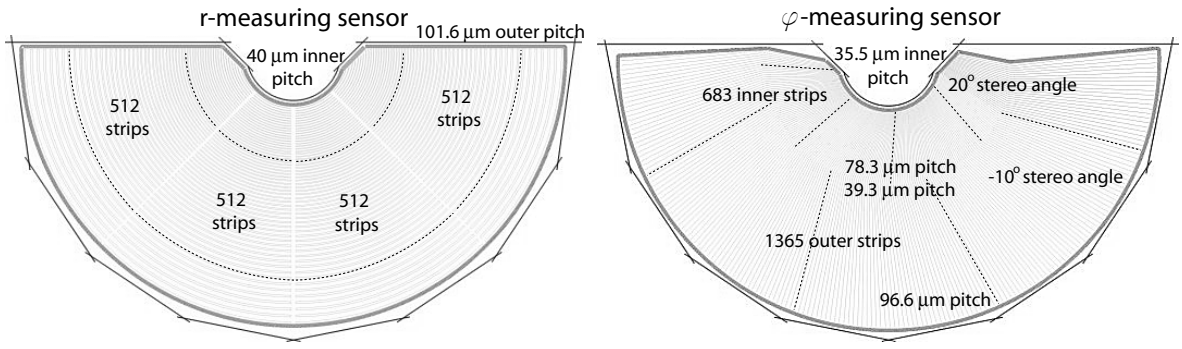

Figure 6.12: Layout of the (left) r and (right) ϕ VELO sensors. The interface between the inner and outer strips of the ϕ sensor contains an approximately 79 µm wide insensitive region. The middle of the r-measuring sensor shows a boundary of a similar size.

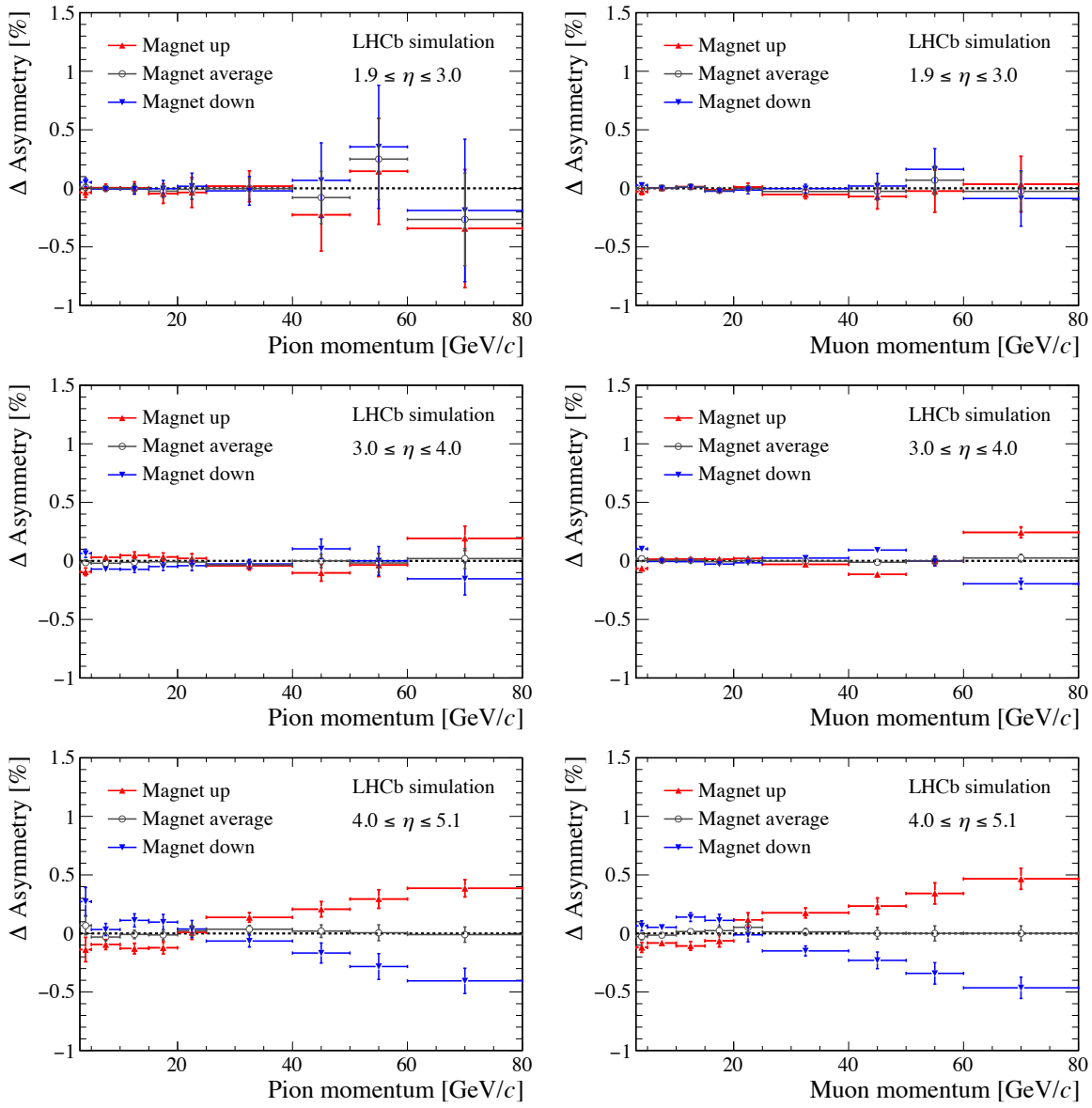

Figure 6.13: Difference in single-track detection asymmetry between the case of a perfect VELO acceptance and a realistic VELO acceptance for (left) π^+ and (right) μ^+ as function of the generated momenta for (top) $\eta \in [1.9, 3.0]$, (middle) $\eta \in [3.0, 4.0]$, and (bottom) $\eta \in [4.0, 5.1]$. No crossing angle is simulated in this sample. The difference is calculated as the asymmetry with the *standard* VELO sensors, minus the asymmetry with a *perfect* VELO efficiency.

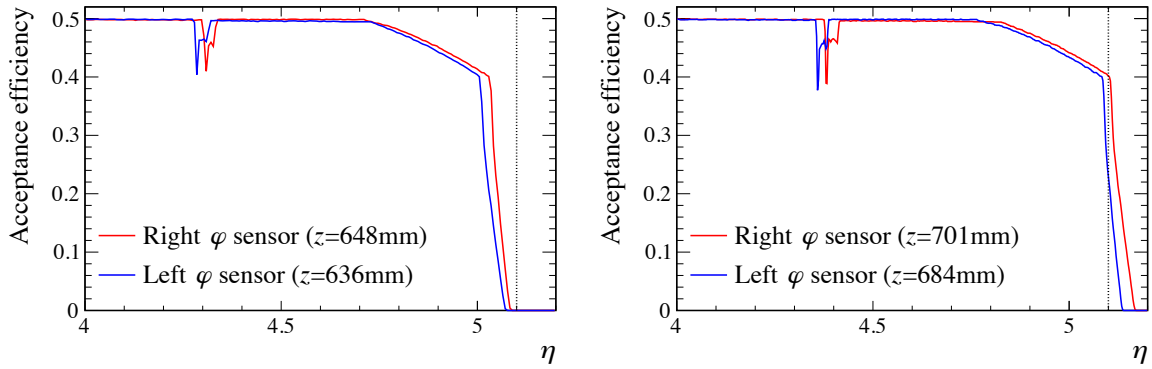

Figure 6.14: Acceptance efficiency of the two-to-last and one-to-last VELO φ sensors, for high-pseudorapidity, $p = 70\,\text{GeV}/c$ particles with a uniform φ distribution. The dotted line indicates the boundary of $\eta = 5.1$, which is considered the edge of the LHCb charged particle acceptance. The efficiency plateaus at 50%, as half of the generated tracks have $p_x > 0$ and the other half has $p_x < 0$. The dips around $\eta = 4.3$ are due to the insensitive area between the inner and outer regions of the VELO sensors.

limits the angle for particles passing through the insensitive region between two modules to $t'_x = p'_x/p'_z = \Delta x/\Delta z \approx 0.03$. This ratio of momentum components concerns the momentum after the magnet, which is different from that upstream of the magnet, $t_x = p_x/p_z$. For this reason, gaps between modules do not directly lead to a loss in efficiency, as the gaps are non-projective for particles originating from the origin, i.e. most particles that travel between two modules in one of the x layers travel through active area in the other, with the exception of the two central (M9) modules. Ina ddition, the arrangement of the modules is not completely left-right symmetric: the two M9 modules are composed of one full-width module and one half-width module (so-called S2 and S3 modules, respectively).

According to the deterministic model, particles with $3.0 \leq \eta \leq 4.0$ and high momenta can travel through the same gap between the two M9 modules in both x layers. The location of the gap is at approximately $x = -84\,\text{mm}$. The asymmetric detector design leads to a contribution to the detection asymmetry which changes sign when reversing the magnet polarity. Modules further away (in x) from the beampipe are positioned symmetrically around the centre, such that no asymmetry is introduced there.

To quantify the effect of the module arrangement, particles are removed for which the approximated position in the first x layer for each T-station is closer than 10 mm to $x = -84\,\text{mm}$ or $x = +84\,\text{mm}$. This veto removes particles from the data set which are potentially influenced by the gap. The resulting asymmetry in bins of pseudorapidity and momentum after the removal of these events is shown in Fig. 6.15. An effect of approximately 0.2% with opposite sign for each magnet polarity is visible for high-

momentum particles with moderate pseudorapidity.

The effect of the gaps between the outer tracker modules is sensitive to the actual alignment of the modules and, therefore, likely different in data compared to simulation. The modules in the x layers of one station are mounted on separate C-frames, which show movements in the order of 100 µm as function of magnet polarity, as reported in Ref. [9]. The additional movement in x of the modules within their C-frame could further alter this asymmetry. These observations from simulation motivate a future study on the impact of the OT alignment on the detector asymmetry.

6.2.6 Detector defects in T-stations

Explicit left-right differences in the efficiency of the downstream tracking stations lead to a magnet-dependent detection asymmetry. Such differences can occur by defects, i.e. dead or noisy channels, in either the OT or IT detectors. Not all inefficiencies immediately lead to a significant loss in efficiency: the placement of two stereo and two x-layers per station provides a redundancy in the sensors with respect to the acceptance requirements of at least one hit per type. Defects become problematic when two consecutive sensors in z of the same type show inefficiencies around the same position in x, y. Note that the majority of reconstructed particles passing through the IT have a high momentum as shown in Fig. 2.5, while the particles passing through the OT are mostly of low momentum. As the implementation of the detector defects in simulation varies for the OT and IT, they are discussed separately.

Inner tracker defects

The performance of the sensors and strips in the IT detector is monitored during its operation. To increase the reliability of the detector simulation, observed defects are implemented in the detector simulation. In total, 1347 defects are simulated for the IT. Most of these defects are distributed randomly over the IT. Therefore, by the redundancy of the layers per station, these defects do not lead to a decrease of efficiency. However, one pair of defect sectors is found around the same location in x, y in two x layers of the same station. The resulting effect on the detection asymmetry for muons, as simulated with $D^+ \to K^-\mu^+\mu^+$ events, is shown in Fig. 6.16 for the relevant bin in pseudorapidity. It is seen that, at high pseudorapidity and $p \geq 10\,\text{GeV}/c$, a magnet-dependent asymmetry of approximately 0.1% is introduced by this defect. The effect is prominent for particles with $p_x \approx 1\,\text{GeV}/c$. A replacement of the sensor in the first x layer of the first IT station would mitigate the impact of IT defects on the detection asymmetry. The asymmetry is no longer present when the data sets of both polarities are averaged.

Outer tracker defects

No description of the OT detector defects is implemented in the detector simulation. The study of the IT defects showed that inefficiencies in the detector can have a non-negligible impact on the detection asymmetry. Therefore, the simulation software is adjusted to study the OT defects observed in data. The efficiency of the OT is extracted from data regularly, for example, with the ageing scans described in Sect. 3.2.2. To simulate the detector efficiency an additional step is introduced in the event simulation. In this step, hits are accepted or rejected based on the layer and position in the detector, using the measured, time-averaged efficiencies in 2017 data. These efficiencies are parametrised in y, x, and measured for each layer separately. For this analysis, known biases in the inferred efficiencies are reduced where possible, following the procedure introduced in Sect. 3.2.3.

The outer regions of the OT cover the acceptance of low-momentum particles. These particles have a steeper slope ($\frac{\mathrm{d}x}{\mathrm{d}z}$) than the particles traversing the IT. Therefore, the efficiency loss is more difficult to extract from the spatial distribution of detector defects.

With the modified detector simulation, $D^+ \to K^-\mu^+\mu^+$ events are generated using the particle gun. The effect of the outer tracker defects on the detection asymmetry is shown in Fig. 6.17, for muons with $\eta \leq 4.0$. The effect is most visible at lower momenta and for $\eta \leq 3.3$. The asymmetry introduced by the OT defects is limited to $\mathcal{O}(0.1\%)$ for particles with low pseudorapidity. It is slightly smaller in comparison to the effect of the IT, but of opposite sign and predominantly at lower momenta. Unlike the IT, no single defect or pair of defects can be singled out as responsible for the observed asymmetry. A study to further understand the impact of the disabled monolayer in the first station, shown in Fig. 3.8, is planned.

While the simulated asymmetry for inner- and outer tracker defects is nullified upon combining the data sets of different magnet polarities, this does not need to hold for data. In simulation, the defects are unchanged for the complete year of data taking and, in particular, between the magnet polarities. The defects in the actual detector change over time, such that the magnitude of the detection asymmetry can differ between magnet polarities. Therefore, to ensure that analyses are not limited by a systematic uncertainty of $\mathcal{O}(0.1\%)$, corrections for the detection asymmetry should be determined and applied separately on the data sets of different magnet polarities.

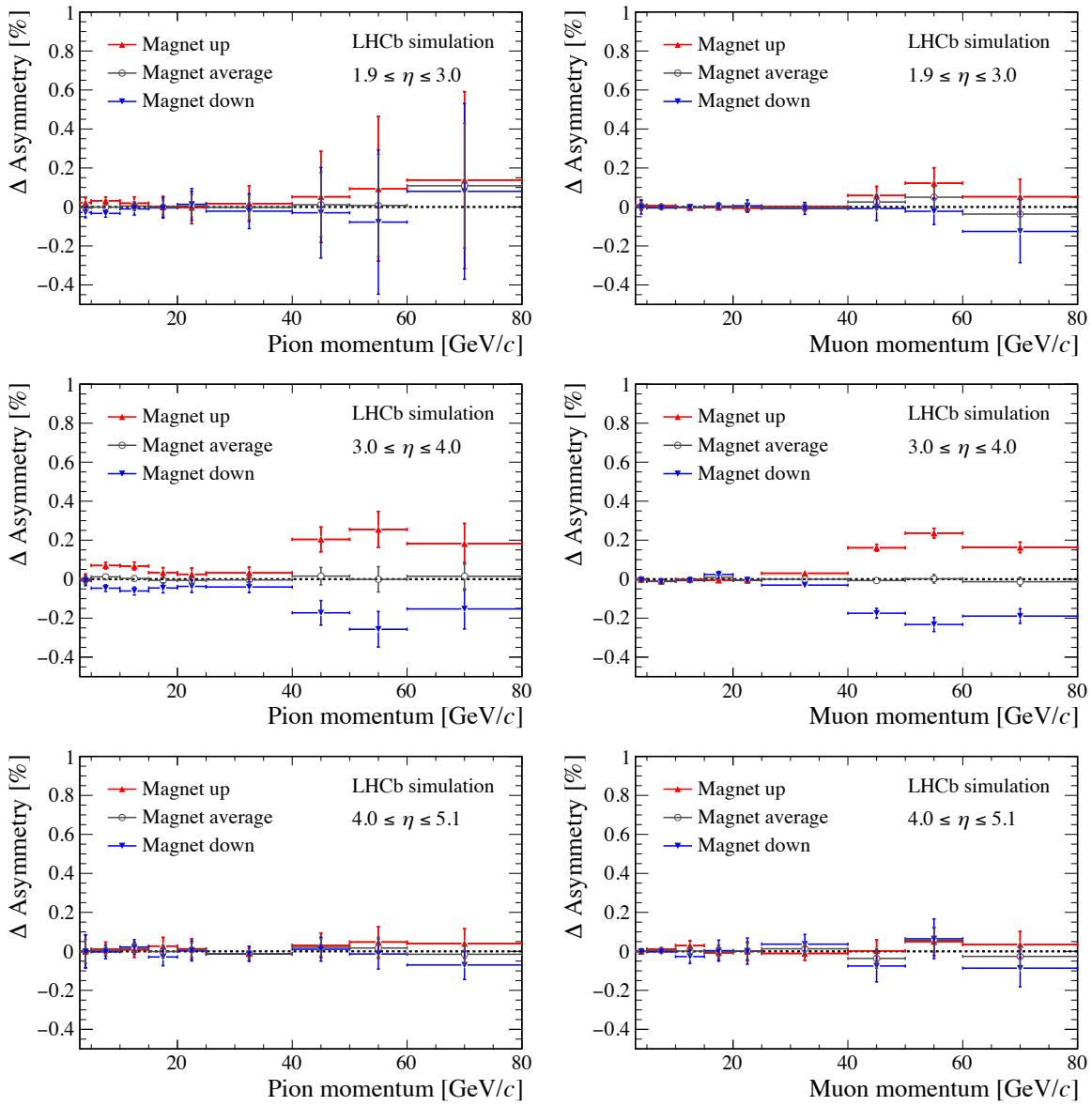

Figure 6.15: Difference in the single-track asymmetry when applying a veto in the calculated x position in all tracking stations for (left) π^+ and (right) μ^+ as function of the generated momenta for (top) $\eta \in [1.9, 3.0]$, (middle) $\eta \in [3.0, 4.0]$, and (bottom) $\eta \in [4.0, 5.1]$. No crossing angle is simulated in this sample. These plots quantify the effect of the OT module arrangement on the detection asymmetry. The small contribution for pions with $\eta \in [3.0, 4.0]$ and low momentum is associated with part of the inner tracker support. The difference is calculated as the asymmetry *without* the veto, minus the asymmetry *with* the veto.

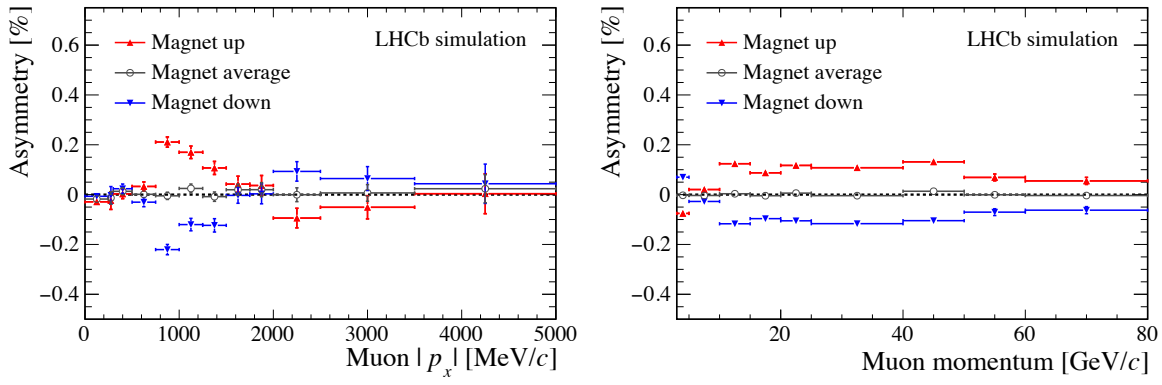

Figure 6.16: Asymmetry found after simulating the IT defects for muons in $D^+ \to K^-\mu^+\mu^+$ events with $\eta \geq 4.0$. Particles considered are required to have sufficient hits in the tracking stations to form a long track.

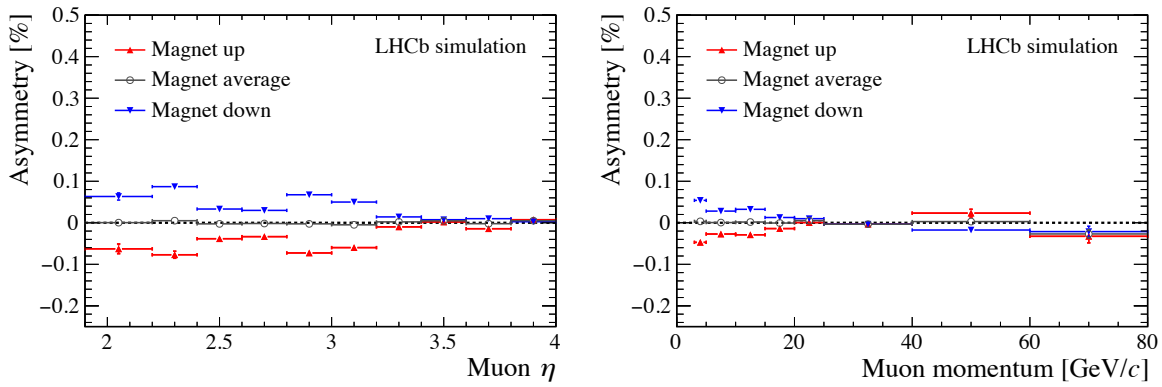

Figure 6.17: Effect of the OT efficiency on the reconstruction of muons in $D^+ \to K^-\mu^+\mu^+$ events. Only muons with $\eta \leq 4.0$ are considered.

6.2.7 Beam-crossing angle

The (horizontal) beam-crossing angle introduces a (left-right) phase-space asymmetry for both charges. The angle differs between the two magnet polarities, as also the LHCb dipole magnet affects the beam. The beam-crossing angle is often considered a potential source for an asymmetric acceptance, but its quantitative effect was never investigated. An overview of beam-crossing angles for Run 1 and Run 2 was presented in Table 2.1 in Chapter 2.

The beam-crossing angle for Run 2 is simulated and its effects are studied using $D^+ \to K^-\pi^+\pi^+$ and $D^+ \to K^-\mu^+\mu^+$ decays. Unlike the acceptance asymmetry studies discussed so far, this time the particle-gun mode from Gauss was not used, and the charm mesons are generated by simulating proton-proton collisions with Pythia. Any production asymmetry of the D^+ is explicitly removed by the introduction of an additional step in the simulation, in which the charge of the D^+ and its daughters are randomised before simulation by Geant4. In addition, all particles irrelevant to the signal decay are removed from the event before the time-demanding simulation in Geant4.

The horizontal beam-crossing angle results in a boost of the generated particles in the x direction, which breaks the left-right symmetry in phase space. The effective boost for a horizontal crossing angle of $-395\,\text{mrad}$, as in Run 2 magnet down, is of the order of $50\,\text{MeV}/c$ for a promptly generated $\rho^0(770)$, but is lower for final-state particles in secondary decays. The simulated D^+ often originates from higher (charm) resonances instead of directly from the proton-proton collision, and the simulated horizontal boost is then reduced to $28\,\text{MeV}/c$. Final-state particles in the $D^+ \to K^-\pi^+\pi^+$ decay are boosted by approximately $12\,\text{MeV}/c$ for the kaon and $7\,\text{MeV}/c$ for the pions. Changing the sign of the horizontal crossing angle also changes the sign of the average p_x, as illustrated in Fig. 6.18. Note that no data was taken with the crossing angle of $+0.395\,\text{mrad}$, and it is included here only for illustration. The effect is relatively small for high-p_T particles, but in particular those with high pseudorapidity can be largely affected by small initial asymmetries.

Figure 6.19 shows the total simulated asymmetry, including the Run-2 beam-crossing angle, for pions and muons. The difference introduced by the beam-crossing angle is shown in Fig. 6.20. A clear magnet-averaged asymmetry is visible for both the muons and the pions, which is dependent on pseudorapidity. A consistent effect of -0.2% is present for muons and pions with momenta above $20\,\text{GeV}/c$ and $\eta > 4.0$. A slight trend in the magnet-averaged asymmetry for moderate pseudorapidity particles is only visible for pions, hinting at a difference in the collision length due to the crossing angle.

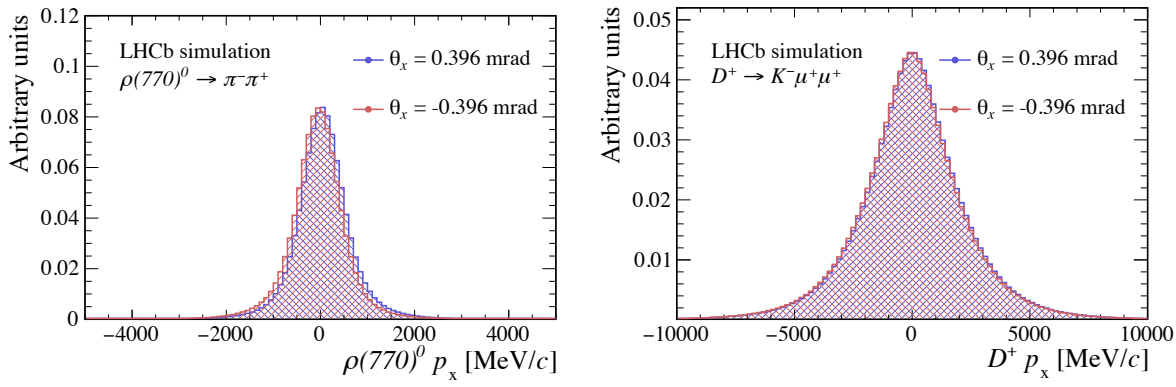

Figure 6.18: The generated horizontal momentum distribution for (left) promptly produced $\rho(770)$ and (right) D^+ for two crossing angles of opposite sign. The simulated spectrum without crossing angle, not shown in these figures, has a mean horizontal momentum compatible with 0. Note that no data was taken with the crossing angle of $+0.395$ mrad, and it is included here only for illustration.

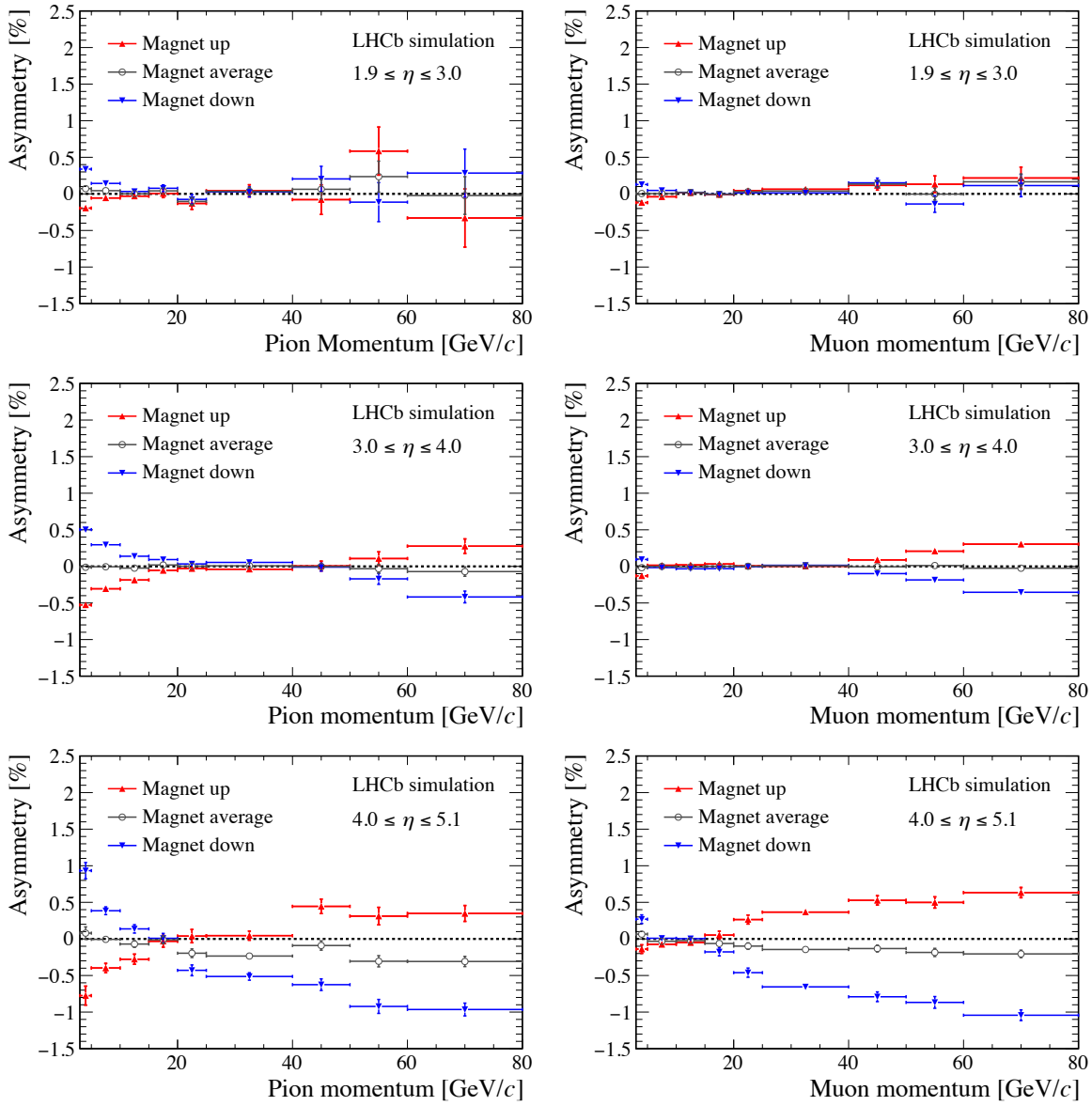

Figure 6.19: Simulated single-track detection asymmetry with the Run-2 beam-crossing angle and beam-spot position, for (left) π^+ and (right) μ^+ as function of the generated momenta for (top) $\eta \in [1.9, 3.0]$, (middle) $\eta \in [3.0, 4.0]$ and (bottom) $\eta \in [4.0, 5.1]$. Note that, unlike most illustrations in this chapter, the total detection asymmetry is shown, and not the difference. These detection asymmetries can be compared to the ones obtained without a crossing angle, as shown in Fig. 6.2.

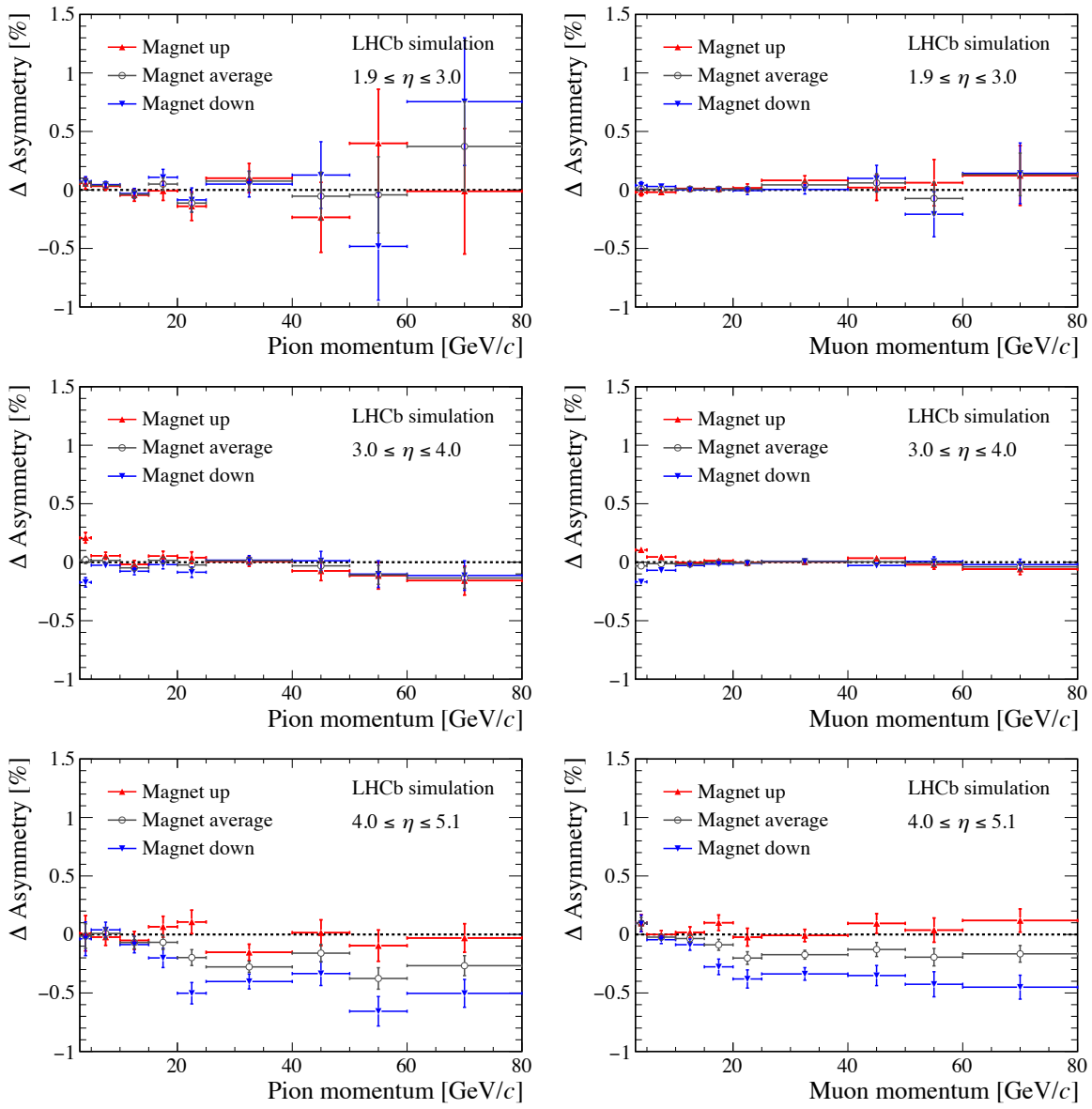

Figure 6.20: Difference in single-track detection asymmetry when applying the beam-crossing angles for 2016 for (left) π^+ and (right) μ^+ as function of the generated momenta for (top) $\eta \in [1.9, 3.0]$, (middle) $\eta \in [3.0, 4.0]$, and (bottom) $\eta \in [4.0, 5.1]$. The difference is calculated as the asymmetry *with* the crossing angle, minus the asymmetry *without*.

The additional horizontal momentum induced by the beam-crossing angle is relatively small for typical selected B decay products, which often have a larger transverse momentum than the earlier-studied D^+ decay products. Therefore, also muons originating from semileptonic B_s^0 decays, $B_s^0 \to D_s^- \mu^+ \nu_\mu X$, are considered. This sample consists of approximately 5 million events for a crossing angle of $\pm 0.236\,\text{mrad}$, corresponding to the 2012 beam conditions. The deterministic model is used to isolate the influence of these beam parameters. The acceptance asymmetry is calculated for samples with both crossing angles, under both magnet conditions. Note that in 2012 a crossing angle of $0.236\,\text{mrad}$ was used for the magnet up polarity only, and $-0.236\,\text{mrad}$ was used for the magnet down polarity.

The results are shown in Fig. 6.21, and show that effects of the beam-crossing angle are also visible for muons from B_s^0 decays. The higher η bin is particularly affected by the beam-crossing angle, while particles with lower η (< 3.5) remain omstly unaffected. This is consistent with the results from simulated D^+ decays. Integrating over pseudorapidity and projecting in bins of momentum, the muons with a higher momentum are affected. This is likely the result of the high transverse momentum of the muon. There is a correlation in the $\eta - p$ spectrum, where higher-momentum tracks carry a larger pseudorapidity. The asymmetry does not cancel when averaging over magnet polarities.

To conclude, the horizontal beam-crossing angle gives rise to both a magnet-dependent and magnet-independent charge asymmetry in the acceptance of charged particles. The component of the crossing angle which does not change upon the magnet polarity change, introduces a magnet-dependent asymmetry, which cancels upon averaging polarities. The component of the crossing angle which is dependent on the magnet polarity, however, causes a dangerous residual asymmetry when averaging over magnet polarities. The asymmetry is sizeable for high pseudorapidity (> 3.5). The asymmetry due to the beam-crossing angle in bins of absolute momentum changes depending on the underlying p_T distribution, with a stronger effect visible for lower-p_T particles. Even for high-p_T muons as originating from semileptonic B_s^0 decays, the effect for high η is approximately $0.2 - 0.3\%$, after averaging over magnet polarities, as read from Fig. 6.21. This asymmetry does not cancel upon averaging the magnet polarities. Therefore, the crossing angle leads to a bias if not corrected properly. It is advisable to include the pseudorapidity in the parametrisation of the detection asymmetry, which can be measured using calibration channels.

Motivated by this study, the possibility of having a different external beam-crossing angle between magnet polarities has been explored for 2018 data taking. In the ideal scenario, the change of external crossing angle compensates for the internal crossing angle, giving the same total angle (both in magnitude and sign) for both polarities. The induced asymmetry by the crossing angle would then cancel when averaging magnet polarities. Unfortunately, this scenario was unfeasible for 2018 data taking. However, optimisations of the beam-crossing angles are considered for Run 3 of the LHC.

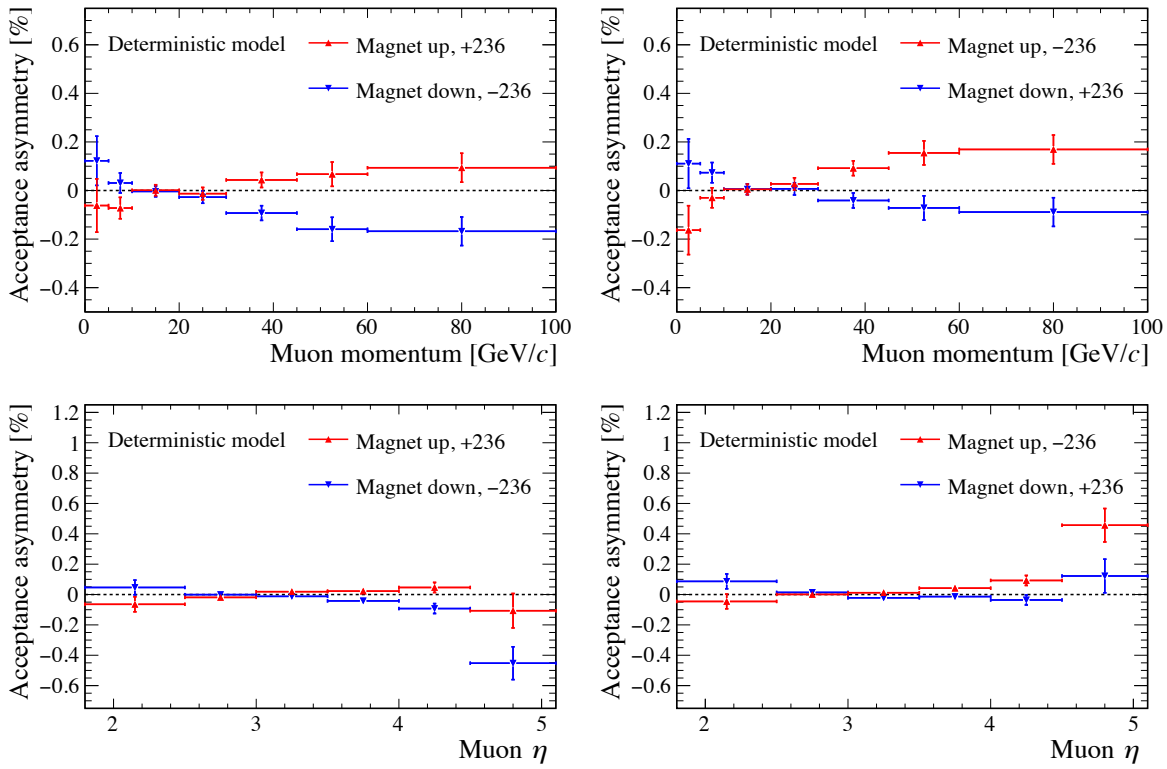

Figure 6.21: Simulated geometrical-acceptance asymmetry for muons from $B_s^0 \to D_s^- \mu^+ \nu_\mu X$ decays for (left) horizontal crossing angles as used in 2012 and (right) opposite horizontal crossing angles. The legend indicates the used crossing angle in µrad. Note the different y-scale.

6.2.8 Overview of acceptance asymmetries

The asymmetry projected in bins of momentum and pseudorapidity for muons and pions after the removal of the effects discussed related to the detector acceptance is shown in Fig. 6.22. This result indicates that, after the consideration of the effects in this chapter, no significant residual detection asymmetry is present in simulation.

The LHCb detector is most efficient for particles with moderate pseudorapidity. For measurements which integrate over pseudorapidity, it is therefore particularly important to calibrate for the effects in the region $3.0 \leq \eta \leq 4.0$. In this chapter it has been shown that this region is dominated by the combined effect of the IT support and the OT module arrangement. The simulation of the defects in the inner tracker and outer tracker show that the contribution of detector inefficiencies to the detection asymmetry is of order $0.05 - 0.1\%$.

For measurements parametrised by the pseudorapidity, e.g. production asymmetries, the measurement becomes sensitive to the beam and VELO alignment for $\eta \geq 4.0$. A shift in the beam spot in x has a strong effect on hadrons interacting with the RICH1 beampipe. The VELO alignment determines the overlap between the left- and right sensors, which is crucial for the angular acceptance at high pseudorapidity. In particular the alignment of the last few VELO sensors is important. The beam-crossing angle is shown to leave an imprint on the magnet-averaged results and therefore is particularly important to correct. To conclude, Table 6.1 summarises all effects discussed in this chapter related to the detector acceptance.

Table 6.1: Summary of discussed sources of acceptance asymmetry, their order of magnitude and their relevant regions of phase space.

Source	Particles	$\mathcal{O}[\%]$	η	$p[\,\mathrm{GeV}/c]$
Cross-sections	π^+, K^+, p	$0, 1, 3$	All	All
IT support	Hadrons, e	0.2	$3.0 - 4.0$	≤ 20
OT geometry	All	0.2	$3.0 - 4.0$	≥ 40
Beam spot	All, small for muons	0.2	$4.0 - 5.1$	≤ 40
Velo geometry	All	0.3	$4.0 - 5.1$	All
Beam crossing angle	All	0.5	$3.5 - 5.1$	≥ 20
IT defects	All	0.1	$4.0 - 5.1$	≥ 10
OT defects	All	0.07	$1.9 - 4.0$	≤ 10

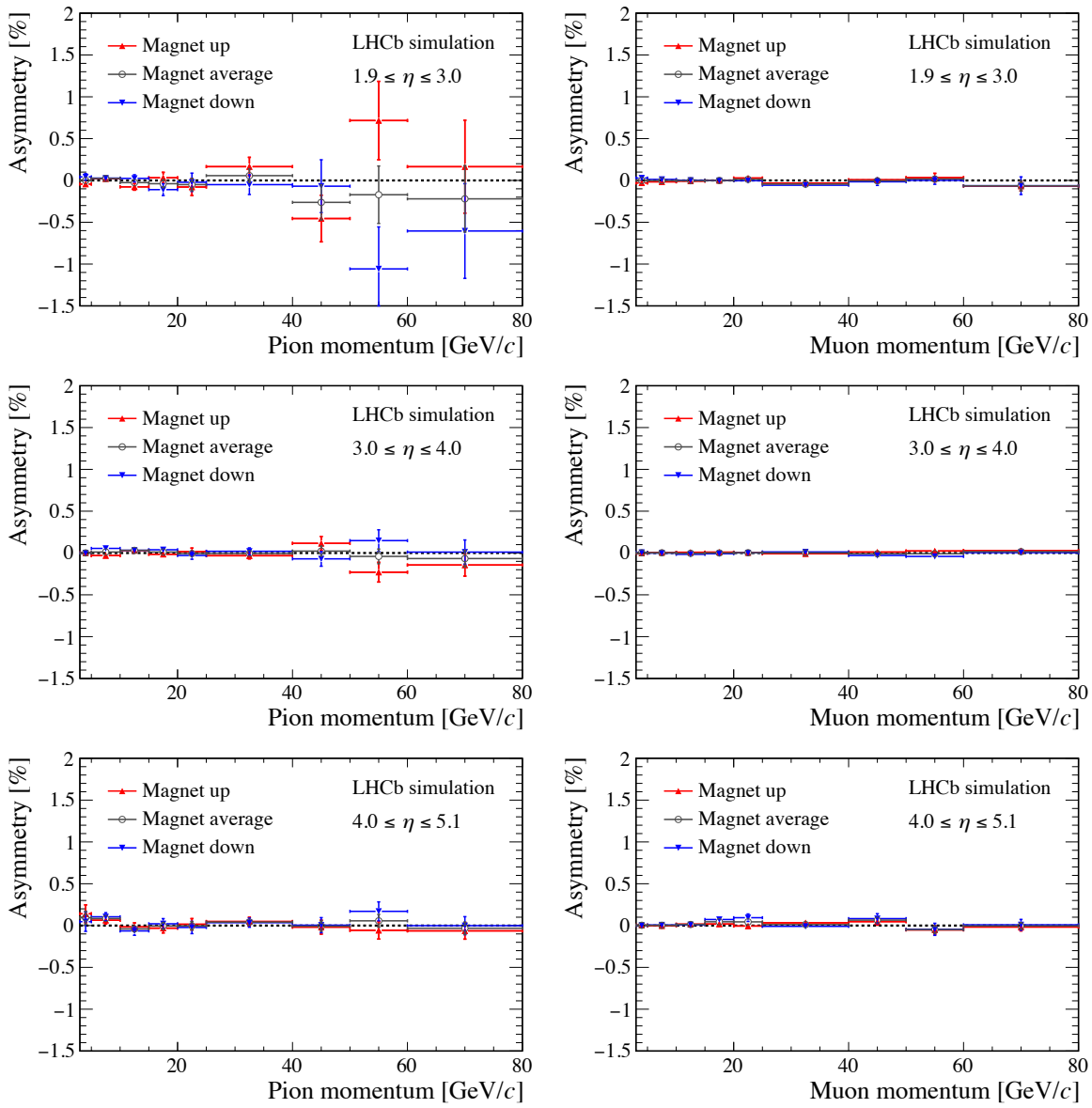

Figure 6.22: Residual asymmetry found in a particle-gun simulation after the removal of the effects discussed in Table 6.1. The asymmetry before removal is shown in Fig. 6.19.

6.3 Track reconstruction

The efficiency of the track reconstruction can depend on the charge of the particle in various ways. One would be by an asymmetric left-right hit treatment in the track-finding algorithms. Such orientation preferences are present in the forward tracking, and could give rise to a magnet-dependent charge asymmetry. The orientation preference in the forward tracking was left unchanged for Run 2, as no unbiased algorithm with

comparable timing was developed and the effect seemed small [65].

A second cause for a charge-asymmetric tracking performance originates from asymmetric hit occupancy. As illustrated in the left panel of Fig. 6.23, the occupancy in the tracking detectors after the magnet is left-right asymmetric, and therefore charge asymmetric. This effect is attributed to the abundant creation of secondary electrons before the magnet, which leads to an increased local hit occupancy for negatively charged particles after the magnet. The overall tracking efficiency decreases with detector occupancy, as is shown in the right panel of Fig. 6.23. Therefore, negatively charged particles are expected to show a decreased tracking performance in comparison to their charge conjugates.

A third, indirect source for tracking asymmetry follows from charge-asymmetric elastic scattering due to hadronic collisions, mostly due to a left-right asymmetric distribution of detector material. This complicates the reconstruction due to large kinks in the particle's trajectory. The impact of such elastic scatters is already included by considering the total hadronic cross-section in Sect. 6.2, and discussed in detail in Appendix A. In addition to hadronic elastic scattering, also Coulomb scattering can contribute. While there is no charge-asymmetry in the Coulomb scattering cross-sections, the left-right asymmetric distribution of material can lead to a magnet-dependent asymmetry. Because the scattering angles are smaller for Coulomb scattering than for hadronic scatters, the left-right asymmetric material distribution is expected to contribute mostly for hadrons. As this source of inefficiency for hadrons was already discussed in Sect. 6.2, only the dependence of this asymmetry on the hit occupancy will be emphasised in this section.

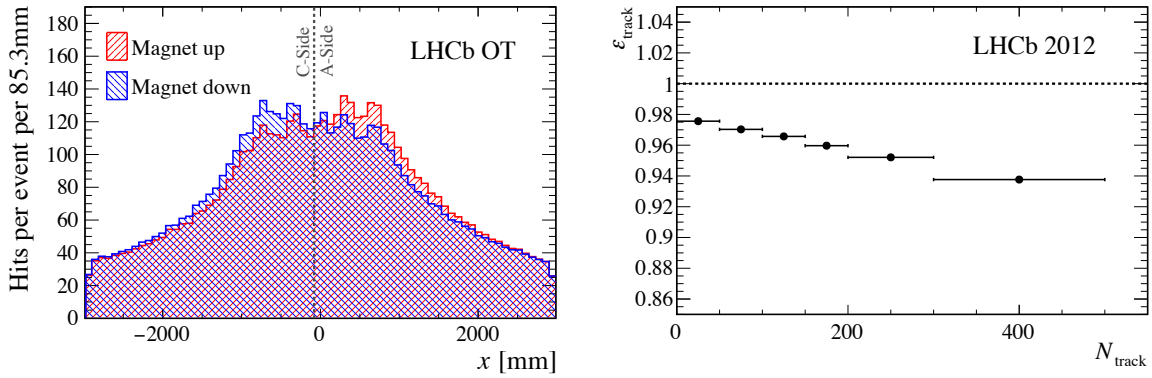

Figure 6.23: (left) Hit distribution in the outer tracker for both magnet polarities, using 30,000 random events for both samples, without any trigger requirement. The vertical dashed line indicates the mechanical split between the two detector halves, at $x = -8$ cm. (right) Tracking efficiency as a function of the total number of tracks reconstructed in the event, determined using the data collected in 2012. Figure adapted from Ref. [62].

Aside from the detector occupancy, the tracking performance depends on the momentum of the particle. Particles with low momentum are sensitive to more scattering through the detector and their trajectory is strongly curved due to the magnetic field. The momentum dependence of the tracking asymmetry shows that little asymmetry is left for particles with $p \geq 25\,\mathrm{GeV}/c$. This indicates that effects from a preference of orientation in the tracking algorithms are limited. The study presented in this section therefore only considers particles with $5 \leq p \leq 25\,\mathrm{GeV}/c$. The tracking asymmetries are studied using events in which the complete proton-proton collisions are simulated. A sample consisting of 70 million events with decays of the type $B^0 \to D^-\mu^+\nu_\mu X$ (where $D^- \to K^+\pi^-\pi^-$) is used, generated with ReDecay, introduced in Sect. 2.4. A new underlying event is generated and re-used for every 100 events, while the B^0 decay is generated for each event separately. To make sure the particles considered are independent, only decay products from the B^0 meson are investigated. The effects of the track reconstruction are isolated by considering only particles of which sufficient hits are recorded to form a long track (referred to as "reconstructible"),

$$\varepsilon_{\text{track}} = \frac{N(\text{reconstructed as a long track})}{N(\text{reconstructible as a long track})}. \tag{6.10}$$

The definition of the tracking asymmetry follows by Eq. 6.1. By construction, the extracted asymmetry is insensitive to acceptance asymmetries, but does include effects of elastic scattering. The muon and pion reconstruction asymmetries are studied for the muon and pion originating from the semileptonic B^0 decay. The p_{T} spectrum of the muons which originate directly from the B^0 decay is different from the p_{T} spectrum for the pions, which originate from the D^- decay. Therefore, this study is presented not only in bins of occupancy, but also in bins of transverse momentum.

The resulting asymmetry for pions and muons is shown in Fig. 6.24. Muons and pions with little p_{T} show a sizeable magnet-dependent and magnet-independent asymmetry in events with a high occupancy. Averaging magnet polarities, the track reconstruction favours positively charged particles over negatively charged particles when the detector occupancy is high. This is consistent with the charge-asymmetric local occupancy, attributed to the abundant production of electrons.

The elastic scattering rate for both muons and pions causes a magnet-dependent charge asymmetry, due to the known material distribution of the RICH1 beampipe and the inner tracker support (discussed in Sect. 6.2.3 and 6.2.2, respectively). The observed asymmetry is stronger for pions than for muons. This difference is attributed to large-angle, hadronic, elastic scatters by the pions in the detector. This would mean that the reconstruction becomes increasingly sensitive to elastic scattering for higher hit multiplicities.

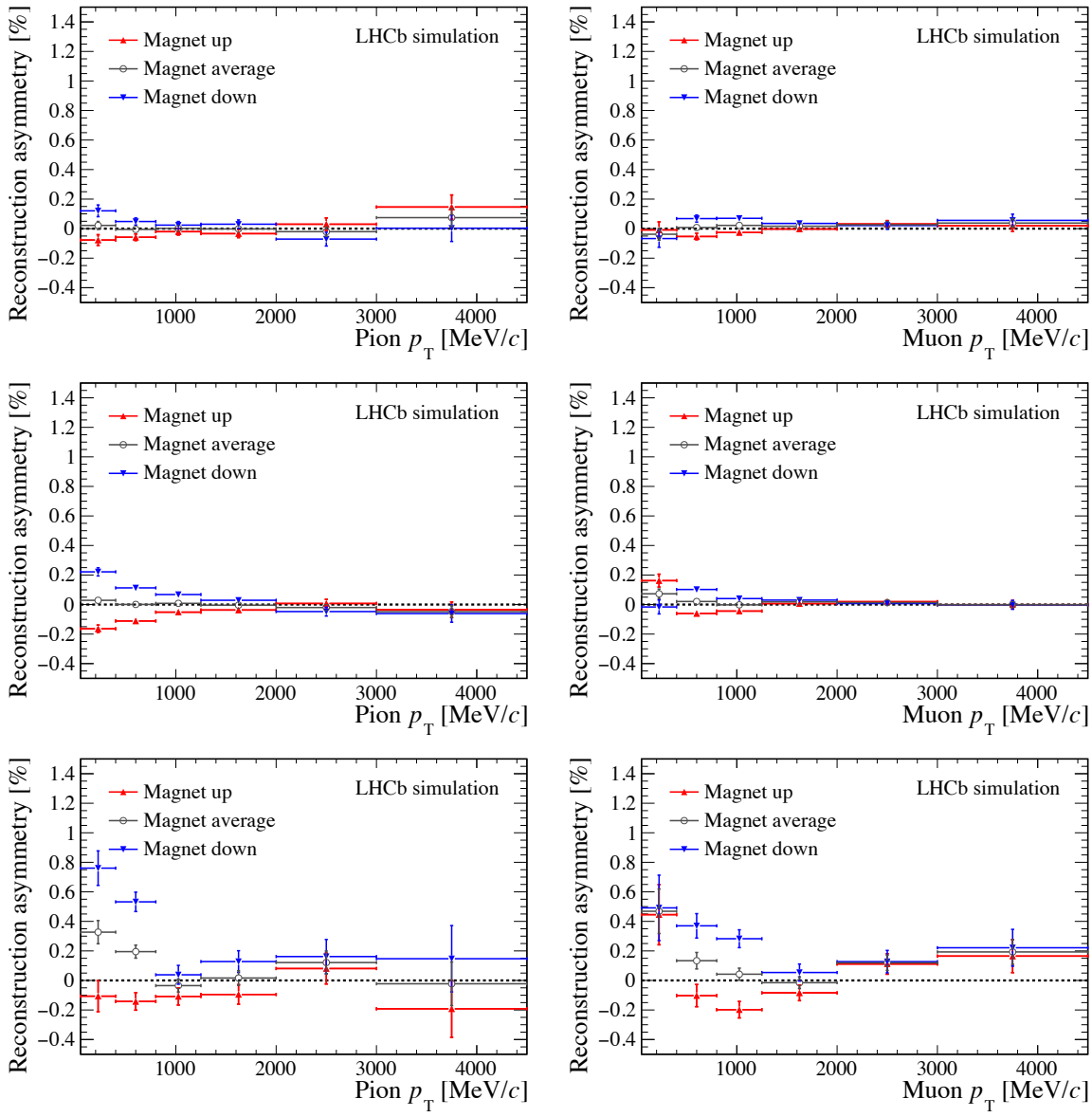

Figure 6.24: Asymmetry attributed to the track reconstruction for (left) pions in $B^0 \to D^-(\to K^-\pi^+\pi^+)\mu^+\nu_\mu X$ events and (right) muons in $B^0 \to D^-\mu^+\nu_\mu X$ events, for an OT hit multiplicity of (top) less than 2000, (middle) between 2000 and 6000 and (bottom) more than 6000 hits. Particles considered are required to have sufficient hits in the relevant tracking stations to form a long track and a momentum between 5 and 25 GeV/c.

6.4 Conclusion

In this chapter, a first decomposition of the dominant effects in the detection asymmetry of charged particles at LHCb was presented. The difference in the detector acceptance dominates the detection asymmetry in events with a low hit multiplicity. The beam-crossing angle and the hadronic (in)elastic cross-sections (especially for kaons and protons) have a large influence on this asymmetry. The beam parameters change with magnet polarity, such that the induced asymmetry does not cancel upon averaging data sets of different magnet polarities. The beam-crossing angle has a particularly strong effect at higher pseudorapidity, i.e. $\eta \geq 3.5$. It is advisable to include η in the parametrisation of the detection asymmetry when correcting for the detector bias.

The simulated defects for the inner tracker affect the detection asymmetry for particles with high pseudorapidity. Inefficiencies in the outer tracker lead to a smaller asymmetry, mostly for particles with low p_{T}. This result underlines the importance of the description of such defects in the simulation, and motivates a future study on the implications of e.g. the VELO sensor ageing. In addition, the resulting asymmetry due to the VELO and OT module arrangement suggests that the detector alignment should be included in a future study as well.

The track reconstruction shows an asymmetry for non-zero detector occupancies, already with moderate outer tracker occupancy. The magnet-dependent asymmetry is larger for hadrons than for muons, which is consistent with a degraded performance of the tracking for particles which undergo large-angle (elastic) scattering. In addition, a magnet-independent asymmetry is present in the track reconstruction. The sign of this asymmetry is compatible with the charge-asymmetric production of secondaries. The track reconstruction is the dominant effect in the overall detection asymmetry for momenta below $7\,\mathrm{GeV}/c$.

Chapter 7

Measurement of the instrumental asymmetry for $K^-\pi^+$-pairs

Positive and negative kaons show a sizeable difference in their nuclear interaction cross sections that also depends on their momentum. This results in a $\mathcal{O}(1\%)$ detection asymmetry, as was discussed briefly in Sect. 6.2.1. Measurements involving kaons therefore rely on a precise calibration of this asymmetry. Experimentally, the determination of the combined asymmetry of $K^-\pi^+$ pairs was found to be easier than a measurement of the detection asymmetry of charged kaons alone. This combined asymmetry is defined as the relative difference in detection efficiencies between $K^-\pi^+$ and $K^+\pi^-$-pairs,

$$A_{\text{det}}^{K^-\pi^+} = \frac{\varepsilon_{\text{det}}(K^-\pi^+) - \varepsilon_{\text{det}}(K^+\pi^-)}{\varepsilon_{\text{det}}(K^-\pi^+) + \varepsilon_{\text{det}}(K^+\pi^-)}, \tag{7.1}$$

where $\varepsilon_{\text{det}}(K^\mp\pi^\pm)$ denotes the absolute detection efficiency of $K^\mp\pi^\pm$ pairs. This calibration measurement provided crucial input for *CP* violation measurements in charm decays [66] and for the measurement of *CP* violation in $B^0 - \overline{B}^0$ mixing [49], both using data from Run 1 of the LHC. This chapter presents a measurement of $A_{\text{det}}^{K^-\pi^+}$ using Run-2 data recorded in 2015 and 2016, with improvements in the selection and the weighting procedure, which is an essential part of this measurement. The presented approach will be used for the entire LHCb data set collected during Run 2 of the LHC.

To a good approximation, the detection asymmetry between oppositely charged particles can be parametrised solely by their individual four-momenta and origin vertex. This means that the asymmetry of a reconstructed decay, e.g. $D^+ \to K^-\pi^+\pi^+$, can be decomposed as the sum of the individual detection asymmetries,

$$A_{\text{det}}(D^+ \to K^-\pi^+\pi^+) = A_{\text{det}}^{K^-}(\phi_1) + A_{\text{det}}^{\pi^+}(\phi_2) + A_{\text{det}}^{\pi^+}(\phi_3),$$

where ϕ_i parametrises the four-momenta and origin vertex of particle i in the decay. This is used to enable a measurement of the $K^-\pi^+$ detection asymmetry by taking the

difference in the measured asymmetry of two Cabibbo-favoured D^+ decay channels,

$$A_{\text{det}}^{K^-\pi^+} = A_{\text{meas}}(D^+ \to K^-\pi^+\pi^+) - A_{\text{meas}}(D^+ \to \overline{K}^0\pi^+) - A(K^0), \tag{7.2}$$

where $A(K^0) = -A(\overline{K}^0)$ signifies the relatively small correction for regeneration and CP violation in the neutral kaon system. The measured asymmetry, $A_{\text{meas}}(D^+ \to f)$, for the final state f is defined as

$$A_{\text{meas}}(D^+ \to f) = \frac{N(D^+ \to f) - N(D^- \to \overline{f})}{N(D^+ \to f) + N(D^- \to \overline{f})}, \tag{7.3}$$

where N denotes the number of observed decays. The measured asymmetries for both modes decompose as

$$A_{\text{meas}}(D^+ \to K^-\pi^+\pi^+) = A_{\text{det}}^{K^-\pi^+} + A_{\text{det}}^{\pi^+} + A_{\text{prod}}^{D^+} + A_{\text{trigger}} \tag{7.4}$$

$$A_{\text{meas}}(D^+ \to \overline{K}^0(\to \pi^+\pi^-)\pi^+) = A(\overline{K}^0) + A_{\text{det}}^{\pi^+} + A_{\text{prod}}^{D^+} + A_{\text{trigger}}, \tag{7.5}$$

such that, by subtracting the measured asymmetries of the two D^+ decay modes, contributions from the production asymmetry, $A_{\text{prod}}^{D^+}$, and the trigger asymmetry, A_{trigger}, are removed. Note that there is no detection asymmetry for the $\overline{K}^0$ decay products, as the $\pi^+\pi^-$ phase-space distribution is charge symmetric. The asymmetries for these decay modes can be measured accurately, as the D^+ meson is produced abundantly at LHCb [67] and can be separated well from backgrounds. While the detector asymmetry is defined in terms of the detection efficiencies per Eq. 6.1, the presented method only relies on the subtraction of asymmetries, and does not measure the detection efficiency directly.

In this chapter the general strategy to determine $A_{\text{det}}^{K^-\pi^+}$ is presented. In addition, motivated by the momentum dependence of the kaon cross-section asymmetry, $A_{\text{det}}^{K^-\pi^+}$ is determined in bins of K^- momentum. This allows for a comparison to the expectations which were presented in Sect. 6.2.1. The chapter is organised as follows. The data selection is explained in Sect. 7.1, followed by a discussion on the required weighting procedure for the cancellation of any nuisance asymmetries in Sect. 7.2. The extraction of the measured asymmetries is presented in Sect. 7.3. Section 7.4 presents the neutral kaon asymmetry, i.e. the last term in Eq. 7.2. After discussing a validation of the method using simulated events in Sect. 7.5, the results from all chapters are combined to a measurement of $A_{\text{det}}^{K^-\pi^+}$ and presented in Sect. 7.6. Finally, comparison of these results with the LHCb simulation is described in Sect. 7.7. The impact on physics measurements is presented separately in the conclusion of this thesis, Chapter 9.

7.1 Data selection

This analysis uses the proton-proton collision data recorded by LHCb in 2015 and 2016, corresponding to an integrated luminosity of $1.9\,\text{fb}^{-1}$. The data were recorded with both

magnet polarities. A total of $0.9\,\text{fb}^{-1}$ was recorded with the magnet-up configuration, and $1.0\,\text{fb}^{-1}$ with the magnet-down configuration. The data sets for each year and magnet polarity are analysed separately.

To ensure the cancellation of the trigger asymmetry between the two decay modes, the used trigger requirements are similar. Only D^+ candidates are considered in which the hardware trigger decision was independent of the D^+ decay products. In the first stage of the software trigger, HLT1, at least one of the pions originating directly from the D^+ decay is required to have $p_\text{T} > 1.0\,\text{GeV}/c$ and good track quality. For the $D^+ \to \overline{K}^0\pi^+$ decay mode, this trigger requirement is always applied to the single pion directly originating from the D^+ decay. All further offline requirements for the pion that was selected by HLT1 in the $D^+ \to K^-\pi^+\pi^+$ decays, referred to as the trigger pion, are identical to those for the $D^+ \to \overline{K}^0\pi^+$ decays. If both pions from the $D^+ \to K^-\pi^+\pi^+$ decay caused a positive trigger decision, one is selected randomly.

In the second stage of the software trigger, HLT2, a full event reconstruction is performed. This is used for a further online selection for each of the two modes. The online-reconstructed data is stripped of all information unrelated to the selected decay, and made available via the so-called Turbo stream, introduced in Sect. 2.3. The presented analysis takes advantage of the reduced event size by using looser selection requirements in the software trigger, in turn recording more D^+ candidates, while requiring less data-acquisition bandwidth per event.

Candidates consistent with the corresponding decay topologies are reconstructed in HLT2 using tracks with $p_\text{T} > 250\,\text{MeV}/c$ and a significant IP with respect to any PV ($\chi^2 > 25$). The background is reduced by requiring a minimal p_T for the D^+ candidate of $2.5\,\text{GeV}/c$. The pions and kaons are distinguished from another by requiring loose PID thresholds. Since 2016, the PID requirements were moved from the online to the offline selection for the $D^+ \to K^-\pi^+\pi^+$ channel to calibrate their effects on the asymmetry. For the 2015 data, the effects of the loose PID requirements are calibrated using other decay channels [63].

The decay products from the neutral kaon are separated from other, random pions by requiring a good quality of the reconstructed vertex, together with a minimum $\overline{K}^0$ lifetime of 2.0 ps with respect to the associated PV. By only reconstructing $\overline{K}^0$ in the $\pi^+\pi^-$ final state, one is restricted primarily to the decay of the K^0_S. The invariant mass of the $\pi^+\pi^-$ combination is therefore required to lie within $50\,\text{MeV}/c^2$ of the K^0_S mass [42]. The two pions are required to be reconstructed as long tracks. This limits the average decay time of the selected $\overline{K}^0$ to be less than approximately 10% of the K^0_S lifetime, and reduces the amount of material traversed by the $\overline{K}^0$ to that within the VELO only. The K^0_S candidates that decay further downstream in the detector are only used to verify the correction of the neutral kaon asymmetry. The background contribution from $\Lambda \to p\pi^-$ decays, in which the proton is mistakenly selected as a pion candidate, is suppressed by PID requirements on both pions which form the K^0_S candidate. This requirement is only

there to increase the signal purity, as any (residual) contribution of this background is eliminated by the fit to the invariant-mass distribution, described in Sect. 7.3.

The D^+ mesons are predominantly produced directly in proton-proton collisions, so-called prompt D^+ mesons. To maximise the signal purity, the offline selection reduces the sample to prompt candidates, by removing events with a too significant D^+ IP ($\chi^2 < 20$). As the branching fraction of the $D^+ \to K^-\pi^+\pi^+$ decay is large and the selection efficiency with respect to the $D^+ \to \overline{K}^0\pi^+$ mode is higher, the number of selected $D^+ \to K^-\pi^+\pi^+$ candidates is over 20 times larger than the number of selected $D^+ \to \overline{K}^0\pi^+$ candidates, and the statistical precision on $A_{\text{det}}^{K^-\pi^+}$ is dominated by the size of the $D^+ \to \overline{K}^0\pi^+$ sample. Therefore, only a quarter of the selected $D^+ \to K^-\pi^+\pi^+$ candidates is saved in the second software trigger stage. This selection is done randomly. Finally, the $D^+ \to K^-\pi^+\pi^+$ data set is split in eight bins of kaon momentum: $3-5$, $5-10$, $10-15$, $15-20$, $20-25$, $25-40$, $40-60$ and $60-80\,\text{GeV}/c$.

7.2 Kinematic weighting

The measured asymmetry in D^+ decays is affected by various nuisance asymmetries: the production asymmetry of the D^+, and the trigger and detection asymmetry of the trigger pion. These asymmetries vary over the phase space, mainly p_T and η. Different reconstruction efficiencies for both D^+ decay modes lead to differences in the kinematic distributions, such that residual nuisance asymmetries may remain in the calculation of $A_{\text{det}}^{K^-\pi^+}$. Therefore, a per-candidate weighting procedure is applied to mitigate the phase-space differences. The phase space is parametrised by the p_T, η distribution of the selected D^+ candidates, along with the p_T, η and ϕ distribution of the trigger pion.

In this analysis, $A_{\text{det}}^{K^-\pi^+}$ is evaluated as a function of kaon momentum. However, the p_T, η spectrum of the D^+ in the $D^+ \to K^-\pi^+\pi^+$ data set varies as a function of kaon momentum as well, shown in Fig. 7.1. Therefore, to correctly subtract the production asymmetry for each bin of kaon momentum, weights need to be assigned as well to the $D^+ \to \overline{K}^0\pi^+$ data set. This somewhat reduces the statistical precision on $A_{\text{det}}^{K^-\pi^+}$, but is inevitable. Three weighting steps are applied to make the most efficient use of the larger $D^+ \to K^-\pi^+\pi^+$ data sample.

In the first weighting step, weights are assigned to the $D^+ \to K^-\pi^+\pi^+$ candidates according to the corresponding D^+ p_T, η distribution of $D^+ \to \overline{K}^0\pi^+$ candidates, using a coarse-binned parametrisation. In the second weighting step, weights are assigned to the $D^+ \to \overline{K}^0\pi^+$ candidates, as to match the p_T, η distributions of both the trigger pion and the D^+ of the (weighted) $D^+ \to K^-\pi^+\pi^+$ candidates. As this is the final step to ensure the cancellation of the production and trigger asymmetries, it is carried out using a fine-binned, four-dimensional parametrisation. Lastly, the weighted distributions of the pion's azimuthal angle are equalised, again by assigning weights to the $D^+ \to \overline{K}^0\pi^+$ candidates. Because the azimuthal angle is uncorrelated with the kinematic variables in-

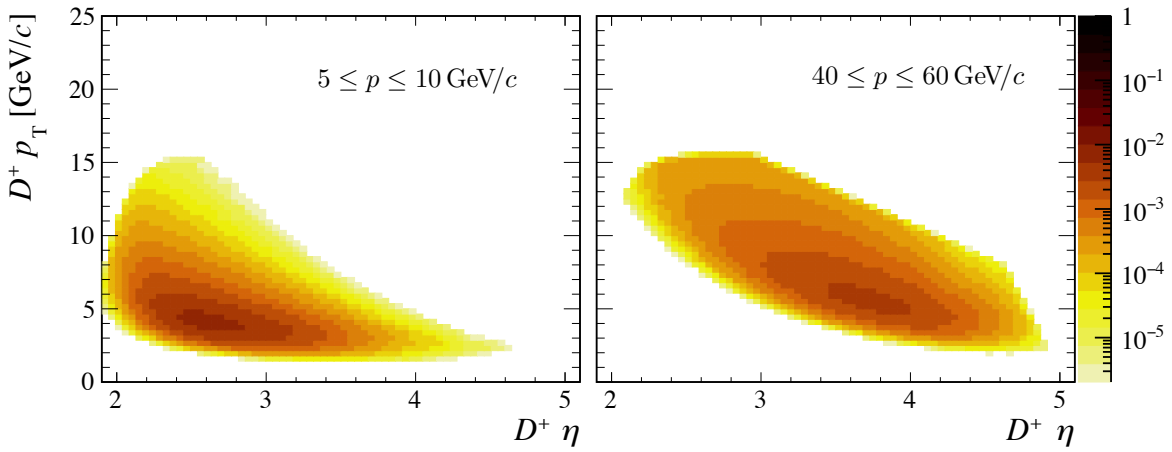

Figure 7.1: Background-subtracted D^+ p_T, η distributions for $D^+ \to K^-\pi^+\pi^+$ candidates in the 2016 magnet up data set for (left) K^- momentum between 5 and 10 GeV/c and (right) K^- momentum between 40 and 60 GeV/c.

volved in the previous weighting steps, this does not change the distributions of variables weighted earlier. The weights of all steps are multiplied to obtain the final kinematic weight for each candidate. For clarification, Fig. 7.2 provides a schematic of the three weighting steps.

7.3 Signal yield extraction

The weighted $K^-\pi^+\pi^+$ and $\pi^+\pi^-\pi^+$ invariant-mass distributions are used to discriminate between genuine D^+ decays and random-track backgrounds. The weighted invariant-mass distributions, along with the result of a binned, weighted maximum-likelihood fit, are shown in Fig. 7.3 for one bin of K^- momentum. For both decay modes, the signal component is modelled as the sum of three Gaussian functions, of which one has a power-law tail on the low-mass side. The means of the Gaussian functions are allowed to vary up to 2.5 MeV/c^2 from each other. Different shape parameters are allowed between D^+ and D^- states, to account for any charge-dependent resolution. The background is modelled using an exponential function. Background-subtracted kinematic distributions, which are required for the kinematic weighting, are created using the *sPlot* procedure [68], which uses the fit model described. This procedure is repeated for every bin of kaon momentum and data set.

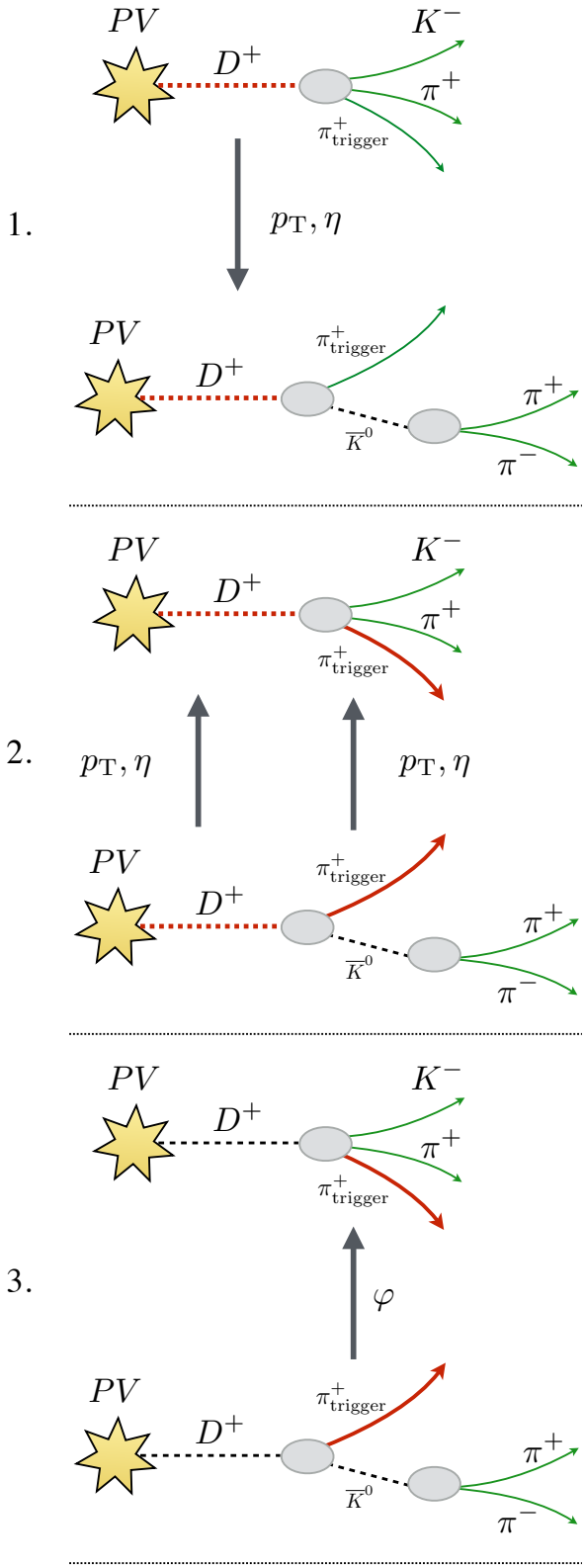

Figure 7.2: Schematic of the three weighting steps applied to equalise the kinematic distributions between the two D^+ decay modes. The kinematic variables in each step are the ones from the track or D^+ candidate highlighted in red.

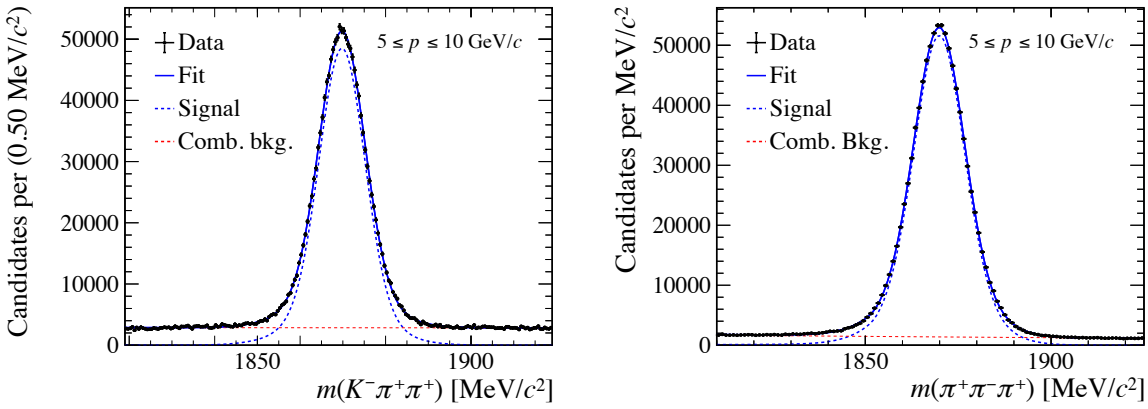

Figure 7.3: Fits to (left) the weighted $D^+ \to K^-\pi^+\pi^+$ invariant-mass distributions with $5 \leq p(K^-) \leq 10\,\text{GeV}/c$, and (right) the weighted $D^+ \to \pi^-\pi^+\pi^+$ invariant-mass distribution, where the weights are calculated to match the phase-space in the $D^+ \to K^-\pi^+\pi^+$ data sample for $5 \leq p(K^-) \leq 10\,\text{GeV}/c$. The data are taken in 2016 with the magnet up polarity. Only the data are shown for the D^+ candidates with a positive charge.

7.4 Neutral kaon asymmetry

Like the neutral B_s^0 mesons, discussed in Chapter 4, mixing also occurs in the $K^0 - \overline{K}^0$ system. However, unlike for the $B_s^0 - \overline{B}_s^0$ system, *CP* violation in mixing has been observed already for neutral kaons. For historic reasons, it is described by the parameter ϵ. This parameter relates to the interference between the dispersive and absorptive mixing amplitudes as

$$\left(\frac{1-\epsilon}{1+\epsilon}\right)^2 = \frac{2M_{12}^* - i\Gamma_{12}^*}{2M_{12} - i\Gamma_{12}},$$

and is thus similar to $|q/p|$ introduced in Eq. 4.4. The *CP* violation in mixing is not the only difference between the K^0 and $\overline{K}^0$, as also the interactions with the detector material introduce differences between the two states, so-called regeneration effects. This is the result of the different valence quarks of the two mesons, as a K^0 ($\overline{s}d$) can only interact (quasi-)elastically with nucleons composing the detector material, while a $\overline{K}^0$ ($s\overline{d}$) can excite a nucleon into a Λ- or Σ hyperon or associated excited states. The *CP* violation in the mixing of neutral kaons, the different interaction rates with the detector material (regeneration) and the interference of both effects lead to an additional asymmetry in the selected $D^+ \to \overline{K}^0\pi^+$ decays. The effects from regeneration and *CP* violation turn out to be of the same order and same sign in LHCb. The description of the $\overline{K}^0$ propagation is described in detail in Refs. [66, 69], and only the essential components are repeated here.

In the description of the $\overline{K}^0$ propagation, the amplitudes are calculated for kaon mix-

ing and *CP* violation, coherently combined with the propagation through the simulated LHCb material. To describe the latter, a description of the interaction rates with the detector material is required. The difference in interaction rates is due to a difference in the interaction cross-section, which depends on the momentum of the kaon and on the number of nucleons in the detector material, A, and is obtained from Ref. [70],

$$\Delta\sigma = \sigma_T(\overline{K}^0) - \sigma_T(K^0) = 23.2\, A^{0.758}[p(\text{ GeV}/c)]^{-0.614}\,\text{mb}\ . \tag{7.6}$$

The difference in interaction cross-sections is related via the optical theorem, $\sigma_T = (4\pi/p)\text{Im}f$, to the difference in forward scattering amplitudes $\Delta f = \bar{f} - f$. The phase of Δf has been determined as $\arg(\Delta f) = (-124.7 \pm 0.8)^\circ$ in Ref. [71]. This amplitude difference is used in the description of the time evolution for neutral kaons. The time evolution of the K^0_L and K^0_S amplitudes which compose an arbitrary neutral kaon state is, modulo a common exponential decay factor, proportional to [69]

$$\alpha_L(t) \propto \alpha_L(0)\cos(\Omega t) - i\frac{\alpha_L(0)\Delta\lambda + \alpha_S(0)\Delta\chi}{2\Omega}\sin(\Omega t), \tag{7.7}$$

$$\alpha_S(t) \propto \alpha_S(0)\cos(\Omega t) + i\frac{\alpha_S(0)\Delta\lambda - \alpha_L(0)\Delta\chi}{2\Omega}\sin(\Omega t), \tag{7.8}$$

where the constant $\Omega \equiv \frac{1}{2}\sqrt{\Delta\lambda^2 + \Delta\chi^2}$ is given by the masses $m_{\text{L,S}}$ and decay widths $\Gamma_{\text{L,S}}$ of the K^0_L and K^0_S states and by the absorption χ ($\bar{\chi}$) of K^0 ($\overline{K}^0$) states through

$$\begin{aligned}\Delta\lambda &= \lambda_\text{L} - \lambda_\text{S} = \Delta m - \frac{i}{2}\Delta\Gamma = (m_\text{L} - m_\text{S}) - \frac{i}{2}(\Gamma_\text{L} - \Gamma_\text{S})\ ,\\ \Delta\chi &= \chi - \bar{\chi} = -\frac{2\pi\mathcal{N}}{m}(f - \bar{f}) = -\frac{2\pi\mathcal{N}}{m}\Delta f\ .\end{aligned} \tag{7.9}$$

where $\mathcal{N}$ is the scattering density of the detector material and m the kaon mass. Note that, in the case of no absorption $\Delta\chi = 0$, and Eq. 7.7 reduces to Eq. 4.5 in the formalism introduced in Sect. 4. A summary of all of the parameters involved can be found in Table 7.1.

To quantify the impact on the measured $D^+ \to \overline{K}^0\pi^+$ asymmetry, the neutral kaon produced in $D^+ \to \overline{K}^0\pi^+$ decays must first be expressed in the K^0_S, K^0_L basis,

$$\begin{aligned}|K^0\rangle &= \sqrt{\frac{1+|\epsilon|^2}{2}}\frac{1}{1+\epsilon}\left[|K^0_\text{L}\rangle + |K^0_\text{S}\rangle\right]\ ,\\ |\overline{K}^0\rangle &= \sqrt{\frac{1+|\epsilon|^2}{2}}\frac{1}{1-\epsilon}\left[|K^0_\text{L}\rangle - |K^0_\text{S}\rangle\right]\ ,\end{aligned} \tag{7.10}$$

where ϵ defines *CP* violation in neutral kaon mixing.

The neutral kaon amplitude is propagated numerically through the simulated detector from the reconstructed D^+ decay vertex to the reconstructed $\overline{K}^0$ decay vertex in the K^0_S and K^0_L basis. This method accounts for the varying material type and density

along the $\overline{K}^0$ trajectory. Finally, the $K^0_{\rm L}$ and $K^0_{\rm S}$ amplitudes are projected to its *CP*-even component to extract the relative difference in measured $\pi^+\pi^-$ candidates. The overall asymmetry is calculated by the expected difference in decay rate when assuming either a K^0 or $\overline{K}^0$ initial state, averaged over all candidates.

The simulated neutral-kaon asymmetry is given in Table 7.2. The dominating systematic uncertainty is coming from the estimated 10% uncertainty in the material budget [62]. The uncertainty on the material budget is propagated by varying the simulated material thickness, and re-computing $A(\overline{K}^0)$. As different weights are assigned to the $D^+ \to \overline{K}^0\pi^+$ candidates for each of the K^- momentum bins, the $\overline{K}^0$ asymmetry needs to be calculated for the bins of K^- momentum separately. The resulting neutral kaon asymmetry is shown in Fig. 7.4.

7.4.1 Downstream-reconstructed $K^0_{\rm S}$ candidates

The majority of the generated $K^0_{\rm S}$ mesons decay downstream of the vertex detector, of which a part can be reconstructed using downstream tracks (defined in Sect. 2.2.1). The neutral-kaon asymmetry is expected to be larger for such candidates, as more material is traversed by the $K^0_{\rm S}$ and the mesons have a larger decay time (thus increasing the contribution from *CP* violation in mixing). The downstream-reconstructed candidates are not included in the nominal selection of this analysis, but are used as a cross-check for the estimation of the $\overline{K}^0$ asymmetry as a function of the decay time. The offline selection used for the downstream-reconstructed sample is tighter to counter the increased background, predominantly due to ghost tracks. The pseudorapidity of the reconstructed D^+ and $K^0_{\rm S}$ candidates is limited to $\eta < 4.5$. The consistency requirement for the D^+ to originate from a primary vertex is further tightened, and all selected candidates should comply with the desired decay topology when applying a decay chain fit [72]. The result-

Table 7.1: Values of the parameters used to calculate the neutral kaon asymmetry [42, 70].

Parameter	Value
Δm	$(0.5293 \pm 0.0009) \times 10^{10}\hbar\,\mathrm{s}^{-1}$
$\tau_{\rm S} \equiv 1/\Gamma_{\rm S}$	$(0.8954 \pm 0.0004) \times 10^{-10}\,\mathrm{s}$
$\tau_{\rm L} \equiv 1/\Gamma_{\rm L}$	$(5.116 \pm 0.021) \times 10^{-8}\,\mathrm{s}$
M	$(497.614 \pm 0.024)\,\mathrm{MeV}/c^2$
$\arg(\Delta f)$	$(-124.7 \pm 0.8)^\circ$
$\lvert\epsilon\rvert$	$(2.228 \pm 0.011) \times 10^{-3}$
$\phi_{+-} \equiv \arg\epsilon$	$(43.51 \pm 0.05)^\circ$

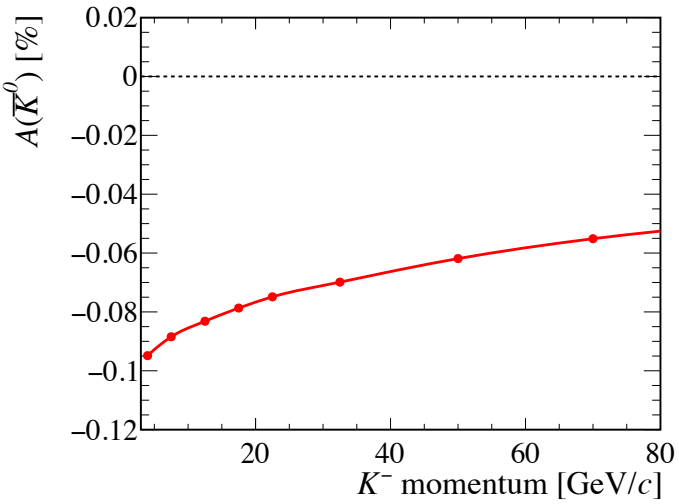

Figure 7.4: Predicted neutral kaon asymmetry using weights obtained per charged-kaon momentum bin in Sect. 7.3. The systematic uncertainty from the material uncertainty is not shown as it is fully correlated between bins.

ing simulated K^0 asymmetry is included at the bottom line in Table 7.2. As expected, the asymmetry of downstream-reconstructed K^0_S candidates is significantly larger than the asymmetry of K^0_S candidates which are reconstructed with long tracks. Therefore, the downstream sample is only used as a cross-check throughout this analysis.

The measured asymmetries in data and the predicted asymmetries are shown as a function of the K^0_S decay time in Fig. 7.5, for both the long- and downstream-reconstructed sample. The measured asymmetries include an overall offset from nuisance asymmetries, i.e. the production and trigger asymmetries, while the neutral kaon asymmetry vanishes for zero decay time. Only the decay-time dependence is of interest for testing the neutral kaon correction. Therefore, the offset is accounted for by shifting

Table 7.2: Calculated asymmetry $A(\overline{K}^0)$ for differnet $D^+ \to K^0_S\pi^+$ samples, including the systematic uncertainty due to the amount of traversed detector material. Weighted means that the $D^+ \to K^0_S\pi^+$ momentum spectrum has been weighted to the $D^+ \to K^-\pi^+\pi^+$ kinematics.

Sample	$A(\overline{K}^0)$ [%]	Systematic uncertainty [%]
Long reconstructed, 2016	−0.1096	0.0057
Long reconstructed, 2016 weighted	−0.0868	0.0050
Downstream reconstructed, 2016	−0.5271	0.0246

the prediction with the average difference between measured and predicted asymmetry. The resulting measured asymmetry follows the predicted downward trend in both samples. The effect is particularly visible in the downstream-reconstructed K^0_S sample.

The projection into bins of d/λ_T is shown in Fig. 7.6. The same trends are visible. This is to be expected, as the decay time and flight distance of a K^0_S candidate are correlated. In the projection onto the K^0_S decay time, the effect of the varying material density is smeared out. Therefore, the difference of observed and expected asymmetry in bins of d/λ_T is more sensitive to the description of the detector. The detector material is less precisely known than the parameters of CP violation in the neutral kaon system, with an uncertainty of 10% [62]. Nevertheless, the agreement is quite good which gives confidence in the the geometry description upstream of the magnet, and in the predicted neutral-kaon asymmetry.

7.5 Partial validation using fast simulation

Simulated $D^+ \to K^0_S\pi^+$ and $D^+ \to K^-\pi^+\pi^+$ decays allow for a validation of the method. With the information of the generated particles, one can extract the (simulated) absolute reconstruction efficiency and the corresponding value of $A_{\text{det}}^{K^-\pi^+}$ with Eq. 7.1. This asymmetry is then compared to the value extracted from the $D^+ \to K^0_S\pi^+$ and $D^+ \to K^-\pi^+\pi^+$ raw asymmetries by using Eq. 7.2. The difference between the two results is used to probe the a systematic error of the method.

Simulating sufficient decays to achieve a precision comparable to the statistical precision found in data is demanding in terms of computational resources. Therefore, the

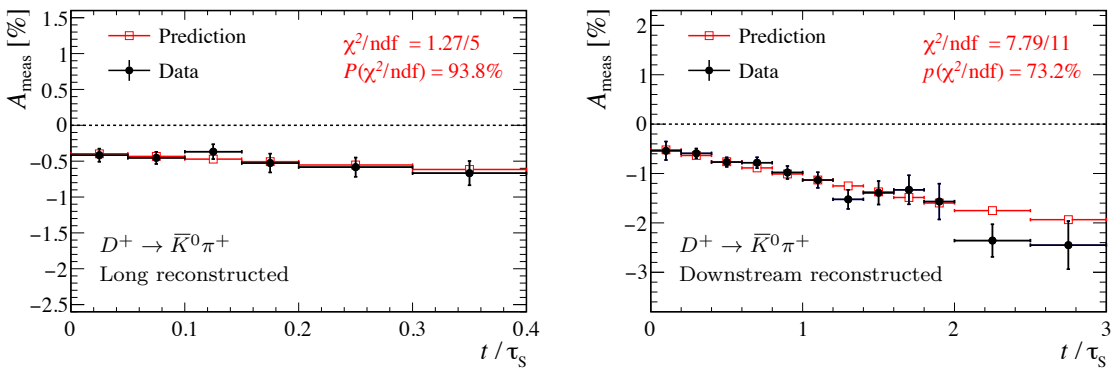

Figure 7.5: Raw asymmetry of $D^+ \to \overline{K}^0\pi^+$ candidates and the predicted neutral kaon asymmetry as function of the K^0_S decay times for (left) long- and (right) downstream-reconstructed candidates. The predicted asymmetry is shifted by the average difference between measured and predicted asymmetry to account for production and other detection asymmetries. The probability for the consistency between data and prediction after the shift is quoted.

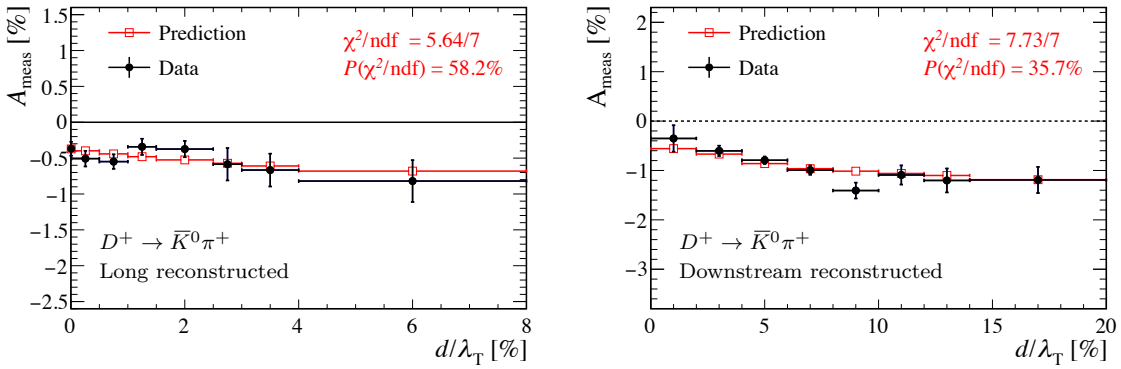

Figure 7.6: Raw asymmetry of $D^+ \to \overline{K}^0\pi^+$ candidates and the predicted neutral kaon asymmetry as function of the amount of traversed material in nuclear collision lengths for the (left) long- and (right) downstream-reconstructed samples. The predicted asymmetry is shifted by the average difference between measured and predicted asymmetry to account for production and other detection asymmetries.

event simulation is simplified by not generating pp collisions, but only D^+ particles which are forced to decay in either of the two considered decay modes, using the particle-gun production in GAUSS. The D^+ p_T, η distribution that is used for this is extracted from $\sqrt{s} = 13\,\text{TeV}$ pp collisions generated in PYTHIA. The generated samples consist of 100M $D^+ \to K^-\pi^+\pi^+$ events, and 300M $D^+ \to K^0_S\pi^+$ events, where the difference in the generated sample sizes accounts for the lower reconstruction efficiency of the latter mode. All K^0_S in the generated $D^+ \to K^0_S\pi^+$ events are forced to decay to $\pi^+\pi^-$, such that the small asymmetry associated to the neutral kaon is not included. A slightly larger sample was created in the magnet up configuration to test polarity-dependent effects with high precision.

No production or trigger asymmetry is included in this simplified simulation. The study presented in this section therefore provides a partial validation of Eq. 7.2. Nevertheless, Sect. 6.2.1 showed that the largest contribution to $A_{\text{det}}^{K^-\pi^+}$ originates from the charge-asymmetric kaon cross-sections, which are included. Similarly to the procedure in data, the results are presented in bins of K^- momentum.

Simulated $D^+ \to K^0_S\pi^+$ candidates have per-candidate weights assigned to equalise the π^+ p_T, η distributions of the $D^+ \to K^-\pi^+\pi^+$ and $D^+ \to K^0_S\pi^+$ modes for each bin in kaon momentum. As the requirements on the hardware trigger are absent in the fast simulation, one of the pions is chosen randomly. The per-candidate weights are calculated using a forest of decision trees with gradient boosting (a GBDT) [73–75]. The results of $A_{\text{det}}^{K^-\pi^+}$ computed with Eq. 7.2 as a function of kaon momentum are shown in Fig. 7.7. Large differences are visible between the magnet polarities. These differences are explained by simulated left-right differences in the detector performance as studied in Chapter 6, and of which an overview was presented in Sect. 6.2.8.

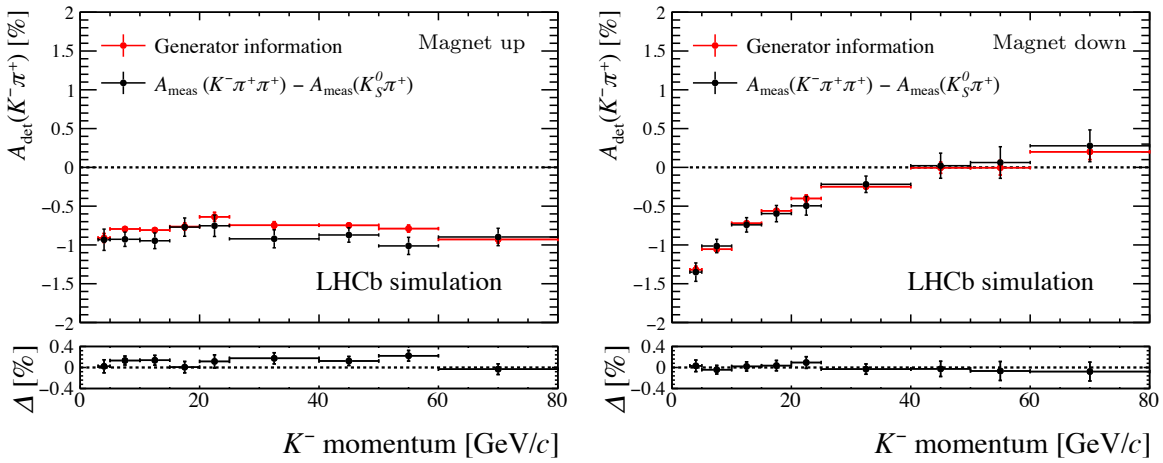

Figure 7.7: In black, the simulated detection asymmetry resulting from a weighting of the $D^+ \to K^0_S\pi^+$ pion to one of the pions in the $D^+ \to K^-\pi^+\pi^+$ sample in p_T and η. In red, the simulated detection asymmetry determined from generator information. On the left the results for magnet up are shown, on the right for magnet down. The bottom plots show the difference between the two methods, correcting for the statistical correlation.

Table 7.3: The fitted bias of $A^{raw}(D^+ \to K^-\pi^+\pi^+) - A^{raw}(D^+ \to K^0_S\pi^+)$ with respect to $A_{det}^{K^-\pi^+}$ as determined from generator-level information.

Magnet polarity	Fitted bias [%]
Magnet Up	0.04 ± 0.04
Magnet Down	-0.02 ± 0.06
Magnet Average	0.02 ± 0.04

There is a statistical correlation of $A_{det}^{K^-\pi^+}$ between the K^- momentum bins, since the same but differently weighted $D^+ \to K^0_S\pi^+$ candidates are reused. The difference between the results from the weighting procedure and the results based on the generator information is fitted with a straight line, by using a minimal-χ^2 fit which takes into account the correlation. The resulting bias for each magnet polarity is shown in Table 7.3. No indication of a bias is found, and Eq. 7.2 is validated with a precision of 0.04%. Adding the small offset on the magnet average, the systematic uncertainty is found to be 0.06%.

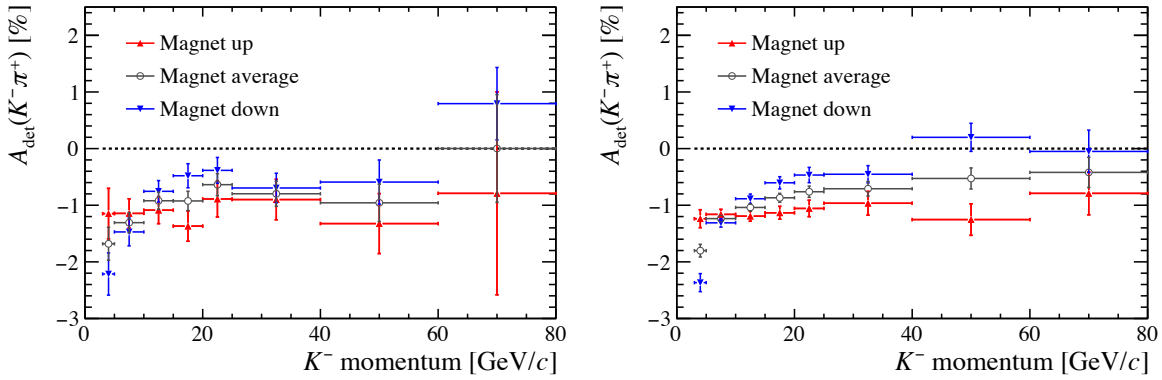

Figure 7.8: Measured values for $A_{\text{det}}^{K^-\pi^+}$ in bins of kaon momentum for (left) 2015 data and (right) 2016 data. There is a statistical correlation between the data points due to the overlap between the $D^+ \to \overline{K}^0\pi^+$ samples used for each bin.

7.6 Results

The measured asymmetries (of Eq. 7.2) are extracted from data using the binned maximum-likelihood fits with the mass models and weights described in Sects. 7.2 and 7.3. The raw asymmetries for the $D^+ \to \overline{K}^0\pi^+$ decay mode are then corrected for the neutral kaon asymmetry, using the momentum-dependent values as shown in Fig. 7.4. The $A_{\text{det}}^{K^-\pi^+}$asymmetries in all momentum bins are displayed in Fig. 7.8. Integrating the asymmetry over K^- momenta $3\,\text{GeV}/c \leq p \leq 125\,\text{GeV}/c$ results in

$$A_{\text{det}}^{K^-\pi^+} = (-0.89 \pm 0.15\,(\text{stat}) \pm 0.06\,(\text{syst}))\% \quad \text{in 2015},$$
$$A_{\text{det}}^{K^-\pi^+} = (-1.03 \pm 0.06\,(\text{stat}) \pm 0.06\,(\text{syst}))\% \quad \text{in 2016}.$$

The systematic error is the one extracted from the validation on the fast simulation. As expected, the asymmetry decreases as a function of K^- momentum and shows a dependence on the magnet polarity. For comparison, the result for the 2011 data set of $1\,\text{fb}^{-1}$ is [66]

$$A_{\text{det}}^{K^-\pi^+} = (-1.10 \pm 0.10\,(\text{stat}) \pm 0.01\,(\text{syst}))\% \quad \text{in 2011},$$

where only a systematic error was assigned to the neutral kaon asymmetry. The increase in statistical precision per fb^{-1} with respect to Run 1 is largest for low K^- momenta. For example, the uncertainty is decreased from from 0.13% (2011, $1\,\text{fb}^{-1}$) to 0.06% (2016, $1.6\,\text{fb}^{-1}$) for $10 \leq p(K^-) \leq 15\,\text{GeV}/c$, significantly more precise than expected from just the increase in luminosity.

7.7 Comparison with fast simulation

The results from Sect. 7.6 form a measure for the accuracy of the LHCb detector simulation. The dominant contribution to the polarity-averaged value of $A_{\text{det}}^{K^-\pi^+}$ is due to the charge-asymmetric material interaction of the kaon. Therefore, simulation of the $K^-\pi^+$ asymmetry depends mostly on the simulated nuclear interaction cross-section asymmetry, as well as the material map of the LHCb detector. To compare the results from data with simulation, the same simulated $D^+ \to K^-\pi^+\pi^+$ data set is used as described in Sect. 7.5. The nuclear interaction asymmetry is simulated using GEANT4 9.5p02, using the settings from `FTFP_BERT`. The fast simulation technique used for these data set neglects the underlying event. In data, polarity-dependent effects which depend on the event occupancy are expected . Therefore, only the polarity-averaged results are considered in the comparison.

The simulated $D^+ \to K^-\pi^+\pi^+$ candidates are weighted in both kaon p_{T}, η and pion p_{T}, η to that of the (weighted) $D^+ \to K^-\pi^+\pi^+$ signal sample for each bin in kaon momentum. The per-candidate weights are calculated by using a BDT classifier [75]. The resulting magnet-averaged asymmetry is shown in Fig. 7.9. A relative 10% uncertainty has been added to account for the uncertainty on the simulated material distribution [62] as systematic. The results are found to be in good agreement, with a p-value of 87.1%, even without the inclusion of the 10% material uncertainty. This indicates that the uncertainty on the material budget likely overestimates this error.

7.8 Conclusion

The charge asymmetry in the detection of $K^-\pi^+$-particles at LHCb has been measured using $D^+ \to K^-\pi^+\pi^+$ and $D^+ \to \overline{K}^0\pi^+$ decays. It is dominated by the asymmetry in the nuclear interaction rate of the charged kaon, and is of percent-level for momenta between 3 and 80 GeV/c, the relevant range for LHCb. Integrated over K^- phase-space and only considering 2016 data, the uncertainty is 0.08% per 1.6 fb^{-1}, where both systematic and statistical errors have been added in quadrature. The results presented show an improvement in precision with respect to Run 1 due to a higher efficiency of the software triggers and a more efficient use of bandwidth by the Turbo stream. A validation using a simplified simulation technique shows no significant bias, with a precision of 0.06%. This ensures the method can be used for the future, high-precision CP-violation measurements.

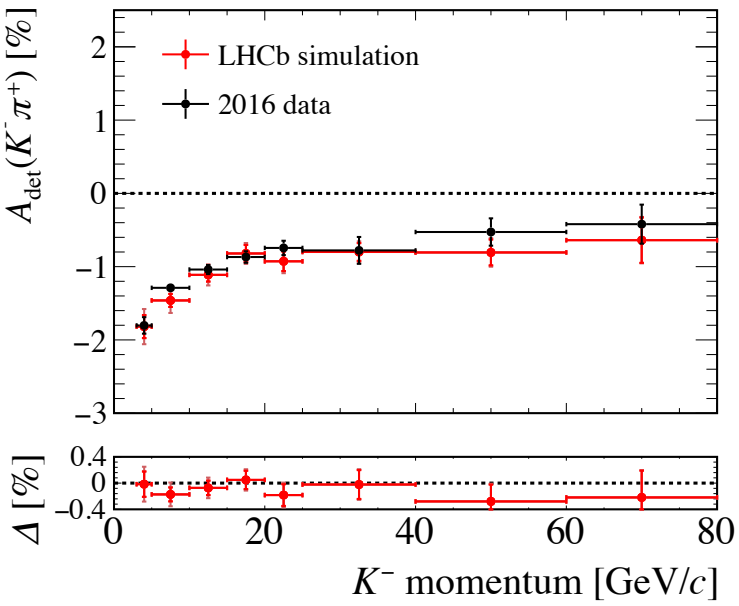

Figure 7.9: Detection asymmetry for the weighted, fast-simulation samples, with $A_{\text{det}}^{K^-\pi^+}$ as extracted from 2016 data superimposed. The red error bars show the statistical and total uncertainty, of which the latter includes a 10% uncertainty from the material map. The simulation is carried out using GEANT4 9.5p02 and the `FTFP_BERT` settings for hadronic physics.

Chapter 8

Measurements of detection efficiencies using VELO tracks

Using the understanding of the sources of detection asymmetries presented in Chapter 6, a new method was developed to determine these asymmetries using proton-proton collision data. Unlike the method described in Chapter 7, which only measured asymmetries, this method also determines absolute detection efficiencies. The detection efficiency of charged particles defines the detection asymmetry via Eq. 6.1. In addition to detection asymmetries, detection efficiencies are important in their own right, e.g. for branching-fraction measurements, such as those performed to test lepton universality. Different interactions with the detector material (e.g. the energy loss of electrons[1] via Bremsstrahlung versus nuclear interactions of hadrons) introduce significant differences in the detection efficiency among charged-particle species. A measurement of the absolute detection efficiency is challenging, as the existence of a "probe" particle must be inferred independently of the track reconstruction. Therefore, for some particle species a data-driven calibration of the detection efficiency had not been developed yet. In the analysis of Run-1 data, some measurements of branching fractions were systematically limited by the uncertainty in the absolute detection efficiency of hadrons [76]. Therefore, a more precise calibration of the absolute detection efficiency is needed. In addition, no calibration of the detector acceptance for leptons exists thus far. Therefore, this chapter focuses on the calibration of detection efficiencies, and the detection asymmetries are only discussed in Sect. 8.5.

All long tracks are required to have a VELO segment. Hence, the efficiency of reconstructing long tracks can be decomposed,

$$\varepsilon_{\text{det}}(\text{long}) = \varepsilon_{\text{det}}(\text{long}|\text{VELO})\varepsilon_{\text{det}}(\text{VELO}). \tag{8.1}$$

[1]The term "electron" is used to refer to both e^+ and e^-.

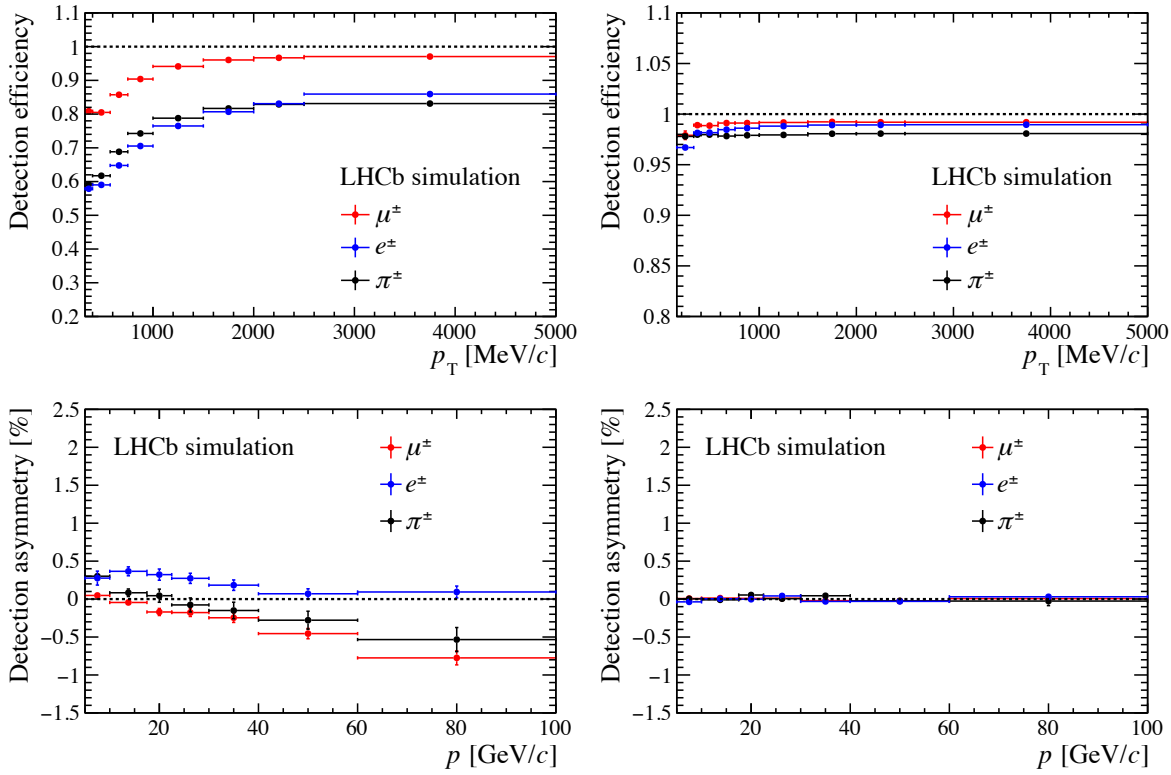

Figure 8.1: Simulated (top) detection efficiency and (bottom) detection asymmetry for pions, muons and electrons with $p \geq 2\,\text{GeV}/c$ for (left) long tracks and (right) VELO tracks. For clarity, the asymmetry of only one magnet polarity (magnet down) is shown. For these plots, a generated particle is considered reconstructed when a long track is formed with at least 70% of the hits due to the generated particle.

Similarly, for the detection asymmetry, one has (Eq. 5.7):

$$A_{\text{det}}(\text{long}) \approx A_{\text{det}}(\text{long}|\text{VELO}) + A_{\text{det}}(\text{velo}). \tag{8.2}$$

This separation is convenient, as most significant differences in the detection efficiency among particle species are introduced downstream of the VELO detector. This is confirmed in Fig. 8.1, which shows the simulated detection efficiency and asymmetry as a function of momentum for VELO and long tracks. The simulated detection efficiency for the VELO detector is close to 100%, and the charge asymmetry is negligible. The VELO detector material is described well in the simulation, with a precision of 6% [77]. In addition, a calibration procedure exists already for the VELO-track reconstruction [62], which also takes into account the ageing of the detector. Therefore, the detection efficiency of VELO track segments is already known precisely. This chapter presents a determination of $\varepsilon_{\text{det}}(\text{long}|\text{VELO})$ for muons, pions and electrons; this, in turn, using the well-known VELO detection efficiency, provides a measurement of the detection efficiency and asymmetry of long tracks.

Because of the lack of information on production cross-sections, measurements of absolute branching fractions are rarely performed at LHCb. Instead, measurements of branching-fraction ratios are determined. In these measurements, only the relative difference in detection efficiencies is relevant, and a correct description of the kinematic dependence of the muon-reconstruction efficiency is crucial. Unfortunately, VELO tracks do not contain any momentum information, aside from the direction. However, an estimate of the absolute momentum is required for the correct parametrisation of the detection efficiency for long tracks, $\varepsilon_{\text{det}}(\text{long}|\text{VELO})$, as is visible by the variation in p_{T} shown in Fig. 8.1. To overcome this complication, the momentum of the VELO track is inferred from kinematic constraints, restricting to VELO tracks associated to decays of the type $B^+ \to J/\psi(\to \mu^+\mu^-)K^+$, $D^{*+} \to D^0(\to K^-\pi^+\pi^+\pi^-)\pi^+$ and $B^+ \to J/\psi(\to e^+e^-)K^+$. If one of the muons, electrons or pions from the J/ψ or D^0 decay (called the "probe" particle) is reconstructed as a VELO track, while all other particles ("tag" particles) are reconstructed as long tracks, the constraint from the J/ψ or D^0 mass is sufficient to obtain an accurate momentum estimate of the VELO track. In addition, the signature of a B^+ or D^{*+} decay removes all VELO tracks composed of unrelated hits, i.e. ghost tracks [2].

Long tracks can be matched to the selected VELO track by common hits in the VELO detector. Exploiting this, the probe particle, which is only reconstructed as a VELO track, is considered reconstructed as a long track when a long track shares at least 6 hits with the VELO track. This defines the "pass" and "fail" categories for candidates, and from the signal yields of both categories the reconstruction efficiency can be determined,

$$\varepsilon_{\text{det}}(\text{match}|\text{VELO}) = \frac{N(\text{reconstructed as VELO track \& matched to long track})}{N(\text{reconstructed as VELO track})}. \tag{8.3}$$

The detection efficiencies for muons, pions and electrons at LHCb are measured with this method using proton-proton collision data recorded in 2017. The general principles behind the momentum inference are discussed first, and afterwards the muon, electron and pion analyses are presented. The determination of the muon detection efficiency is used as the main example, and is explained in most detail. The goal of this chapter is to disclose the general principles behind the method, show its application in the various channels, and determine the expected precision of the detection asymmetry. The method presented here is validated, but since the evaluation of the systematic errors is incomplete, the results should be considered preliminary.

[2] By its use of kinematic constraints, the presented method is inspired by the Run-1 calibration measurement using partially reconstructed $D^{*+} \to D^0(\to K^-\pi^+\pi^-\pi^+)\pi^+$ decays, discussed in Sect. 5.5.2. The presented method aims to have a better momentum resolution, which allows for a better control of systematic uncertainties. Therefore, it is also suited for the determination of the detection efficiencies.

8.1 Momentum inference

The probe particles originate from decays of a particle with a relatively narrow natural decay width, such as the D^0 or J/ψ. If all other decay products are fully reconstructed and the opening angles between all tracks are known, the momentum of the probe particle can be inferred from the conservation of four-momentum:

$$\begin{aligned} m^2 &= \left(E_{\text{probe}} + E_{\text{tag}}\right)^2 - p_{\text{tag}}^2 - p_{\text{probe}}^2 - 2p_{\text{tag}}p_{\text{probe}}\cos\theta \\ &= m_{\text{probe}}^2 + m_{\text{tag}}^2 + 2E_{\text{probe}}E_{\text{tag}} - 2p_{\text{tag}}p_{\text{probe}}\cos\theta, \end{aligned} \tag{8.4}$$

where θ is the opening angle between the probe and tag particles. To infer the momentum of the probe particle, the mass of the decaying particle, m, along with the mass of the probe particle, m_{probe}, are constrained to their known values. The angles are reconstructed well with VELO tracks, such that p_{probe} is the only unknown. Equation 8.4 can then be solved for p_{probe} by first taking the square of both sides:

$$\begin{aligned} \left(\Delta m^2\right)^2 &= 4E_{\text{probe}}^2E_{\text{tag}}^2 + 4p_{\text{probe}}^2p_{\text{tag}}^2\cos^2\theta - 8E_{\text{tag}}E_{\text{probe}}p_{\text{tag}}p_{\text{probe}}\cos\theta \\ &= 4\left[E_{\text{tag}}^2(m_{\text{probe}}^2 + p_{\text{probe}}^2) - p_{\text{probe}}^2p_{\text{tag}}^2\cos^2\theta - \Delta m^2 p_{\text{probe}}p_{\text{tag}}\cos\theta\right], \end{aligned} \tag{8.5}$$

where $\Delta m^2 = m^2 - m_{\text{probe}}^2 - m_{\text{tag}}^2$ (in the second line Eq. 8.4 was used again to rewrite $E_{\text{tag}}E_{\text{probe}}$). This allows to express the momentum of the probe, p_{probe}, as

$$\begin{aligned} p_{\text{probe}} &= \frac{-b \pm \sqrt{b^2 - 4ac}}{2a} \\ a &= 4\left(E_{\text{tag}}^2 - p_{\text{tag}}^2\cos^2\theta\right) \\ b &= -4p_{\text{tag}}\Delta m^2\cos\theta \\ c &= 4E_{\text{tag}}^2m_{\text{probe}}^2 - \left(\Delta m^2\right)^2. \end{aligned} \tag{8.6}$$

Out of the two solutions given by Eq. 8.6, one is often unphysical. If both solutions are positive, one is often chosen randomly, unless other (kinematic) constraints are available. If the candidate decay is reconstructed only partially, as in $D^0 \to K^-\pi^+\pi^-\pi^+\pi^0$ decays, and, to a lesser extent, in $J/\psi \to \mu^+\mu^-\gamma$ decays, the mass constraint will overestimate the probe's momentum due to the missing particle.

The decay topology not only provides momentum information, but also allows to distinguish between muons, electrons, pions, and fake tracks. For example, in $B^+ \to J/\psi(\to \mu^+\mu^-)K^+$ decays, the J/ψ-constrained B^+ mass can be used to ensure that the VELO track corresponds to a genuine muon.

The signal-to-noise ratio in a selection based only on the mass-constrained momentum information is poor. Additional information is used to reject most of the low-momentum background. The D^0 and B^+ candidates are required to have a significant flight distance with respect to its associated primary vertex. The momentum of the

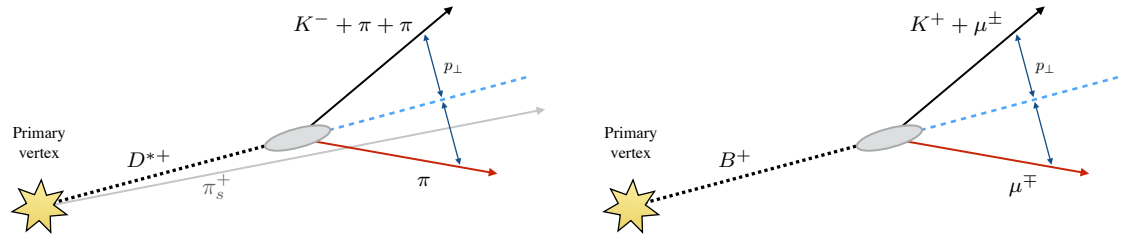

Figure 8.2: Schematic of the vertex constraint used to infer the momentum of the VELO track (in red) in (left) $D^{*+} \to D^0(\to K^-\pi^+\pi^+\pi^-)\pi^+$ decays and (right) $B^+ \to J/\psi\,(\to \mu^+\mu^-)K^+$ decays. The pion directly originating from the D^{*+} decay is denoted by π_s^+.

probe can also be inferred from this flight direction alone, associating all missing momentum transverse to the flight direction to the probe particle:

$$\sum \vec{p}_{\text{tag}} \times \hat{d}_{\text{f}} = -\vec{p}_{\text{probe}} \times \hat{d}_{\text{f}}, \tag{8.7}$$

where $\hat{d}_{\text{f}}$ denotes the normalised flight-direction vector. This constraint is known as the "(primary) vertex constraint"[3], and is illustrated in Fig. 8.2. The momentum inferred by the vertex constraint alone is less precise than the mass constraint, as shown in Fig. 8.3. However, the estimated momentum does not assume any mass for the J/ψ or D^0, and is an effective tool in the selection of signal candidates to keep the background to an acceptable level. Moreover, in case of partially reconstructed backgrounds, only the transverse component of the missing particle's momentum is incorrectly assigned to the probe particle. In addition, the vertex constraint helps to select one of the two solutions in Eq. 8.6.

The spread in the reconstructed momentum with the vertex constraint is mainly due to the resolution of the D^0 or B^+ decay-vertex position. This error is approximately constant as a function of the D^0 or B^+ flight distance. Consequently, by selecting decays with a significant flight distance, the relative uncertainty of the vertex position decreases. The right panel of Fig. 8.3, which shows the momentum resolution as a function of the flight distance, confirms this hypothesis. Therefore, the D^0 or B^+ candidates are required to have a minimal flight distance. Further improvements of the vertex resolution can be obtained considering multibody decays, e.g. $B^0 \to J/\psi\,(\to \mu^+\mu^-)K^{*0}(\to K^+\pi^-)$ decays. These decays will be considered in future analyses.

[3]This is similar to the corrected mass, defined in Eq. 5.5, but with a well-known flight direction of the probe particle.

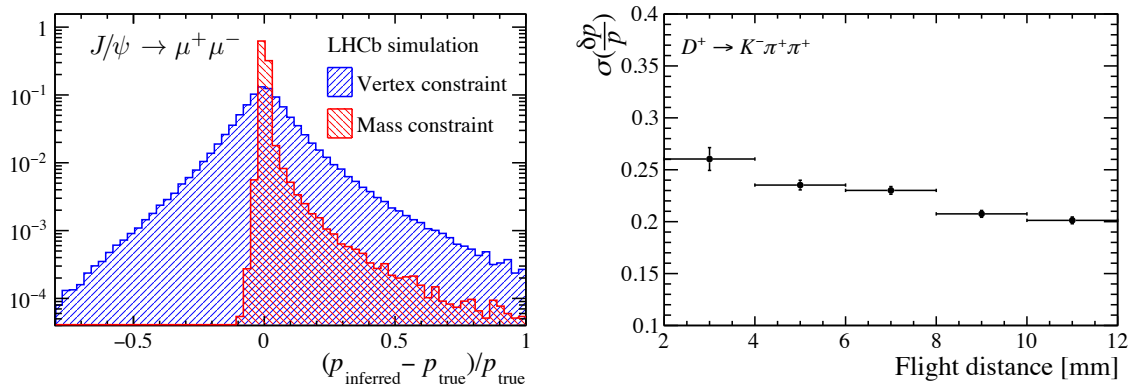

Figure 8.3: (left) Resolution of the momentum inferred from the J/ψ-mass constraint and vertex constraint for simulated $B^+ \to J/\psi(\to \mu^+\mu^-)K^+$ decays. The event selection of the muon-efficiency analysis, later described in Sect. 8.2.2, is applied. The visible tail at higher momenta is due to radiative J/ψ decays, $J/\psi \to \mu^+\mu^-\gamma$. (right) Resolution of the momentum inferred from the vertex constraint, defined as the RMS of the $\frac{\delta p}{p} = \frac{p_{\text{inferred}} - p_{\text{true}}}{p_{\text{true}}}$ distribution, as a function of the flight distance for $D^+ \to K^-\pi^+\pi^+$ decays, using data recorded in 2016. The event selection described in Chapter 7 is applied.

8.2 Measurement of the muon detection efficiency

Because of their minimal energy loss, low collision rate and long lifetime, muons are the most efficient particle species to reconstruct in LHCb. The main cause of a loss in detection efficiency for muons at low transverse momenta, shown in Fig. 8.1, is the loss of low-momentum muons in the dipole magnet. This source of inefficiency was not calibrated for yet in the already existing calibration of the muon *tracking* efficiency [62], while the presented analysis is the first measurement of the complete detection efficiency for muons. In this analysis, the $\mu^\pm$-detection efficiency is determined using $B^+ \to J/\psi(\to \mu^+\mu^-)K^+$ decays. The kaon and one of the muons tag the decay, while the other is only reconstructed as a VELO track, as shown in Fig. 8.4.

8.2.1 Efficiency definition and contribution of ghost tracks

Not all reconstructed tracks correspond to genuine particle trajectories. Among the tracks are ghosts, tracks accidentally composed of unrelated hits. A fraction of the ghost tracks are formed by incorrectly combining genuine tracks in the T-stations and hits in the VELO detector, so-called "matching ghosts". For such tracks, the momentum estimate is incorrect and, in some cases, even an incorrect charge is associated to them. Ghost tracks contribute to the numerator of Eq. 8.3, and thus lead to a higher inferred track-reconstruction efficiency.

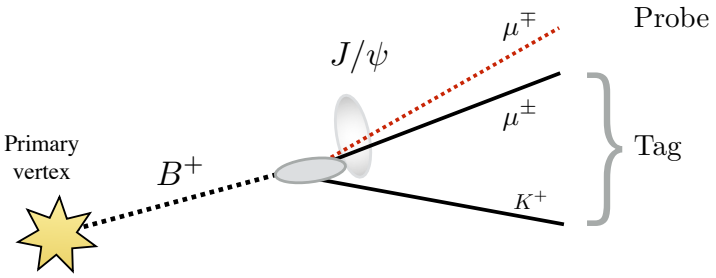

Figure 8.4: Schematic of the $B^+ \to J/\psi(\to \mu^+\mu^-)K^+$ decay, with the role of all particles described.

Whether ghost tracks should be included in the efficiency depends on the physics analysis. In a typical physics analysis, the invariant-mass spectrum is used to separate signal decays from backgrounds. In case the track is reconstructed incorrectly, the candidate is often absorbed in the random-track background contribution to the invariant-mass distribution, and gets statistically subtracted in the determination of the signal yield. In such cases, the contribution of ghost tracks needs to be removed from the efficiency definition.

Ideally, a similar approach is applied to discriminate between ghosts and correctly reconstructed tracks, and the data set of matched candidates is split based on the $m_{\text{long}}(\mu^+\mu^-)$ (constructed with the long-track information) and the $m(J/\psi\, K^+)$ (constructed with the VELO track information and kinematic constraints) distributions:

- **Correctly reconstructed** candidates are those which peak in $m_{\text{long}}(\mu^+\mu^-)$ and $m(J/\psi\, K^+)$.
- **Ghost tracks** peak in $m(J/\psi\, K^+)$, but are considered background in $m_{\text{long}}(\mu^+\mu^-)$.
- **Background** candidates are absorbed in the random-track background component in both $m_{\text{long}}(\mu^+\mu^-)$ and $m(J/\psi\, K^+)$.

Ideally, candidates which are counted as backgrounds in physics analyses are subtracted, by performing a fit to the $_{\text{long}}(\mu^+\mu^-)$ distribution as well. However, since the background of ghosts in $J/\psi \to \mu^+\mu^-$ decays is small, the ghost-corrected efficiency, $\varepsilon(\text{long}|\text{VELO})$, can be approximated. A comparison between the reconstructed momentum of the matched long track, p_{long}, and that inferred from the decay topology is used as a measure of reconstruction quality in this approximation,

$$\varepsilon(\text{long}|\text{VELO}) = \frac{N\,(\exists \text{ matched long track with } |\delta p/p_{\text{inferred}}| < 0.2 \text{ \& right charge})}{N\,(\text{reconstructed as VELO track})}, \quad (8.8)$$

where $\delta p = p_{\text{long}} - p_{\text{inferred}}$. Because p_{inferred} is determined using the J/ψ mass constraint, effectively all candidates are accepted with $m_{\text{long}}(\mu^+\mu^-)$ within $300\,\text{MeV}/c^2$ of the J/ψ

mass. The inferred efficiency is stable under changes of the seemingly arbitrarily chosen tolerance of a 20% difference in the reconstructed and inferred momentum. As a future analysis would apply a fit to the $m_{\text{long}}(\mu^+\mu^-)$ distribution, no additional effort is taken to optimise this requirement.

8.2.2 Data selection

The analysis of the muon efficiency uses all proton-proton data collected by LHCb in 2017, corresponding to $1.7\,\text{fb}^{-1}$ of integrated luminosity. In the online event reconstruction, information downstream of the magnet is used in both the hardware- and software triggers. For an unbiased measurement of the detection efficiency, it is therefore crucial that all events are triggered independently of the probe particle. Therefore, the events used for the efficiency determination are selected based on the tag particles only. This is achieved by making use of the inclusive topological trigger (Sect. 2.3) of HLT2, and of the single-track triggers in all other trigger stages.

In the event selection, the B^+ candidates are formed by combining reconstructed $K^+\mu^\mp$-pairs with a VELO track. Both tag and probe tracks are required to have a significant IP with respect to any PV. The muon is required to have a significant transverse momentum, $p_{\text{T}} > 1.2\,\text{GeV}/c$, and pass stringent PID requirements. A similarly stringent PID selection is applied to the kaon, along with $p_{\text{T}} > 500\,\text{MeV}/c$. The mass of the $K^+\mu^\mp$ tag combination must be smaller than $5000\,\text{MeV}/c^2$ to reject random-track backgrounds. To optimise the momentum resolution inferred from the vertex constraint, the reconstructed vertex of the tag and probe combination must be at least 4 mm displaced from the PV.

The expected signal purity achieved with a selection based solely on the individual tracks is poor. Therefore, momentum information is added to the selection based on a simplified version of the J/ψ-mass constraint. The approximation $m^2_{\text{probe}}/p^2_{\text{probe}} \approx 0$ is used, such that $E_{\text{probe}} \approx p_{\text{probe}}$, and Eq. 8.4 reduces to

$$\Delta m^2 \approx 2p_{\text{probe}}\left(E_{\text{tag}} - p_{\text{tag}}\cos\theta\right). \tag{8.9}$$

This yields a value for p_{probe} of

$$p_{\text{probe}} \approx \frac{\Delta m^2}{2\left(E_{\text{tag}} - p_{\text{tag}}\cos\theta\right)}, \tag{8.10}$$

that can then be used to approximate the $J/\psi\,K^+$ invariant mass[4]. This simplified J/ψ-mass-constrained $J/\psi\,K^+$ mass is required to lie between 5000 and $5700\,\text{MeV}/c^2$. Finally, flight direction based on the vertex information, and mass-constrained momentum vector for the B^+, are required to agree well.

[4]Out of the two solutions of Eq. 8.6, this approximation leads to the solution with the highest momentum.

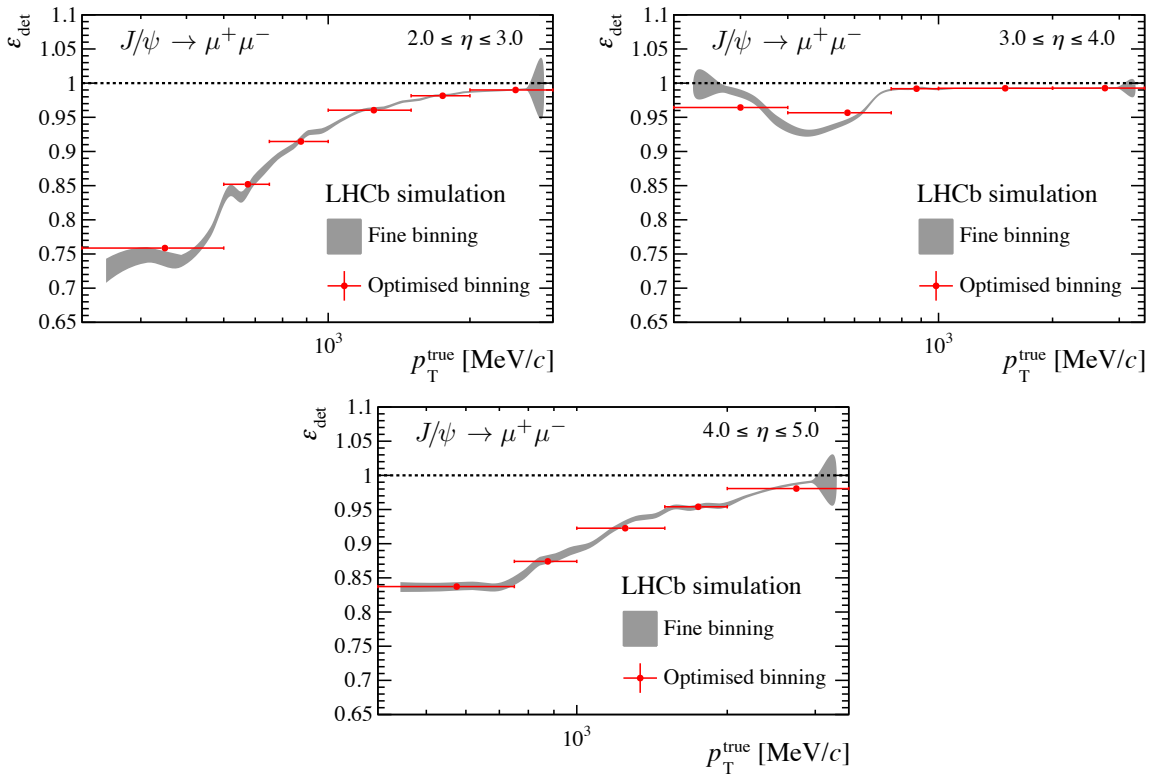

Figure 8.5: Simulated detection efficiency versus p_{T} in the three pseudorapidity bins, parametrised by the optimised binning scheme in p_{T}. Shown errors correspond to the statistical errors of all simulated events of all data sets, thus integrating over magnet polarities and the charge of the probe particle. The statistical errors in data are larger.

8.2.3 Efficiency parametrisation

Simulated events are used to determine the optimal parametrisation of the detection efficiency. These events are generated using the simulation of proton-proton collisions with the Gauss software (Sect. 2.4). The simulated events include the radiative decays of the J/ψ. The efficiency is parametrised as a function of the η and of the inferred p_{T} of the probe particle. The choices of p_{T} bins is done adaptively, optimising for a minimal variation of the simulated efficiency within the bin while still retaining a number of signal candidates for each bin, sufficient to reliably determine the efficiency from data using an invariant-mass fit. The parametrisation presented here is only meant to illustrate the main features of the detection efficiency; for specific physics analyses, weights are to be assigned to each candidate to determine the efficiency for the appropriate region of phase-space.

The resulting bins in p_{T} and η along with the efficiencies estimated from simulation are shown in Fig. 8.5. A finer binning can be used once more data have been collected.

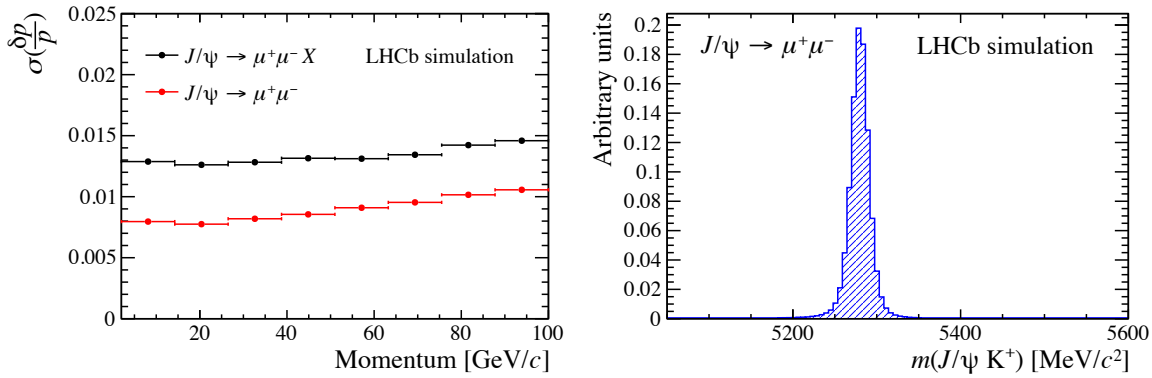

Figure 8.6: (left) Momentum resolution from the J/ψ-mass constraint as a function of the generated momentum of the probe particle in simulated $B^+ \to J/\psi(\to \mu^+\mu^-)K^+$ decays. The red data points were determined considering only candidates for which the generated $\mu^+\mu^-$ invariant mass lies close to the J/ψ mass, $|m_{\mathrm{gen}}(\mu^+\mu^-) - m_{J/\psi}| < 1\,\mathrm{MeV}/c$, thus rejecting radiative decays. The upwards trend is due to the smaller opening angle in the laboratory frame at higher momenta. (right) Distribution of the $J/\psi K^+$ invariant mass, obtained using the probe momentum as determined from the J/ψ-mass constraint.

8.2.4 Momentum resolution

The resolution of the momentum inferred from the J/ψ-mass constraint, introduced in Sect. 8.1, is sufficient for the description of the momentum-dependence of the muon detection efficiency. Figure 8.6 shows the momentum resolution determined from simulated $J/\psi \to \mu^+\mu^-$ events as function of the probe momentum. The momentum resolution varies slightly, but is still below 1.5% for high momenta, even when including radiative decays, $J/\psi \to \mu^+\mu^-\gamma$. The systematic uncertainty in the muon efficiency due to the momentum resolution is negligible. The B^+ mass distribution is shown in the right panel of Fig. 8.6, and provides a clear signature to distinguish the decay from random background.

8.2.5 Efficiency estimation and background rejection

The signal yields for both pass and fail categories are determined using a one-dimensional, binned, maximum-likelihood fit to the $J/\psi K^+$ invariant-mass distribution. An example of the mass distributions for both categories is shown in Fig. 8.7. The fit range is limited to suppress the contribution of partially reconstructed $B \to J/\psi K\pi$ decays. This simplifies the fit to a component for the random-track background, and a component for the B^+ signal. The B^+ shape is modelled using a Gaussian with a power-law tail on each side, and the random background is described using an exponential function. The tail parameters of the signal peak are determined from simulated events. The data

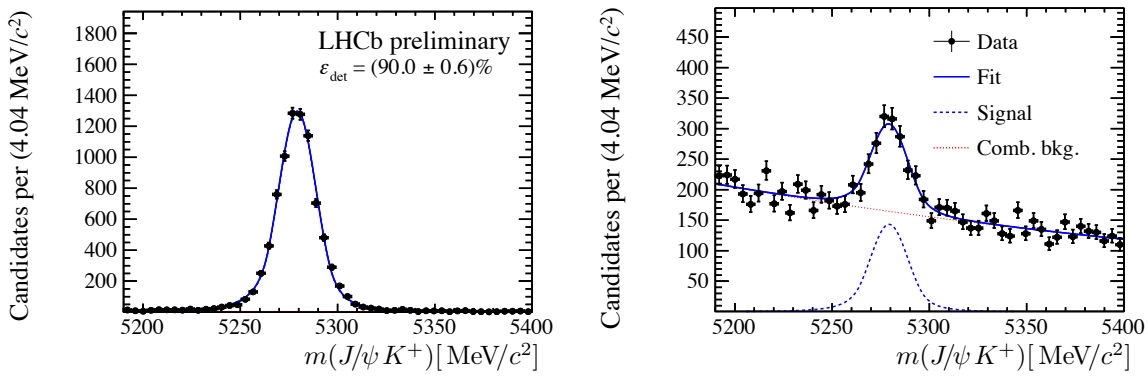

Figure 8.7: Distribution of the $\mu^+\mu^-K^+$ mass, obtained using the probe track's momentum determined from the J/ψ-mass constraint, for the case in which (left) a long track was found with the correct momentum (per Eq. 8.8) and (right) no such long track was found matching the VELO segment. The data shown corresponds to the 2017 magnet up data set, for $2 \leq \eta \leq 3$ and $750 \leq p_{\text{T}} \leq 1000\,\text{MeV}/c$.

sets are split based on the charge of the probe particle, and whether a matching long track was found. The detection asymmetry and charge-averaged detection efficiency are included as parameters in a simultaneous fit to the four categories.

8.2.6 Results

The ghost-corrected detection efficiency, $\varepsilon_{\text{det}}(\text{long}|\text{VELO})$, is determined for each bin of p_{T} and η for each polarity separately, and then combined into a magnet- and charge-averaged efficiency. To make a fair comparison with simulated data, the underlying distributions of p_{T} and η must be similar. The simulated kinematic distributions overlap well with those in data. Nonetheless, per-event weights are applied to the simulated data, ensuring similar underlying η distributions for each bin. The weights vary between 80 and 120%, indicating only small corrections.

Figure 8.8 shows the resulting efficiencies, along with a comparison to the simulated data. In general the simulation overestimates the reconstruction efficiency. This is consistent with results from the *tracking* efficiency calibration in Ref. [62], and part of this result can likely be explained by the different tracking performance between simulated events and data. The measured detection asymmetry is discussed separately at the end of this chapter, in Sect. 8.5.

8.2.7 Measurement of ghost fraction

The distinction between well-reconstructed tracks and misreconstructed long tracks, Eq. 8.8, allows for a definition of an effective, conditional ghost fraction as well (condi-

tional on being reconstructed as VELO track). Using $\delta p = p_{\text{long}} - p_{\text{inferred}}$ to compare the reconstructed momentum to that inferred from the decay topology, this fraction is defined as

$$g_{\text{eff}}(\text{long}|\text{VELO}) = \frac{N\,(\text{matched long track with } |\delta p/p_{\text{inferred}}| > 0.2 \text{ or wrong charge})}{N\,(\text{reconstructed as VELO})}. \tag{8.11}$$

As there can be more than one long track associated to a VELO track, this ghost fraction can be larger than unity.

The resulting ghost fractions for simulation and data are shown in Fig. 8.8. The ghost fraction is $\mathcal{O}(2\%)$. Given the limited sample size available, the statistical precision is insufficient to resolve the ghost probability in kinematic bins. In the last bin in pseudorapidity, a higher ghost fraction is observed in data throughout all p_{T} bins. However, data and simulation are compatible with a p-value of 0.13. These results are considered a demonstration of the method.

8.2.8 Method validation using simulation

In the simulated events, the muon detection efficiency can be determined using generator-level information. This allows to validate the method by a closure test. The closure test includes the use of the fit and the use of the inferred momentum, such that the individual systematic uncertainty of both components can be evaluated.

The detection efficiency changes as a function of p_{T} and η. In the comparison between the generator-level information and the measured efficiency, the underlying kinematic distributions must agree well for a sensible comparison. Therefore, per-event weights are assigned to the generator-level data set, such that the generated p_{T}, η and ϕ spectra match those of the inferred kinematics of the VELO track in the selected $B^+ \to J/\psi\, K^+$ decays. Ghosts are rejected by applying the approximation given in Eq. 8.8. Figure 8.9 shows the resulting efficiencies for each bin of p_{T} and η. The agreement between the efficiencies obtained from the presented method and the generator-level information is nearly perfect. The p-values of the compatibility are also shown in the figures.

Note that, regardless of the excellent agreement, any systematic bias in this method is mitigated when only the correction to the simulated data is considered,

$$r = \frac{\varepsilon^{\text{calibration}}_{\text{data}}}{\varepsilon^{\text{calibration}}_{\text{simulation}}}, \tag{8.12}$$

such that the efficiency for candidates in a physics analysis, $\epsilon^{\text{signal}}_{\text{data}}$, is obtained from the simulated efficiency, $\varepsilon^{\text{signal}}_{\text{simulation}}$, as

$$\varepsilon^{\text{signal}}_{\text{data}} = r\,\varepsilon^{\text{signal}}_{\text{simulation}}.$$

This reduces the measurement to a correction to the simulated detector, but allows for its use beyond the statistical reach of this closure test.

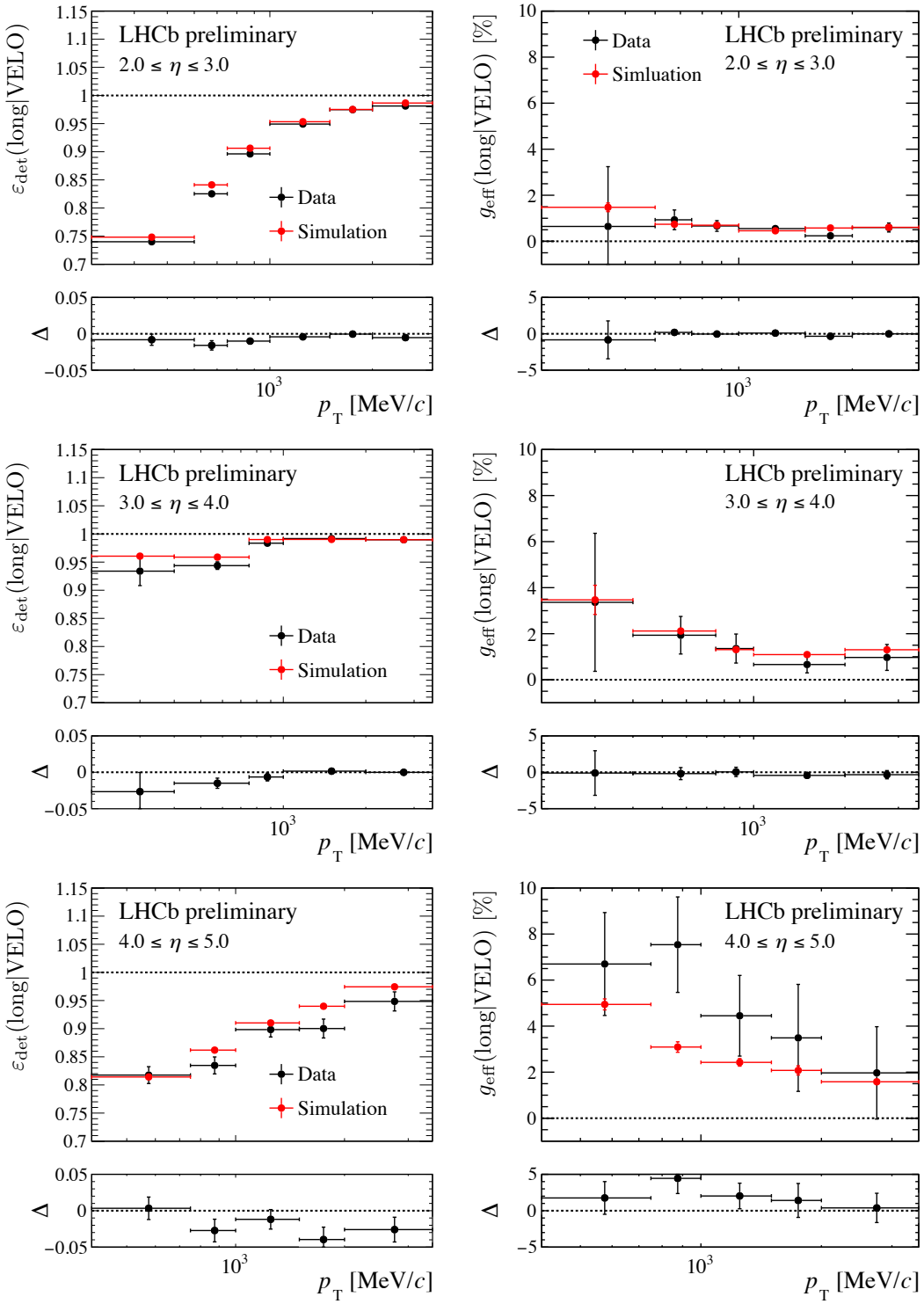

Figure 8.8: (left) Charge-averaged and polarity-averaged muon efficiency as a function of $p_{\rm T}$ and η in data and simulation. Results from simulation are shown in red. (right) Measured ghost fraction for muons reconstructed as a VELO track in bins of $p_{\rm T}$ and η in data and simulation. Results from simulation are shown in red. The difference between the results in data and simulation, Δ, is shown below.

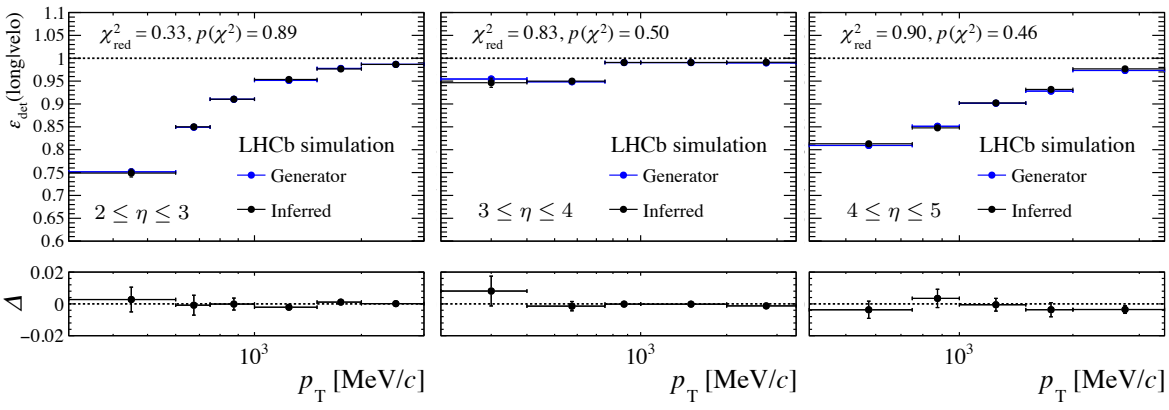

Figure 8.9: Results from the closure test for the muon detection efficiency on simulated data as a function of $p_{\rm T}$ and η. Blue points correspond to the efficiency obtained using the generator-level information. Black points correspond to the inferred efficiency obtained by the full method, including the mass fit. The generated $p_{\rm T}$ is used for the blue points, while the momentum inferred from the J/ψ-mass constraint is used for the black points. Below the differences between the two efficiencies, Δ, are shown.

8.3 Measurement of the electron detection efficiency

Electrons suffer from energy loss via Bremsstrahlung as they traverse the detector material. A particular concern is the energy loss upstream of the dipole magnet, which affects the measurement of the particle's momentum. The left panel of Fig. 8.10 shows the distribution of energy loss for electrons. On average, 30% of the energy is lost before the first T-station is reached for electrons with $\eta \leq 4.0$, and up to an average of 47% for $\eta \geq 4.0$. Part of this energy is recovered by associating clusters in the ECAL with the reconstructed track. However, in some cases the electrons have little energy left as they propagate through the magnet, and are deflected outside of the acceptance. Such electrons are no longer reconstructed as a long track. This is shown in the right panel of Fig. 8.10. The detection efficiency for electrons has to describe not only the performance of the track-reconstruction algorithms for electrons, but also the impact of this acceptance loss.

Thus far, no calibration of the single-track electron detection efficiency exists at LHCb. Tests of lepton universality in $b \to s\ell\ell$ ($\ell = \mu, e$) transitions, as published in e.g. Ref. [78], instead calibrate this efficiency by measuring the ratio of branching fractions $\mathcal{B}(J/\psi \to e^+e^-)/\mathcal{B}(J/\psi \to \mu^+\mu^-)$, which is constrained by external measurements to 0.3% precision [42]. A measurement of the single-track electron efficiency is not only a complementary check to this calibration, but also allows tests of lepton universality in decays with a single electron in the final state, such as $B^0 \to D^+\ell^-\overline{\nu}_\ell$ decays.

The electron detection efficiency is measured with $B^+ \to J/\psi(\to e^+e^-)K^+$ decays, a decay channel similar to that used in the determination of the muon efficiency. While

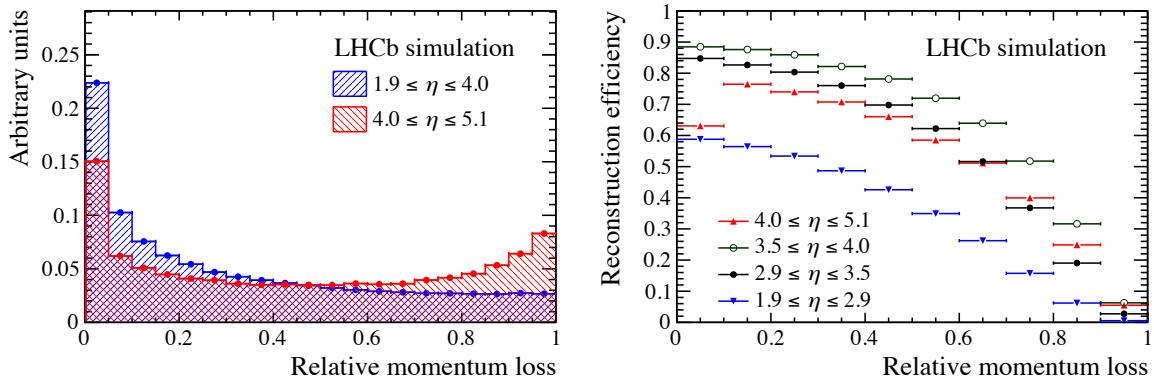

Figure 8.10: (left) Distribution of energy loss for electrons with different η. (right) Electron reconstruction efficiency as a function of momentum loss, as determined from the hit information available in the detector simulation. Both illustrations are made with simulated $D^0 \to K^-e^+\nu_e$ events, generated with ReDecay. The momentum-loss fraction is determined by the relative difference between the particle's momentum at the end of the magnet and the momentum at creation.

the general principle of the method is the same, significant differences arise due to the energy loss of electrons.

8.3.1 Contribution from ghost tracks

The energy loss of electrons leads to a poor momentum resolution for electrons reconstructed as long tracks. For physics analyses, which often restrict to long tracks, this worsened momentum resolution impacts the resolution of the invariant mass, such that it no longer provides a clear distinction between genuine electron trajectories and ghost tracks. No standard treatment exists in the selection of electrons. A selection based on the invariant mass, which is often applied in the event selection for analyses involving other particle species, inevitably also rejects genuine electrons which suffered from significant energy loss. To provide a general performance number, contributions from ghosts are included in the efficiency presented here. However, this definition can be changed when evaluating the efficiency for physics analyses in order to reflect the applied selection criteria which affect the ghost fraction. In the presented efficiency, the only quality requirement for the matched long track is the inferred charge,

$$\varepsilon(\text{long}|\text{VELO}) = \frac{N\left(\exists \text{ matched long track with the right charge}\right)}{N\left(\text{reconstructed as VELO}\right)}. \tag{8.13}$$

8.3.2 Momentum resolution

The J/ψ-mass constraint provides a good estimate of the probe momentum for muons in $J/\psi \to \mu^+\mu^-$ decays. However, the momentum resolution as a result of the J/ψ mass constraint shows a bias towards higher momenta for electrons originating from $J/\psi \to e^+e^-$ decays, as illustrated in Fig. 8.11. This is attributed to the energy loss of the tag electron, which is incorrectly compensated for by assigning a higher momentum to the probe track. Bremsstrahlung is emitted mostly collinear with the electron. This leads to a good estimate of the particle's direction, but not of its momentum. The bias is reduced to a level similar to that achieved for $J/\psi \to \mu^+\mu^-$ decays by also constraining the B^+ mass to its known value [42], while fitting the tag and probe electron momenta simultaneously. The momentum estimate originating from the J/ψ-mass constraint is used as an initial value to this kinematic fit.

The resulting estimate of the probe and tag momenta cannot be used to construct an unbiased distribution of the $e^+e^-K^+$ mass. Instead, to discriminate between genuine $B^+ \to J/\psi K^+$ decays and backgrounds, the J/ψ-constrained B^+ mass is used. To avoid confusion, the two relevant kinematic strategies and their uses are repeated below.

- The momentum estimate from the combined $B^+ + J/\psi$ mass constraints has the best resolution, but is only used in the definition of the kinematic bins.

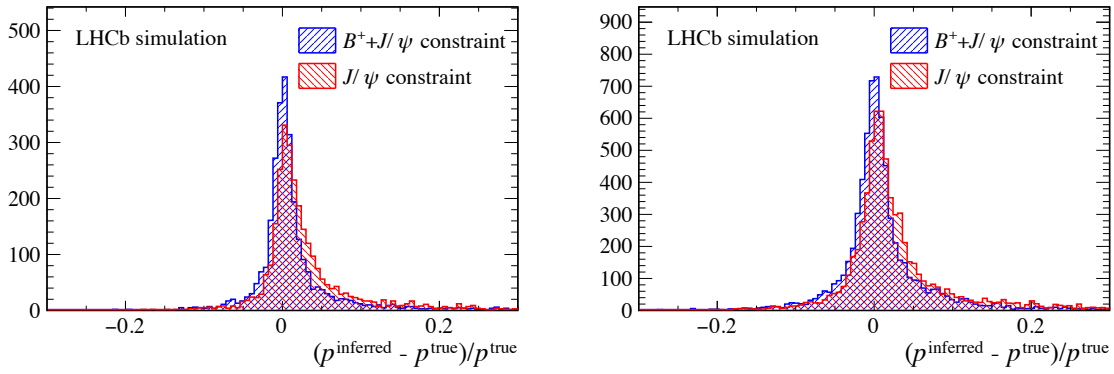

Figure 8.11: Momentum resolution for simulated signal candidates using the J/ψ-mass constraint and applying a subsequent B^+ mass constraint, shown for (left) $p_{\mathrm{T}}^{\mathrm{true}}_{\mathrm{probe}} \leq 3\,\mathrm{GeV}/c$ and (right) $p_{\mathrm{T}}^{\mathrm{true}}_{\mathrm{probe}} \geq 7\,\mathrm{GeV}/c$.

- The momentum estimate from the J/ψ mass constraint is used to construct the $m(J/\psi\,K^+)$ invariant-mass distribution, used to distinguish signal and background.

8.3.3 Data selection

The analysis of the electron efficiency makes use of a dedicated step in the online event selection, introduced in August 2017. Therefore, it uses a subset of proton-proton data collected by LHCb in 2017, corresponding to $1.3\,\mathrm{fb}^{-1}$ of luminosity. The trigger conditions for the events selected in this analyses are chosen carefully to avoid a bias in measured efficiency. Before the events are analysed offline, a positive hardware-trigger decision must be based on the tag electron. This reduces the data set to events in which the tag electron has $p_{\mathrm{T}} \geq 2.5\,\mathrm{GeV}/c$, approximately. The events are subsequently processed by the first-level software trigger, HLT1, where it is required that one of the long tracks (the kaon or tag electron) must pass the stringent trigger requirements. In the last phase of the software trigger, HLT2, a dedicated selection was implemented for this analysis to ensure an unbiased and efficient selection of signal candidates. The selection of the tag kaon and tag electron are similar to that described in Sect. 8.2.2. Also here a simplified J/ψ mass constraint is applied to select candidates based on the inferred $J/\psi\,K^+$ mass. As the electron carries little mass, the approximation $m^2/p^2 \approx 0$ is more accurate than for the muon selection. All tracks must have a significant impact parameter with respect to any primary vertex and the $J/\psi\,K^+$ vertex must be displaced by at least 4 mm from the associated primary vertex.

The J/ψ-mass constraint is insufficient to reject the dominating random-track background. The primary-vertex constraint is used as an independent estimate for the probe's momentum to require $m_{\mathrm{vertex}}(e^+e^-) \geq 1400\,\mathrm{MeV}/c^2$ and $3000 \leq m_{\mathrm{vertex}}(e^+e^-K^+)$

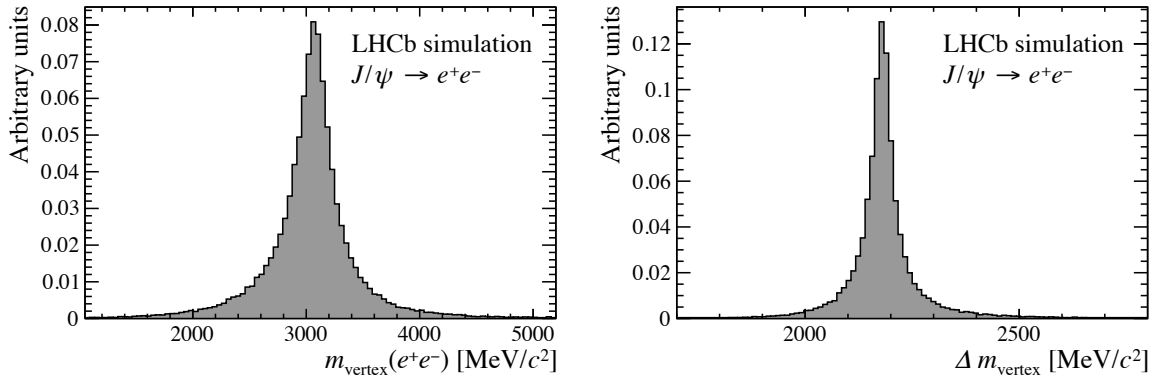

Figure 8.12: (left) Simulated e^+e^- invariant-mass distribution when using the vertex-constraint momentum estimate. (right) Simulated distribution of the mass difference, again using the vertex-constraint momentum estimate.

$\leq 7500\,\text{MeV}/c^2$. While the resolution on these masses is poor, most of the uncertainty cancels when considering the mass difference, $\Delta m_{\text{vertex}} = m_{\text{vertex}}(e^+e^-K^+) - m_{\text{vertex}}(e^+e^-)$, shown in Fig. 8.12. Therefore, the requirement $1500 \leq \Delta m_{\text{vertex}} \leq 3200\,\text{MeV}/c^2$ reduces the contribution from backgrounds even further. The mass windows are chosen broad, such that the distribution of the random-track background in $m(J/\psi\, K^+)$ can be described by a simple analytic function.

8.3.4 Efficiency parametrisation

Motivated by the kinematic dependences of the detection efficiency observed for muons, the electron detection efficiency is measured in bins of p_{T}, η. The bins in p_{T} are chosen adaptively, to account for the data yield. The recovery of Bremsstrahlung by the ECAL is less efficient for $\eta \geq 4.5$ and analyses typically consider electrons only with $\eta \leq 4.5$. Therefore, the electron efficiency is determined only for $\eta \leq 4.5$.

The distribution of detector material is highly non-uniform as a function of η and ϕ. The average radiation length traversed inside the VELO is shown in the left panel of Fig. 8.13. The structure around $\pi/2$ and $-\pi/2$ are due to structures in the RF-foil, which allow for the overlap of the left and the right half of the VELO. This structure is still visible for particles traversing three r and 3 ϕ VELO sensors, which is the requirement for particles to be reconstructible as a VELO track; this is shown in the right panel of Fig. 8.13. The data sample is therefore split in two bins of the VELO track's azimuthal angle as follows:

- **RF-foil region**: $|\phi - \pi/2| < \pi/8$, or, $|\phi + \pi/2| < \pi/8$,
- **Non-RF-foil region**: The remaining phase space.

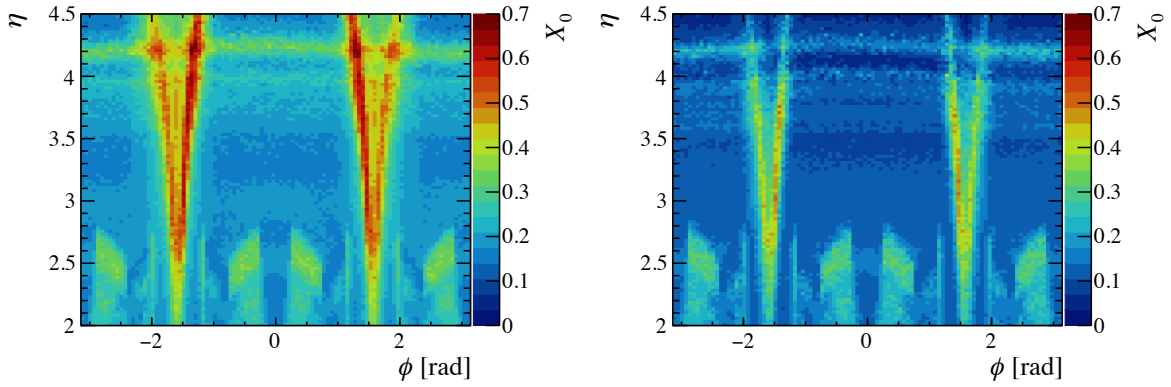

Figure 8.13: Distribution of the radiation length (displayed on the z-axis), X_0, as a function of η and ϕ for muons in simulated $J/\psi \to \mu^+\mu^-$ events. Only the detector material inside the VELO detector is considered. The left panel shows the all encountered material, from the decay vertex onwards, and the right panel shows only the material downstream of the third r or ϕ sensor traversed.

For both regions in ϕ, the same binning in p_{T} and η is used.

The resulting bins in p_{T} and η along with the efficiencies (combining the two bins in ϕ) from simulation are shown in Fig. 8.14. In comparison to the simulated efficiencies for muons, electrons show a lower efficiency at low p_{T} for all bins in pseudorapidity.

8.3.5 Efficiency estimation and background rejection

The signal yields for both pass and fail categories are determined using an unbinned maximum-likelihood fit to the $J/\psi K^+$ mass. The mass distributions for both categories are shown in Fig. 8.15. Partially reconstructed decays of the type $B \to J/\psi K\pi$ are included in the mass window and modelled using an Argus function, convoluted with a resolution function. The signal is described by a Gaussian with power-law tails on each side. Shape parameters for the signal model are determined from simulated events for each kinematic bin separately, and fixed in the fit to the data, except from the width and mean of the Gaussian core. The random-track background is modelled with a second-degree polynomial function, motivated by the shape in the long-matched wrong-sign data (i.e. $B^+ \to J/\psi(\to e^\pm e^\pm)K^+$ candidates). The fit is also shown in Fig. 8.15. The fit is repeated for each kinematic bin. The efficiency is included as a parameter in the fit, such that its statistical uncertainty is determined directly from a simultaneous fit to the pass and fail data.

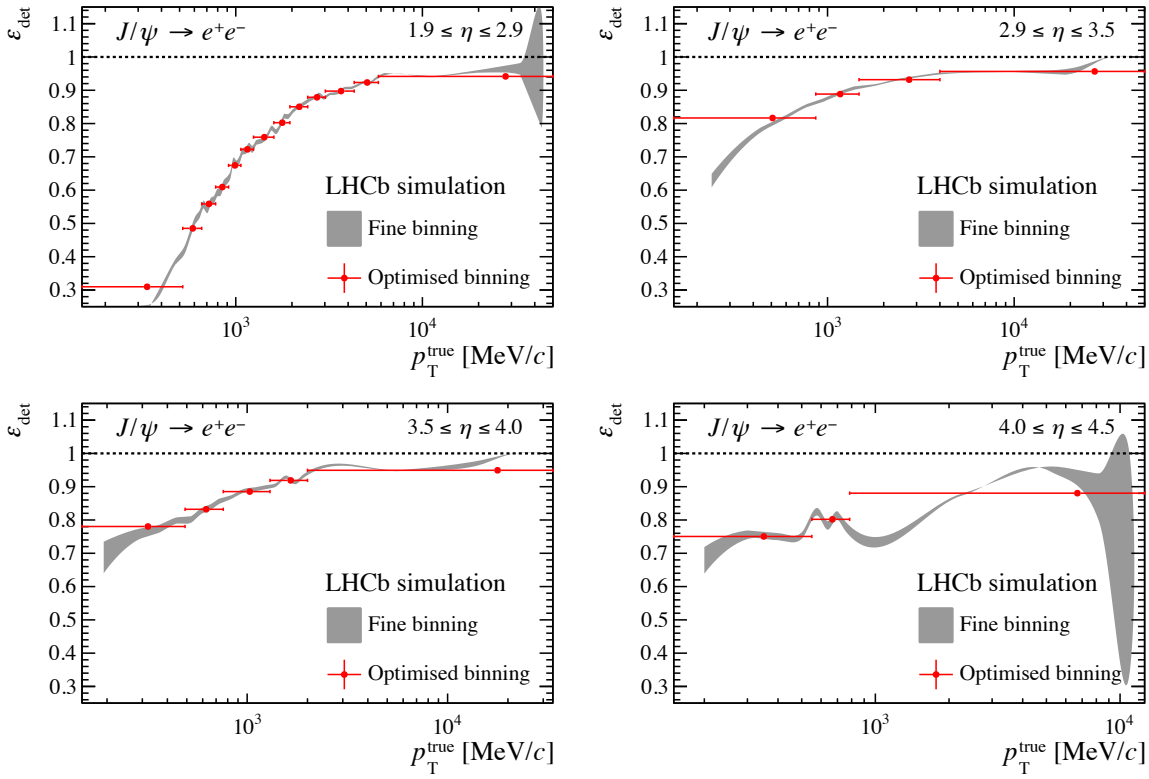

Figure 8.14: Simulated electron detection efficiency versus $p_{\rm T}$, overlaid with the chosen, optimised binning scheme for the four pseudorapidity bins. The error bars correspond to the statistical errors of simulated events of the total simulated data set (combining both magnet polarities). The statistical errors in data are larger. Candidates from both ϕ bins have been added.

8.3.6 Results

The inferred efficiencies in different kinematic regions from simulated events and 2017 data are shown in Figs. 8.16 and 8.17. The measured data efficiency is compared to the simulation through the ratio between the two results, also shown in the figures, where the uncertainties are statistical only. Differences are visible at low pseudorapidity, and are larger than observed for the muon efficiency. No dependence on the ϕ bin is observed for the differences between data and simulation, even though more material is traversed in the RF-foil bin. This behaviour might seem counterintuitive, as more energy loss (and thus efficiency loss) is expected when more material is traversed. The observed similarity in efficiencies is understood as the result of the acceptance, as particles traveling through the RF-foil are more rarely deflected out of acceptance by the magnet, which is one of the main losses of efficiency for the electrons in the other ϕ bin.

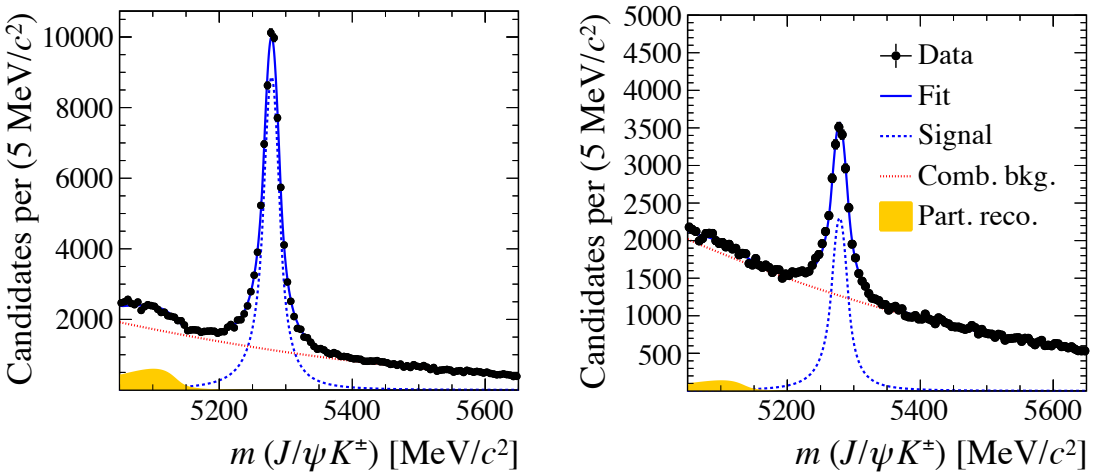

Figure 8.15: Distribution of the $J/\psi K^+$ invariant mass, where the probe particle momentum is inferred from the J/ψ mass constraint. The data shown correspond to the full 2017 data set, with (left) the candidates for which a long track was found and (right) the candidates where no suitable long track was found.

8.3.7 Method validation using simulation

The method is partially validated by comparing the measured efficiencies to those determined from the generator-level information. Ghost tracks, which are included in $\varepsilon_{\text{det}}(\text{match}|\text{VELO})$, are anyways expected to increase the measured efficiency. Systematic effects due to ghosts are separated from those due to the method itself by changing the matching criterion. The downstream segment of the matched track is required to originate from the sought-for electron, by requiring that 70% of the hits in the T-stations were due to the generated particle (note that this information is only available in simulated events). In this way, nearly all contribution from ghost tracks is removed from the matching efficiency.

The results from the validation are shown in Figs. 8.18 and 8.19 for the two regions of ϕ. Differences in the kinematic distributions of the electrons are eliminated by only considering the same events, based on a matching of considered simulated run and event numbers. Differences up to 2% are visible, in particular at higher pseudorapidity, for both bins in ϕ. The discrepancy is attributed to the imperfection of the matching criterion. These differences are used as a systematic error on the inferred electron efficiency for now. Efforts are being made to lower these systematic errors.

The systematic error determined in this chapter does not necessarily propagate directly to a systematic error in a physics analysis which makes use of this calibration. For a suitable correction to data, only the differences with respect to the detector simulation can be considered, as introduced in Eq. 8.12. The systematic errors are expected to be

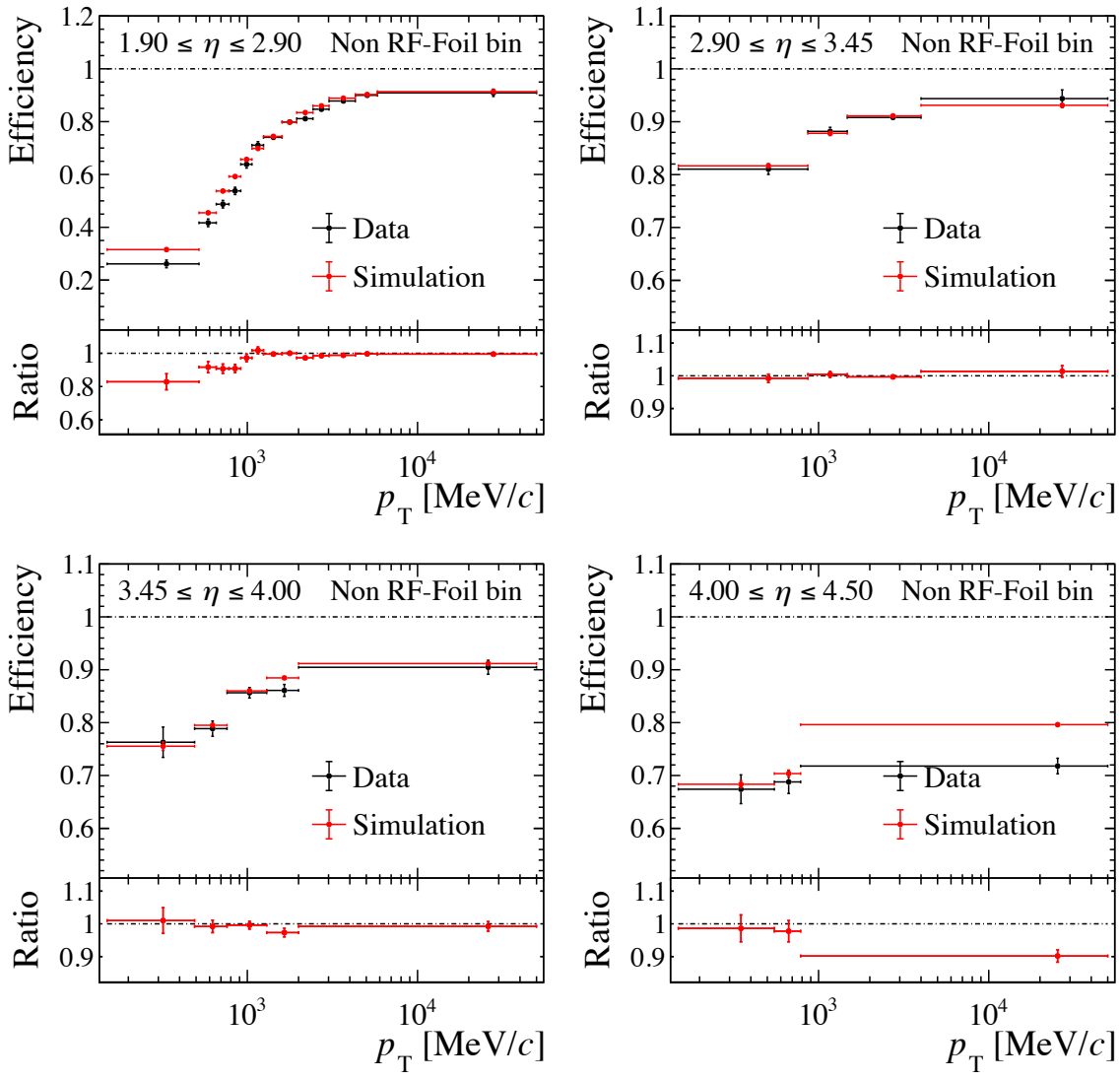

Figure 8.16: Measured electron detection efficiency in each p_{T}, η bin in data and simulation, for electrons which do not fall into the RF-foil bin. Below the ratios between the results from data and simulation for each bin are shown.

mitigated in this ratio. However, even a conservative systematic error of 2% is currently not limiting for the application in tests of lepton universality in $b \to s\ell^+\ell^-$ decays [78].

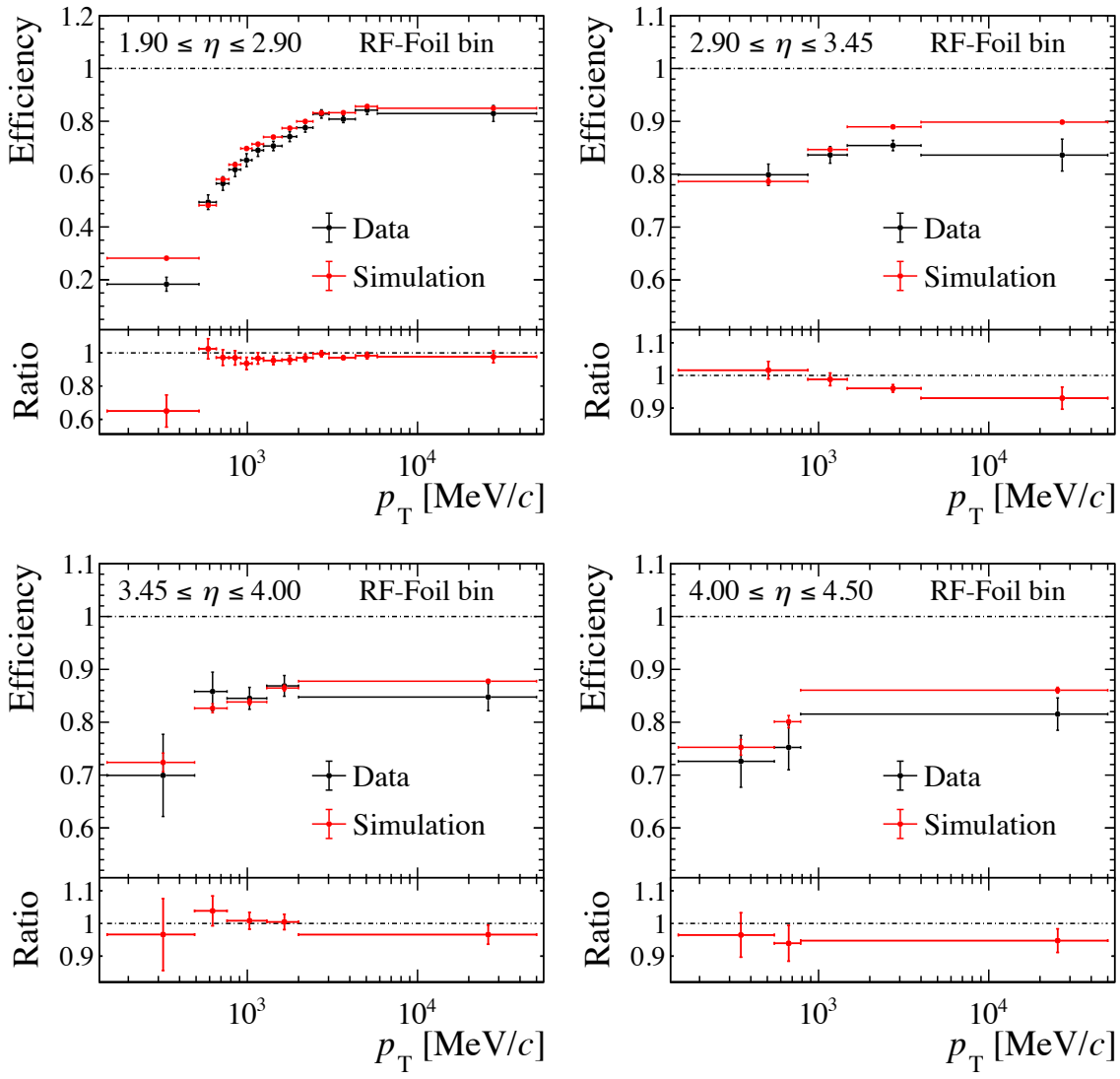

Figure 8.17: Measured electron detection efficiency in each p_{T}, η bin in data and simulation, for electrons which fall into the RF-foil bin. Also shown are the ratios between the results from data and simulation for each bin.

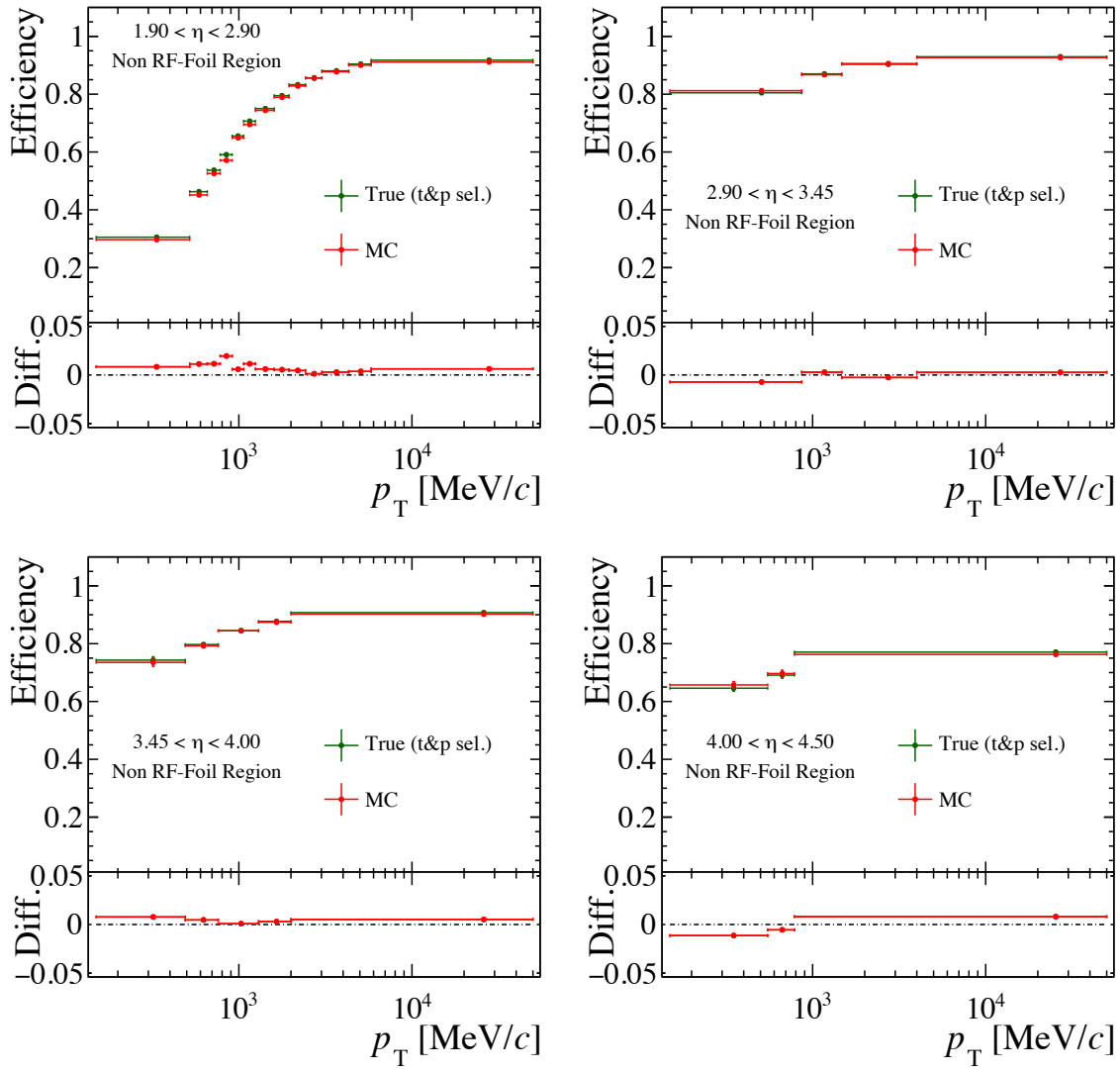

Figure 8.18: Comparison of the simulated detection efficiency obtained from the tag-and-probe method with that obtained from the generator-level information, for probe electrons which fall outside the RF-foil ϕ region.

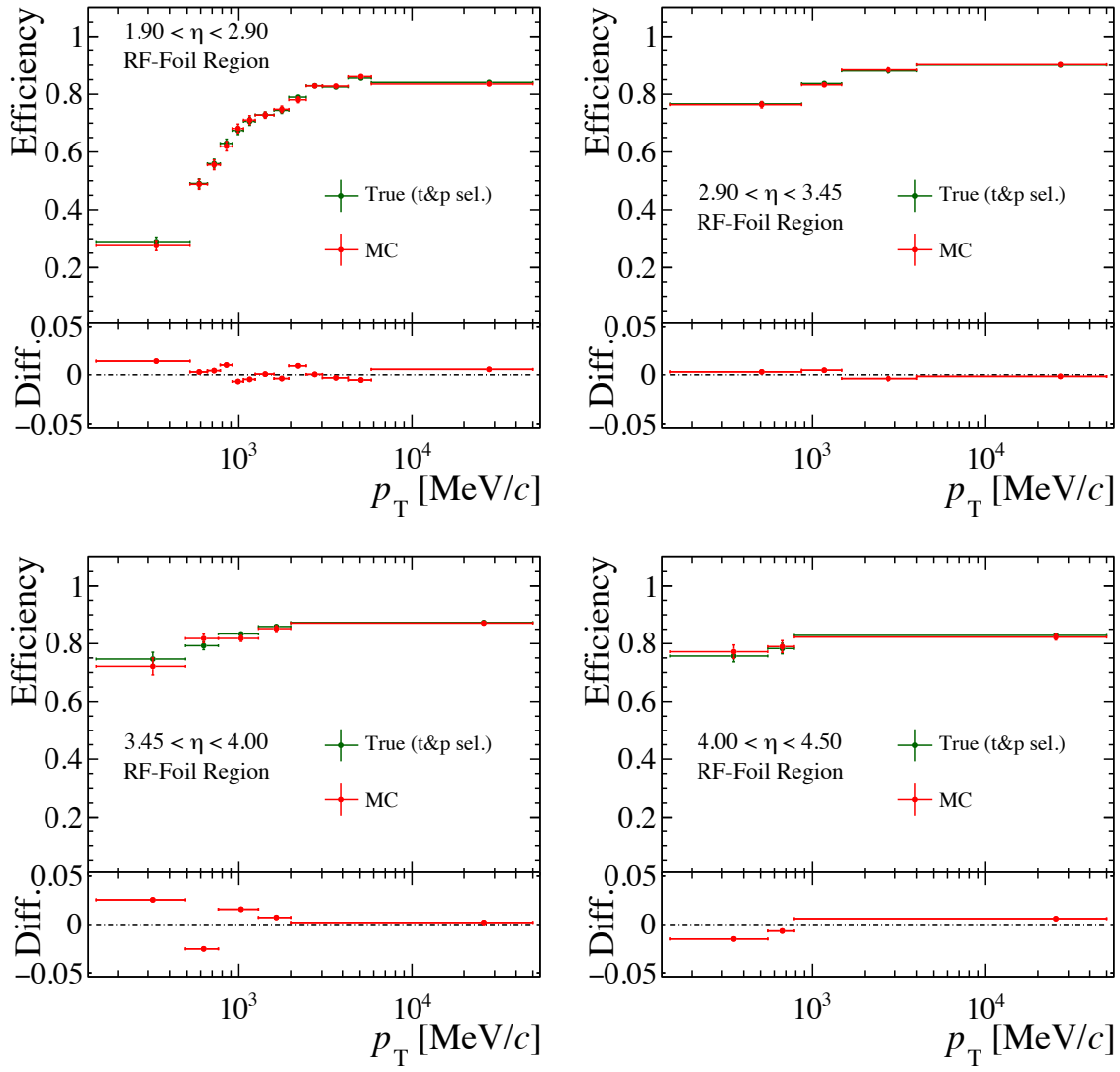

Figure 8.19: Comparison of the simulated detection efficiency obtained from the tag-and-probe method with that obtained from the generator-level information, for probe electrons which fall inside the RF-foil ϕ region.

8.4 Measurement of the pion detection efficiency

While the mass of the pion is similar to that of the muon, the detection efficiency of pions is different because of their hadronic interactions. For most physics analyses, the impact of hadronic interactions is estimated through simulation. The relative uncertainty of approximately 10% on the simulated material budget introduces a systematic error for all branching-fraction measurements involving pions [62]. To estimate this systematic error, the percentage of pions that undergoes a collision before the last T-station is usually conservatively approximated as 20%. Combined with the 10% uncertainty on the material budget, this results in a 2% uncertainty in the pion detection efficiency. The first determination of the pion detection efficiency in the LHCb detector [79] was performed using the ratio of branching fractions $\mathcal{B}\left(D^0 \to K^-\pi^+\pi^+\pi^-\right)/\mathcal{B}\left(D^0 \to K^-\pi^+\right)$ (measured precisely by the CLEO collaboration [80]), with a precision of 2%, similar to that obtained from the detector simulation.

This section presents a novel measurement of the pion detection efficiency using prompt $D^{*+} \to D^0 \to (K^-\pi^+\pi^+\pi^-)\pi^+$ decays with one partially reconstructed track, with the use of the same strategy used throughout this chapter, i.e. the use of kinematic constrained VELO tracks. One of the pions originating from the D^0 decay is reconstructed as a VELO track, while all other particles are reconstructed as long tracks; using the D^0 mass constraint, the invariant mass, $m(D^0\pi^+)$, is calculated and its distribution is used to discriminate signal and backgrounds. However, unlike the $J/\psi \to \mu^+\mu^-$ decays, this analysis is more prone to partially reconstructed backgrounds from other D^0 decay modes, which have a non-trivial structure in the $m(D^0\pi^+)$ distribution. To reduce such backgrounds, stringent selection criteria had to be applied. Nonetheless, due to the abundant production of charm hadrons in $\sqrt{s} = 13\,\text{TeV}$ proton-proton collisions, sufficient signal candidates are retained for a precise measurement of the detection efficiency The simulation of a comparable number of signal candidates is demanding task, as the selection efficiency is low, $\mathcal{O}(0.5\%)$. Unlike the analysis of the electron and muon detection efficiencies, this analysis uses only simulation samples generated with the Particle-Gun method.

The goal of this analysis is to calibrate the pion detection efficiency with an uncertainty below 1%, and calibrate the detection asymmetry with a precision of 10^{-3}. The aim of this section is to explain the concepts of this calibration, and provide an expected precision for Run-2 data.

8.4.1 Efficiency definition and ghost tracks

In cases where a pion scatters inelastically, hits generated by the decay products can still be used to reconstruct a long track which matches the original VELO track. The resulting kinks in the reconstructed trajectory affect the measurement of the momentum

for the long track. A similar effect occurs in cases where the hadron scatters elastically, as the diffraction angle for hadronic elastic scattering is relatively large (see Appendix A). Therefore, the momentum estimate of the matched long tracks is worse for pions than for muons. The same quality threshold for the reconstructed track is applied as was used as for the muon detection efficiency, i.e.

$$\varepsilon(\text{long}|\text{VELO}) = \frac{N\left(\exists \text{ matched long track with } |\delta p/p_{\text{inferred}}| < 0.2 \text{ \& right charge}\right)}{N\left(\text{reconstructed as VELO}\right)}. \tag{8.14}$$

Tracks whose reconstructed momentum estimate differs over 20%, or have an incorrect charge associated, are counted as ghost tracks.

In physics analyses, the separation between backgrounds and signals is often provided through a fit made to invariant-mass distributions. A similar quality criterion could be applied here, when applying a fit to the distribution of the invariant mass, $m_{\text{long}}(K^-\pi^+\pi^+\pi^-\pi^+)$, reconstructed using the long-track momentum estimates. A combined fit to $m_{\text{long}}(K^-\pi^+\pi^+\pi^-\pi^+)$ and $m(D^0\pi^+)$ then provides a discrimination between ghosts and correctly reconstructed tracks which is similar to analyses. This is a possible future improvement, in view of more detailed studies of the pion detection efficiency.

8.4.2 Data selection

A subset of proton-proton collision data collected by LHCb in 2017, corresponding to $1.3\,\text{fb}^{-1}$ of luminosity, is used for this analysis. The selection of events involves a careful choice of trigger conditions. Due to the coarse transverse segmentation of the hadronic calorimeter, the energy deposited by the probe particle can increase the energy that is measured in the calorimeter and associated to the tag particles. To make sure the event selection is independent of the probe particle, only events that are accepted by the muon hardware trigger are considered, and no use is made of the hadronic triggers. Effectively, this means that events are considered in which another decay produced an energetic muon. This requirement reduces the number of signal events by about 50%.

In the second stage of the software trigger, a dedicated trigger line was implemented to combine three long tracks with a significant IP with respect to any PV and a combined $p_{\text{T}} \geq 2.5\,\text{GeV}/c$ with a VELO track (which also has a significant IP) to form a D^0 candidate. This combination is required to have a minimum flight distance of 4.0 mm, and a vertex-constrained mass between 1415 and $2315\,\text{MeV}/c^2$. The kaon track is required to pass stringent PID requirements to reject the background from other particle species (mostly pions). The D^0 candidate is combined with another long track to form a D^* candidate. The vertex-constrained mass difference, $\Delta m = m_{\text{vertex}}(D^*) - m_{\text{vertex}}(D^0)$ must be less than $225\,\text{MeV}/c^2$ in order to reject most of the random tracks that form a background for the pion from the D^{*+} decay. In the case that more candidates for this pion exist within the same event, while sharing the same D^0 candidate, one D^{*+}

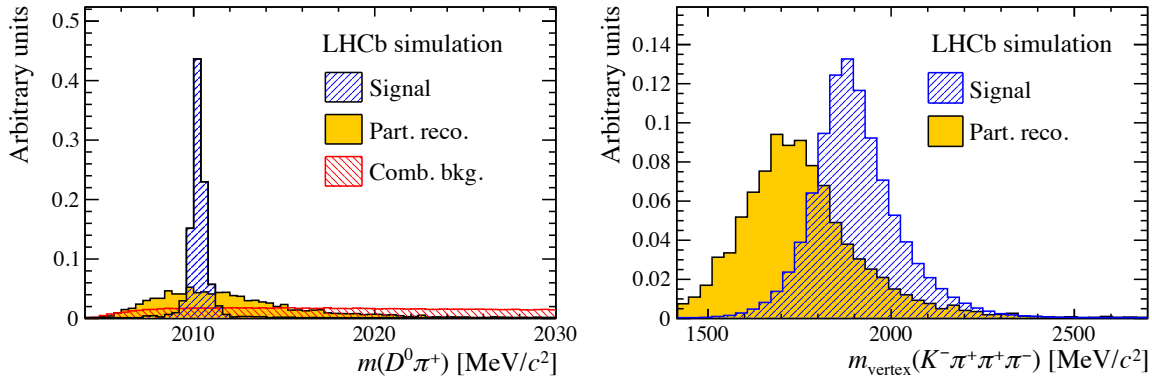

Figure 8.20: (left) Normalised distributions of $m(D^0\pi^+)$ from simulation for partially reconstructed $D^{*+} \to D^0(\to K^-\pi^+\pi^+\pi^-\pi^0)\pi^+$ and fully reconstructed signal events, along with the shape of the random-track background as fitted in data. (right) Distribution of $m_{\text{vertex}}(K^-\pi^+\pi^+\pi^-)$ from simulation for partially reconstructed $D^{*+} \to D^0(\to K^-\pi^+\pi^+\pi^-\pi^0)\pi^+$ and fully reconstructed signal events, when using only the vertex constraint to infer the probe momentum. The offline selection requires $m_{\text{vertex}}(D^0) \geq 1780\,\text{MeV}/c^2$ to reduce the contribution from partially reconstructed decays.

candidate is selected randomly. Finally, a fit to the global decay chain is performed [72] offline, combining the vertex and D^0-mass constraints. Candidates where this fit does not converge are removed from the data set. The resulting estimate for the probe momentum is used to construct an invariant-mass distribution, $m(D^0\pi^+)$, in which the signal is expected to peak around the D^{*+} mass.

The pion detection efficiency depends on the kinematics of the probe pion. The data set is therefore split in bins of the kinematics of the probe, i.e. η and p_{T}.

Partially reconstructed background

Partially reconstructed decays of the type $D^0 \to K^-\pi^+\pi^+\pi^-\pi^0$ happen approximately half as frequent as the sought-for $D^0 \to K^-\pi^-\pi^-\pi^+$ decays [42]. For such mistakenly selected candidates, the D^0-mass constraint overestimates the momentum of the probe track, by incorrectly compensating for the missing π^0 energy and momentum. The D^0 mass inferred from the vertex constraint provides some additional separation between signal decays and this background, as shown in the right panel of Fig. 8.20; therefore, an additional requirement of $m_{\text{vertex}}(D^0) \geq 1780\,\text{MeV}/c^2$ is applied offline, that reduces the yield of genuine signal decays by approximately 15%, while rejecting about 60% of the $D^0 \to K^-\pi^+\pi^+\pi^-\pi^0$ background, according to simulated data.

Misidentified background

Tracks reconstructed with only VELO hits lack PID information. Decays of the type $D^{*+} \to D^0(\to K^-K^+\pi^-\pi^+)\pi^+$ are Cabibbo suppressed, but could still mistakenly be included in the selection. As the $m(D^0\pi^+)$ and $m_{\text{vertex}}(D^0)$ distributions for $D^{*+} \to D^0(\to K^-K^+\pi^+\pi^-)\pi^+$ decays are similar to those for $D^{*+} \to (D^0 \to K^-\pi^+\pi^+\pi^-\pi^0)\pi^+$ decays and the contribution from $D^{*+} \to D^0(\to K^-K^+\pi^+\pi^-)\pi^+$ decays is small, this background is not treated separately.

Signal decays in which at least two hadrons are mistakenly interchanged are suppressed significantly by stringent PID requirements on all final-state particles. The remaining contribution is assumed to be negligible.

8.4.3 Sample composition

The composition of the data sample is further analysed with the help of candidates in which a long track was matched to the VELO track. For these candidates, the long-track momentum is used to construct another, independent, invariant-mass distribution, $m_{\text{long}}(K^-\pi^+\pi^+\pi^-\pi^+)$. A fit to this mass distribution is used to verify that no prominent contribution has been neglected. Nearly all components in this fit are described using shapes from simulation, but the combinatorial-background component is described using decays with the wrong reconstructed charge, $D^0 \to K^-\pi^+\pi^-\pi^-$. The result is shown in Fig. 8.21. In addition to these backgrounds, a component for $D^+ \to K^-\pi^+\pi^-\pi^+\pi^+$ is added, barely visible in the figure; this is absorbed well in the random-pion background in the $m(D^0\pi^+)$ distribution, whose description is then considered sufficiently accurate for this study.

8.4.4 Signal modelling and efficiency determination

Genuine $D^{*+} \to D^0(\to K^-\pi^+\pi^+\pi^-)\pi^+$ decays are discriminated from backgrounds using a binned, maximum-likelihood fit to the D^0-mass-constrained and vertex-constrained D^{*+} mass, $m(D^0\pi^+)$. This distribution is described using three components: the signal, the random-track background, and that of partially reconstructed decays.

As insufficient simulated events are available in which the full proton-proton collision was simulated, the shape of the signal component in the $D^0\pi^+$-mass distribution cannot be determined from simulation. Instead, it is extracted from data, using a signal-enriched selection. This selection restricts to the candidates for which a long track was matched to the probe. Using the momentum information of the long-matched track, the distribution of $m(D^0\pi^+)$ is constructed for mostly genuine signal decays by requiring $1900 \leq m_{\text{long}}(K^-\pi^+\pi^+\pi^-\pi^+) \leq 2200\,\text{MeV}/c^2$, in addition to a PID selection based on the long track information. Figure 8.22 shows an example of the distribution of the D^{*+} mass for candidates which satisfy the signal-enriched selection. Motivated by an earlier

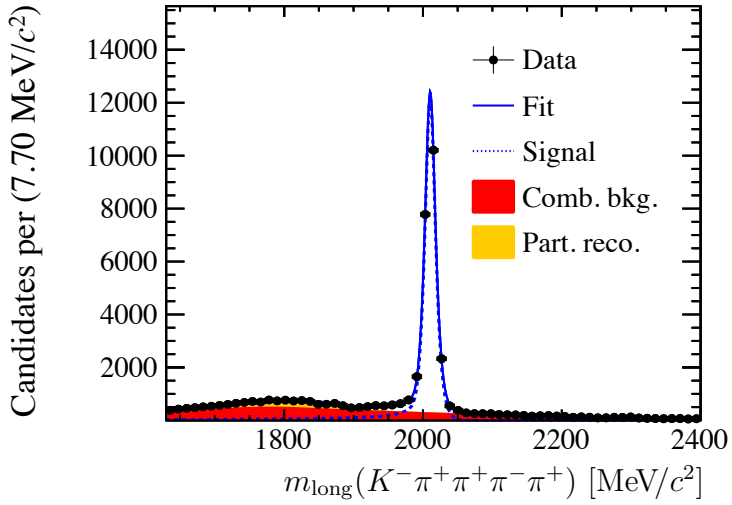

Figure 8.21: Distribution of the $K^-\pi^+\pi^+\pi^-\pi^+$ invariant mass, constructed using the matched long track candidates for candidates where the probe satisfies $2.0 \leq \eta \leq 3.0$ and $1.5 \leq p_{\mathrm{T}} \leq 2.0\,\mathrm{GeV}/c$. Data from both magnet polarities have been added for this figure.

analyses of a similar decay channel [81], the signal shape is empirically modelled using a combination of a Johnson S_U distribution [82] and two Gaussian functions. Similarly motivated, the random-track background is modelled by a threshold function of the form

$$\left(m(D^0\pi^+) - m_0\right)^{\alpha} e^{-b\left(m(D^0\pi^+)-m_0\right)},$$

where the threshold m_0 is fixed to the sum of the D^0 and π^+ mass [42]. The result of the binned maximum likelihood fit to the signal-enriched data set is also shown in Fig. 8.22.

After the shape of the signal component has been determined from the signal-enriched data set, it is used in the fit of the complete data set, which includes candidates for which no long track was found. All parameters of the signal shape, except from the mean, are fixed in the fit to the complete data set. The data sample which determines the signal shape is statistically independent of the data set for which the efficiency is determined, by using the data sample of the opposite magnet polarity for each magnet polarity.

The complete data set not only includes genuine signal decays and a background from random-track combinations, but also partially reconstructed D^0 decays, $D^{*+} \to D^0(\to K^-\pi^+\pi^+\pi^-)\pi^+$. The fit to the $m(D^0\pi^+)$ distribution also requires a model for this contribution. Following the distribution in simulated events, this component is described using a Johnson S_U function, whose parameters are determined by a fit to simulated events. This additional component completes the model of the $m(D^0\pi^+)$ distribution for all candidates.

An example of a fit to the $m(D^0\pi^+)$ distribution is shown in Fig. 8.23. The detection efficiency, $\varepsilon_{\mathrm{det}}(\mathrm{long}|\mathrm{VELO})$, is determined via a simultaneous fit to the candidates in

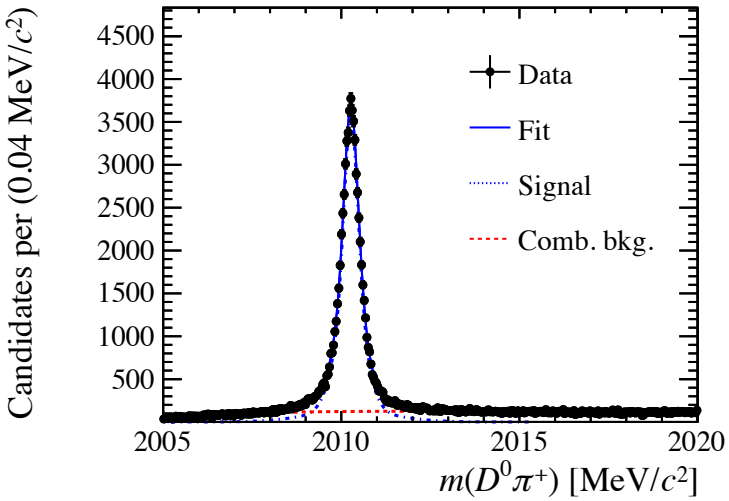

Figure 8.22: Distribution of $m(D^0\pi^+)$ for candidates satisfying the signal-enriched selection based on the long-track information. The data shown corresponds to the data set for which $2 \leq \eta \leq 3$ and $1000 \leq p_{\mathrm{T}} \leq 1500\,\mathrm{MeV}/c$.

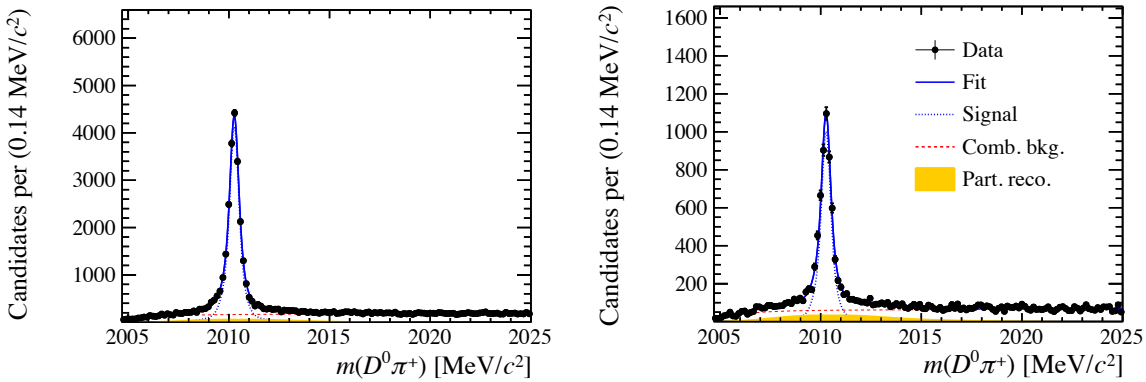

Figure 8.23: Fit to the $m(D^0\pi^+)$ distribution for candidates where (left) a long track was found matching the VELO track and (right) no long track was found matching the VELO track. The probe is required to have a negative charge, and satisfy $2 \leq \eta \leq 3$ and $1000 \leq p_{\mathrm{T}} \leq 1500\,\mathrm{MeV}/c$. Only the data for the magnet down polarity are shown. The same legend applies to both panels.

the pass and fail categories, by including it as a floating parameter in the maximum-likelihood fit. Other floating parameters are those of the combinatorial background (2), the yields of all three components, and the mean of the signal shape.

8.4.5 Results

Figure 8.24 shows the charge-averaged and polarity-averaged detection efficiencies, as a function of p_{T} and in bins of pseudorapidity. At low pseudorapidity and p_{T}, the efficiency is dominated by the geometrical acceptance of the detector as well as the reconstruction efficiency. In particular, the influence of the increased amount of traversed detector material at higher pseudorapidity is visible at lower p_{T}. At higher p_{T} the efficiency "recovers". This is consistent with the expectation from hadronic scattering: at higher momenta the diffraction angle of the scattered particle(s) is smaller and a good track can be reconstructed from the resulting trajectory.

As a cross-check, the efficiencies have been determined separately for the pions with opposite charge of the kaon in the $D^0 \to K^-\pi^+\pi^+\pi^-$ decay. The obtained results are compatible.

Only a fast simulation sample is available for this preliminary study. In these simulated events, the detector occupancy is not representative of that of proton-proton collision data. Despite this shortcoming, a qualitative comparison with simulation can be made. While efficiency losses due to the reconstruction are not well modelled, effects due to hadronic and Coulomb scattering and the geometric acceptance are well described in the fast simulation. The results are shown in Fig. 8.24. The trend agrees well with the results from data. In nearly all bins, the efficiency obtained from the fast simulation is higher than seen in data. This is expected, as the performance of the track reconstruction decreases with an increase of detector occupancy.

The measured effective ghost fraction (as introduced in Eq. 8.11) can be compared to that obtained for muons in Fig. 8.8. The ghost fraction for low-momentum pions is higher than that observed for low-momentum muons. This can be attributed to elastic hadronic scattering, which happens more frequently at low momenta and of which the diffraction angle also increases (see Appendix A).

The statistical uncertainties of the pion detection efficiency varies from $\mathcal{O}(0.1\%)$ for low momenta to $\mathcal{O}(1\%)$ for high momenta. If all systematic uncertainties, including those related to the background modelling, are sufficiently controlled, this method is thus able to significantly reduce the uncertainty of the pion detection efficiency to below the desired 1% level.

Comparison to hadronic cross-sections

The measured pion detection efficiency, at high pseudorapidity, is higher than what is expected from the distribution of the detector material, shown in Fig. 6.5. Note that the total, hadronic cross-section for pions, shown in Fig. 6.6, is approximately constant for $p \geq 15\,\mathrm{GeV}/c$. Following Eq. 6.6, a maximum efficiency of $\exp(-d/\lambda_T) \approx \exp(-0.26) = 0.77$ is expected, while that measured at high p_{T} and η is higher. This behaviour is reproduced also in the simulation, and is attributed to three effects.

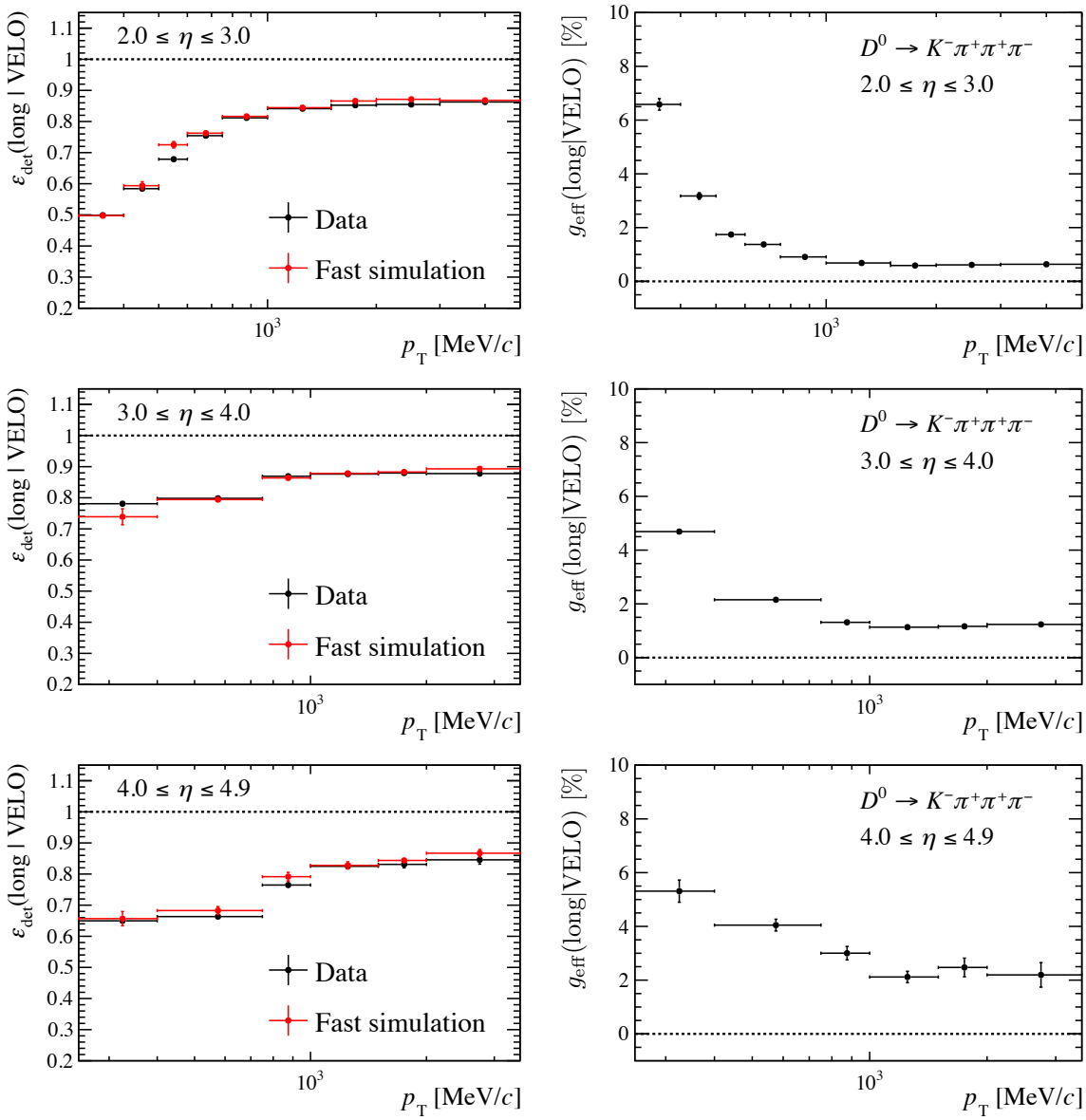

Figure 8.24: (left) Charge-averaged and polarity-averaged pion detection efficiency as a function of $p_{\rm T}$ and η for (in black) data and (in red) simulation. (right) Measured effective ghost fraction for pions reconstructed as a VELO track in bins of $p_{\rm T}$ and η in data.

First, as all other hadrons in the D^0 decay are required to be reconstructed as long tracks, the underlying distribution in pseudorapidity is different from that of the pions in Fig. 6.5. This is the result of the steep increase of the material thickness for $\eta \geq 4.5$, as shown in Fig. 6.5 as well. The correct amount of traversed detector material is therefore determined separately for simulated signal events, making use of the deterministic toy introduced in Sect. 6.1.2. The expected efficiency loss due to the traversed material is shown in the right panel of Fig. 8.25. The observed trend in traversed material agrees with the trend seen in the detection efficiency.

The second effect is inherent to this method. As the efficiency considered requires the reconstruction of a VELO track, it is insensitive to part of the VELO detector material. The material material of the VELO detector forms a significant part of the total material budget. In particular, the RF foil contributes significantly at high pseudorapidity. To make a fair comparison, also the efficiency loss due to traversed material downstream of three traversed VELO r and ϕ sensors, corresponding to the requirement of forming a VELO track, is considered and shown in Fig. 8.25.

The third (and last) effect is due to the fact that the scoring plane for Eq. 6.6 was determined using particles of all momenta. However, the diffraction cone for elastic scattering is expected to decrease with higher p_{T} [83]. Therefore, efficiency losses due to elastic scattering are likely overestimated in Eq. 6.6. Similarly, the secondaries produced in inelastic collisions in the first or second T-station are more likely to follow the original particle's trajectory, such that a long track with the correct momentum estimate can still be reconstructed. A more detailed estimation of the inefficiency due to the detector material requires more detailed studies of these effects, and will be the subject of future studies.

8.5 Detection asymmetry for muons and pions

Once efficiencies are determined as illustrated in the previous sections, detection asymmetries can be calculated according to Eq. 6.1. Electrons are not considered here, as they mainly are of interest for analyses which test lepton universality, but are rarely considered for measurement of *CP* asymmetries. The detection asymmetries for muons and pions determined using $J/\psi \to \mu^+\mu^-$ and $D^0 \to K^-\pi^+\pi^+\pi^-$ decays are shown in Fig. 8.26.

To make a comparison to results from simulation, a large sample of simulated $B^0 \to D^-\mu^+\nu_\mu X$ decays, introduced in Sect. 6.3, is used. As the detection asymmetry depends on the kinematics of the probe particle, differences in the underlying kinematic distributions of the muons and pions between the simulated events and data can spoil this comparison. Such differences are mitigated by assigning per-candidate weights to the simulated candidates which ensure that the underlying $p_{\mathrm{T}}, \eta, \phi$ distributions are similar to those in data. These weights are computed using the same technique

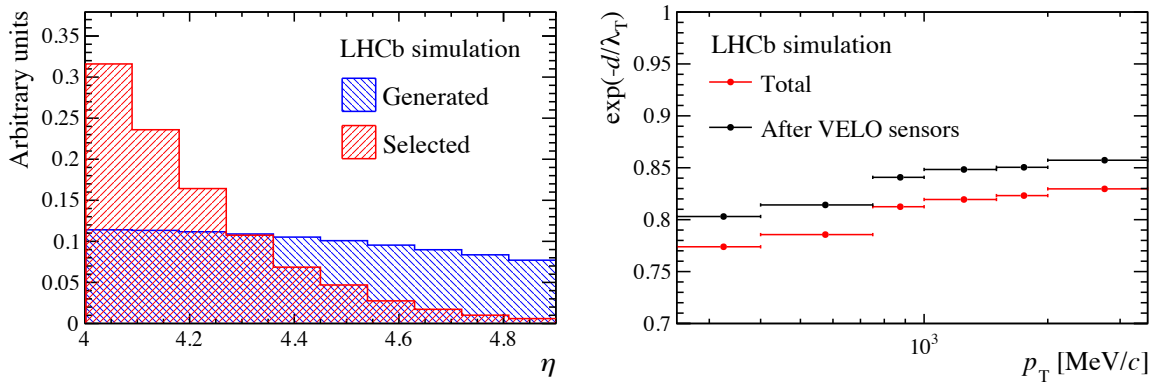

Figure 8.25: (left) Impact on the distribution of the pion's pseudorapidity due to the reconstruction and selection of the other decay products in the $D^{*+} \to D^0(\to K^-\pi^+\pi^+\pi^-)\pi^+$ decay. (right) Simulated detection efficiency due to the traversed material up to, and including, the second T-station (in red) considering all material encountered between the D^0 decay vertex and the second T-station and (in black) considering only the material encountered up to the second T-station after sufficient VELO sensors have been traversed to create a VELO track.

as used throughout Sect. 7.2. Figure 8.26 shows the results from the weighted simulated data set. A deviation from the simulated asymmetries is visible at low momenta. This can partially be attributed to the fact that the detector occupancy differs between simulation and data, while at low momenta, the occupancy-dependent reconstruction asymmetry is expected to dominate (see Sect. 6.3).

In comparison to the study presented in Chapter 6, the current statistical precision of both the pion and muon detection asymmetries does not allow to resolve all features of the detection asymmetry, yet. The statistical precision of the magnet-averaged detection asymmetry for the pion (obtained with a data set of $1.3\,\text{fb}^{-1}$) varies from 0.10% at $15 \leq 25\,\text{GeV}/c$ to 0.28% at $40 \leq p \leq 60\,\text{GeV}/c$, integrated over pseudorapidity. The muon detection asymmetry analysis makes use of a larger data set ($1.7\,\text{fb}^{-1}$), but the statistical uncertainty for the muon detection asymmetry is even larger than for the pions due to the lower production rate of B^+ mesons in comparison to D^{*+} mesons. In particular, the muon asymmetry is less precise at lower momenta, and varies from 0.11% for $15 \leq p \leq 25\,\text{GeV}/c$ to 0.33% for $2 \leq p \leq 5\,\text{GeV}/c$.

As the detection asymmetry depends on η and ϕ as well, the statistical uncertainty due to this calibration will finally depend on the analysed decay channel. As a case study, expectations for a Run-2 measurement of the *CP* violation in B_s^0 mixing, compared with the precision achieved with Run-1 calibrations, are presented in Sect. 9.2.

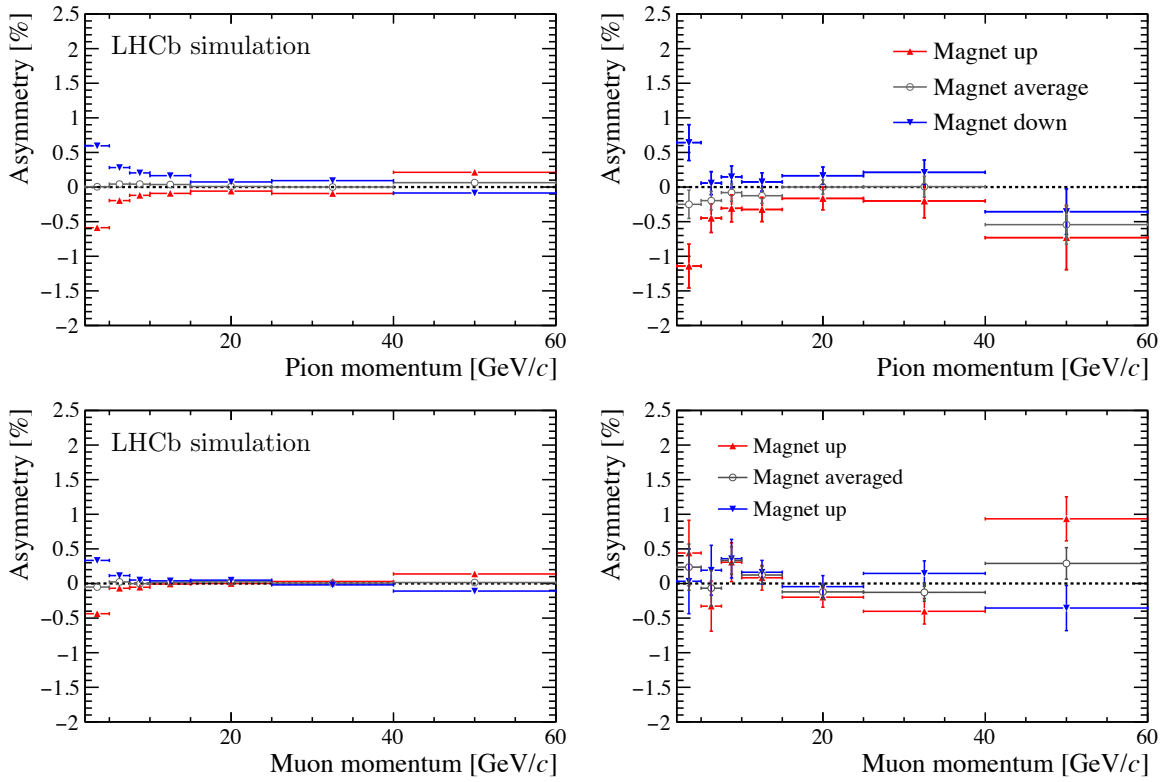

Figure 8.26: Measured detection asymmetry for pions and muons in bins of momentum for (left) simulation and (right) data. Data from all pseudorapidities are added in this plot.

8.6 Prospects for other decay channels

At the time of the present analyses, it was still unclear whether the random-track background could be controlled sufficiently with one of the decay products only reconstructed in the VELO. While decays of the type $D^{*+} \to D^0(\to K^-\pi^+\pi^+\pi^-)\pi^+$ can be discriminated from the random-track background even when one of the D^0 decay products is not reconstructed at all, this does not hold for $B^+ \to J/\psi K^+$ decays. This chapter has shown that the background rejection provided by the vertex-constrained mass and the flight distance requirements is sufficient for this task. This permits the same technique to be applied to other decay modes, which in turns allows to increase the overall statistical precision in the calibration of the detection efficiency and asymmetry. Moreover, additional decay modes provide a useful cross-check. In this section, a short discussion on alternative decay modes is presented.

8.6.1 Calibration of the muon and electron detection efficiency

Starting from 2018, a dedicated selection in the second-level software trigger, HLT2, has been implemented to select decays of the type $B^0 \to J/\psi(\to \ell^+\ell^-)K^*(892)^0(\to K^+\pi^-)$ and $B_s^0 \to J/\psi(\to \ell^+\ell^-)\phi(\to K^-K^+)$ ($\ell = \mu, e$), where again one of the J/ψ decay products is only reconstructed as a VELO track. The presence of an additional track in the decay further reduces the contribution of random-track backgrounds, such that other selection requirements, e.g. the IP requirements, can be relaxed. Unfortunately, the detection efficiency of the additional hadron ($\approx 75\%$), reduces the reconstruction efficiency of these decay modes, in comparison to the $B^+ \to J/\psi(\to \ell^+\ell^-)K^+$ decays considered in the previous sections. Adding these decay channels is therefore expected to approximately double the sample size available for the muon and electron calibrations.

8.6.2 Calibration of the pion detection efficiency

With a branching fraction approximately half the size of $D^{*+} \to D^0(\to K^-\pi^+\pi^+\pi^-)\pi^+$, the decay mode $D^{*+} \to D^0(\to K^-\pi^+)\pi^+$ is an obvious candidate to expand the phase-space coverage of the pion detection efficiency and asymmetry measurements. Decays of this type, where the pion produced in the D^0 decay is reconstructed as a VELO track only, are already selected by the software trigger since early 2016. The number of selected candidates per fb^{-1} is comparable to the $D^{*+} \to D^0(\to K^-\pi^+\pi^+\pi^-)\pi^+$ decay mode, as the reconstruction efficiency of the $D^{*+} \to D^0(\to K^-\pi^+)\pi^+$ decay is higher. The distributions in pseudorapidity of the two decays, shown in the left panel of Fig. 8.27, largely overlap, but they are quite complementary at low and high pseudorapidities. Unfortunately, contributions from mistakenly-selected $D^0 \to K^-\mu^+\nu_\mu$ and $D^0 \to K^-\pi^+\pi^0$ decays complicate the analysis significantly. The mass spectrum as constructed with the long-track information, shown in the right panel of Fig. 8.27, shows that these backgrounds are prominently present among the selected candidates. Like with the partially reconstructed background encountered in Sect. 8.4.2, the $m_{\text{vertex}}(K^-\pi^+\pi^+)$ distribution provides additional signal discrimination, but not enough to reduce the backgrounds to a negligible component. Fitting the $m_{\text{vertex}}(K^-\pi^+\pi^+)$ distribution relies on the correct modelling of the prominent backgrounds, and ideally these models are extracted from data. Because of these complications, the feasibility of this analysis is still under study.

To circumvent the complexity of modelling the partially reconstructed backgrounds, decays of the type $D^+ \to (\overline{K}^0 \to \pi^+\pi^-)\pi^+$ can be considered. In this case, one of the pions in the $\overline{K}^0$ decay is reconstructed as a VELO track, while all other particles are reconstructed as long tracks. Partially reconstructed decays, e.g. $\overline{K}^0 \to \pi^+\pi^-\pi^0$, are phase-space suppressed. By selecting the two-body decay mode, one mostly selects the K_S^0 decay mode. Because the lifetime of the K_S^0 is relatively high, however, the trajectory of the pions is not completely representative for of that of pions produced e.g. in B decays. Therefore, this efficiency can not be applied directly as a correction

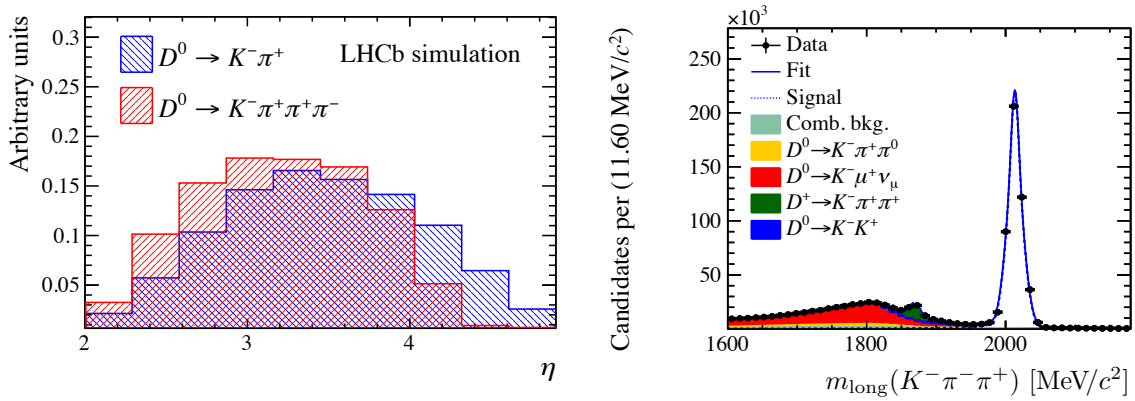

Figure 8.27: (left) Pseudorapidity distribution of the probe pion in simulated $D^{*+} \to D^0(\to K^-\pi^+)\pi^+$ and $D^{*+} \to D^0(\to K^-\pi^+\pi^+\pi^-)\pi^+$ decays, for candidates passing all selection criteria. (right) Invariant-mass distribution of the selected $D^{*+} \to D^0(\to K^-\pi^+)\pi^+$ candidates, constructed using the momentum measurement of the matched long track. A fit to the data is shown as well, to illustrate the prominent backgrounds. The shapes for this fit are determined from simulation. The data sets of both magnet polarities are added. Candidates considered satisfy $3.0 \leq \eta \leq 4.0$ and $1.0 \leq p_{\mathrm{T}} \leq 1.5\,\mathrm{GeV}/c$.

to physics analyses, but can be used to calibrate the simulated detection efficiency, as in Eq. 8.12.

8.6.3 Calibration of the kaon detection efficiency

Partially reconstructed backgrounds, such as $D^0 \to K^-\mu^+\nu_\mu$ and $D^0 \to K^-\pi^+\pi^+\pi^-\pi^0$, complicate the measurement of the pion detection efficiency significantly in comparison to the measurement of the muon detection efficiency in $J/\psi \to \mu^+\mu^-$ decays. Motivated by the simplicity of the $J/\psi \to \mu^+\mu^-$ analysis, a dedicated online event selection was implemented in 2018 to record $D_s^+ \to \phi(\to K^-K^+)\pi^+$ decays, in which one of the kaons is reconstructed as a VELO track. Due to the limited phase-space, no partially reconstructed backgrounds are present in the decay of the ϕ meson, such that the ϕ-mass constraint can safely be used to infer the VELO track's momentum. Although a significant background of $D^+ \to K^-\pi^+\pi^+$ decays is expected, this background does not show any peaking structure in the constrained mass, $m(\phi\pi^+)$, according to simulation. A data sample of $(300 \pm 30)\,\mathrm{pb}^{-1}$ shows that approximately 6 million signal candidates per fb^{-1} are expected. The selection also includes the contribution from the Cabibbo-suppressed $D^+ \to \phi(\to K^-K^+)\pi^+$ decays, which are expected to provide an additional 50% of useable probe tracks. This detection asymmetry will be the first measurement of the single-track kaon asymmetry at LHCb, with a roughly estimated precision of 10^{-3} per fb^{-1}.

8.7 Conclusion

The main concepts and preliminary results for the calibration of the detection efficiency and asymmetry of muons, pions and electrons in Run 2 using a novel technique have been presented. It has been shown that, even without a momentum estimate for one of the tracks, signal decays can be discriminated from the abundant random-track background. A closure test on simulation has shown that the determined efficiencies are unbiased in the case of muons, and show a percent-level bias in the case of electrons. The muon and electron detection efficiencies show a good agreement with simulation, except at low pseudorapidity. This deviation is still under study.

The statistical uncertainty in the pion detection efficiency is much better than the aimed-for 1%. However, the separation between partially reconstructed and genuine decays is challenging, and can limit the overall accuracy of the measured efficiency. These backgrounds are currently reduced significantly in the offline selection. In addition, as more data are collected, the offline selection requirements can be tightened further to mitigate such backgrounds.

Chapter 9

Prospects for high-precision measurements of CP asymmetries

With Run 2 of the LHC, the centre-of-mass energy increased from 8 TeV to 13 TeV, which approximately doubled the production rate of b-hadrons [84]. The calibrations of the detection efficiency and asymmetry presented here have been developed to ensure that measurements of CP asymmetries can benefit from the larger data samples. To quantify these improvements, the statistical uncertainties related to the detection asymmetry are estimated for a measurement of CP violation in mixing for B^0 and B_s^0 mesons using simulated data. In addition, an improvement in the rejection of backgrounds for the measurement of a_{sl}^s is discussed. The chapter concludes with a discussion of the prospects for the detector calibration beyond Run 2 of the LHC, along with an overview of the projected results.

9.1 Prospects for CP violation in $B_s^0 - \overline{B}_s^0$ mixing

To achieve a better precision in a new measurement of a_{sl}^s, improvements related to the main contributions of the uncertainty are most beneficial. All contributions to the uncertainty of a_{sl}^s were presented in Table 5.3. To reduce the main contributions to the overall uncertainty, other decay modes can be added, the contribution from backgrounds can be reduced, and the detector calibration can be improved. The branching fraction of the already considered $D_s^+ \to K^-K^+\pi^+$ decay is high. Therefore, adding other decay modes that can be reconstructed efficiently at LHCb, e.g. $D_s^+ \to \pi^+\pi^-\pi^+$, does not provide more than 25% additional signal candidates. As adding decay modes increases the complexity of the analysis while the gain in statistical precision is relatively small, this option is not discussed in further detail in this thesis, while the two other options are discussed in detail.

9.1.1 Controlling irreducible backgrounds

While the high branching fraction of semileptonic decays is beneficial for the statistical precision of $a^s_{\rm sl}$, the partial reconstruction is prone to backgrounds from other b-hadron decays, as out of all of the B^0_s decay products, only the $D^-_s\mu^+$ pairs are reconstructed. The asymmetry that is measured, $A_{\rm meas}$, is therefore diluted by these backgrounds. Even though the contribution of these backgrounds was already reduced in the event selection in the Run-1 analysis, a residual contribution affected $A_{\rm meas}$ by a factor $(1 - f_{\rm bkg})^{-1} \approx (1.22 \pm 0.09)$. Separating such, previously irreducible, backgrounds from genuine $B^0_s \to D^-_s\mu^+\nu_\mu X$ decays would reduce the uncertainty of $a^s_{\rm sl}$ from 0.33% to 0.27% for a measurement of $a^s_{\rm sl}$ on the Run-1 data set[1]. Some separation between the signal and backgrounds is provided through the corrected mass, which was already introduced in Sect. 5.4 as part of the event selection. A recent result from LHCb, published as Ref. [85], proved that this separation is sufficient to fit for the various contributions of b-hadron decays, shown in Fig. 9.1. By the increase of the B^0_s production rate and integrated luminosity (from $3\,{\rm fb}^{-1}$ to over $6\,{\rm fb}^{-1}$), the statistical error is expected to shrink by over a factor of 2. Assuming this naive scaling for both systematic and statistical errors, a perfect separation between backgrounds and signal would to 0.13% for an analysis of $a^s_{\rm sl}$ on the complete Run-2 data set (to be compared with 0.16% without this separation, obtained when the same background fractions are assumed). Aside from the reduction of the overall uncertainty, a study of the corrected mass will provide a valuable cross-check for the estimated composition of the $D^-_s\mu^+$ candidates that is currently obtained from simulation and measured branching fractions.

9.1.2 Improved detector calibration

The impact of the improved calibration of the pion detection asymmetry presented in Sect. 8.5 is estimated using simulated $B^0_s \to D^-_s(\to \phi(\to K^-K^+)\pi^-)\mu^+\nu_\mu X$ events. To compare the new calibration procedure of the pion detection asymmetry to that applied in Run 1, which also used $D^0 \to K^-\pi^+\pi^+\pi^-$ decays, the original strategy is followed. In this strategy, the pion and muon detection asymmetries are treated identically, and measured as a function of the particle's momentum only. The resulting uncertainty associated to the combined detection asymmetry, $A^{\mu^+\pi^-}_{\rm track}$, for simulated $D^-_s \to \phi\pi^-$ events is only 0.10%, for an integrated luminosity of $1.3\,{\rm fb}^{-1}$. This is the same precision as the one for the analysis of the 2012 data set, which corresponds to $2.0\,{\rm fb}^{-1}$.

With the increase of statistical precision, also the effects in the detection asymmetries due to differences in angular distributions between the calibration and signal channels can become significant, and must be accounted for. For this, the one-dimensional parametrisation of the pion detection asymmetry in terms of the absolute momentum

[1] In this projection, it is assumed that the statistical error on $A_{\rm meas}$, which is the dominating uncertainty, scales as $\sqrt{1 + f_{\rm bkg}}$.

is insufficient. While an increase in statistical precision is welcome, the new calibration of the detection asymmetry is developed mainly to provide an adequate calibration of the detection asymmetry with a multidimensional parametrisation. Using the calibration of the detection asymmetry in bins of p_{T}, η reduces the statistical precision for the correction to the $B_s^0 \to D_s^-(\to \phi(\to K^-K^+)\pi^-)\mu^+\nu_\mu$, from the earlier-mentioned 0.10% to 0.14%.

9.2 Prospects for CP violation in B^0-$\overline{B}^0$ mixing

Similar to the measurement of CP violation in B_s^0 mixing, also the CP violation in the mixing of $B^0 - \overline{B}^0$ mesons, a_{sl}^d, can be measured at LHCb. Reference [49] describes the analysis on the Run-1 data set, which used $B^0 \to D^-(\to K^+\pi^-\pi^-)\mu^+\nu_\mu X$ and $B^0 \to D^{*-}(\to D^0(\to K^-\pi^+)\pi^+)\mu^+\nu_\mu X$ decays. Most of the precision originates from the analysis of the $B^0 \to D^-\mu^+\nu_\mu X$ decays, which will be the focus for this section. The measurement of a_{sl}^d in this decay mode is limited by the precision of $A_{\mathrm{det}}^{K^-\pi^+}$,

$$a_{\mathrm{sl}}^d = \left(-0.19 \pm 0.21\,(\mathrm{signal}) \pm 0.22\,(A_{\mathrm{det}}^{K^-\pi^+}) \pm 0.20\,(\mathrm{rest})\right)\%,$$

where the first error is the statistical error associated to A_{meas}, the second corresponds to $A_{\mathrm{det}}^{K^-\pi^+}$ and the last corresponds to the combination of all other systematic and statistical

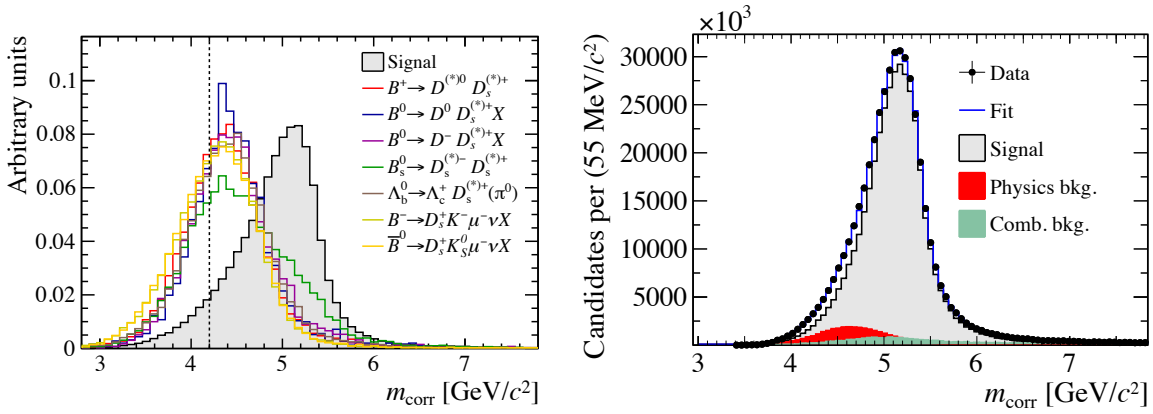

Figure 9.1: (left) Distribution of the corrected mass for $K^+K^-\pi^-\mu^+$ candidates in simulated events, selected for the measurement of a_{sl}^s. The selection applied in the analysis is indicated by a dotted line in the right figure. The size of the contributions are not to scale; each of the contributions is normalised to unity. (right) Distribution of the corrected mass for $K^+K^-\pi^-\mu^+$ candidates in data recorded in 2011 and 2012, along with a fit, as presented in Ref. [85]. All fit shapes, except from the one for the combinatorial background, are obtained from simulated events. The event selection for candidates in the right plot differs from that applied in the a_{sl}^s analysis.

uncertainties.

To estimate the impact of the improved calibration presented in Chapter 7 on a measurement of a^d_{sl}, the contribution of $A^{K^-\pi^+}_{\text{det}}$ to the uncertainty of a^d_{sl} in Run 2 is determined. A suitable estimate of the statistical precision requires to weigh calibration candidates to match the kinematic distributions of the B^0 decay products. The correction, $A^{K^-\pi^+}_{\text{det}}$, is determined for simulated $B^0 \to D^-(\to K^+\pi^-\pi^-)\mu^+\nu_\mu$ events, generated in $\sqrt{s} = 8\,\text{TeV}$ and $\sqrt{s} = 13\,\text{TeV}$ proton-proton collisions. For the two pions, the distribution of the pion with the lowest momentum is used, in agreement with the analysis strategy of Ref. [49]. A selection which is representative for the analysis is applied to these events, including PID requirements on the final-state hadrons. The impact of the PID requirements on the measured charge asymmetry is included in the calibration of $A^{K^-\pi^+}_{\text{det}}$. For simplicity, only the calibration samples recorded in 2012 (for $\sqrt{s} = 8\,\text{TeV}$) and 2016 (for $\sqrt{s} = 13\,\text{TeV}$) with the magnet down polarity are considered, and the same sample size for the opposite magnet polarity are assumed. The weighting strategies for both data sets are identical.

The resulting uncertainties are shown in Table 9.1, for both years. The results for 2012 are comparable to those found in the published analysis. While the recorded luminosity for 2016 is lower than for 2012, the statistical uncertainty for $A^{K^-\pi^+}_{\text{det}}$ improves from 0.15% to 0.10%. Part of this improvement is attributed to the higher production rate of D^+ mesons [67]. However, the increase in statistical precision is higher than what is expected from the production rate alone, and is also due to the improved event selection.

Like the analysis of *CP* violation in $B^0_s - \overline{B}^0_s$ mixing, a^d_{sl} is measured using untagged B^0 mesons. Equation 5.3 relates the measured asymmetry, A_{meas}, to a^d_{sl}. Approximating $\Delta\Gamma_d \approx 0$, the measured, time-dependent asymmetry, $A_{\text{meas}}(t)$, is related to a^d_{sl} as

$$A_{\text{meas}}(t) \approx A_{\text{det}} + \frac{a^d_{\text{sl}}}{2} + \left(A_P - \frac{a^d_{\text{sl}}}{2}\right)\cos(\Delta m_d t),$$

where A_P denotes the $B^0 - \overline{B}^0$ production asymmetry. The uncertainty of a^d_{sl} scales with approximately twice the uncertainty of A_{det}. With this approximation, the expected contribution due to $A^{K^-\pi^+}_{\text{det}}$ to the statistical uncertainty of a^d_{sl} determined on $6\,\text{fb}^{-1}$ of Run-2 data is about 0.07%. A challenge resides in the control of all systematic errors related to $A^{K^-\pi^+}_{\text{det}}$, which will require even more precise tests than those presented in Sect. 7.5. A naive scaling of all other uncertainties reported in the Run-1 analysis results in an expected precision on a^d_{sl} for Run-2 data of 0.16%.

9.3 Prospects in detector calibration beyond Run 2

The future plans for the LHCb experiment include an upgrade to facilitate an increase of instantaneous luminosity, increasing the average number of visible proton-proton col-

lisions per event from 1.1 (Run 2) to 5.7 [86]. This upgraded detector will record a data sample corresponding to $50\,\text{fb}^{-1}$ of integrated luminosity throughout the years 2021 to 2029, covering Run 3 and Run 4 of the LHC. With this larger data set, measurements of *CP* asymmetries in decays with high branching fractions, such as semileptonic B decays, will reach a statistical precision of $\mathcal{O}(5 \times 10^{-4})$. Therefore, these measurements will likely be limited by systematic errors related to the detector calibration. In particular, the parametrisation in the calibration of the detection asymmetry, along with the assumptions related to the factorisation, e.g. $A_{\text{det}}(K^-\pi^+) = A_{\text{det}}(K^-) + A_{\text{det}}(\pi^+)$, contribute to this systematic error. In this section, additional analyses are proposed to control and estimate these systematic uncertainties, such that high-precision measurements of *CP* asymmetries can still profit from the increase in luminosity. First, the changes to the detector and planned beam conditions are discussed.

9.3.1 Detector design and operation

The LHCb detector will change significantly to prepare for the start of Run 3. This includes changes to a few of the main contributors to the acceptance asymmetry, which were discussed in Sect. 6.2. Amongst others, the IT and OT will be replaced by a new scintillating fibre tracker which covers the entire acceptance downstream of the magnet. With this change, the support structure of the inner tracker is removed, which will mitigate the polarity-dependent detection asymmetry for hadrons at moderate pseudorapidity. Meanwhile, the increased number of proton-proton collisions per event will increase the detector occupancy, and extra care must be taken to reduce the charge asymmetry related to the track reconstruction discussed in Sect. 6.3. Currently, the development of the event reconstruction is still ongoing.

After Run 2, the beam energy will be increased slightly from $\sqrt{s} = 13\,\text{TeV}$ to $\sqrt{s} = 14\,\text{TeV}$. This reduces the internal horizontal crossing angle slightly from $145\,\mu\text{rad}$ to $135\,\mu\text{rad}$ as well. The current plans for the external beam-crossing angle are similar to those used for Run-2 data taking, with the same horizontal angle of $-250\,\mu\text{rad}$. However,

Table 9.1: Statistical uncertainties for $A^{\text{raw}}(D^+ \to K^-\pi^+\pi^+)$ and $A^{\text{raw}}(D^+ \to \overline{K}^0\pi^+)$, determined on data sets weighted to the kinematic distributions of simulated $B^0 \to D^-\mu^+\nu_\mu$ events. Only the data sets recorded with the magnet down polarity are used.

Sample	$\sigma\left(D^+ \to \overline{K}^0\pi^+\right)$ [%]	$\sigma\left(D^+ \to K^-\pi^+\pi^+\right)$ [%]
2012, $\sqrt{s} = 8\,\text{TeV}$, $1.0\,\text{fb}^{-1}$	± 0.13	± 0.07
2016, $\sqrt{s} = 13\,\text{TeV}$, $0.8\,\text{fb}^{-1}$	± 0.09	± 0.04

at this moment, the possibility is explored to compensate the internal crossing angle by different external crossing angles for each magnet polarity.

9.3.2 Control of systematic errors

Determining a suitable correction for analyses of *CP* asymmetries with statistical uncertainties below 0.05% is a delicate procedure. The study presented in Chapter 6 has shown that a one-dimensional parametrisation of the detection asymmetry is insufficient for high-precision measurements. While the presented study is detailed, checks using data are required to ensure that no effects are overlooked. One way to test the understanding and the parametrisation of the detector bias, is the study of the consistency among multiple, independent control channels. Ultimately, part of the available data set can be used to perform a determination of the detection asymmetry exploiting multiple decay modes, maximising the total precision. Three potential measurements to validate the detection calibrations are briefly discussed here.

The final states in the decays of the type $D^0 \to \pi^+\pi^-$, $D^0 \to K^-K^+$, $K^0_S \to \pi^+\pi^-$ and $J/\psi \to \mu^+\mu^-$ are charge symmetric. Therefore, no detection asymmetry related to the reconstruction of the final-state particles can be present. However, the reconstructed phase-space spectra for the positively and negatively charged final-state particles are affected by the different detection efficiencies. Only after correcting for the instrumental asymmetries with the right parametrisation, the symmetry in the phase-space is restored. Exploiting this property allows to calibrate the parametrisation of the detection asymmetry, as was proposed in Ref. [87]. Decays of this type are abundant in the LHCb detector, such that the systematic error can be determined with a high precision (of the order of 0.1% per fb^{-1}).

The calibration of the detection asymmetry using abundant charm decays relies on the factorisation of detection asymmetries. Thus far, this factorisation has only been tested using fast simulation, as presented in Sect. 7.5. The factorisation can be tested explicitly using data-driven methods, by comparing the consistency of the two-track detection asymmetry calibration for kaons and pions, $A_{\text{det}}^{K^-\pi^+}$, as measured in Chapter 7, with the sum of the individual detection asymmetries, $A_{\text{det}}^{K^-} + A_{\text{det}}^{\pi^+}$. For this validation, independent calibrations are required for the pion and kaon detection asymmetries, for which the results presented in Sect. 8.4 and the proposed calibration presented in Sect. 8.6.3 can be used. Note that, if the factorisation of detection asymmetries is validated independently, $A_{\text{det}}^{K^-\pi^+}$ can be used to improve the precision on the single-track detection asymmetries as well.

Another, independent test of the factorisation of detection asymmetries is provided through a measurement of $A_{\text{det}}^{K^+} - A_{\text{det}}^{\pi^+}$, using decays of the type $D_s^+ \to \overline{K}^0(\to \pi^+\pi^-)K^+$ and $D_s^+ \to \phi(\to K^-K^+)\pi^+$. The measured asymmetries of these decay modes include

nuisance asymmetries related to the production of the D_s^+, $A_{\text{prod}}^{D_s^+}$, and the trigger, A_{trigger},

$$A_{\text{meas}}(D_s^+ \to \overline{K}^0(\to \pi^+\pi^-)K^+) = A_{\text{det}}^{K^+} + A_{\text{prod}}^{D_s^+} + A_{\text{trigger}} \tag{9.1}$$

$$A_{\text{meas}}(D_s^+ \to \phi(\to K^-K^+)\pi^+) = A_{\text{det}}^{\pi^+} + A_{\text{prod}}^{D_s^+} + A_{\text{trigger}}, \tag{9.2}$$

but nuisance asymmetries related to the ϕ or $\overline{K}^0$ decay products are absent by the charge-symmetric final-state. By subtracting the measured asymmetries corresponding to the two decay modes, the nuisance asymmetries cancel, and a measurement of $A_{\text{det}}^{K^+} - A_{\text{det}}^{\pi^+} = -A_{\text{det}}^{K^-\pi^+}$ remains. Trigger selections can be restricted to the $\overline{K}^0$ and ϕ decay products, such that all asymmetry related to the software trigger vanishes by the charge-symmetric final state. Note that, while the production rate of D_s^+ mesons is lower than that of D^+ mesons [67], this loss of statistical precision is not a concern, as $A_{\text{det}}^{K^-\pi^+}$ is expected to be systematically limited in the future.

9.4 Conclusion and outlook

Table 9.2 shows the expectations for *CP* violation in mixing for Run 2, which include the improvements related to the detector calibration and the analysis strategy. The precision of a_{sl}^d is improved mostly due to the precise calibration of $A_{\text{det}}^{K^-\pi^+}$. The improvements in a_{sl}^s are mostly due to the improved background separation and, in this naive scaling, the improved calibration of the pion detection asymmetry has only a negligible impact on the precision of a_{sl}^s. However, this scaling assumes that all systematic errors scale similarly with luminosity as the statistical error. This assumption does not hold, as is shown by the necessary use of an improved parametrisation of the detection asymmetry.

Assuming the Standard Model values for a_{sl}^d and a_{sl}^s, given in Eq. 4.11, the expected precision in Run 2 is insufficient for the observation of *CP* violation in $B^0 - \overline{B}^0$ or $B_s^0 - \overline{B}_s^0$ mixing, and even more data are required. Run 3 and Run 4 of the LHC will improve the statistical precision further to $\mathcal{O}(5 \times 10^{-4})$. This estimated precision is of similar order as the central value of the current Standard Model expectation for a_{sl}^d. An even more ambitious upgrade is planned for LHCb in Run 5 and beyond, taking advantage of the so-called High-Luminosity LHC, in which the instantaneous luminosity is increased by another order of magnitude. A total data set of $300\,\text{fb}^{-1}$ is to be collected in these conditions, which improves the statistical precision on a_{sl}^d further to $\mathcal{O}(2 \times 10^{-4})$. In this prognosis, evidence of *CP* violation in $B^0 - \overline{B}^0$ mixing is an ambitious but realistic goal for an optimised analysis on the final LHCb data set, assuming the current Standard Model value for a_{sl}^d.

However, to take advantage of these increases in luminosity, details related to the detector geometry and alignment will have to be studied more carefully, and calibrations have to be carried out using multiple, independent methods to control systematic uncertainties. For these studies, and thus the success of the LHCb upgrades as experiments

for high-precision measurements of *CP* asymmetries, the continuous development and improvement of the detector simulation and calibration are essential.

Table 9.2: Current and expected precision for *CP* violation in $B^0 - \overline{B}^0$ and $B_s^0 - \overline{B}_s^0$ mixing, a_{sl}^d and a_{sl}^s, including the improvements proposed in this thesis. The projections for the High-Luminosity LHC are only based on the statistical uncertainty of the signal samples, and assume a perfect control of instrumental asymmetries.

Sample	Integrated luminosity	$\sigma\left(a_{\mathrm{sl}}^d\right)$ [%]	$\sigma\left(a_{\mathrm{sl}}^s\right)$ [%]
Run 1 [10, 49]	$3\,\mathrm{fb}^{-1}$ (7, 8 TeV)	± 0.36	± 0.33
Run 2	$6\,\mathrm{fb}^{-1}$ (13 TeV)	± 0.16	± 0.13
Run 3+4	$50\,\mathrm{fb}^{-1}$ (14 TeV)	± 0.06	± 0.05
High-Luminosity LHC	$300\,\mathrm{fb}^{-1}$ (14 TeV)	± 0.02	± 0.02

Appendix A

Impact of hadronic elastic scattering

In Sect. 6.1.2 the impact of hadronic interactions on the reconstruction efficiency of hadrons was discussed. Therein, the simulation of hadronic interactions is based on the total cross-sections, i.e. elastic and inelastic, regardless of the potential differences in the reconstruction efficiency between the two. This approximation is advantageous, as the total cross-sections are measured with a higher precision than the elastic and inelastic cross-sections individually [42]. In this appendix, this approximation is examined.

The average diffraction cone for hadronic elastic scattering is larger than for Coulomb scattering: the typical cone size for a single hadronic scatter is estimated [64] to be of the order of 10 mrad, while integrating all Coulomb scattering for a single T station amounts to an average diffraction of 0.2 mrad. Large scattering angles can cause inefficiencies in the track reconstruction as the χ^2 from the track fit becomes so large that the standard quality cuts remove such particles. In addition, these hits may lie outside the search windows in the pattern recognition, which causes that certain particles are not found in the early phases of the track reconstruction. According to Ref. [42], elastic scatterings occur in $\sigma_{\mathrm{E}}/\sigma_{\mathrm{T}} \approx 16\%$ of the hadronic collisions for 20 GeV/c pions. Using an average d/λ_T of 0.17 for $\eta < 4.0$ (see Fig. 6.5) the chance for a hadronic elastic scatter up to the second T-station can be estimated as 2.7%. In this appendix, this number is compared with a simulation of elastic hadronic scattering. The impact of this on the reconstruction efficiency is further investigated. This is done in two steps: first, the angle distribution for hadronic elastic scattering is determined; second, this distribution is combined with an estimate of the reconstruction efficiencies as a function of scattering angle. Both of these steps rely on the event simulation.

The elastic scattering angle, θ, is extracted from simulation by comparing expected and simulated hit positions. The expected hit positions are calculated numerically by extrapolating between consecutive hits ascending in z through the magnetic field, without accounting for elastic scattering. The simulated hit positions are a result of the GEANT4 detector simulation, which includes both Coulomb and hadronic elastic scattering. In the simulation an integration is performed over the material between two

hits. As the elastic hadronic scattering probability is estimated as $\mathcal{O}(3\%)$, it is unlikely that multiple hadronic scatters occur. According to simulation, elastic scatterings do not lead to a loss of efficiency due to the acceptance itself for particles with $\eta < 4.0$. Restricting to particles which have hits in the tracking stations therefore does not influence the scattering angle distribution.

To disentangle hadronic elastic scattering from Coulomb scattering, the distribution of the elastic scattering angle is considered for both muons in $D^+ \to K^-\mu^+\mu^+$ and pions in $D^+ \to K^-\pi^+\pi^+$ decays. The contribution associated to hadronic scattering is only expected for pions, while the contribution from Coulomb scattering is expected to be similar. Figure A.1 shows the distribution of θ for muons and pions in $D^+ \to K^-\mu^+\mu^+$ and $D^+ \to K^-\pi^+\pi^+$ events, respectively. The distribution for pions shows a distinctive transition between two contributions. The data are fit with the use of a single exponential for the hadronic contribution and a double exponential function for the Coulomb contribution. The second exponential contribution for the Coulomb θ spectrum is added to account for any (non-Gaussian) effects for large Coulomb scattering angles. In the fit to the distribution shown in the right panel of Fig. A.1, the parameter describing the large-angle multiple scattering is fixed to the value extracted from the fit to the distribution obtained for muons. The model for the Coulomb scattering agrees well between the two samples. The mean hadronic scattering angle extracted from the exponential distribution is $\theta = (8.5 \pm 0.2)\,\text{mrad}$, slightly lower than that found in Ref. [64] (10 mrad). From this fit the hadronic elastic scattering probability up to $z = 8.9\,\text{m}$ is estimated as $(3.5 \pm 0.7)\%$. Because this elastic collision probability is estimated using particles which did not have any inelastic scattering, the estimated fraction for all particles is reduced to $(3.5 \pm 0.7)\%/\left(1 + \exp(d/\lambda_I)\right) = (3.0 \pm 0.6)\%$. This number is compatible with the earlier estimation of 2.7%.

For the study of the effect of large scattering angles on the track reconstruction efficiency, the shape of the θ distribution, determined from the fit to the distribution shown in Fig. 6.3, is the most important input. It is also illustrative to separate the effects of elastic scattering before and after the first measurement in the VELO, defined as the first cluster (in z) used in the construction of a long track. The scattering angle before the first measurement will be referred to as θ_i, while the total scattering angle up to $z = 8.9\,\text{m}$ will be referred to as θ_{all}. When θ_i is large, the reconstructed direction is affected, but the probability to reconstruct a long track remains unchanged. The error in the reconstructed angle of the particle impacts the reconstructed invariant-mass spectrum, which is a function of the opening angle of the decay products. This is shown in Fig. A.2, which shows the reconstructed D^+ invariant-mass distribution for simulated $D^+ \to K^-\pi^+\pi^+$ decays for a large and small initial scattering angle θ_i (as there are three hadrons in produced in the decay, θ_i refers to the maximum θ_i of all reconstructed D^+ daughters in this case). From these distributions it is clear that scattering before the first measurement deteriorates the invariant-mass resolution.

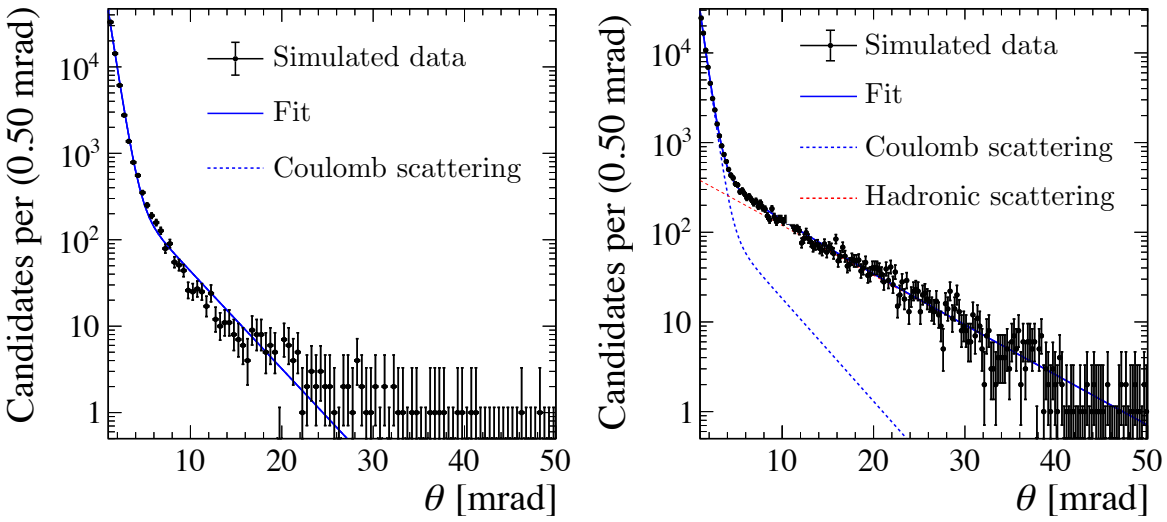

Figure A.1: Distribution of the maximal elastic scattering angle for particles up to $z = 8.9m$ for (left) muons and (right) pions as extracted from the GAUSS event simulation. Only particles with momenta above $5\,\text{GeV}/c$, $\eta < 4.0$ and $p_\text{T} > 100\,\text{MeV}/c$ were used. All considered particles must have deposited sufficient hits in the tracking detectors to be reconstructible as a long track, following the definition in Sect. 6.3.

The invariant-mass distribution is often used to discriminate genuine signal decays from random track combinations. Candidates with a large spread in the mass distribution are likely to be attributed to the background contribution in this procedure. In addition, the quality of the reconstructed decay vertex worsens as the track angles are estimated incorrectly. To estimate the typical loss in efficiency due to the loss of resolution in the reconstructed angle, the data set is split in bins of the initial scattering angle, θ_i, for which the reconstructed invariant-mass distributions are fitted with a typical signal and background shape. The signal shape, $S(m)$, is modelled by convolving three Gaussian functions with a function describing the final-state radiation:

$$S(m) \propto [-m\Theta(-m)]^s \times [f_{G1}G(m|\mu,\sigma_1) + f_{G2}G(m|\mu,\sigma_2) + (1 - f_{G1} - f_{G2})G(m|\mu,\sigma_3)]\,,$$

where Θ is the Heaviside function and the parameter s governs the amount of final-state radiation. The efficiency to count an event as signal as a function of the maximum scattering angle θ for all three tracks is defined as

$$\epsilon^\text{fit}(\theta) = \frac{N^\text{fitted}(D^+ \to K^-\pi^+\pi^+, \theta)}{N^\text{generated}(D^+ \to K^-\pi^+\pi^+, \theta)}.$$

The parameters of the signal shape, $S(m)$, are determined from a fit to the total data set and fixed in the fits to the split data sets. The right panel of Fig. A.3 shows the

efficiency of a large first scatter as a function of θ_i (which includes the loss of efficiency due to the vertexing requirement). The efficiency as a function of maximum scattering angle integrating over all angles up to $z = 8.9\,\text{m}$ rapidly drops up to 10 mrad but does not reach 0%. This is due to the contribution of scattering in the second tracking station, which impact the track-reconstruction efficiency to a lesser degree than elastic scattering upstream of the dipole magnet.

By combining the track-reconstruction efficiency as function of θ_{all} (Fig. A.3) with the distribution of θ_{all} for hadronic elastic scattering (Fig. A.1), the average inefficiency due to hadronic elastic scattering is estimated. Integrating over all material up to $z = 8.9\,\text{m}$ results in an average efficiency of $(46 \pm 1)\%$ for a single elastic hadronic scatter. Taking the estimated hadronic elastic scattering rate for pions of $(3.0 \pm 0.6)\%$, this implies that about $(1.4 \pm 0.7)\%$ of pions are not reconstructed due to hadronic scattering.

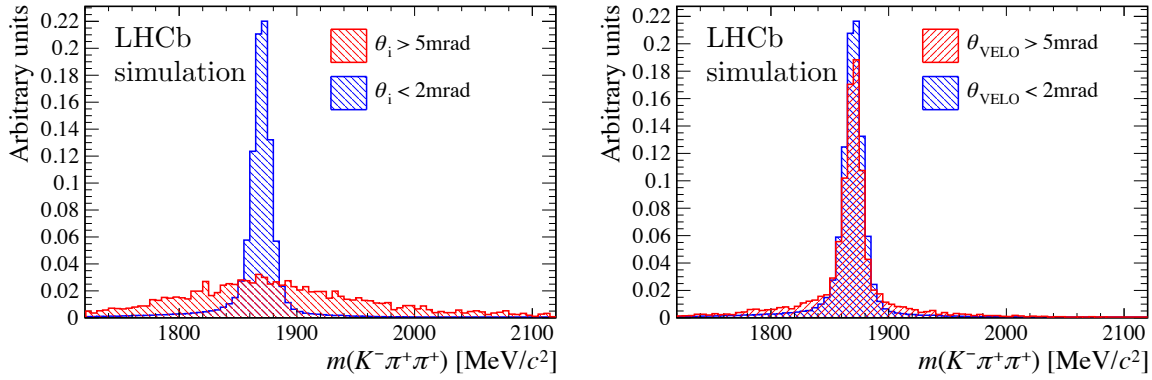

Figure A.2: The reconstructed invariant mass for (left) different initial scattering angles and (right) VELO scattering angles after the first used cluster.

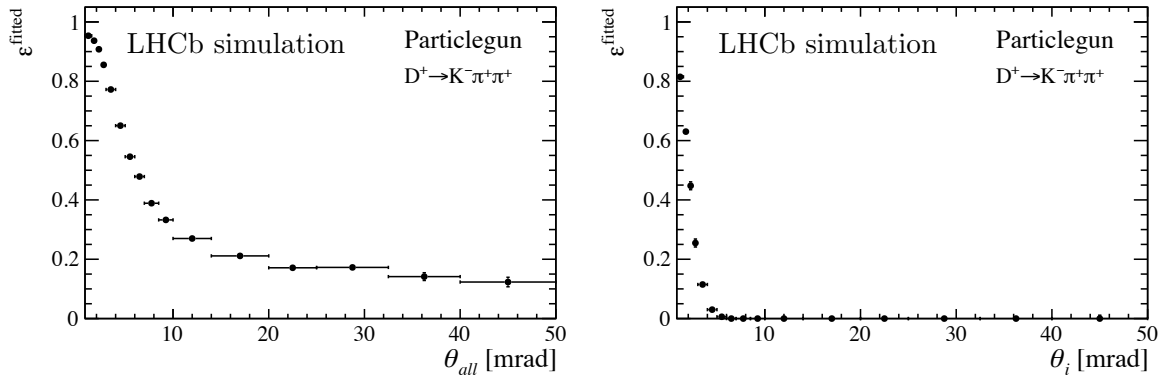

Figure A.3: Efficiency of the reconstruction of the $D^+ \to K^-\pi^+\pi^+$ decays using a nominal mass fit for different values of the maximal scattering angle up to $z = 8.9\,\text{m}$ (left) and the initial scattering angle (right).

Using this average efficiency, a more accurate description of the loss of particles due to elastic scattering is given by

$$N^{\text{measured}} \propto \exp(-\frac{d^{8.9\,\text{m}}}{\lambda_E}0.54). \tag{A.1}$$

The systematic uncertainty due to the usage of the total cross-section for the estimate of the reconstruction efficiency (Eq. 6.6) can be estimated by combining Eq. A.1 with $\frac{\sigma_E}{\sigma_T} \approx 16\%$:

$$\begin{aligned} N^{\text{measured}} &\propto \exp(-(\frac{d^{8.9\,\text{m}}}{\lambda_E}0.54 + \frac{d^{8.9\,\text{m}}}{\lambda_I})) \approx \exp(-\frac{d^{8.9\,\text{m}}}{\lambda_T}(0.08 + 0.84)) \\ &= \exp(-0.92\frac{d^{8.9\,\text{m}}}{\lambda_T}). \end{aligned} \tag{A.2}$$

Thus, the reconstruction efficiency as determined using the total cross-section is overestimated by approximately 8%. For kaons, for which the total detection asymmetry due to material interaction is about 1% (c.f. Sect. 7.5), this results in a systematic uncertainty of about 0.08%.

Note that, as the tracking performance depends on the occupancy of the detector, the efficiency as function of the scattering angle as determined in this study can be overestimated when applied to events with a higher hit multiplicity. With the increase of the number of *pp* collisions per event for Run 3 and onwards, this estimate can be improved by repeating the study using events with a representative track multiplicity.

References

[1] A. D. Sakharov, *Violation of CP invariance, C asymmetry, and baryon asymmetry in the universe*, Pisma Zh. Eksp. Teor. Fiz. **5** (1967) 32.

[2] Particle Data Group, M. Tanabashi *et al.*, *Review of particle physics*, Phys. Rev. D **98** (2018) 030001.

[3] J. H. Christenson, J. W. Cronin, V. L. Fitch, and R. Turlay, *Evidence for the 2 π decay of the $K^0{}_2$ meson*, Phys. Rev. Lett. **13** (1964) 138.

[4] BaBar, B. Aubert *et al.*, *Observation of CP violation in the B^0 meson system*, Phys. Rev. Lett. **87** (2001) 091801, arXiv:hep-ex/0107013.

[5] LHCb collaboration, R. Aaij *et al.*, *Precision measurement of CP violation in $B^0_s \to J/\psi\, K^+K^-$ decays*, Phys. Rev. Lett. **114** (2015) 041801, arXiv:1411.3104.

[6] CMS and LHCb collaborations, V. Khachatryan *et al.*, *Observation of the rare $B^0_s \to \mu^+\mu^-$ decay from the combined analysis of CMS and LHCb data*, Nature **522** (2015) 68, arXiv:1411.4413.

[7] LHCb collaboration, R. Aaij *et al.*, *First observation of CP violation in the decays of B^0_s mesons*, Phys. Rev. Lett. **110** (2013) 221601, arXiv:1304.6173.

[8] LHCb collaboration, R. Aaij *et al.*, *Observation of $J/\psi p$ resonances consistent with pentaquark states in $\Lambda^0_b \to J/\psi pK^-$ decays*, Phys. Rev. Lett. **115** (2015) 072001, arXiv:1507.03414.

[9] LHCb Outer Tracker Group, P. d'Argent *et al.*, *Improved performance of the LHCb Outer Tracker in LHC Run 2*, JINST **12** (2017), no. 11 P11016, arXiv:1708.00819.

[10] LHCb collaboration, R. Aaij *et al.*, *Measurement of the CP asymmetry in B^0_s–$\overline{B}^0_s$ mixing*, Phys. Rev. Lett. **117** (2016) 061803, arXiv:1605.09768.

[11] LHCb collaboration, R. Aaij *et al.*, *Measurement of $D^\pm_s$ production asymmetry in pp collisions at $\sqrt{s} = 7$ and 8 TeV*, JHEP **08** (2018) 008, arXiv:1805.09869.

[12] A. Davis *et al.*, *Measurement of the instrumental asymmetry for $K^-\pi^+$-pairs at LHCb in Run 2*, CERN-LHCb-PUB-2018-004.

[13] LHCb collaboration, A. A. Alves *et al.*, *The LHCb Detector at the LHC*, JINST **3** (2008) S08005.

[14] LHCb collaboration, *LHCb reoptimized detector design and performance: Technical Design Report*, CERN-LHCC-2003-030.

[15] W. Herr, *Pushing the limits: crossing angles, aperture and beta**, CERN-2011-005.261. Presented at the Chamonix 2011 Workshop on LHC Performance.

[16] LHCb collaboration, *LHCb inner tracker: Technical Design Report*, CERN-LHCC-2002-029.

[17] LHCb collaboration, R. Aaij *et al.*, *LHCb detector performance*, Int. J. Mod. Phys. **A30** (2015) 1530022, arXiv:1412.6352.

[18] LHCb collaboration, *LHCb outer tracker: Technical Design Report*, CERN-LHCC-2001-024.

[19] J. van Tilburg, *Track simulation and reconstruction in LHCb*, PhD thesis, NIKHEF, 2005, CERN-THESIS/2005-040.

[20] P. David, *Search for exotic long-lived particles with the LHCb detector*, PhD thesis, NIKHEF, Feb, 2016, CERN-THESIS/2016-077.

[21] M. De Cian, S. Farry, P. Seyfert, and S. Stahl, *Fast neural-net based fake track rejection in the LHCb reconstruction*, CERN-LHCb-PUB-2017-011.

[22] R. Aaij *et al.*, *The LHCb trigger and its performance in 2011*, JINST **8** (2013) P04022, arXiv:1211.3055.

[23] B. Sciascia, *LHCb Run 2 Trigger Performance*, PoS **BEAUTY2016** (2016) 029. 7.

[24] B. Storaci, *Optimization of the LHCb track reconstruction*, J. Phys. Conf. Ser. **664** (2015), no. 7 072047.

[25] M. Williams *et al.*, *The HLT2 Topological Lines*, CERN-LHCb-PUB-2011-002.

[26] T. Likhomanenko *et al.*, *LHCb Topological Trigger Reoptimization*, J. Phys. : Conf. Ser. **664** (2015) 082025. 8 p, 21st International Conference on Computing in High Energy Physics (CHEP2015).

[27] I. Belyaev *et al.*, *Simulation application for the LHCb experiment*, arXiv:http://arXiv.org/abs/physics/0306035.

[28] T. Sjöstrand, S. Mrenna, and P. Skands, *PYTHIA 6.4 physics and manual*, JHEP **05** (2006) 026, arXiv:hep-ph/0603175.

[29] I. Belyaev *et al.*, *Handling of the generation of primary events in Gauss, the LHCb simulation framework*, J. Phys. Conf. Ser. **331** (2011) 032047.

[30] D. J. Lange, *The EvtGen particle decay simulation package*, Nucl. Instrum. Meth. **A462** (2001) 152.

[31] P. Golonka and Z. Was, *PHOTOS Monte Carlo: A precision tool for QED corrections in Z and W decays*, Eur. Phys. J. **C45** (2006) 97, arXiv:hep-ph/0506026.

[32] GEANT4, S. Agostinelli *et al.*, *Geant4: A simulation toolkit*, Nucl. Instrum. Meth. **A506** (2003) 250.

[33] D. Müller, M. Clemencic, G. Corti, and M. Gersabeck, *ReDecay: A novel approach to speed up the simulation at LHCb*, arXiv:1810.10362.

[34] LHCb Outer Tracker Group, R. Arink *et al.*, *Performance of the LHCb Outer Tracker*, JINST **9** (2014), no. 01 P01002, arXiv:1311.3893.

[35] S. Bachmann *et al.*, *Ageing in the LHCb outer tracker: Phenomenon, culprit and effect of oxygen*, Nucl. Instrum. Meth. **A617** (2010) 202.

[36] D. van Eijk *et al.*, *Radiation hardness of the LHCb Outer Tracker*, Nucl. Instrum. Meth. **A685** (2012) 62.

[37] E. L. Visser, *Preventing, monitoring and curing the ageing in the LHCb Outer Tracker*, Master's thesis, NIKHEF, Amsterdam, 2010.

[38] D. van Eijk, *Ageing and the Decay of Beauty: Radiation Hardness of the LHCb Outer Tracker and Time-Dependent CP violation using $B_s^0 \to J/\psi\,\phi$*, PhD thesis, NIKHEF, 2012, CERN-THESIS/2012-137.

[39] R. Koopman, *Ageing of the LHCb outer tracker & b-hadron production and decay at $\sqrt{s}$=7 TeV*, PhD thesis, NIKHEF, 2015, CERN-THESIS/2015-226.

[40] V. Weisskopf and E. Wigner, *Berechnung der natürlichen linienbreite auf grund der diracschen lichttheorie*, Zeitschrift für Physik **63** (1930) 54.

[41] M. Artuso, G. Borissov, and A. Lenz, *CP violation in the B_s^0 system*, Rev. Mod. Phys. **88** (2016), no. 4 045002, arXiv:1511.09466.

[42] Particle Data Group, C. Patrignani *et al.*, *Review of Particle Physics*, Chin. Phys. **C40** (2016), no. 10 100001.

[43] A. Lenz and U. Nierste, *Theoretical update of $B_s - \bar{B}_s$ mixing*, JHEP **06** (2007) 072, arXiv:hep-ph/0612167.

[44] D0 collaboration, V. M. Abazov *et al.*, *Study of CP-violating charge asymmetries of single muons and like-sign dimuons in $p\overline{p}$ collisions*, Phys. Rev. **D89** (2014) 012002, arXiv:1310.0447.

[45] Belle collaboration, E. Nakano *et al.*, *Charge asymmetry of same-sign dileptons in B^0-$\overline{B}^0$ mixing*, Phys. Rev. **D73** (2006) 112002, arXiv:hep-ex/0505017.

[46] BaBar collaboration, J. P. Lees *et al.*, *Search for CP violation in $B^0 - \overline{B}^0$ mixing using partial reconstruction of $B^0 \to D^{*-} X \ell^+ \nu_\ell$ and a kaon tag*, Phys. Rev. Lett. **111** (2013) 101802, arXiv:1305.1575.

[47] BaBar collaboration, J. P. Lees *et al.*, *Study of CP asymmetry in $B^0 - \overline{B}^0$ mixing with inclusive dilepton events*, Phys. Rev. Lett. **114** (2015) 081801, arXiv:1411.1842.

[48] D0 collaboration, V. M. Abazov *et al.*, *Measurement of the semileptonic charge asymmetry in B^0 meson mixing with the D0 detector*, Phys. Rev. **D86** (2012) 072009, arXiv:1208.5813.

[49] LHCb collaboration, R. Aaij *et al.*, *Measurement of the semileptonic CP asymmetry in B^0–$\overline{B}^0$ mixing*, Phys. Rev. Lett. **114** (2015) 041601, arXiv:1409.8586.

[50] LHCb collaboration, R. Aaij *et al.*, *Measurement of the flavour-specific CP-violating asymmetry $a^s_{\rm sl}$ in B^0_s decays*, Phys. Lett. **B728** (2014) 607, arXiv:1308.1048.

[51] D0 collaboration, V. M. Abazov *et al.*, *Measurement of the semileptonic charge asymmetry using $B^0_s \to D_s \mu X$ decays*, Phys. Rev. Lett. **110** (2013) 011801, arXiv:1207.1769.

[52] LHCb collaboration, R. Aaij *et al.*, *Measurement of CP asymmetry in $B^0_s \to D^\mp_s K^\pm$ decays*, JHEP **03** (2018) 059, arXiv:1712.07428.

[53] LHCb collaboration, R. Aaij *et al.*, *Measurement of the $\overline{B}^0$–B^0 and $\overline{B}^0_s$–B^0_s production asymmetries in pp collisions at $\sqrt{s} = 7$ TeV*, Phys. Lett. **B739** (2014) 218, arXiv:1408.0275.

[54] D. Martinez Santos and F. Dupertuis, *Mass distributions marginalized over per-event errors*, Nucl. Instrum. Meth. **A764** (2014) 150, arXiv:1312.5000.

[55] LHCb collaboration, R. Aaij *et al.*, *Measurement of b hadron production fractions in 7 TeV pp collisions*, Phys. Rev. **D85** (2012) 032008, arXiv:1111.2357.

[56] LHCb collaboration, R. Aaij *et al.*, *Determination of f_s/f_d for 7 TeV pp collisions and measurement of the $B^0 \to D^- K^+$ branching fraction*, Phys. Rev. Lett. **107** (2011) 211801, arXiv:1106.4435.

[57] LHCb collaboration, R. Aaij *et al.*, *Measurement of the fragmentation fraction ratio f_s/f_d and its dependence on B meson kinematics*, JHEP **04** (2013) 001, arXiv:1301.5286.

[58] LHCb collaboration, *Updated average f_s/f_d b-hadron production fraction ratio for 7 TeV pp collisions*, LHCb-CONF-2013-011.

[59] LHCb collaboration, R. Aaij *et al.*, *Study of the productions of Λ_b^0 and $\overline{B}^0$ hadrons in pp collisions and first measurement of the $\Lambda_b^0 \to J/\psi p K^-$ branching fraction*, Chin. Phys. C **40** (2016) 011001, arXiv:1509.00292.

[60] LHCb collaboration, R. Aaij *et al.*, *Measurement of CP asymmetries in the decays $B^0 \to K^{*0}\mu^+\mu^-$ and $B^+ \to K^+\mu^+\mu^-$*, JHEP **09** (2014) 177, arXiv:1408.0978.

[61] M. Vesterinen, *A study of Hlt2 asymmetries using semileptonic B decays and the topological lines*, Tech. Rep. LHCb-INT-2014-024, CERN, Geneva, May, 2014. Private communication.

[62] LHCb collaboration, R. Aaij *et al.*, *Measurement of the track reconstruction efficiency at LHCb*, JINST **10** (2015) P02007, arXiv:1408.1251.

[63] L. Anderlini *et al.*, *The PIDCalib package*, LHCb-PUB-2016-021. CERN-LHCb-PUB-2016-021.

[64] H. Gordon, R. W. Lambert, J. van Tilburg, and M. Vesterinen, *A Measurement of the $K\pi$ Detection Asymmetry*, LHCb-INT-2012-027. Private communication.

[65] M. Stahl and S. Stahl, *Forward tracking improvements for 2016 data taking*, .

[66] LHCb collaboration, R. Aaij *et al.*, *Measurement of CP asymmetry in $D^0 \to K^-K^+$ and $D^0 \to \pi^-\pi^+$ decays*, JHEP **07** (2014) 041, arXiv:1405.2797.

[67] LHCb collaboration, R. Aaij *et al.*, *Measurements of prompt charm production cross-sections in pp collisions at $\sqrt{s} = 13$ TeV*, JHEP **03** (2016) 159, Erratum ibid. **09** (2016) 013, arXiv:1510.01707.

[68] M. Pivk and F. R. Le Diberder, *sPlot: A statistical tool to unfold data distributions*, Nucl. Instrum. Meth. **A555** (2005) 356, arXiv:physics/0402083.

[69] W. Fetscher *et al.*, *Regeneration of arbitrary coherent neutral kaon states: A new method for measuring the $K^0 - \overline{K}^0$ forward scattering amplitude*, Z. Phys. **C72** (1996) 543.

[70] A. Gsponer *et al.*, *Precise coherent K^0_S regeneration amplitudes for C, Al, Cu, Sn and Pb nuclei from 20 to* 140 GeV/c *and their interpretation*, Phys. Rev. Lett. **42** (1979) 13.

[71] R. A. Briere and B. Winstein, *Determining the phase of a strong scattering amplitude from its momentum dependence to better than 1°: The example of kaon regeneration*, Phys. Rev. Lett. **75** (1995) 402.

[72] W. D. Hulsbergen, *Decay chain fitting with a Kalman filter*, Nucl. Instrum. Meth. **A552** (2005) 566, arXiv:physics/0503191.

[73] J. H. Friedman, *Greedy function approximation: A gradient boosting machine*, Ann. Statist. **29** (2001) 1189.

[74] J. H. Friedman, *Stochastic gradient boosting*, Comput. Stat. Data Anal. **38** (2002) 367.

[75] A. Rogozhnikov, *Reweighting with boosted decision trees*, J. Phys. Conf. Ser. **762** (2016) 012036, arXiv:1608.05806.

[76] LHCb collaboration, R. Aaij *et al.*, *Observation of the decay $\Lambda_b^0 \to \Lambda_c^+ p\overline{p}\pi^-$*, Phys. Lett. **B784** (2018) 101, arXiv:1804.09617.

[77] R. Aaij *et al.*, *Performance of the LHCb Vertex Locator*, JINST **9** (2014) P09007, arXiv:1405.7808.

[78] LHCb collaboration, R. Aaij *et al.*, *Test of lepton universality with $B^0 \to K^{*0}\ell^+\ell^-$ decays*, JHEP **08** (2017) 055, arXiv:1705.05802.

[79] LHCb collaboration, R. Aaij *et al.*, *Measurement of $\sigma(pp \to b\bar{b}X)$ at $\sqrt{s} = 7$ TeV in the forward region*, Phys. Lett. **B694** (2010) 209, arXiv:1009.2731.

[80] CLEO, G. Bonvicini *et al.*, *Updated measurements of absolute D^+ and D^0 hadronic branching fractions and $\sigma(e^+e^- \to D\overline{D})$ at $E_{\rm cm} = 3774$ MeV*, Phys. Rev. **D89** (2014), no. 7 072002, arXiv:1312.6775, [Erratum: Phys. Rev.D91,no.1,019903(2015)].

[81] LHCb collaboration, R. Aaij *et al.*, *Observation of D^0–$\overline{D}^0$ oscillations*, Phys. Rev. Lett. **110** (2013) 101802, arXiv:1211.1230.

[82] N. L. Johnson, *Systems of frequency curves generated by methods of translation*, Biometrika **36** (1949) 149.

[83] I. M. Dremin, *Elastic scattering of hadrons*, Phys. Usp. **56** (2013) 3, arXiv:1206.5474.

[84] LHCb collaboration, R. Aaij *et al.*, *Measurement of the b-quark production cross-section in 7 and 13 TeV pp collisions*, Phys. Rev. Lett. **118** (2017) 052002, Erratum ibid. **119** (2017) 169901, arXiv:1612.05140.

[85] LHCb collaboration, R. Aaij *et al.*, *Measurement of B_s^0 and D_s^- meson lifetimes*, Phys. Rev. Lett. **119** (2017) 101801, arXiv:1705.03475.

[86] LHCb collaboration, *Framework TDR for the LHCb Upgrade: Technical Design Report*, CERN-LHCC-2012-007.

[87] F. Jansen, *Unfolding single-particle efficiencies and the Outer Tracker in LHCb*, PhD thesis, NIKHEF, 2011, CERN-THESIS/2011-168.

Summary

The Standard Model (SM) has proven to be a very successful theory, describing the physics of elementary particles at the smallest scales. However, when looking at larger scales, striking shortcomings become visible, including a missing description of gravity, dark matter and an unexplained abundance of matter over antimatter. The lattermost shortcoming is the central theme of this thesis.

To explain the imbalance between matter and antimatter, a source of *CP* symmetry violation is needed. In the SM, the violation of this symmetry is present in the weak interaction; a single parameter determines the total amount of *CP* violation for quarks, in a description referred to as "the CKM model". In this description, even though the amount of *CP* violation can differ per process, all *CP*-violation observables in the quark sector are related in the end. Unfortunately, measurements have shown thus far that this single source of *CP* violation is insufficient to explain the matter-antimatter difference in the universe. A possible explanation is that physics beyond the Standard Model changes the *CP* violation in the quark sector, thus making the CKM model incomplete. By measuring *CP* violation in as many different decay channels as possible, one can overconstrain the CKM parameters; additional, anomalous *CP* violation can then appear as inconsistencies in the combination of measurements. In 2013, the D0 collaboration reported evidence for such an inconsistency in the mixing of neutral B mesons.

B mesons and meson mixing

Neutral B mesons are well suited to search for additional *CP* violation. These mesons consist of an anti-b quark, and a (much) lighter quark: either a strange (B_s^0) or down (B^0) quark. Because of this large mass difference, theoretical predictions concerning the amount of *CP* violation in specific processes are easier to calculate, which make these processes attractive tests of the CKM model. In the SM, these mesons transform over time into their own antiparticle, and vice-versa: a process referred to as "neutral meson mixing". This makes the meson and antimeson a coupled, two-state system. *CP* violation in this mixing process means that the probability of an initial meson, for example the B_s^0, to transform after a time t into its anti-meson, the $\overline{B}_s^0$, differs from its

Figure S.1: The mixing between neutral B_s^0 mesons is shown schematically. In the right figure, it is pictorially indicated that the probability of one transition is higher than the reversed, such that $a_{\rm sl}^s \neq 0$.

charge-conjugate process, diagrammatically shown in Fig. S.1. There are two quantities associated to the *CP* violation in the mixing of neutral mesons containing a b quark: $a_{\rm sl}^s$ for the $B_s^0 - \overline{B}_s^0$, and $a_{\rm sl}^d$ for the $B^0 - \overline{B}^0$ meson systems.

The D0 collaboration reported an anomaly in a combined measurement of $a_{\rm sl}^s$ and $a_{\rm sl}^d$, shown as a yellow ellipse in Fig. S.2. In the SM, values for $a_{\rm sl}^s$ and $a_{\rm sl}^d$ can be predicted by using other measurements as an input. This resulting SM prediction is shown in the figure as well, and its uncertainties are much smaller than the scale of the axes. The result of the D0 collaboration disagrees with the SM value with a significance of 3.6σ.

Measuring *CP* violation in mixing at LHCb

A measurement of $a_{\rm sl}^s$ is presented in this thesis, which is the most precise to date. This measurement is performed using data recorded by the LHCb experiment, one of the four large experiments which exploit the proton-proton collisions provided by the Large Hadron Collider (LHC), schematically shown in Fig. S.3. The B_s^0 and $\overline{B}_s^0$ mesons that are produced in these collisions live shortly, and fly a few millimetres before decaying. While in flight, the B_s^0 and $\overline{B}_s^0$ have the time to mix. After its decay, a combination of lighter particles remain, of which some decay again. Only charged kaons, muons, electrons, protons and charged pions[1] have a lifetime long enough to traverse the entire LHCb detector and leave traces behind in the tracking detectors. To determine $a_{\rm sl}^s$ from the data, the B_s^0 and $\overline{B}_s^0$ candidates are counted that have decayed to a so-called "flavour-specific final state": from the charges of the reconstructed particles, one can infer whether it decayed as a B_s^0 or a $\overline{B}_s^0$. Finding the probability of a B_s^0 mixing to a $\overline{B}_s^0$ then involves counting the number of mesons which were produced as a B_s^0 but decayed as a $\overline{B}_s^0$. In the measurement presented, the meson decayed as a B_s^0 ($\overline{B}_s^0$) if it is reconstructed from the final state $K^+K^-\pi^-\mu^+$ ($K^-K^+\pi^+\mu^-$). The B_s^0 meson oscillates many times before it decays. Therefore, even when an unequal number of B_s^0 and $\overline{B}_s^0$ mesons are produced,

[1] This also includes their charge-conjugates.

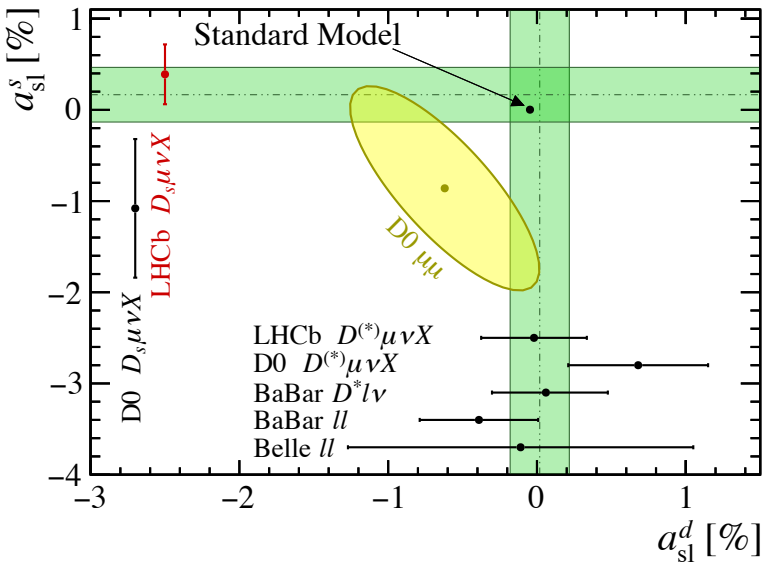

Figure S.2: Overview of the published measurements of $a^d_{\rm sl}$ and $a^s_{\rm sl}$, including (in red) the $a^s_{\rm sl}$ measurement discussed in this thesis. The horizontal and vertical bands indicate the naive averages of pure $a^s_{\rm sl}$ and $a^d_{\rm sl}$ measurements, which are individually represented by the black points. The yellow ellipse represents the D0 measurement. The error bands and contours correspond to 68% confidence level. Details and references can be found in the caption of Fig. 5.10.

any preference of the oscillation direction is visible already when one just counts the total, i.e. decay-time independent, number of $K^+K^-\pi^-\mu^+$ or $K^-K^+\pi^+\mu^-$ combinations reconstructed in the detector, modulo backgrounds (see Fig. S.4). A measurement of $a^s_{\rm sl}$ thus seemingly boils down to a mere counting experiment. However, the result of this counting experiment is spoiled in case that the reconstruction efficiency of the B^0_s decay products differs from that of the $\overline{B}^0_s$. The level of precision required for a competitive measurement of $a^s_{\rm sl}$ turns the determination of the instrumental effects into a delicate experimental challenge.

While the LHCb detector is designed to measure *CP* asymmetries, still the instrumental asymmetries require a correction of about 0.1%. As these asymmetries can arise in all of the stages of the event reconstruction and selection, different calibration samples are used to describe the asymmetries due to the track reconstruction, the particle identification and the event trigger. All of them take advantage of the abundance of charm decays in the LHCb detector. The additional uncertainty introduced by these calibrations is about the same size as the uncertainty due to the B^0_s-$\overline{B}^0_s$ sample size. The resulting, corrected and combined value for $a^s_{\rm sl}$ is found to be

$$a^s_{\rm sl} = (0.39 \pm 0.26 \pm 0.20)\%,$$

and shown as the red data point in Fig. S.2.

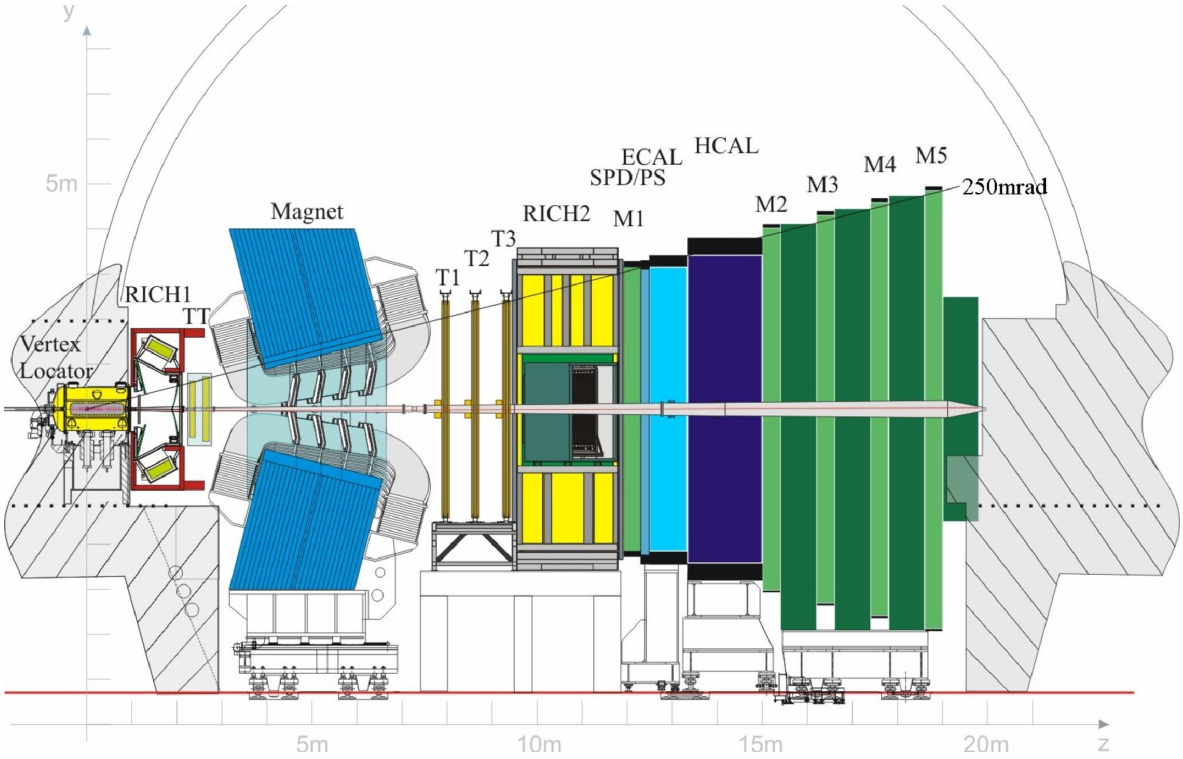

Figure S.3: Schematic view of the LHCb detector, along with the coordinate system used in this thesis. The x-axis is defined as $\hat{x} = \hat{y} \times \hat{z}$, pointing inwards for this schematic. Figure from Ref. [14].

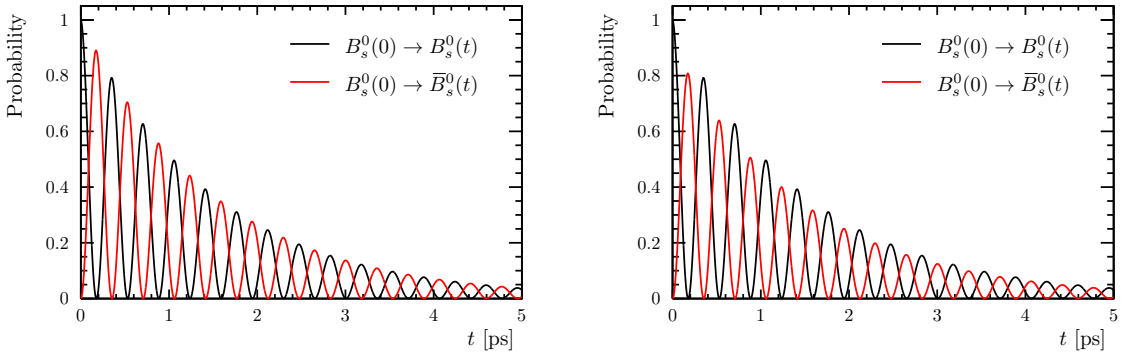

Figure S.4: Probability for a B_s^0 meson produced as a B_s^0 to decay as B_s^0 or $\overline{B}_s^0$, (left) in the realistic case of a small value of a_{sl}^s and (right) in case of $a_{\text{sl}}^s = 10\%$. Integrating over the decay time between $2 - 4\,\text{ps}$, the probability to observe a $\overline{B}_s^0$ or B_s^0 are approximately equal in the scenario displayed on the left, while there is an excess of B_s^0 decays visible in the scenario displayed on the right. In the absence of backgrounds, the scenario shown on the right would result in a 5% excess of $K^+K^-\pi^-\mu^+$ candidates over $K^-K^+\pi^+\mu^-$ candidates in the LHCb detector.

Improving the experimental reach

The measurement of $a^s_{\rm sl}$ presented here used data collected in Run 1, covering the years 2011 and 2012. In Run 2, covering the years 2015 up to 2018, the LHC provided LHCb with two times more pp collisions. With the increase of centre-of-mass energy also the production rate of B^0_s mesons increased, such that the data sample quadrupled in comparison to Run 1. To ensure that measurements of CP asymmetries can benefit optimally from this larger data sample, new techniques for the calibrations of the instrumental asymmetries are required. To develop these techniques, detailed studies have been performed to determine the main underlying causes of the instrumental asymmetries related to the track reconstruction. Charge-dependent hadronic cross-sections and choices in the design of the LHCb detector were found to be among the main causes.

Motivated by the results of these studies, new procedures to calibrate the efficiency and asymmetry for reconstructing electrons, muons and pions have been developed and presented in this thesis. The technique combines the charge-unbiased track reconstruction in the vertex detector with kinematic constraints from decay topologies. The control of peaking backgrounds forms the main challenge for the application of this technique. Despite these complications, the method has been demonstrated to an improved control of the systematic uncertainties, necessary for future high-precision measurements of CP violation.

Samenvatting

Het Standaard Model (SM) heeft zich bewezen als een succesvolle theorie in het beschrijven van de natuurkunde op de kleinste schaal, die van elementaire deeltjes. Op grote schaal verandert dit plaatje vanwege grote tekortkomingen in de beschrijving van zwaartekracht, donkere materie en een onverklaard verschil in de waargenomen hoeveelheid materie en antimaterie. Deze laatste tekortkoming vormt het centrale thema van dit proefschrift.

Om de verstoorde balans tussen materie en antimaterie te verklaren is er een schending nodig van charge-parity symmetrie, *CP* symmetrie, in de fundamentele natuurkrachten. De zwakke interactie, onderdeel van het SM, lijkt deze rol te vervullen. Het SM bevat een enkele parameter die alle *CP* schending beschrijft in de zwakke wisselwerking tussen quarks. Dit onderdeel van het SM wordt vaak het "CKM model" genoemd. Omdat er slechts één vrije parameter is voor de *CP* schending, zijn alle mogelijke waarnemingen van een *CP* asymmetrie aan elkaar gerelateerd. Echter, alle metingen tot nu toe hebben uitgewezen dat deze bron van *CP* schending niet voldoende is om de grote waargenomen verschillen tussen materie en antimaterie in het heelal te beschrijven. Er is daarom een andere bron van *CP* schending in de natuur nodig die niet opgenomen is in het SM. Terwijl alle waarnemingen van *CP* schending gerelateerd zijn via de bekende CKM parameters, zou een nieuwe bron van *CP* schending er voor kunnen zorgen dat deze relaties niet meer gelden, wat gezien zou worden als inconsistenties tussen verschillende *CP* schendende grootheden. In 2013 rapporteerde de D0 collaboratie een sterke aanwijzing voor een dergelijke inconsistentie bij neutrale B mesonen.

Neutrale B mesonen

Neutrale B mesonen bestaan uit een anti-b quark, samen met een (veel) lichtere partner quark: een strange (B_s^0) of down (B^0) quark. Vanwege het grote verschil in massa tussen de twee quarks kunnen nauwkeurige voorspellingen van *CP* schending in bepaalde processen worden gemaakt met het SM. Op deze manier zijn de relaties in het CKM model te testen met precisiemetingen. Een zodanig proces is dat van het "mengen" van neutrale mesonen. Neutrale mesonen veranderen gedurende de tijd in hun eigen antideeltje en vice versa: het meson en het antimeson "mengen". *CP* schending in het

Figuur S.5: Het mengen van neutrale B_s^0 mesonen schematisch weergegeven. De linker figuur illustreert een balans tussen de transities, $a_{\rm sl}^s = 0$. De rechter figuur benadrukt de situatie waarin een van de transities vaker gebeurt dan het omgekeerde proces, zodat $a_{\rm sl}^s \neq 0$.

mengen van deze mesonen betekent dat de kans dat een meson (bijvoorbeeld het B_s^0 meson) verandert in een antimeson ($\overline{B}_s^0$) niet even groot is als het omgekeerde proces, zoals schematisch weergegeven in Fig. S.5. Omdat er twee neutrale B mesonen zijn die mengen, de B^0 en de B_s^0, zijn er twee grootheden die de hoeveelheid CP schending in het mengingsproces kwantificeren: $a_{\rm sl}^s$ voor het $B_s^0 - \overline{B}_s^0$ meson systeem, en $a_{\rm sl}^d$ voor het $B^0 - \overline{B}^0$ meson systeem.

De D0 collaboratie rapporteerde een afwijking in een gecombineerde meting van $a_{\rm sl}^s$ en $a_{\rm sl}^d$, weergegeven als een gele ellips in Fig. S.6. Door gebruik te maken van andere metingen kunnen nauwkeurige voorspellingen van $a_{\rm sl}^s$ en $a_{\rm sl}^d$ worden gemaakt met het SM. De resulterende voorspelling is ook weergegeven in dezelfde figuur, waarbij de onzekerheden op deze schaal kleiner zijn dan zichtbaar. De meting van de D0 collaboratie wijkt met een significantie van 3.6σ af van het SM.

Meten van CP schending in het mengen van B_s^0 mesonen

Voorliggende dissertatie presenteert een nieuwe meting van $a_{\rm sl}^s$, de meest nauwkeurige meting tot dusver. Deze meting is verricht met gebruik van de data van het LHCb experiment, schematisch weergegeven in Fig. S.7 en een van de vier grote experimenten die gebruik maken van de proton-proton botsingen van de Large Hadron Collider (LHC). De B_s^0 en $\overline{B}_s^0$ mesonen die worden geproduceerd in deze botsingen leven kort, maar lang genoeg om nog enkele millimeters door de detector te vliegen voordat ze vervallen. In dit korte leven hebben de B_s^0 en $\overline{B}_s^0$ mesonen de tijd om te mengen. Na hun verval blijven lichtere deeltjes over, van welke sommigen zelf ook weer vervallen na enkele millimeters te hebben afgelegd. Enkel elektronen, muonen, geladen pionen en kaonen en hun antideeltjes hebben de kans om een groot deel van de detector te doorkruisen en signalen achter te laten in de sensoren. Om $a_{\rm sl}^s$ te bepalen uit de data, wordt het aantal B_s^0 en $\overline{B}_s^0$ kandidaten geteld die zijn vervallen in een combinatie van deeltjes die prijsgeven of het meson is vervallen als een B_s^0 of een $\overline{B}_s^0$ meson. De kans dat een B_s^0

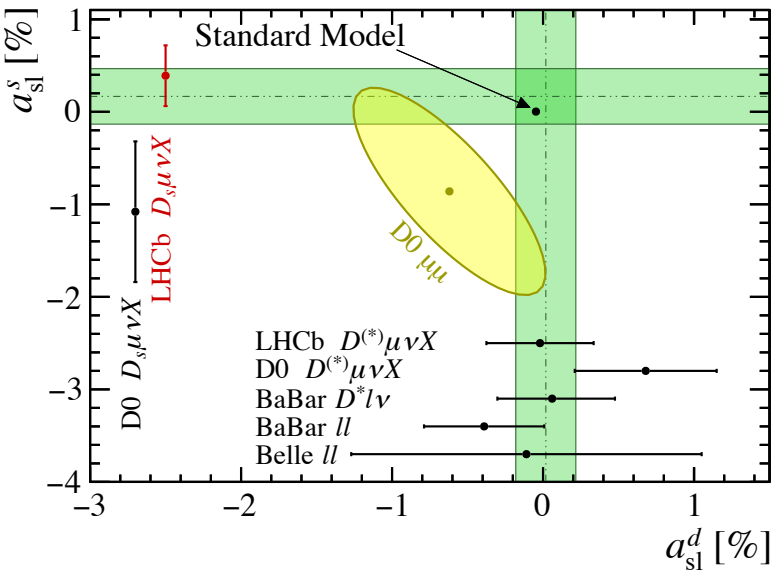

Figuur S.6: Overzicht van gepubliceerde metingen van $a^d_{\rm sl}$ en $a^s_{\rm sl}$, inclusief (in het rood) de meting van $a^s_{\rm sl}$ besproken in deze dissertatie. De verticale en horizontale banden geven de naïeve gemiddelden van pure metingen van $a^s_{\rm sl}$ en $a^d_{\rm sl}$ weer, die individueel zijn weergegeven met zwarte punten. De gele ellips laat het resultaat zien van de D0 meting. De onzekerheden corresponderen tot de 68% waarschijnlijkheidsintervallen. Meer informatie en referenties met betrekking tot deze figuur kunnen worden gevonden in het onderschrift van Fig. 5.10.

zich mengt tot een $\overline{B}^0_s$ kan vervolgens worden bepaald door het tellen van het aantal gebeurtenissen waarin een oorspronkelijk geproduceerd B^0_s mesonen vervalt als een $\overline{B}^0_s$ meson, aan de hand van de vervalsproducten. Als het meson is gereconstrueerd als een combinatie van $K^+K^-\pi^-\mu^+$ ($K^-K^+\pi^+\mu^-$), dan is het meson vervallen als een B^0_s ($\overline{B}^0_s$) meson.

Het B^0_s meson verandert vaak voordat het vervalt: de mengfrequentie is hoog. Dat levert een experimenteel voordeel op: zelfs als er een oneven aantal B^0_s en $\overline{B}^0_s$ mesonen zijn geproduceerd, zal enige voorkeur in het mengingsproces nog zichtbaar zijn als men slechts het aantal B^0_s en $\overline{B}^0_s$ vervalsproducten telt zonder daadwerkelijk de vervalstijden te meten en zonder te weten of het meson was geproduceerd als een B^0_s of $\overline{B}^0_s$ meson. Dit is geïllustreerd in Fig. S.8. Een meting van $a^s_{\rm sl}$ lijkt daarom neer te komen op een eenvoudige opgave: het aantal $K^+K^-\pi^-\mu^+$ en $K^-K^+\pi^+\mu^-$ combinaties tellen. Hierbij geldt dat het relatieve verschil tussen deze aantallen gelijk is aan $0.5 \times a^s_{\rm sl}$. Met een dergelijke telling alleen komt men echter bedrogen uit: kleine verschillen in de efficiëntie van het meetinstrument tussen de B^0_s vervalsproducten en $\overline{B}^0_s$ vervalsproducten beïnvloeden ook deze metingen. De uitdaging bij een competitieve meting van $a^s_{\rm sl}$ ligt daarom in de bepaling van deze subtiele verschillen, de zogenoemde instrumentele asymmetrie.

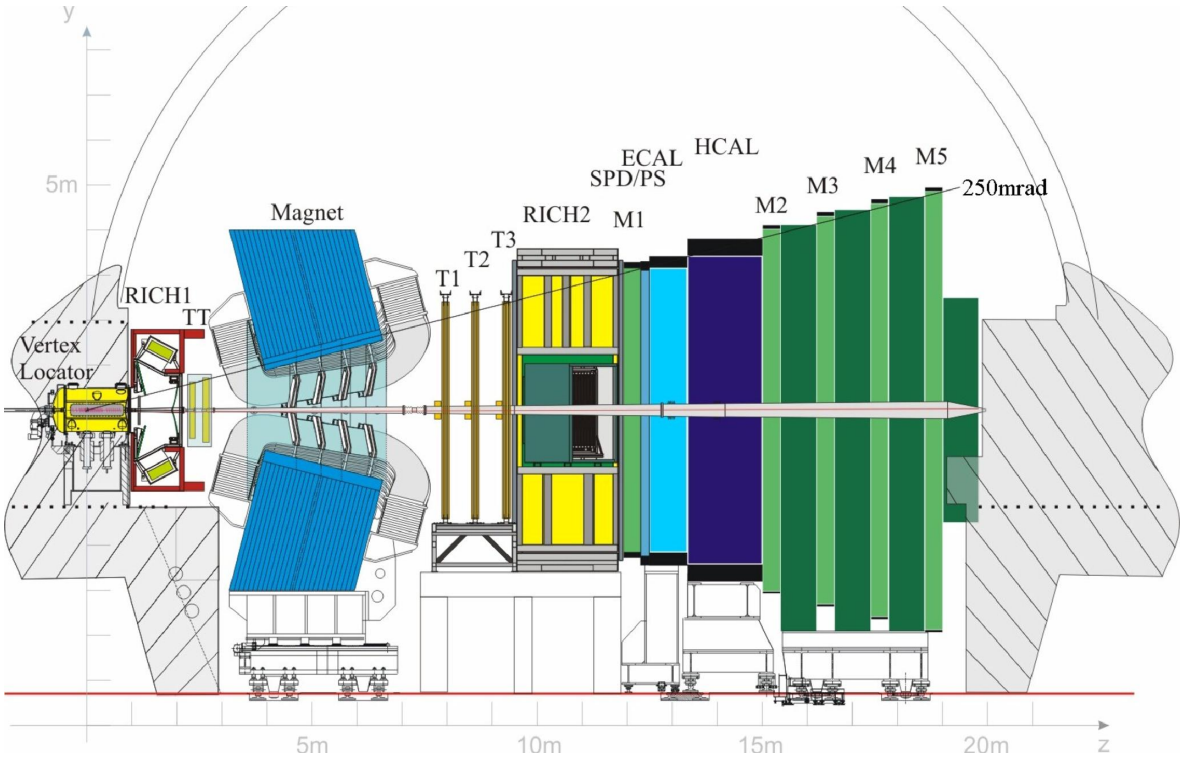

Figuur S.7: Schematische weergave van de LHCb detector. Figuur van Ref. [14].

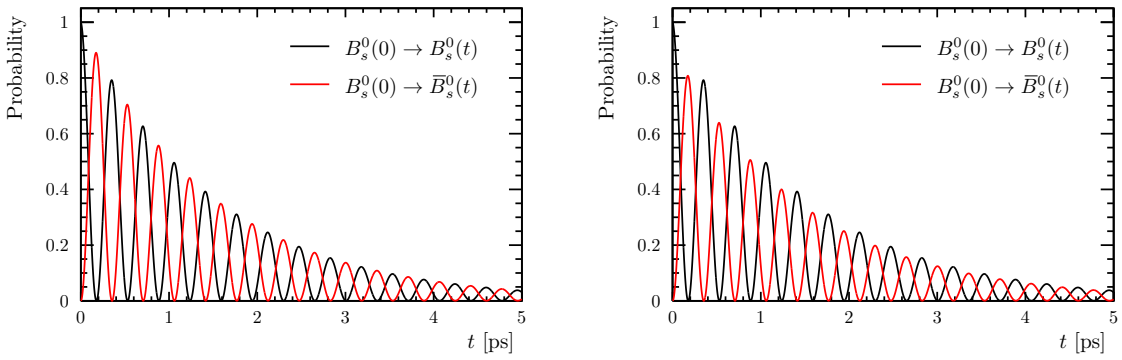

Figuur S.8: Waarschijnlijkheid van een B_s^0 meson geproduceerd als een B_s^0 om te vervallen als een B_s^0 of $\overline{B}_s^0$ meson, (links) in het realistische scenario van een kleine waarde van $a_{\rm sl}^s$ en (rechts) in het geval dat $a_{\rm sl}^s = 10\%$. Als men integreert over de vervalstijd van 2 tot 4 ps, zijn de waarschijnlijkheden in het linker scenario ongeveer gelijk, terwijl er een overmaat aan B_s^0 vervallen zou worden waargenomen in het rechter scenario. In de afwezigheid van achtergronden, zou het rechter scenario zorgen voor een overmaat van 5% van $K^+K^-\pi^-\mu^+$ kandidaten ten opzichte van $K^-K^+\pi^+\mu^-$ kandidaten.

Hoewel de LHCb detector ontworpen is om *CP* asymmetrieën te meten, zijn er nog steeds correcties nodig van ongeveer 0.1% voor een meting van $a^s_{\rm sl}$. Asymmetrieën kunnen optreden op alle niveaus van de reconstructie en selectie. Daarom zijn verschillende, passende vervallen gebruikt voor de kalibratie van de asymmetrie in de spoorreconstructie, de deeltjesidentificatie en de eerste fases van de selectie (de "trigger"). Al deze kalibraties maken gebruik van de omvangrijke productie van charm deeltjes in de LHCb detector. De totale onzekerheid ten gevolge van deze kalibraties is ongeveer van gelijke grootte als de totale statistische onzekerheid ten gevolge van het beperkte aantal geproduceerde B^0_s en $\overline{B}^0_s$ mesonen. De resulterende, gecorrigeerde waarde van $a^s_{\rm sl}$ is

$$a^s_{\rm sl} = (0.39 \pm 0.26 \pm 0.20)\%,$$

waarbij de eerste onzekerheid de statistische, en de tweede de systematische onzekerheden representeert. Dit resultaat is opgenomen als een rood datapunt in Fig. S.6.

Het verbeteren van het experimentele bereik

De meting van $a^s_{\rm sl}$ die beschreven is in deze dissertatie maakt gebruik van data verzameld in Run 1 van de LHC, in de jaren 2011 en 2012. Van 2015 tot en met 2018 leverde de LHC aan LHCb bijna twee keer zo veel proton-proton botsingen en ook nog met een hogere botsingsenergie. Deze hogere botsingsenergie zorgt voor een hogere B^0_s-meson productie per botsing, zodat de nieuwe data bijna viermaal zo veel B^0_s mesonen bevat in vergelijking met Run 1. Om er voor te zorgen dat nauwkeurige metingen van *CP* asymmetrieen zoals $a^s_{\rm sl}$ profijt hebben van deze nieuwe data, zijn er nieuwe technieken nodig om de detectorkalibratie te verbeteren. Voor deze ontwikkeling is eerst een gedetailleerde studie gedaan naar de onderliggende oorzaken van de instrumentele asymmetrieën. Interacties met het detectormateriaal en keuzes in het ontwerp van de LHCb detector zijn hier als hoofdzakelijke oorzaken uitgekomen.

Gemotiveerd door deze studie zijn er nieuwe procedures voorgesteld die de reconstructie-efficiëntie en asymmetrie bepalen van elektronen, muonen en pionen. Deze techniek maakt gebruik van de reconstructie in enkel de vertex detector, welke zeer efficiënt is. Het onderscheiden van signaal en achtergrond is de voornaamste uitdaging in deze techniek. Ondanks deze complicaties, is er in deze dissertatie aangetoond dat deze techniek geschikt is om *CP* asymmetriën te meten met de hogere precisie die nodig is voor de interpretatie van Run-2 data.

Acknowledgements

Writing this booklet and doing research has been a joy thanks to the many people that contributed, directly or indirectly, for which I'm very grateful. Out of these people, there are a few I would like to thank in particular, in Dutch or English.

Allereerst wil ik mijn grote dank uitspreken voor een geweldige fysicus en begeleider. Jeroen, het was een groot genoegen om door jou geïntroduceerd te worden tot het veld van de deeltjesfysica. Het geduld dat je hierbij had is minstens net zo bewonderenswaardig als de goede intuïtie. Ik ben je heel dankbaar voor het vertrouwen dat je sinds de eerste dag in mij hebt gehad.

Marcel en Antonio, ik wil jullie beiden hartelijk bedanken voor het grondig lezen van dit boekje en jullie kritische vragen die dit manuscript leesbaar hebben gemaakt voor de normale sterveling. En, Marcel, ik wil je hartelijk bedanken voor jouw rol als groepsleider. De bfys groep voelde als een hechte familie met ruimte voor iedereen, wat niet vanzelfsprekend is. Ook buiten de werkuren zorgde je voor de lijm in de groep, en de nachten carnaval met jou (en Céline) zal ik niet snel vergeten.

I enjoyed my time in the Nikhef group, and I would like to thank my former bfys colleagues (Veerle, Rose, Pieter, Mick, Vasilis, Mauricio, the other Jeroen, Suvayu, Roel, Tim, Elena, Silvia, Cristina, Lex, Flavio, Katya, Lennaert, Sean, Roman, Gerhard, Patrick, Wouter, Niels, Tjeerd, Daniel, Igor, Michele, Sevda, Jordy and Carlos) for discussing physics and having a drink together. It was a pleasure to see the boundaries between the experiments fade at the social events. Playing table football on the Friday afternoon with Remco, Tristan and Karel was great, and I hope that this tradition will last for many generations. Also a special thanks go to my two paranimfen, Jacco and Maarten, who had to deal with me daily either in the office or at home. Dank jullie wel, jullie zijn fantastisch!

During my stay at CERN there was room for fun and physics as well. I would like to thank Mika for his help on the reconstruction efficiencies and asymmetries. Meanwhile, the fun was provided by Marian, Greg, Sascha, Alex and Basem, who made the stay at CERN very enjoyable, such that I could return without any doubt in 2019.

Als laatste zou ik graag Naomi willen bedanken, mijn grootste steun tijdens het schrijven van dit proefschrift en de rest van het leven.